Fabrication and Characterization of Micro-Tubular Solid Oxide Fuel Cells

Yanhai Du

THE UNIVERSITY OF
WAIKATO
Te Whare Wānanga o Waikato

A Dissertation
Submitted in Partial Fulfilment
of the
Requirements for the Degree of

Doctor of Philosophy

in Materials and Process Engineering

The University of Waikato, Hamilton, New Zealand
March 2004

Abstract

Solid oxide fuel cells (SOFC) are an energy efficient, low pollution technology for generating power and have the potential to revolutionize energy generation. Tubular and planar concepts are the most common SOFC systems. The primary objective of this study was to develop a cost-effective process for fabricating micro-tubular SOFCs and to investigate how to improve fuel cell performance.

Two technical approaches were investigated for increasing the cell performance and reducing SOFC costs: (a) reducing electrolyte resistance by minimizing the electrolyte thickness, which consequently increases oxygen flux to the anode; and (b) using new electrolyte materials thereby making it possible for the fuel cell to operate at lower temperatures.

The new material primarily investigated for the SOFC was strontium- and magnesium-doped lanthanum gallate (LSGM), in which the single-phase perovskite LSGM region was determined. Yttria-stabilized zirconia (YSZ) and gadolinium doped ceria (CGO) electrolyte systems were also studied.

Paste extrusion was identified as a suitable method for high-speed manufacture of the tubular support components of SOFCs. Procedures were developed to extrude dense, straight, round (OD: 4.0±0.1 mm), thin walled (0.2±0.02 mm) tubular LSGM and YSZ electrolytes. The research systematically investigated developing a fabrication process, designing the extrusion die, the effects of formulation and process additives and how to handle, dry and sinter the extrudate.

The three-point bending strength of extruded and sintered LSGM was determined to be 287 MPa, 195 MPa, 184 MPa and 147 MPa at room temperature, 600°C, 800°C and 1000°C respectively. Room temperature burst strengths of the tubular electrolytes made from YSZ, LSGM and CGO were 127 MPa, 40 MPa and 63 MPa respectively. The average thermal expansion coefficients between room temperature and 800°C were 10.18×10^{-6}/°C, 11.01×10^{-6}/°C and 12.04×10^{-6}/°C, for YSZ, LSGM, and CGO respectively.

The maximum power density at 800°C for a 220-μm thick LSGM electrolyte was 460-482 mW/cm^2, which is more than double the power density for YSZ cells (200-220 mW/cm^2) at 850°C. Reducing LSGM thickness from 550 μm to 220 μm increased the maximum power densities by more than 30%. Repeatable cell power outputs per cell of 2.5 W at 800°C and 2.8 W at 850°C were obtained. Cell performance degradation was measured at 12% during the 500-hour test.

A novel tubular stack design concept was developed to significantly increase stack volumetric power packing density by 84% for a three-cell module or 116% for a five-cell module, compared to a single-tube cell design. This design can also increase fuel efficiency.

Recommendations for future work are given. It is suggested that (1) an anode-supported nanosize LSGM electrolyte system be used for the next generation of intermediate-temperature SOFCs; (2) the LSGM layer be applied by plasma spraying; and (3) nickel-free anodes for LSGM electrolyte systems are developed.

This comprehensive study discusses the relationship between the materials, processing, manipulation of the microstructure, properties and tubular SOFC performance. The unique process developed for producing tubular support components has been scaled to commercial production and represents a significant scientific, engineering and commercial perspective contribution to fuel cell technology.

Acknowledgements

Several people helped me with this project over the past few years and I would like to take this opportunity to thank them.

Firstly, I would like to express my deep appreciation to my supervisors, Professor Nigel Sammes, for introducing me to the fuel cell field, which has led me to this new career, and for all his guidance, support and advice throughout the course of this research; Associate Professor Janis Swan and Associate Professor Deliang Zhang for their willingness to take over the formal supervision roles after Professor Sammes left the University of Waikato, and for their help and advice on aspects of the study, especially their comments and suggestions when preparing this dissertation.

Thanks are due to various colleagues and our research group: Dr. Geoffrey Tompsett for many fruitful discussions and unflagging encouragement, and for proof-reading the manuscript; and Dr. Ray England, Dr. Fanglin Chen, and Dr. Alan Feighery for their encouragement and reading chapters.

I would also like to praise Yuanji Zhang and Alf Harris for technical assistance with the XRD and SEM. To my friends, Wei Wang, Darleen Blood, and Charles Oliveira – thank you for making my life meaningful.

Finally, on a more personal level, I would like to express my heartfelt thanks to my family for their understanding, encouragement and emotionally support, especially my wife Jie Yao, who has unquestioningly and unwaveringly stood behind me, looking after our daughter Yanxi and son Kevin, and for not stopping me from spending hundreds of weekends and thousands of evenings in the lab and office to complete this thesis while working full time.

Yanhai Du

Table of Contents

Chapter One: Solid Oxide Fuel Cell Technology

Chapter Two: Fabrication Techniques for Tubular SOFCs

Chapter Three: Experimental Methods and Equipment

Chapter Four: Optimising Extrusion of Thin YSZ Tubes For SOFC Electrolytes

Chapter Five: Synthesising and Fabricating Strontium- and Magnesium-Doped $LaGaO_3$ Tubular Electrolytes

Chapter Six: Mechanical and Thermal Properties of Tubular Solid Oxide Fuel Cells

Chapter Seven: Electrical Performance of Micro-Tubular SOFCs and a Novel Stack Design Concept

Chapter Eight: Conclusions and Recommendations

List of Figures

List of Tables

Notation

1. Abbreviations

8YSZ	8 mole% yttria stabilized zirconia
AFC	alkaline fuel cell
AMP-95	90 wt% 2-amino-2-methyl-1-propanal, 5 wt% 2-(methylanino)-2-methyl-1-propanol and 5 wt% water
BIMEVOX	bismuth, dopant metal, vanadium and oxygen
BOP	balance-of-plant
CGO/GDC	gadolinia-doped ceria
CTE/TEC	thermal expansion coefficient
CVD	chemical vapor deposition
DC	direct current
EVD	electrochemical vapor deposition
GDC/CGO	gadolinia doped ceria
GT	gas turbine
HHV	high heating value
IEP	isoelectric point
JVD	jet vapor deposition
LDC	$Ce_{0.6}La_{0.4}O_{1.8}$
LG	$La_4Ga_2O_9$
LHV	low heating value
LSC/LSCo	La-Sr-cobaltite
LSCF	$La_{1-x}Sr_xCo_yFe_{1-y}O_3$
LSF	$La_{1-x}Sr_xFeO_3$
LSG	$LaSrGa_3O_7$ and/ or $LaSrGaO_4$
LSGM	strontium- and magnesium-doped lanthanum gallate, $La_{1-x}Sr_xGa_{1-y}Mg_yO_{3-(x+y)/2}$
LSGM-1010	$La_{0.9}Sr_{0.1}Ga_{0.9}Mg_{0.1}O_{3-\delta}$
LSGM-1015	$La_{0.9}Sr_{0.1}Ga_{0.85}Mg_{0.15}O_{3-\delta}$
LSGM-2015	$La_{0.8}Sr_{0.2}Ga_{0.85}Mg_{0.15}O_{3-\delta}$
LSGM-2020	$La_{0.8}Sr_{0.2}Ga_{0.8}Mg_{0.2}O_{3-\delta}$
LSGMCo	$La_{0.8}Sr_{0.2}Ga_{0.8}Mg_{0.15}Co_{0.05}O_{3-\delta}$
LSM	strontium doped lanthanum manganite, $La_{0.8}Sr_{0.2}MnO_3$
LZ	$La_2Zr_2O_7$
MCFC	molten carbonate fuel cell
MEKET	methyl ethyl ketone
Methocel	methyl cellulose
MIEC	mixed ionic-electronic conductor
MOR	modulus of rupture
MTFC	multiple tubular fuel cell
Ni/8YSZ Ni/YSZ	Ni and YSZ cermet (anode material)
OCV	open circuit voltage

P	single perovskite phase
PAFC	phosphoric acid fuel cell
PEG	polyethylene glycol
PEM	proton exchange membrane, polymer electrolyte membrane
PEMFC	polymer electrolyte membrane fuel cell
PEO	poly(ethylene oxide)
PVA	polyvinyl alcohol
PVB	polyvinyl butyral
PVP	polyvinyl pyrrolidone
SCF	$SrCo_{0.8}Fe_{0.2}O_3$
ScZ, SDZ	scandium doped zirconia
SDC	$Ce_{0.8}Sm_{0.2}O_{1.9}$
SDZ	scandia-doped zirconia
SEM	scanning electron microscope
SG	$Sr_3Ga_2O_8$
SmSrCo	$Sm_{0.5}Sr_{0.5}CoO_3$
SOFC	solid oxide fuel cell
SZ	$SrZrO_3$
TEC	thermal expansion coefficient
TPB	triple phase boundary, three-phase boundary
UPS	uninterruptible power service
VPPD	volumetric power packing density
XRD	X-ray diffraction
YSZ	yttria-stabilized zirconia

2. Symbols

α	(i) velocity factor (ii) thermal expansion coefficient
β	(i) wall velocity factor are parameters characterizing the paste (ii) wall velocity factor
Φ_E	the electric efficiencies
Φ_F	fuel efficiencies
η	fuel efficiency
η_{max}	maximum (or theoretical) efficiency
η_{act}	activation polarization
η_{anode}	anode polarization
$\eta_{cathode}$	cathode polarization
η_{conc}	concentration polarization
η_{ohm}	ohmic polarization
μ_f	fuel utilization efficient
θ	extrusion die entry half-angle
σ_0	paste yield stress at zero velocity
σ	burst stress of tube
τ_0	wall shear stress at zero velocity

Δd	ID difference between the two neighbouring tubes
D	die-land diameter
D, d	inside diameter of tube
d_1	smallest tube inside diameter
D_0	barrel diameter
D_{Ni}	density of Ni
D_{YSZ}	density of YSZ
E	ideal potential
E	(i) ideal standard potential for cell reaction (ii) ideal equilibrium potential
E_{anode}	anode potential
$E_{cathode}$	cathode potential
E_{ocv}	open circuit voltage
E_r	reversible voltage
F	(i) Faraday constant (ii) rupture force
ΔG_f	Gibbs free energy
H	height of bar
ΔH_f	enthalpy of formation
L	(i) die-land length (ii) span between the lower supports of three-point bend
L_0	initial sample length
M_{Ni}	molecular weight of Ni
M_{NiO}	molecular weight of NiO
n	(i) number of electron (ii) number of tubes in a module
P	(i) extrusion pressure drop (ii) gas pressure (iii) burst pressure
P_1	pressure drop at die-entry
P_2	pressure drop in the die-land
P_a	cell area power density
P_v	volumetric power packing density
R	(i) total cell resistance (ii) universal gas constant (iii) radius of rod
t	wall thickness of tube
T_g	glass transition temperature
V	paste velocity in die-land
V_{Zr}^{4}	free vacancies
W	width of bar

Chapter One

Solid Oxide Fuel Cell Technology*

Solid Oxide Fuel Cells (SOFCs) are emerging electrochemical energy conversion devices that can deliver clean, quiet, and potentially renewable energy for primary, base-load and back-up power. This technology now has to be commercialised. Recently fuel cell studies have focused on reducing operating temperatures and developing new materials and fabrication techniques. The overall objectives of this thesis are to develop a cost-effective process for fabricating micro-tubular SOFCs using new intermediate temperature electrolyte materials, and to understand the interplay of material-process-microstructure on performance. This chapter presents an overview of SOFC technology including operating principles, component and material requirements, cell designs, and the benefits of SOFCs. It highlights current trends in SOFC research and development and technical challenges remaining to commercialise SOFC technology.

1.1 Fuel Cell Technology

1.1.1 The Fuel Cell

A fuel cell is an electrochemical device that converts chemical energy of gaseous fuels (e.g., hydrogen, natural gas, and biomass) directly into electrical energy (and heat) via an electrochemical process, without the limitations inherent in the thermal engine cycle (the Carnot cycle). The basic physical structure of a fuel cell consists of a dense electrolyte layer in contact with a porous anode and cathode on either side. In contrast to conventional methods, fuel cells offer a fundamentally different way of generating electrical power from a variety of fuels. For example, besides pure hydrogen (H_2), both natural gas and coal gas may be used. A fuel cell can be regarded as a battery with an external rather than internal energy source. Although a fuel cell has components and characteristics similar to a typical

---

* Some information in this Chapter have been published as: Yanhai Du and N.M. Sammes, in *Proceedings of the 5th Annual New Zealand Engineering and Technology Postgraduate Conference*, ed. B. Teekman, P. Milliken and N. Body, Massey, New Zealand, November, 1998.

battery, it has several differences. Prominent among these differences is the fact that a battery is an energy storage device, while a fuel cell is an energy conversion device. All batteries will eventually run down or require recharging but a fuel cell generally can produce electricity as long as the fuel and oxidant are supplied to the electrodes. In reality, the life of a fuel cell is limited by component degradation, primarily from corrosion.

The fuel cell effect and principles were discovered by the Swiss professor Christian Friedrich Schoenbein (1777-1868) at the University of Bassel in 1838 [1]. After initial experiments in 1839, Sir William Robert Grove (1811-1896), a London lawyer with a strong engineering background, invented the fuel cell concept and in 1845 demonstrated an apparatus for replacing batteries. This was regarded as the first fuel cell in the world [2]. The Grove cell, as the new fuel cell was called, operated at room temperature with dilute sulphuric acid as the electrolyte and platinum (Pt) electrodes. In 1889, Mond and Langer used porous electrodes to improve the fuel cell performance and/or the power density to 3.5 mA/cm^2 at 0.73 V, while operating on hydrogen and oxygen (O_2) [3]. In 1933, Bacon, the first recipient of the Grove Medal, started developing a fuel cell system capable of delivering a power density of 1000 mA/cm^2 at 0.8 V [3]. Bacon's cell was operated on hydrogen and oxygen at elevated pressure.

Over the years, there have been many attempts to develop fuel cells as power sources. In the early 1960s, alkaline fuel cells were developed as electrical generators and a source of drinking water for Apollo spacecraft; which could be considered as a significant milestone for fuel cell technology development [4]. The recent drive for more efficient and less polluting distributed power generating technologies has resulted in substantial resources being directed into fuel cell development [5, 6].

The general characteristics of fuel cell generators include [7]: high energy conversion efficiency; low environmental pollution; quiet; no moving parts in the energy converter; fuel flexibility; modular installations to match load (this allows power generation to be shifted from central stations to the user sites); and increased reliability. The drawbacks of fuel cells include: expense, public unfamiliarity with the technology, and lack of fuel infrastructure.

1.1.2 Merits of Fuel Cells

Fuel cells offer a new alternative to conventional electrical power sources for many applications. Studies [8] have shown that 33% of the carbon dioxide emissions come from industrial use, 32% from transportation, 20% from residential and 15% from commercial use. Fuel cells, such as SOFCs, have lower emissions than an equivalent power plant using natural gas. For example, a typical fuel cell generates less than 0.5 ppm nitric oxides (NO_x), almost zero sulphurous oxides (SO_x) or carbon monoxide (CO), the lowest carbon dioxide (CO_2), and zero volatile organic components (VOC_s) [9]. The low output of pollutants is primarily due to the high operating efficiency of the fuel cell.

The fuel flexibility is one of the major benefits of fuel cell technology. Depending on the type of fuel cells and the fuel processing/reformer, any of the following fuels can be used: hydrogen (H_2), methane (CH_4), methanol (CH_3OH), ethanol (C_2H_5OH), propane, anaerobic digester gas, natural gas, coal gas, landfill gas, gasoline, or even diesel. At present, gaseous H_2 is the fuel used for most applications due to its high reactivity when suitable catalysts are used, ability to be produced from hydrocarbons for terrestrial applications, and high energy density when stored cryogenically for closed environment applications such as in space. However, alternatives such as CH_4 can be electrochemically oxidized in a fuel cell, while air is the commonly used oxidant. To use hydrocarbon fuels, such as natural gas or even gasoline, a fuel processor or reformer is often needed. This can be either an external reformer (where the fuel is processed outside the fuel cell) or an internal reformer (where the fuel is processed inside the fuel cell).

1.1.3 Fuel Cell Applications

Fuel cell power ratings are from a few watts to mega watts, for example, 1-10 kW for domestic/residential applications, 10-300 kW for residential/commercial applications, up to 250 kW-10 MW for power stations [4]. Because of their mobility and variable size, fuel cells are alternatives to conventional electrical power sources for many applications. They can be used to power vehicles and appliances (from lawnmowers to laptop computers), buildings, data centres, hospitals, and other users who demand round-the-clock, reliable electrical power. The major applications are as stationary electric power plants, including cogeneration units; as motive power for vehicles; and as on-board electric power for apace shuttles or other closed environments such as ocean-going freighter [7].

The US Department of Defence Fuel Cell Demonstration Program (Figure 1-1) has 29 sites, including eight categories of buildings and span 17 states in the USA. Seven of the fuel cells are configured to provide back-up electrical power if there is a grid power outage. Thermal output from the fuel cell is used to heat boiler make-up water, domestic hot water, space heating, or condensate return.

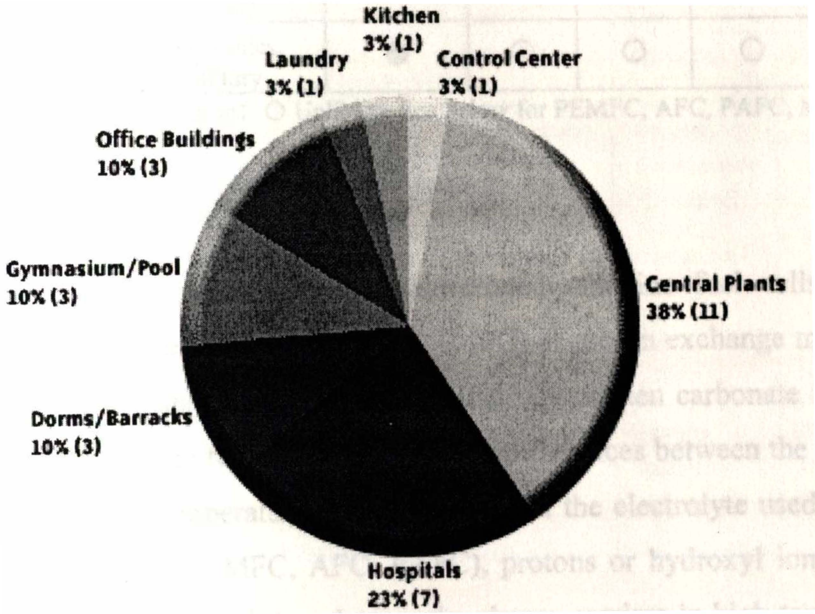

Figure 1-1 US Department of Defence Fuel Cell Demonstration Program Sites [10].

The global SOFC market is expected to approach 20 GW/year by 2010, with half of that market being in the USA and Europe [7]. Current cell life is estimated to be 5-10 years and Siemens Westinghouse believes cell life for commercial cells will be 10-20 years [11]. Transportation sectors worldwide have shown remarkable interest in fuel cells: nearly every major vehicle manufacturer is supporting fuel cell technology development. Table 1-1 summarises the suitability of fuel cells for different categories of applications. SOFCs are believed more suitable for large stationary power applications, niche stationary and distributed power, and some mobile applications [5].

Table 1-1 Fuel Cell Technologies and Their Applications [5].

Target Applications			PEMFC	AFC	PAFC	MCFC	SOFC
Stationary-distributed	Grid sited	Central	○	○	○	●	●
		Distributed	○	○	○	●	●
		Re-powering	○	○	●	●	●
	Customer sited cogeneration	Residential	●	◉	○	◉	●
		Commercial	●	◉	●	●	●
		Light industrial	◉	◉	●	●	●
		Heavy industrial	○	○	●	●	●
Transportation	Propulsion	Light duty	●	○	○	○	○
		Heavy duty	●	○	◉	◉	◉
	Auxiliary power unit	Light & heavy duty	●	○	○	○	●
Portable	Premium	Recreational, military	●	○	○	○	●
	Micro	Electronics, military	●	○	○	○	○

● Likely; ◉ Under consideration; ○ Unlikely. See below for PEMFC, AFC, PAFC, MCFC.

1.1.4 Different Fuel Cell Technologies

Several types of fuel cells have been developed: alkaline fuel cells (AFC), polymer electrolyte membrane fuel cells (PEMFC) or proton exchange membrane fuel cells (PEM), phosphoric acid fuel cells (PAFC), molten carbonate fuel cells (MCFC), and solid oxide fuel cells (SOFC). The differences between the types are mainly the operating temperatures and the nature of the electrolyte used. In low-temperature fuel cells (PEMFC, AFC, PAFC), protons or hydroxyl ions are the charge carriers in the electrolyte, whereas the charge carriers in high-temperature fuel cells (SOFC, MCFC) are usually oxygen ions or carbonate ions. Major characteristics and differences between the various fuel cells are summarized in Table 1-2.

Of the different fuel cells, most attention has been given to PEMFCs and SOFCs. PEMFCs operating at ambient or near 100°C are considered the best contenders to replace internal combustion engines in motor vehicles. SOFCs offer the highest system efficiency and widest application potential, and are considered more suitable in large-scale multi-MW stationary plants because cogeneration is possible.

Table 1-2 Summary of Different Types of Fuel Cells [7, 12, 13].

Fuel Cell Type	PEMFC	AFC	PAFC	MCFC	SOFC
Operating temperature	60-100°C	60-120°C	160-220°C	600-650°C	700-1000°C
Electrolyte	Proton exchange membrane	Potassium hydroxide	Liquid phosphoric acid	Liquid molten carbonate	Ceramic
Charge carrier	H^+	OH^-	H^+	$CO_3^=$	$O^=$
Catalyst	Pt	Pt	Pt	Ni	Perovskites
Prime cell components	Carbon-based	Carbon-based	Graphite-based	Stainless steel-based	Ceramic
CO impact	Poison	Poison	Poison	Fuel	Fuel
S impact	Few studies	Unknown	Poison	Poison	Poison
External reformer for CH_4	Yes	Yes	Yes	No	No
Co-generation	No	No	Yes	Yes	Yes
Efficiency (LHV)	30-45%	30-50%	30-45%	45-60%	45-75%
Major Advantages / disadvantages	• Quick start-up • H_2 preferable • Heat & water management issues	• Pure H_2 • Good performance • Expensive	• Lower performance than AFC • Need external reformer • Expensive	• Wider fuel choices • Co-generation • Corrosive liquid electrolyte • CO_2 at cathode	• All ceramic • Wider fuel choices • Co-generation • High temperature
Installed large units	250 kW (Ballard)	12 kW (for space shuttles) (ZeTek)	1.2 MW 5,000 h (Milan)	2 MW 4,000 h (Fuel Cell Energy)	300, 220 kW; 100kW-17500h (SWPC)
Major Applications	Transportation Stationary	Space Stationary Transportation	Stationary	Stationary	Stationary Power station

1.1.5 Advantages of Solid Oxide Fuel Cells

SOFCs are so named because they use solid oxide materials as the electrolytes. This type of fuel cell originated with the discovery of solid-oxide electrolytes in 1899 [14] and the operation of the first ceramic fuel cell at 1000°C by Baur and Preis in 1937 [15]. There are two major types of SOFCs depending on the type of electrolyte conduction: oxygen-ion conductor or proton-conductor. The most advanced SOFCs, which operate at 850-1000°C, are based on oxygen-ion-conducting yttria-stabilized zirconia (YSZ) as the electrolyte, nickel/YSZ cermet for anodes, doped lanthanum manganite for cathodes, and doped lanthanum chromite for interconnects.

SOFCs have the following advantages over other types of fuel cells: (1) high efficiency; (2) ability to use CO along with H_2 as fuel; (3) lack of noble catalysts used; (4) no humidification management issue; and (5) longer cell lifetime. The temperature from the exhaust is high enough for it to be used for further electrical production in co-generation, thereby increasing efficiency to 80%. Theoretically, it should be possible to construct devices of 80-90% efficiency [16]. High conversion efficiency, wider fuel choices and lower cost are the main drivers of SOFCs. Breakthroughs in SOFC technology in ceramic materials, design, and manufacturing indicate that substantially enhanced power densities are possible, comparable to PEM fuel cells [17].

Low temperature fuel cells, such as PEMFCs, require noble metal electrocatalysts (for example, Pt) and expensive membrane materials to achieve practical reaction rates at the anode and cathode, and H_2 is the preferred fuel. However, SOFCs can use a wider choice of fuels and less expensive catalytic materials (for example Ni). The catalytic function of electrodes in SOFCs is less important than that in low temperature fuel cells because ionisation reaction rates and ionic transport are high at elevated temperatures. Carbon monoxide "poisons" a noble metal anode catalyst such as Pt in low-temperature fuel cells, but it serves as a potential source of H_2 in high-temperature fuel cells. CH_4 and CO can be used in SOFCs because of the inherently rapid electrode kinetics and the reduced need for high catalytic activity at high temperature. In the presence of a catalyst, hydrogen can be reformed from natural gas and steam from around 760°C [7]. The high temperatures in SOFCs can favour the conversion of CH_4 and CO to H_2. Because of the all-ceramic character in all SOFC components, there is no liquid electrolyte with its attendant material corrosion and electrolyte management problems.

The high operating temperature (900-1000°C) of SOFCs is required to provide sufficient oxygen ion conductivity for the YSZ electrolyte. This temperature, however, places stringent requirements on materials therefore manufacturing costs are high, primarily because expensive high-temperature alloys must be used for the balance-of-plant (BOP) structures. The key technical challenges facing SOFCs are developing low-cost materials and identifying cost-effective methods to fabricate the ceramic structures. These costs would be substantially reduced if the operating temperature could be lowered to 600-800°C. Lower temperature operation allows cheaper structural components, such as stainless steel, to be used. This is the major reason to develop intermediate temperature SOFC systems.

Intermediate-temperature SOFCs combine the best available attributes of fuel cell technology with intermediate temperature (600-800°C) operation. Ceramic components are used for electrodes and electrolytes. Using solid-state components avoids some design issues such as corrosion and handling inherent in liquid electrolyte fuel cells. The reduced temperature from YSZ based electrolyte fuel cells allows stainless steel construction, thus reducing manufacturing costs. The major drawback in using a lower operating temperature is that the electrolyte conductivity and electrode kinetics decrease significantly. Present technology development is addressing these issues through thin-film electrolyte development and searching for alternate materials.

1.2 Solid Oxide Fuel Cell Operation

1.2.1 Operating Principles

A SOFC is an all-ceramic electrochemical device that converts the chemical energy of fuel directly and efficiently into electrical energy without combustion. The simplified basic operation principles of SOFCs are shown in Figure 1-2. A fuel (for example, H_2) is fed to the anode where it is electrochemically oxidized, and electrons are released to an external circuit. An oxidant (for example, O_2) is supplied to the cathode where it is reduced, and electrons are accepted from the external circuit. The oxygen ions flow internally from the cathode across the electrolyte to the anode.

As well as pure H_2, CO and hydrocarbons such as CH_4 can be used as fuels in SOFCs. It is feasible that the water gas shift involving CO ($CO+H_2O \rightarrow H_2+CO_2$) and the steam reforming of CH_4 ($CH_4+H_2O \rightarrow 3H_2+CO$) occurs at the high operating temperature of SOFCs to produce H_2 that is easily oxidized at the anode. Direct oxidation of CO in fuel cells is well established; however, reforming methane to hydrogen predominates in the present SOFC development. SOFC designs for the direct oxidation of CH_4 have not been thoroughly investigated.

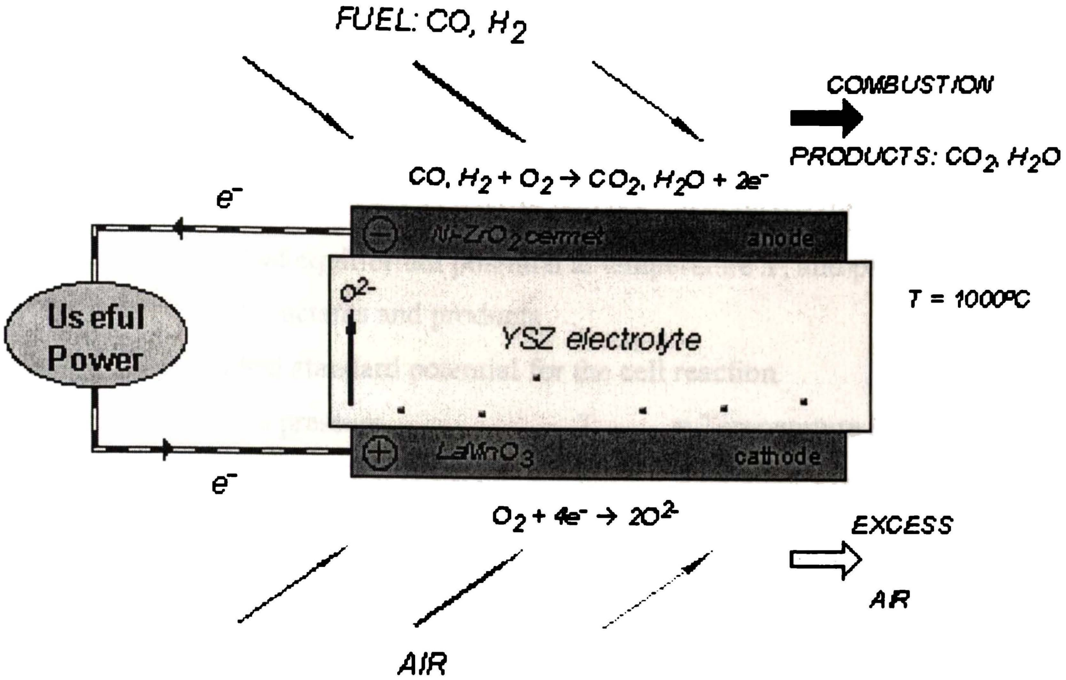

Figure 1-2 Concept Diagram of Solid Oxide Fuel Cell [18].

The main electrochemical reactions in a SOFC system are:

At cathode site: $\frac{1}{2}O_2 + 2e' \rightarrow O^{2-}$

At anode: $H_2 + O^{2-} \rightarrow H_2O + 2e'$

$CO + O^{2-} \rightarrow CO_2 + 2e'$

$CH_4 + 4O^{2-} \rightarrow 2H_2O + CO_2 + 8e'$

Typically, the overall cell reaction in a fuel cell using hydrogen is represented by:

$$H_2 + \frac{1}{2}O_2 \rightarrow H_2O$$

The open circuit voltage (E_{ocv}) or reversible voltage (E_r) of the cell is given by the free energy (ΔG) of the fuel oxidation reaction [6], according to E_{ocv} (E_r) = -(ΔG)/nF, Where n = number of electrons transferred, and F = Faraday constant. The corresponding Nernst equations for the above reactions are in Table 1-3.

Standard conditions are one atmosphere and 25°C. The standard Nernst potential E^o is the ideal cell voltage at standard conditions. It does not include losses in an operating fuel cell. Thus, E can be thought of as the open circuit voltage (OCV).

Table 1-3 Fuel Cell Reactions and Corresponding Nernst Equations [7].

Cell reactions	Nernst equations
$H_2 + ½O_2 \rightarrow H_2O$	$E = E^o + (RT/2F)\ln[P_{H_2}/P_{H_2O}] + (RT/2F)\ln[P^{½}_{O_2}]$
$CO + ½O_2 \rightarrow CO_2$	$E = E^o + (RT/2F)\ln[P_{CO}/P_{CO_2}] + (RT/2F)\ln[P^{½}_{O_2}]$
$CH_4 + 2O_2 \rightarrow 2H_2O + CO_2$	$E = E^o + (RT/8F)\ln[P_{CH_4}/P^2_{H_2O}P_{CO_2}] + (RT/8F)\ln[P^2_{O_2}]$

Where: E = Ideal equilibrium potential at temperature T, and partial pressures of reactants and products

E^o = Ideal standard potential for the cell reaction

P = Gas pressure   T = Temperature (K)

R = Universal gas constant   F = Faraday's constant

1.2.2 Performance

Theoretical performance of a fuel cell depends on the electrochemical reactions that occur with different fuels and oxygen, and is defined by its Nernst potential. For example, the H_2 oxidation potential is 1.229 volts with liquid water product and 1.18 volts with gaseous water product [19]. For a single fuel cell, the OCV is typically in the range of 1.1-1.2 V. Under load conditions, however, the voltage of a single cell decreases and the peak power is typically observed at half of the OCV (0.6-0.7 V is the usual target voltage).

In a practical fuel cell, when drawing current (the useful work in electrical energy form), the actual cell potential is decreased from its theoretical potential due to irreversible losses. Several sources contribute to the irreversible losses (also called polarization or overpotential). They are (Figure 1-3): activation polarization (η_{act}), ohmic polarization (η_{ohm}), and concentration polarization (η_{conc}). These losses give an actual cell voltage (V_{cell}) less than the theoretical potential E (E=V-Losses). The activation polarization occurs at low current density due to electronic barriers that need to be overcome before current and ion flow. Ohmic losses are attributed to resistance to ion and electron resistance flow in the electrolyte, electrode, and interconnect materials, respectively. Ohmic polarization varies directly with current, increasing over the whole range of current because cell resistance remains essentially constant for a given fuel cell. Gas transport or concentration losses occur over the entire range of current density but become prominent at high current. Activation and concentration polarization can exist at both cathode and anode in a fuel cell.

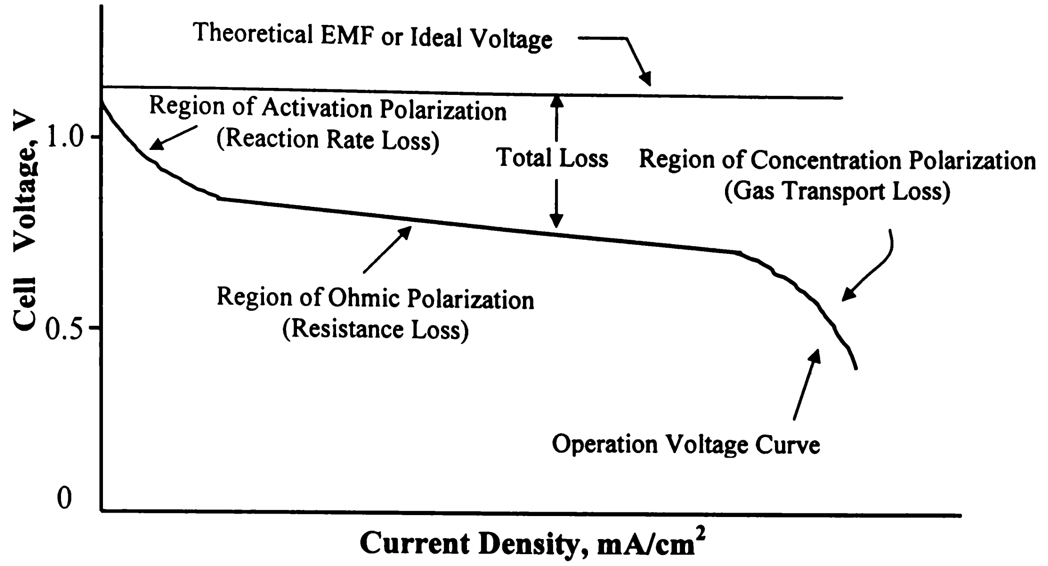

Figure 1-3 J-V Characteristic of a Typical Fuel Cell [7].

Ohmic losses through the electrolyte can be reduced by decreasing electrolyte thickness and enhancing its ionic conductivity. These losses can be expressed using Ohm's law for both the electrolyte and the electrodes: $\eta_{ohm} = iR$, where i is the current flowing through the cell, and R is the total cell resistance, which includes electronic, ionic, and contact resistance.

Voltage losses in SOFCs are governed by ohmic losses in the cell components. The cathode ohmic polarization (iR) in a cathode supported tubular SOFC dominates the total ohmic loss (Table 1-4) despite the high specific resistivities of the electrolyte and cell interconnection. This is because there is a relatively short conduction path through these components compared with the long current path in the cathode. The cell voltage of a fuel cell (V_{cell}) is given by Equation 1-1 [7].

$$\mathbf{V_{cell} = (E_{cathode} - E_{anode}) - |\eta_{cathode}| - |\eta_{anode}| - iR} \qquad \textbf{Equation 1-1}$$

Where $E_{cathode}$ = cathode potential
E_{anode} = anode potential
$\eta_{cathode}$ = cathode polarization
η_{anode} = anode polarization
R = total cell resistance
i = current flow through the cell

Table 1-4 Contribution to Ohmic Resistance (iR) in a Cathode Supported SOFC, after [20].

Cell components	Cathode	Anode	Electrolyte	Interconnect
Material	Doped $LaMnO_3$	Ni/YSZ cermet	YSZ	Doped $LaCrO_3$
Thickness	202 mm	0.1 mm	0.04 mm	0.085 mm
Resistivity (1000°C)	0.013 ohm cm	3×10^{-6} ohm cm	10 ohm cm	1 ohm cm
Contribution to ohmic losses	45%	18%	12%	25%

One of the goals of fuel cell development is to minimize polarization so that cell voltage (V_{cell}) can approach the theoretical maximum value $\Delta E = E_{cathode} - E_{anode}$. Technical approaches to this goal include: improving anode and cathode structures, having better electrocatalysts, obtaining higher electrolyte ionic conduction, and/or using thinner components. For a given cell design, cell performance can also be improved by optimising operating conditions, for example, using higher gas pressure, higher temperature, or using purer gas. According to the Nernst equation for the hydrogen reaction (Table 1-3), the ideal cell potential at a given temperature can be increased by operating a fuel cell at higher reactant pressures. Improvements in fuel cell performance have, in fact, been observed at higher pressures as shown in Figure 1-4. However, increasing system pressure increases system cost because of the high pressure BOP.

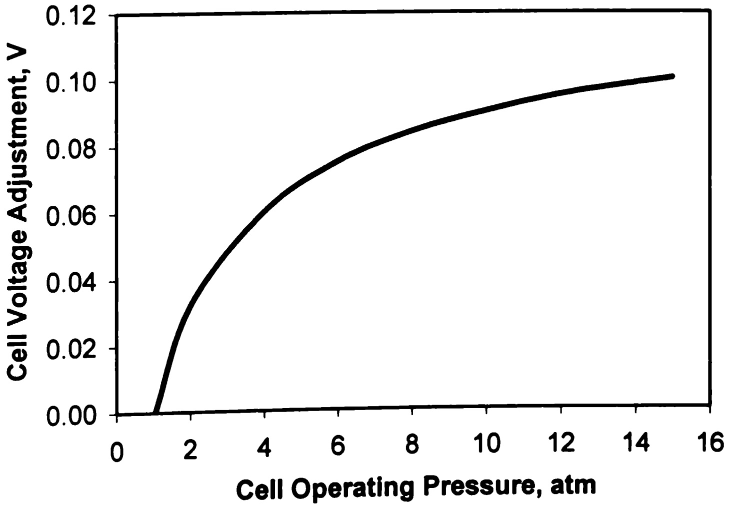

Figure 1-4 Effect of Pressure on Cell Voltage [21].

On the other hand, cell voltage decreases as fuel utilization increases due to mass transfer limitation through the thick anode structure. A steep voltage drop occurs when fuel utilization is higher than 80% (Figure 1-5). Performance and efficiency can be improved by reducing the thickness and increasing the porosity of the anode.

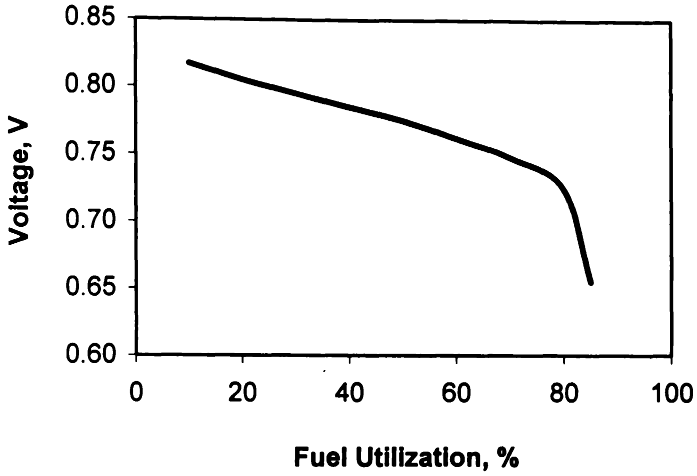

Figure 1-5 Effect of Fuel Utilization on Cell Voltage in an Anode-Supported Planar SOFC Operated at 750°C [22].

1.2.3 Efficiency

A SOFC can convert more than 50-60% of the energy in its fuel source to electricity and at the same time produces high temperature exhaust gases from the electrochemical process. When the high quality waste heat produced by the fuel cell is used, e.g. for cogeneration, the overall efficiency could reach 85% [23].

Different terms are used to describe efficiencies in fuel cell operation: fuel cell efficiency, fuel utilization coefficient, and system efficiency. Fuel cell efficiency (η) is defined as the ratio of electricity produced from a fuel cell and the energy content of the fuel supplied. Maximum (or theoretical) efficiency (η_{max}) is the ratio between the change in specific Gibbs free energy (ΔG_f) and the change in enthalpy of formation (ΔH_f), as shown in Equation 1-2. If water is the product, ΔH_f is -241.83 kJ/mole for steam, and -285.84 kJ/mole for liquid. Therefore the maximum efficiency (lower heating value) of hydrogen fuel cells is calculated to be 98%, 94%, and 80% at 25°C, 80°C and 800°C respectively [13].

$$\eta_{\max} = \frac{\Delta G_f}{\Delta H_f} \times 100\% \qquad \textbf{Equation 1-2}$$

Fuel utilization coefficient (μ_f) is the ratio between the mass of fuel reacted in a cell and the mass of fuel fed to the cell. System efficiency is the ratio of net electricity output and heat recovered from a stack to the fuel fed into the system. The term lower heating value (LHV) is used when water product is steam while the higher heating value (HHV) is used when the product is in the liquid state [24]. The net reaction for a pure hydrogen and oxygen fuel cell is as follows (Equation 1-3).

$$2H_2+O_2 \rightarrow 2H_2O+\text{Electricity}+\text{Heat} \qquad \textbf{Equation 1-3}$$

Fuel cell efficiency (η) is actual cell voltage (V_{cell}) divided by maximum EMF: $\eta=(V_{cell}/1.25)\text{x}100\%$ (LHV). The efficiency of a working hydrogen fuel cell can then be determined from Equation 1-4.

$$\eta = \mu_f \frac{V_{cell}}{1.25} \times 100\% \qquad \textbf{Equation 1- 4}$$

Additional energy is available as high quality heat, allowing operation of combined cycle systems with expander, gas and/or steam turbines, further boosting system efficiency. The efficiency of an advanced gas turbine system is about 30-40% while SOFC efficiency is 50-65%. The efficiency of a SOFC/gas turbine combined cycle system has the potential to reach 70-85% (Figure 1-6). Table 1-5 shows the system efficiency increases with the increase of operation pressure.

Table 1-5 Effect of Operating Pressure on System Efficiency [9].

Operating pressure (atm)	System efficiency (AC/LHV)	Siemens Westinghouse systems
- 1	46-50%	250 kW-1 MW SOFC cogeneration
3	57-60%	300 kW-1 MW SOFC/GT hybrid
7	60-70%	2 MW-20 MW SOFC/GT hybrid

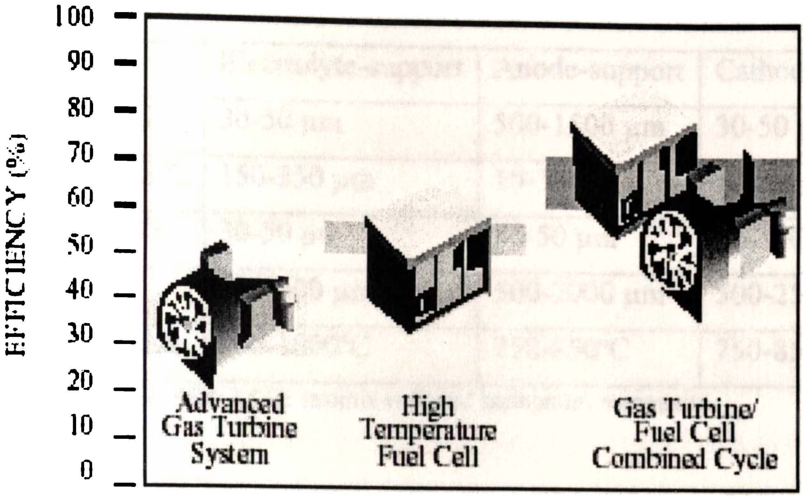

Figure 1-6 Combination of a SOFC with a Gas Turbine Engine to Improve Efficiency [7].

1.3 Solid Oxide Fuel Cell Designs

A SOFC is a multilayer ceramic and metallic composite structure. Cell design affects cell performance and is thus important in SOFC development. The main cell design configurations are tubular [25], planar [26], segmented-cell-in-series [24], and monolithic [27]. Each design differs in geometry, cell performance, method of sealing and fabrication. Cell designs may also be classified by the mechanical support mechanism, as electrolyte-, anode-, cathode-, or interconnect-supported. An electrolyte-supported system can be used in a small cell or small unit because thin electrolyte can support the cell structure. In a large cell or system, however, electrode-supported designs are normally desirable because of the manufacturing and assembly problems associated with the thin electrolyte. For example, a thin electrolyte membrane may not be strong enough to support the cell components (electrodes and current collectors). In electrode-supported designs, the YSZ electrolyte layer can be reduced to 15-20 µm or lower, significantly reducing the electrolyte ohmic resistance. Cell designs in terms of component thickness and cell operating temperatures are summarized in Table 1-6. The overall cell thickness of an electrolyte-supported cell is less than that of electrode-supported systems, while the operating temperatures of the former are higher than that of the electrode-supported systems.

Table 1-6 SOFC General Structure on Various Supports.

Support component		Electrolyte-support	Anode-support	Cathode-support
Thickness	Anode (Ni/YSZ)	30-50 μm	500-1500 μm	30-50 μm
	Electrolyte (YSZ)	150-350 μm	10-30 μm	10-30 μm
	Cathode (LSM)	30-50 μm	30-50 μm	500-2000 μm
Overall thickness		200-500 μm	500-2000 μm	500-2500 μm
Operating temperature		900-1000°C	750-850°C	750-850°C

Ni/YSZ: cermet of Ni and YSZ; LSM: strontium doped lanthanum manganite.

Further discussion is limited to the comparing of the two most-used designs: tubular and planar. Generally speaking, a planar design has higher power density and lower cell mass production costs. However fuel-to-air seal, interconnect, and structural materials are challenging. A tubular SOFC is based upon a single cell of tubular geometry, which allows rapid thermal cycling and a simpler fuel-to-air seal. The goal in SOFC development and the currently achieved level is summarized in Table 1-7.

Table 1-7 The Goal in SOFC Development and Commercialisation [28].

		Goals	Current status
Stack capacity		kW to MW	300 kW
Degradation rate		1% per 1000 hr	
Cell life		10-20 year	
Power per mass			200 W/kg (stack) 388 W/kg (active volume)
Cost	Stack	$400/kW	$1000/kW
	Plant	$2000/kW	

1.3.1 Planar Design

A planar or flat plate structure is commonly used in PEMFCs, PAFCs and MCFCs, as well as SOFCs. The basic planar SOFC design is shown in Figure 1-7. Repeating the unit of anode, electrolyte, cathode, and interconnect forms a planar stack. A planar design allows a simple series electrical connection between cells without the need for external cell interconnections such as those used in the Siemens Westinghouse Power Corporation (SWPC) tubular configuration. Using perpendicular current collection in a cell stack with a bipolar design should give a lower ohmic polarization than in a tubular design because the current path is reduced.

This planar concept was evaluated as early as the mid-seventies [29, 30] and has been widely investigated in recent years [31-33]. Many researchers believe it has the potential to become the cheapest SOFC unit. Cell components in this configuration can be produced by traditional ceramic processes. For example, the support component can be formed by tape casting, while thin films can be screen-printed or plasma sprayed onto the support. Maximum cell size is currently limited by the capacity of the available tape casting equipment (220×220 mm^2 after sintering [34]). Interconnect plates with gas channels are fabricated individually from ceramic materials or suitable high temperature alloys.

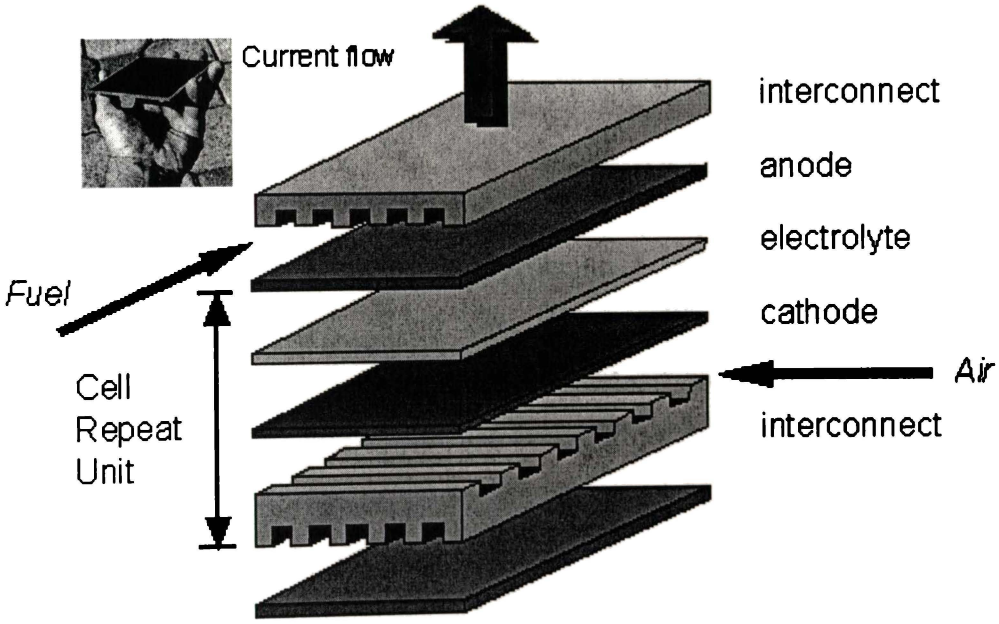

Figure 1-7 Planar Design of Solid Oxide Fuel Cell [18].

The major technical difficulties with these structures are the seals, interconnect materials, brittleness of the electrolyte, and thermal shock resistance [6]. The tensile strength of ceramics is generally only about 20% of their compressive strength. Also, high thermo-mechanical stresses arise from differential thermal expansion coefficients of adjacent component materials. Fabricating large flat, thin cells and obtaining adequate gas seals also present problems. Thermal stresses at interfaces between dissimilar materials lead to mechanical degradation of cell components as well as degrade cell performance. Planar stacks usually require long start-up and shut-down cycles to prevent cell component from cracking.

Interconnects in a common planar design generally have a multi-functional role as gas distributor, electrical interconnect and structural support. There has been a move away from an electrolyte-supported system towards an electrode-supported, and bipolar current collection supported systems because of advances in gas sealing and component fabrication techniques. Figure 1-8 illustrates schematically an anode-supported planar SOFC.

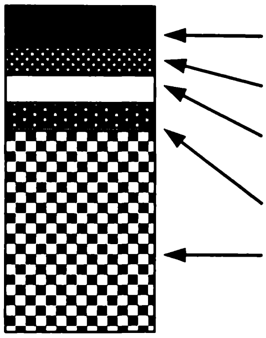

Cathode current collector:	LSM	25-40 μm
Cathode layer:	LSM/YSZ	10-35 μm
Electrolyte layer:	YSZ	15-20 μm
Anode layer:	NiO/YSZ	10-15 μm
Anode current collector: (support)	NiO/YSZ	200-250 μm

Figure 1-8 Schematic of an Anode-Supported Planar SOFC [34].

The major players in planar SOFC development include Ceramic Fuel Cell Limited (Australia), Delphi Corporation (USA), GE Power Systems (USA), Global Thermoelectric Inc (Canada), McDermott Technologies (SOFCo, USA), Mitsubishi Heavy Industries (Japan), and Sulzer Hexis (Switzerland).

Ceramic Fuel Cells Ltd constructed and tested a 25-kW planar SOFC stack running on natural gas at 80-85% fuel utilization and at 850°C [35]. This stack was a 4×4 cell planar array with 240 layers and the individual cell size was 110×90 mm. The progress Global Thermoelectric made in developing planar SOFCs is summarized in Table 1-8. In February 1999, Siemens (Germany), a key player in fuel cell technology, decided to discontinue its research on planar SOFCs and concentrate only on the tubular SOFC technology developed by Westinghouse (USA). This decision was partly because the tubular design was more advanced [36].

Table 1-8 Power Density of Planar SOFCs Developed by Global Thermoelectric Inc [37].

Time Line	Power density (W/cm^2) (Fuel: H_2, at 0.7 V)				
	600°C	650°C	700°C	750°C	800°C
1998	-	-	-	0.150	0.250
1999	0.156	0.318	0.487	0.528	0.594
2000	0.200	0.416	0.723	1.093	1.216

1.3.2 Tubular Design

A tubular SOFC essentially consists of two porous electrodes separated by a dense, oxygen-ion conducting electrolyte. Different component thin layers (10-50 μm) are overlapped on a support tube. Mechanically, tubular designs can be anode-supported, cathode-supported, electrolyte-supported, or extra porous tube-supported. Tubular configurations tend to reduce the problems with gas seal and fabricating thin layer structures. The tubular design, especially with one closed end, eliminates gas seals between cells. The tubular support component, such as the cathode in the Siemens Westinghouse case, is formed by extrusion. The electrolyte and interconnection are then deposited by electrochemical vapour deposition (EVD) and plasma spraying, respectively. The anode is sequentially applied on the electrolyte by slurry deposition. The tubular and planar designs are compared in Table 1-9.

The major companies investigating tubular SOFCs are Siemens Westinghouse Power Corporation (SWPC, USA), Mitsubishi Heavy Industries (MHI, Japan), and recently Acumentrics Corporation (USA). SWPC has been developing tubular SOFCs since the 1950s [7] and is regarded as the leader in this field. The Westinghouse design (Figure 1-9) is a cathode-support close end tubular design. Oxidant (air or oxygen) is introduced through a ceramic injector tube positioned inside a closed-end tubular cell. Fuel flows from the closed end to the open end on the outside of the cell. The exhaust gas containing some unused fuel passes through a diffuser plate and combines with the partially oxygen-depleted air to preheat incoming air and/or fuel. The cathode tube is made of strontium doped lanthanum manganite (LSM), and has 15~22 mm outside diameter, 1500 mm length and 1.5~2.2 mm wall thickness. The YSZ electrolyte layer is about 40 μm thick and the Ni/YSZ anode is about 100 μm thick [36]. Stacks are constructed by bundling several tubes together and connecting them with Ni felt pads. Typically, 50~90% of the fuel is utilized in the electrochemical cell reaction [38]. It takes about 5 hours to go from ambient temperature to 1000°C [6]. Several stacks, rating from a few kilowatts to 300 kW, have been tested.

Table 1-9 Comparison of Tubular Design with Planar Design.

Cell design concept	Tubular	Planar
Power density	0.25-0.5 W/cm^2	0. 5-1 W/cm^2
Volumetric power density	Low	High
Sealing	Less seal requirements	High temp. seals required
Cell resistance	Long current path	Lower ohmic polarization
Interconnect	Difficult	High cost
Manufacturing cost	High	Lower cost feasible
Examples [38] (SWPC)	100 kW (1998) 1152 tubes stack 200-250 mA/cm^2 1000°C 83% on natural gas	7.2 kW (1998) Two 50x4x4 stacks 400 mA/cm^2 900°C 30% on H_2

A 100 kW-cogeneration prototype (150 cm cells) developed by SWPC has been operating in the Netherlands for more than one and half years. Westinghouse claims that its tubular SOFC prototype has an eight-year lifetime and is able to withstand over 100 thermal cycles with cell voltage degradation of less than 0.1% per 1000 hours [39]. A 200 kW SOFC/gas turbine hybrid power system (1152 cells, 22 mm OD, 1500 mm active length) was tested for over 14,000 hours, with an efficiency of 43% at 1 atm and 57% at 3.5 atm. If the high-grade heat is recovered, total fuel efficiency will be 73%. Stack voltage degradation less than 0.1% per 1000 hours has been reported [6, 38]. Because the current flows around the electrode circumference in the SWPC tubular design, there is a relatively large ohmic loss, which places an upper limit on the tube diameter. This design is more suitable for large power station applications because it has high fuel efficiency and can use natural gas as a fuel.

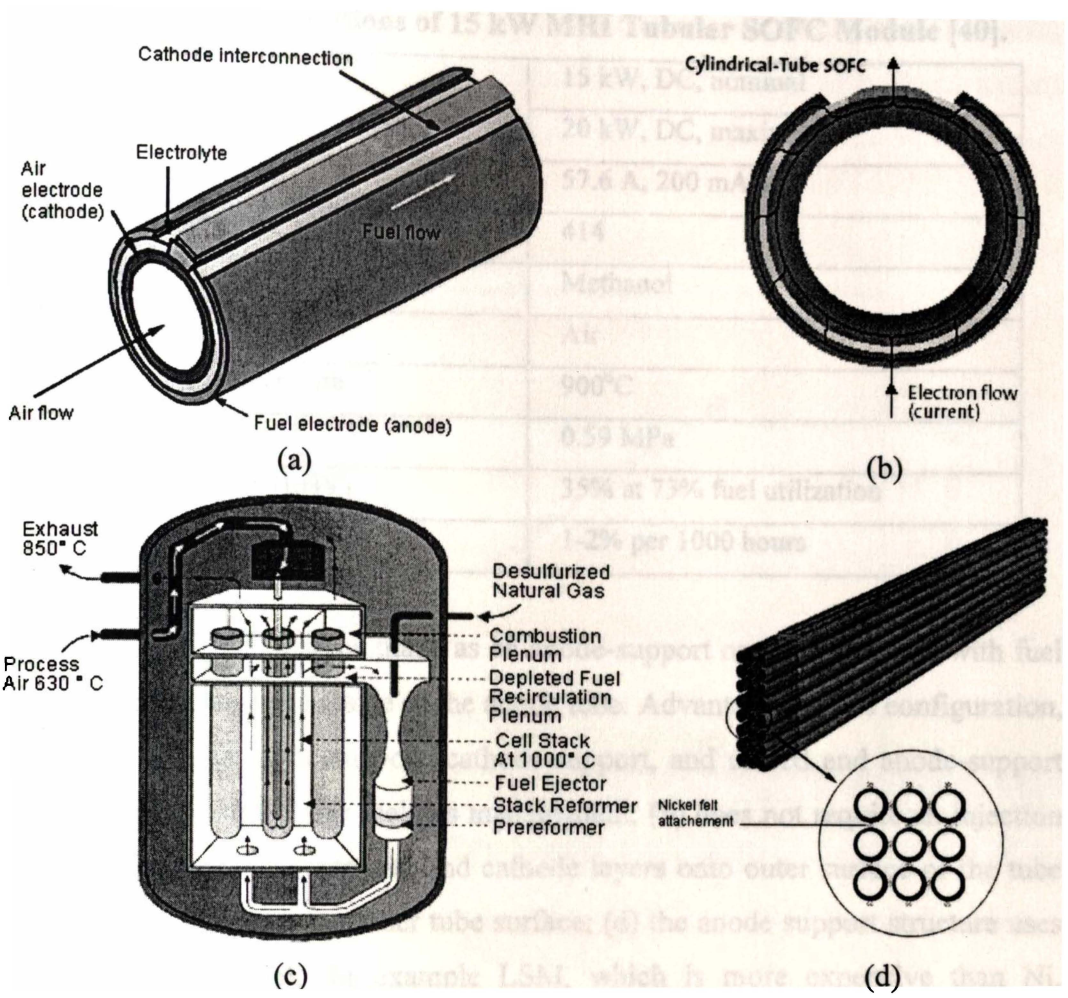

Figure 1-9 Siemens Westinghouse Tubular SOFC Technology (a) Schematic of Single Cell, (b) Current Flow Direction, (c) Operation Layout, and (d) Bundled into a Stack [39].

The MHI tubular design differs from SWPC by injecting fuel into the inside of the cells. The anode tube is 21 mm in diameter and 500 mm in length. The cathode thin layers were fabricated using a plasma-spray coating process. The MHI tubular SOFC design is shown in Figure 1-10. A single cell was segmented with 22 bands to enhance cell performance. MHI has reported that a 10 kW stack has operated on pressurized coal gas for more than 7000 hours [40]. The specifications for a 15 kW MHI module are given in Table 1-10.

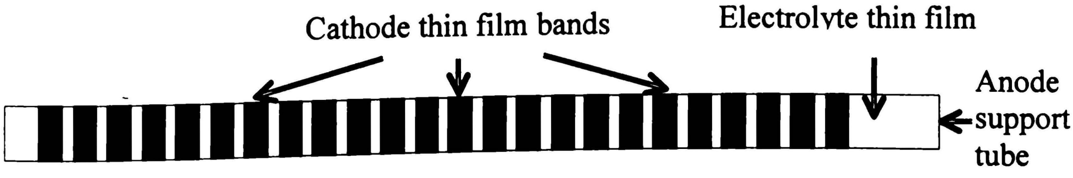

Figure 1-10 Structure of a MHI Tubular SOFC, 720 mm Long and with 22 Bands (cells) [40].

Table 1-10 Specifications of 15 kW MHI Tubular SOFC Module [40].

Power output	15 kW, DC, nominal
	20 kW, DC, maximum
Operating current	57.6 A, 200 mA/cm^2
Number of tubes	414
Fuel	Methanol
Oxidant	Air
Operating temperature	900°C
Operating pressure	0.59 MPa
Max. efficiency (LHV)	35% at 73% fuel utilization
Power degradation	1-2% per 1000 hours

Tubular SOFCs can also be made as an anode-support open-end system with fuel gas passing through the inside of the anode tube. Advantages in this configuration, compared to electrolyte-support, cathode-support, and closed end anode-support systems, include (a) easier fuel gas management; (b) does not require an injection tube; (c) coating the electrolyte and cathode layers onto outer surface of the tube are easier than coating the inner tube surface; (d) the anode support structure uses less cathode material, for example LSM, which is more expensive than Ni. Materials and their thickness for an anode-supported tubular SOFC are summarized in Table 1-11.

Table 1-11 Specification of an Anode-Supported Tubular SOFC [41]

Component	Material	Thickness
Anode current collector	Ni felt	0.8-0.9 mm
Anode	Ni-8YSZ	1.7 mm
Electrolyte	8YSZ	20-30 μm
Cathode	LSM	30-40 μm
Cathode current collector	Pt mesh	0.3 mm

Small diameter tubular SOFCs were initiated by Kendall *et al.* [42, 43] in 1996, and thermal integrating and reforming issues were addressed by Sammes [44]. The small-scale tubular SOFCs are more practical for SOFC units in the few to multi-hundred watts power range. As shown in Figure 1-11, the smaller tube size offers a higher volumetric power packing density. This means that for a given power requirement, the stack will occupy less volume as a function of decreasing tube size. For a given tube size, the volumetric power density of a tubular system can be increased by optimising the physical packing scheme of the tubes (Figure 1-12).

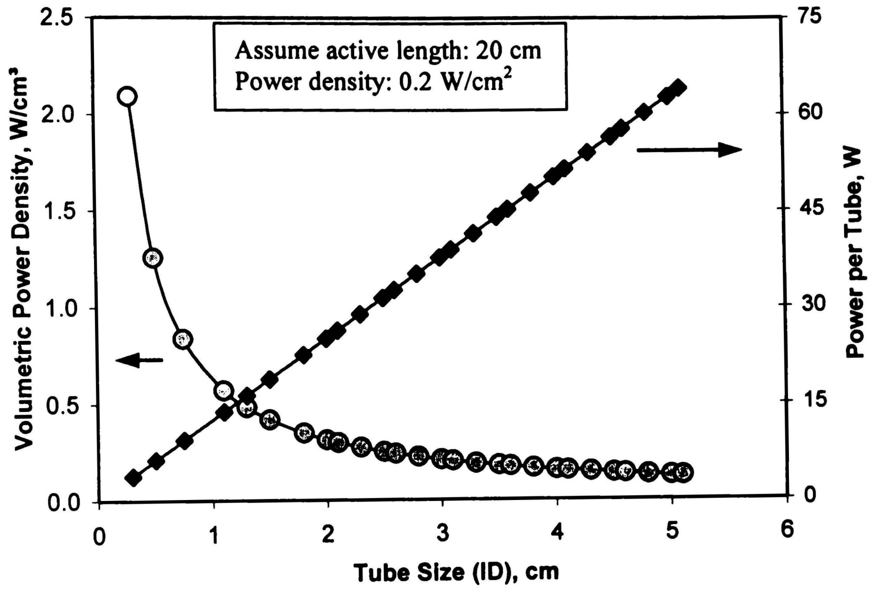

Figure 1-11 Effect of Tube Size on Single Cell Power and Power Packing Density [45].

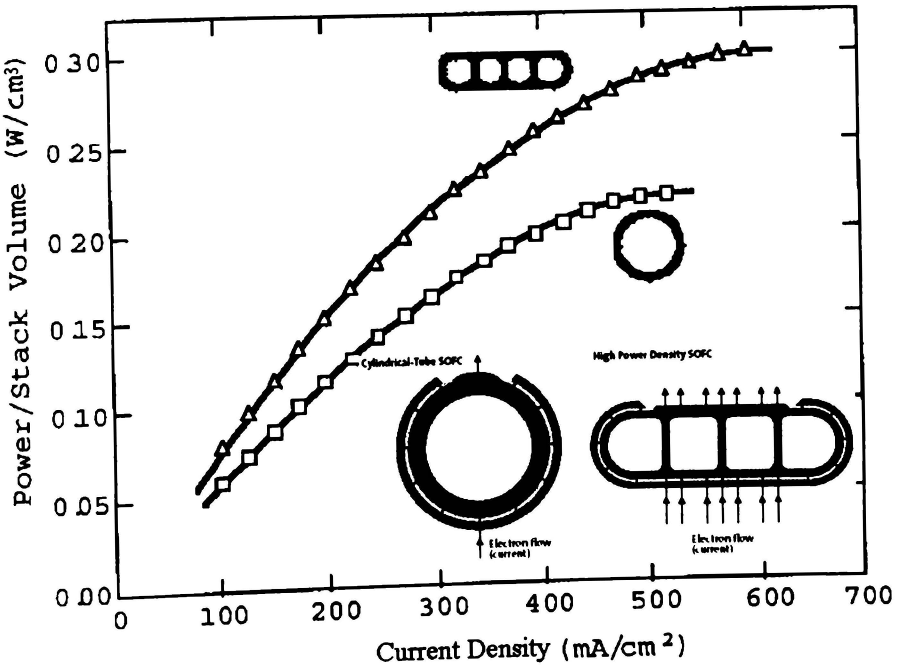

Figure 1-12 Effect of Efficient Cell Arrangement on Stack Power Densities of a Cathode Supported Tubular SOFC (cell OD: 22 mm, thickness: 2.2 mm, active length: 1.5 m) [38].

This type of small scale tubular SOFC normally consists of YSZ electrolyte-support tube, thin film anode and cathode layers. The small-scale tubular SOFC can withstand greater thermal cycling than typical planar or SWPC large-scale tubular designs due to its excellent thermal shock resistance [46]. A fuel cell stack system with such a design can be started up or shut down in a few minutes instead of hours. Major difficulties associated with these very small size electrolyte-supported tubular cells are (1) fabricating thin-walled, pinhole free, round and straight tubes, and (2) current collecting within the tube.

Overall the major advantages of the tubular over planar SOFC designs are: good thermomechanical stability and less or no requirement of hot seals for the closed-end tube design. Drawbacks include low power density and difficulty of mass production [5].

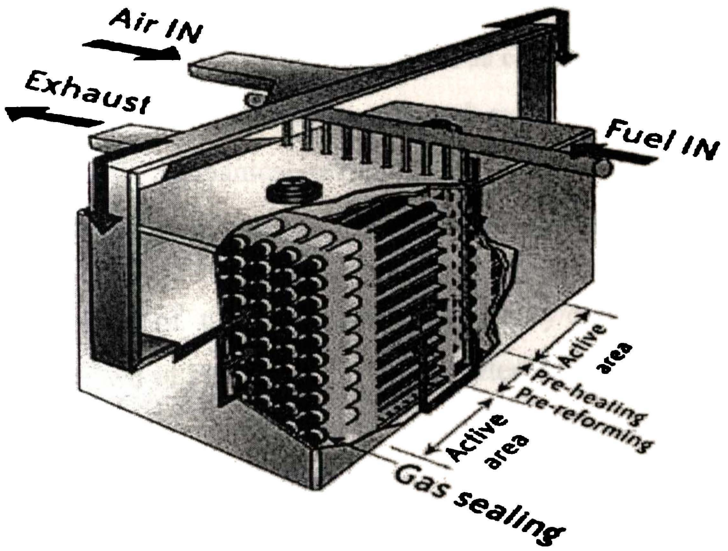

Figure 1-13 Schematic of a Module Developed by NEDO [47].

Practical fuel cells are not operated as a single cell unit. Rather, they are arrays of single cells, referred to as a stack, connected in electrical series to build voltage. This is because single cell open-cell potential is only 0.5-1.0 V. There are different ways to stack individual tubular SOFCs, e.g. tubes can be positioned either vertically or horizontally. Great effort has been made to optimise heat management, mass transfer kinetics, and integration of component form and function. Most stack developers keep their stack design details confidential or protected by patents. As an example, Figure 1-13 shows the schematic drawing of a module developed by the New Energy & Industrial Technology Development Organization (NEDO). The stack consists of two arrays of small single-cell tubes using a centreline gas manifolding configuration. The fuel is pre-heated, pre-reformed (converted into hydrogen, carbon monoxide and methane) inside the cells, and flows into the active area of the cells.

1.4 Component Requirements of Tubular SOFCs

The basic components of a SOFC unit include electrolyte, anode, cathode and interconnect or current collectors. Each component serves one or several functions in the fuel cell and must fulfil certain requirements. Generally speaking, SOFC materials are selected according to the following criteria [7, 38]:

- Conductivity (electronic, ionic, or mixed);
- Chemical stability in oxidizing, reducing, or both environments, at high temperatures during cell operation as well as cell fabrication;
- Thermomechanical compatibility (thermal expansion coefficient, thermal shock resistance, mechanical strength);
- Availability (low cost, available resource and easy fabrication).

Individual components of the cell have conductivity/oxygen partial pressure characteristics as shown in Figure 1-14. Anode materials are usually n-type semi-conductors and cathodes are generally p-type semi-conductors. Electrolyte materials must be pure ionic conductors.

Table 1-12 lists the material evolution of different cell components in Siemens Westinghouse SOFC development. The main functional requirements and materials for electrolyte, anode, cathode, and interconnect are summarized in Table 1-13 while Table 1-14 gives typical specification of each of the components. Detailed requirements and material choices for each individual component are discussed below.

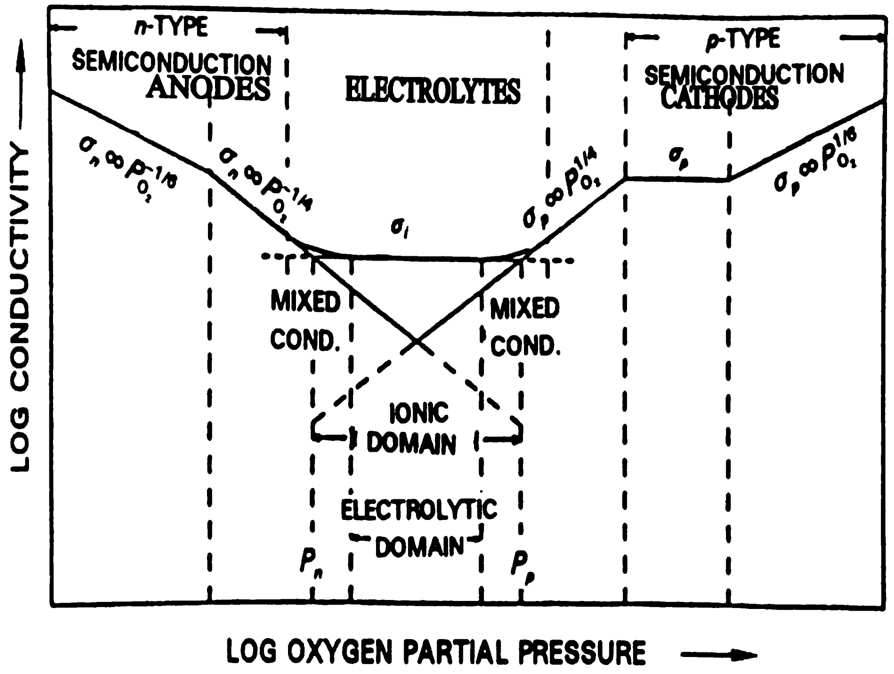

Figure 1-14 Frenkel Defects [48].

Table 1-12 Material Evolution of Tubular SOFC Technology in SWPC [7].

Component	ca. 1965	ca. 1975	SWCP current status
Cathode	• Porous Pt	• Stabilized ZrO_2 impregnated with praseodymium oxide and covered with SnO doped In_2O_3	• Doped lanthanum manganite • Extrusion and sintering as support • ~2 mm thickness • TEC: 11×10^{-6}/°C, RT-1000°C • 30-40% porosity
Electrolyte	• YSZ • 0.5 mm thickness	• YSZ	• YSZ (8 mol% Y_2O_3) • EVD • 30-40 μm thickness • TEC: 10.5×10^{-6}/°C, RT-1000°C • Dense
Anode	• Porous Pt	• Ni/YSZ cermet	• Ni/YSZ cermet • EVD, or slurry deposition • ~150 μm thickness • TEC: 12.5×10^{-6}/°C, RT-1000°C • 20-40% porosity
Interconnect	• Pt	• Mn doped cobalt chromite	• Doped lanthanum chromite • Plasma spray • ~100 μm thickness • TEC: 10×10^{-6}/°C, RT-1000°C

EVD: electrochemical vapour deposition; TEC: thermal expansion coefficient.

Table 1-13 Summary of the Main Functional Requirements and Materials for SOFC Components.

Component	Main functional requirements	Materials
Electrolyte	• High ionic conductivity • Negligible electronic conductivity • Fully dense	*ZrO_2-Y_2O_3 (YSZ) ZrO_2-Sc_2O_3 $Ce_{1-x}(Gd,Sm)_xO_2$ Bi_2O_3-MO_y coated $Ce(Gd,Sm)O_2$
Cathode	• High electronic, ideally with ionic conductivity • Porous • High rates for oxygen reduction	*$La_{1-x}Sr_xMnO_3$ $(La_{1-x}Sr_x)Co,FeO_3$ $(La_{1-x}Sr_x)Co,FeO_3$
Anode	• High electronic, ideally with ionic conductivity • Porous • High rates for fuel oxidation	*Ni/ZrO_2-Y_2O_3 cermet Ru/ ZrO_2-Y_2O_3 Ni/CeO_2-ZrO_2-M_2O_3, Ni/CeO_2
Current collector	• High electronic conductivity	*Ag, Pt, *Ni, Cu alloy
Interconnect	• High electronic and thermal conductivity • Negligible ionic conductivity • Fully dense	*High-temperature alloy: $La_{1-x}Sr(Ca,Mg)_x$-CrO_3 Cermets: $YCrO_3$

* Most commonly used materials, others are suggested alternatives.

Table 1-14 Example of SOFC Materials and Component Characteristics [12].

Component	Composition	Thickness (mm)	Porosity (%)	Conductivity (S/cm, at 1000°C)
Cathode	$L_{0.65}Sr_{0.3}MnO_3$	50×10^{-3}	~ 40	≥200
Electrolyte	$Y_{0.15}Zr_{0.85}O_{1.93}$	$10\text{-}20\times10^{-3}$	≤4*	0.13-0.18
Anode	Ni:8YSZ (50:50 wt%)	1.5-2	~40	300-400
Interconnect	Fe 17Cr 1Al 1Si	~ 3	~ $0^{\#}$	≥1000

Original data were: * "≥96%", # "≈100%". These may be considered as density instead of porosity.

1.4.1 Electrolyte

The electrolyte in a fuel cell has physical and electrochemical functions and is the most important fuel cell component in SOFCs. It usually is an oxygen ionic conductor. From the electrochemical perspective, the electrolyte transports dissolved reactants to the electrode and conducts ionic charge between the electrodes thereby completing the cell electric circuit. The electrolyte also needs to provide a physical barrier to prevent the fuel and oxidant gas streams from directly mixing.

To achieve the above roles, electrolyte materials must meet the following technical requirements [6]:

- Pure ionic conductivity (>0.05 S/cm at operating temperature) with minimum electronic conductivity;
- Stability (chemically, morphologically and dimensionally stable in both oxidizing and reducing atmospheres);
- Compatibility with other components (chemically and thermo-mechanically);
- Dense and free of porosity, not to permeate the gas from one side of the electrolyte layer to the other;
- Thin to minimize ohmic loss.

Zirconia-based electrolytes are suitable for SOFCs because they exhibit pure ionic conductivity at high temperatures over a wide range of oxygen partial pressures ($1\text{-}10^{-20}$ atm). YSZ electrolytes must be operated at very high temperatures, 900-1000°C for example, to enable the YSZ electrolyte providing sufficient oxygen ion conductivity. This high temperature limitation has prompted the search for intermediate temperature SOFC electrolytes. Strontium- and magnesium-doped lanthanum gallate (LSGM), gadolinium-doped ceria (GDC), and scandium-doped zirconia (SDZ) are new alternatives to YSZ for intermediate temperature SOFCs. Individual electrolyte materials are discussed in Section 1.5.

1.4.2 Anode

The anode is the material placed next to electrolyte on the fuel side of a fuel cell. It has the following functions in a SOFC:

- To provide surface sites where fuel oxidation can take place;
- To conduct oxygen ions from the electrolyte into the three-phase interface;
- Most importantly, to conduct electrons.

To fulfil these functions, an anode should have high electrical conductivity, high catalytic activity, adequate porosity for gas transport, and sufficient stability when contacting other cell components (electrolyte and current collector) under the processing and operating conditions.

In a pure electronic conductor, the electrochemical reactions are restricted to the triple phase boundaries (TPBs). A three-phase interface is established among the reactant, electrolyte, and catalyst at the porous anode. The nature of TPB critically affects the electrochemical performance of a SOFC. Transport of oxygen ions within the anode material is advantageous to increase the possible reaction pathways. Therefore, ideally the anode should be composites of an electronic and an ionic conducting phases, or made from mixed conducting materials to enhance the active area into the anode volume [49]. Mixed ionic-electronic conductors (MIECs) are materials that conduct both ions and electronic charge carriers (electrons and/or holes). MIECs can be a single-phase material such as strontium-doped lanthanum cobaltite, which conducts both oxygen ions and electrons, or a composite where one phase conducts ions and the other phase conducts electrons/holes such as Ni-YSZ cermets commonly used as anodes for SOFCs. Figure 1-15 illustrates the enhancement of the TPBs using MIECs.

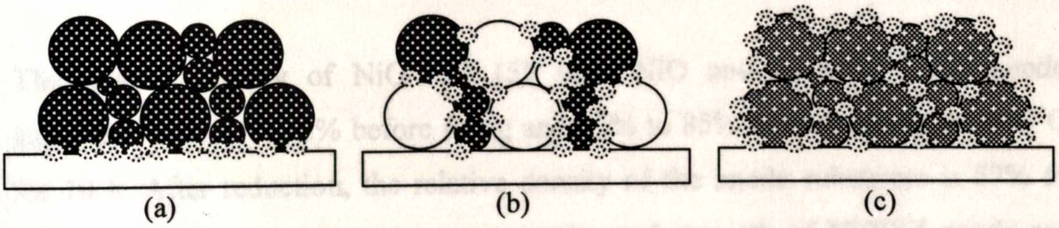
(a) (b) (c)

Figure 1-15 Triple Phase Boundary (⁘) in: (a) Pure Electronic Conductors (●), (b) Electronic and Ionic (○) Composite Conductors, and (c) Single Phase Mixed Conductors (◍).

The fuel gases produce a reducing atmosphere, which may have CO, H_2, CH_4, CO_2, and/or some sulphur. Metals such as Ni, Pt, Ru or Co, are considered as anode materials. Pt and Ru have excellent performance and stability but are very expensive. Co has good electric conductivity, however, it is unstable at high temperatures. Ni is preferred because it is chemically compatible with YSZ electrolyte, low cost and has good hydrogen catalytic performance. However, Ni has low resistance to grain growth at high temperature. Furthermore, if the fuel contains sulphur, NiS, NiS_2 or $NiSO_4$ can form by hot corrosion of Ni in O_2+SO_2 and/or SO_3 atmospheres [50].

Pure nickel anode would have excellent electrical conductivity. However, its thermal expansion coefficient (TEC) is 50% greater than the YSZ electrolyte, creating a thermal mismatch and then leading to mechanical instability and delamination. Mixing YSZ with Ni or NiO reduces this thermal mismatch, but the trade-off between the amounts of Ni (to achieve high conductivity) and YSZ (to better match the TEC of the other components and increase TPB) is 30:70 vol% (Ni/YSZ) [26] (equivalent to 44:56 wt% of NiO:YSZ). The YSZ skeleton in this Ni/YSZ cermet inhibits sintering of the metal particles, stabilizes the anode structural dimensions and gives a TEC comparable to the other cell materials.

The anode structure is fabricated with 20-40% porosity to facilitate mass transfer of reactant and product gases. The cermet microstructure plays a critical role in determining performance and long-term stability in fuel cell operating environments. A desirable anode microstructure can be achieved by optimising the Ni/NiO and YSZ particle size, surface area, connectivity of Ni or YSZ particles, porosity, and triple phase contact area. The major causes of anode degradation are attributed to agglomeration of Ni particles and Ni dewetting of zirconia [51].

The relative density of NiO/YSZ (55 wt% NiO and 45 wt% YSZ) anode substrates is 25% to 40% before firing and 75% to 85% after sintering at 1400°C for 10 h. After reduction, the relative density of the anode substrates is 57% to 67% [12]. Effects of Ni content on porosity and strength of Ni/YSZ anode are shown in Figure 1-16.

In general, the electrochemical activity of Ni/YSZ cermet anode strongly depends on the ratio of Ni to YSZ in the anode and resultant morphology such as the grain size, connection of each grain and porosity. This is because the fuel and oxide ion for generation occurs only at the Ni-YSZ-pore three phase boundary. Increasing the TPB area will significantly increases electrochemical activity. Therefore, being able to fabricate an optimised Ni-YSZ microstructure is critical to achieving better anode performance [52].

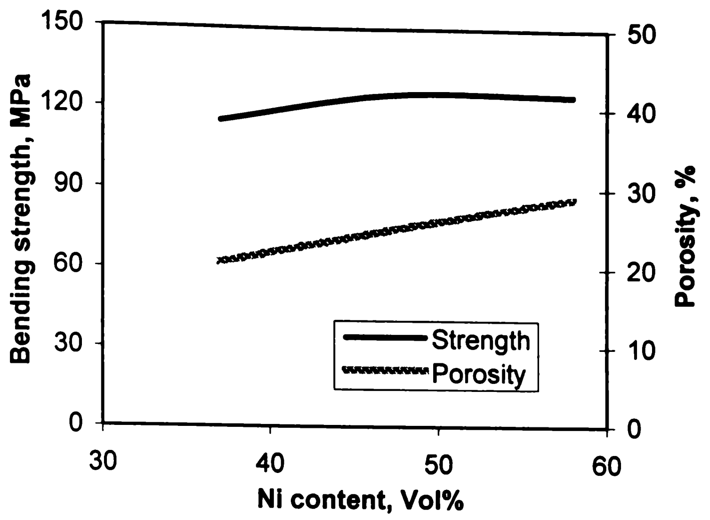

Figure 1-16 Effect of Ni Content on Bending Strength and Porosity of Ni/YSZ Anode [53].

The morphology, powder population statistics and chemistry of raw materials significantly affect the ceramic processing and the performances. Tietz *et al.* [12] found that the sintering abilities of some commercial NiO powders varied widely. Relative densities varied from 40% to 60% for powders and 70% and 90% after sintering (1400°C for 10 h). The sintering start temperature for black NiO powder was below 500°C, whereas, the temperature for green NiO powders depended on the green tones (grey-green: 600°C; dark-green: 780°C; olive-green: 1200°C). Therefore, black NiO powder has better sintering ability and is preferable.

1.4.3 Cathode

The cathode is the electrode on the oxidant side of a fuel cell and is bonded to the electrolyte. The functions of a SOFC cathode include:

- Providing reaction sites for oxidant reduction;
- Conducting oxygen ions from the three phase interface to the electrolyte once they are formed; and
- Conducting electrons from the external circuit to the reaction sites.

To do this, the cathode must have:

- Sufficient electronic conductivity in an oxidizing environment;
- Good catalytic activity;

- Stability in an oxidizing atmosphere during SOFC operation and fabrication;
- A porous structure that allows mass transfer of reactant and product gases;
- Chemical and thermomechanical compatibility with other fuel cell components.

Cathodic activity involves many steps such as: chemisorption of oxygen, oxygen reduction and ionisation, and oxygen ion transport from the reaction sites to the electrolyte interface. If the cathode is a pure electronic conductor, oxygen reduction occurs at the TPB where gaseous oxygen, the cathode, and the electrolyte share a common boundary. Traditionally, relatively thick and porous cathode/electrolyte composite films are used to increase the TPB surface area. However, this creates tortuous conduction pathways that both the ions and electrons must traverse. If the electrode is made of a mixed conductor, the reaction sites will be extended beyond the TPBs to the mixed conductor/gas interface. Therefore, cathode materials should ideally be mixed conductors. One of the goals in cathode development is to identify or develop advanced mixed conductors.

The most common cathode material currently used in SOFC systems is strontium doped lanthanum manganite (La,Sr)MnO_3 (LSM), a p-type semiconductor. It has reasonably good electrocatalytic activity for oxygen reduction, a TEC close to YSZ and does not react with YSZ electrolyte at SOFC operating temperatures. However, YSZ may react with LSM at fabrication temperatures and form resistive pyrochlore $La_2Zr_2O_7$ or perovskite $SrZrO_3$ phases at the cathode/electrolyte interface [54].

Another study by Roosamen *et al.* [55] showed that the chemical reactions between $La_{1-x}Sr_xMnO_3$ and ZrO_2 (Figure 1-17). The $LaMnO_3$ reacts with 8YSZ occurs at temperatures as low as 879°C to form $La_2Zr_2O_7$ (LZ), whereas reactions between $La_{0.7}Sr_{0.3}MnO_3$ and 8YSZ take place at temperatures higher than 1087°C. $SrZrO_3$ (SZ) was also detected in a fired mixture of $La_{1-x}Sr_xMnO_3$ and 8YSZ. The higher the Sr-doping level, the lower the reaction temperatures (to form $SrZrO_3$). The temperatures for x=0.15, 0.3, 0.5 are 1382°C, 1282°C, and 997°C, respectively. Both $SrZrO_3$ and $La_2Zr_2O_7$ (LZ) have a cubic structure and low electronic conductivity. Their existence at the cathode-electrolyte interface increases resistance and overpotential losses, giving relatively poor cell performance [55, 56].

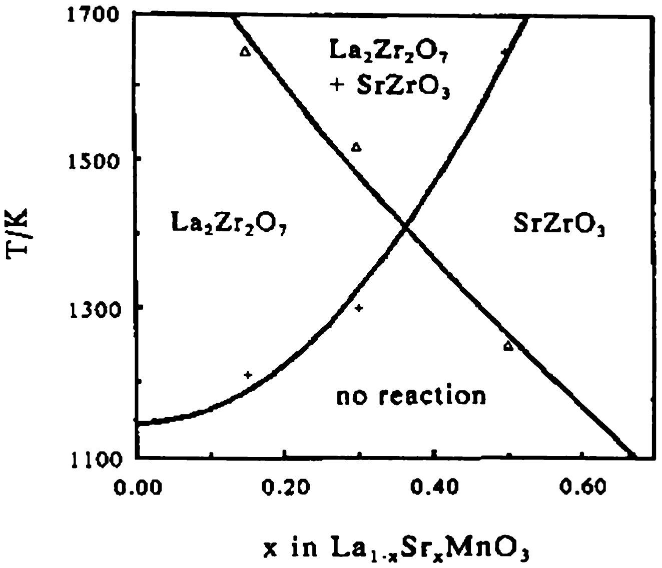

Figure 1-17 Temperature-Phase Relationship between $La_{1-x}Sr_xMnO_3$ and ZrO_2 [55].

Several other materials have been considered for cathodes, including $La_{1-x}Sr_xFeO_3$ (LSF) and La-Sr-cobaltite (LSC) [57]. Both have much higher electronic and ionic conductivity compared with LSM. However, LSC materials have a higher TEC and lower stability due to interfacial reactions with the electrolyte. The TEC of $La_{0.8}Sr_{0.2}FeO_3$ ($12.6x10^{-6}$/K) is closer to that of YSZ (~$11x10^{-6}$/K), and no diffusion or reaction between LSF and YSZ phases has been detected [6]. Therefore, LSF appears to be both chemically and thermally compatible with YSZ. Doping on the B-site with Fe to form materials with the composition $La_{1-x}Sr_xCo_{1-y}Fe_yO_{3-\delta}$ (LSCF) were found to better match the TEC of YSZ [58].

Anode and cathode overlap area also affects the cell performance. The overlap area difference between the anode and cathode gave a measurable difference in power densities. The maximum power densities at 800°C for an anode-supported Ni+YSZ//YSZ//LSC+SDC cell (anode area 3.14 cm^2, thickness 1 mm) were 1.65 W/cm^2 when the cathode area was 1.1 cm^2, and 1.45 W/cm^2 when the cathode area was 2 cm^2. However, the power density difference was less than 10% if the anode area and cathode area overlapped more closely [59].

1.4.4 Current Collect or Interconnect

A current collector is an electronic conductor that provides a conduction path for the electrons generated from anode or cathode. In some designs, the function of a current collector may be combined with an interconnect and/or a fuel to air seal. An interconnect is a structural component that electronically connects individual cells to the external circuit. The interconnect separates air (cathode) and fuel (anode) gases in planar SOFCs. An interconnect must also be chemically stable under oxygen partial pressures from ambient to about 10^{-18} atmospheres at temperatures up to 1000°C as it is exposed to both the cathode and anode environments [7]. Interconnects in the Westinghouse tubular design are made with $La_{1-x}(Sr, Mg)_xCrO_3$ ceramic layers and the cells are connected with nickel felt pads. SWPC, in conjunction with Plansee AG, has developed a Cr-based alloy with high corrosion resistance and the TEC matching with YSZ over a wide temperature range [60].

1.5 SOFC Electrolyte Materials

The discovery of solid oxide electrolytes in 1899 [14] made it possible to develop SOFCs. The electrolyte materials must have high ionic conductivity with no or minimal electronic conductivity. High efficiency SOFCs require electrolytes that have sufficient oxygen-ion conductivity at elevated temperatures and remain ionic conductors in oxidising and reducing atmospheres. The ionic transport number ideally should be close to unity between 1 and 10^{-20} atm. Typical SOFC electrolytes include doped-zirconia, doped-ceria, and a new family of perovskites based on $LaGaO_3$ which are doped at A-site with Sr and at B-site with Mg. The oxygen-ion conductivity of these materials generally increases in the order zirconia system, doped-ceria, doped-lanthanum gallate (Figure 1-18).

Notably in Figure 1-18, yttria-stabilized Bi_2O_3 shows the highest conductivity. Stabilized bismuth oxide based materials have oxygen ion conductivity over ten times greater than that of conventional SOFC electrolytes such as stabilized zirconia [61] at comparable temperatures, and are excellent candidates for solid electrolytes and electrodes in electrochemical devices. However, these materials have the following undesirable properties that limit their practical use [62]: (1)

reduction under low oxygen partial pressures; (2) poor mechanical strength; and (3) reactivity with other fuel cell components. Another family of oxide ion conducting solids based on $Bi_2VO_{5.5}$ known by the acronym BIMEVOX (BI-bismuth, ME-dopant metal, V-vanadium, OX-oxygen), can also be used. The highest reported oxide ion conductivity value in the BIMEVOX family is 4×10^{-4} S/cm at 227°C in γ-$Bi_2V_{0.85}Ti_{0.15}O_{5.425}$ [63]. The following is a discussion of the three most common solid electrolyte systems: stabilized zirconia, doped lanthanum gallate and doped ceria.

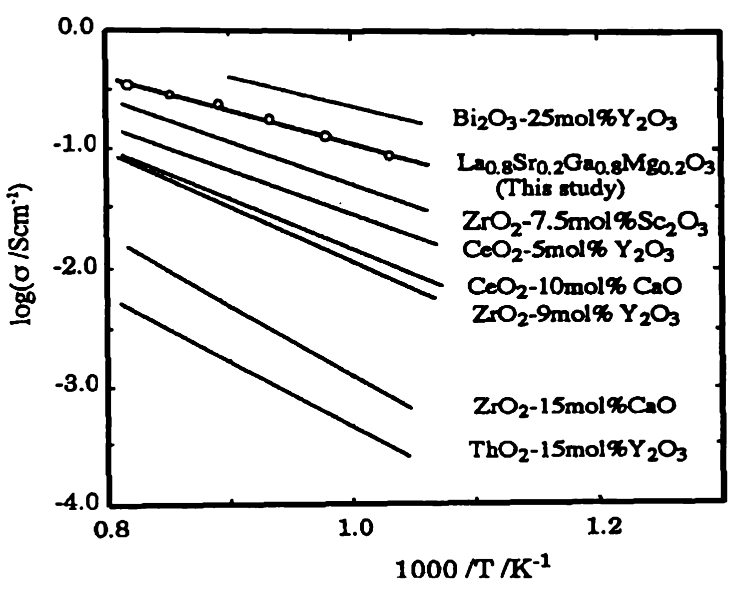

Figure 1-18 Effect of Temperature on Ionic Conductivity of Oxygen Ionic Conductors for SOFC Electrolytes [64].

1.5.1 Stabilized Zirconia

Pure zirconia (ZrO_2) is polymorphic and exists in three different crystal structures: the monoclinic (m) phase, the tetragonal (t) phase, and the cubic phase (FCC). The polymorphs are stable at different temperatures as shown in Figure 1-19.

$$\text{Monoclinic} \underset{\sim950^{\circ}\text{C}}{\overset{1170^{\circ}\text{C}}{\rightleftarrows}} \text{Tetragonal} \overset{2370^{\circ}\text{C}}{\longleftrightarrow} \text{Cubic} \overset{2706^{\circ}\text{C}}{\longleftrightarrow} \text{Melt}$$

Figure 1-19 Phase Transformations in Pure Zirconia (ZrO_2) [65].

When heated, the room temperature monoclinic zirconia phase transforms to tetragonal phase at 1170°C, and then to cubic phase at 2370°C. The cubic phase (Figure 1-20) is stable up to the melting point (2706°C) of zirconia. All these phase transformations are reversible on cooling, although the temperature for the tetragonal to monoclinic transformation is somewhat lower (950-1000°C). More importantly, the phase transformation between tetragonal and monoclinic is accompanied by a large volume change (3-5%) [65].

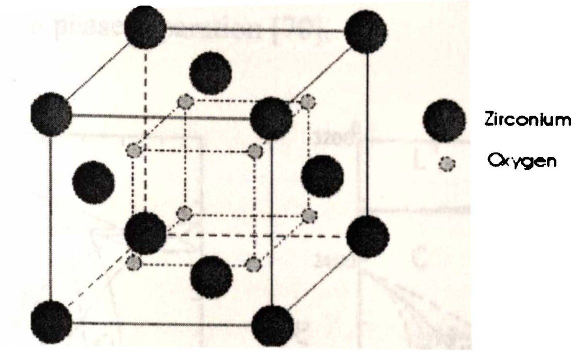

Figure 1-20 Cubic Phase (FCC) Zirconia [66]

The room temperature monoclinic zirconia has little use as a SOFC electrolyte because it is predominantly an electronic conductor with low oxygen ion conductivity [65]. Cubic zirconia has high ionic conductivity but needs to be stabilized so that it retains its cubic structure at room temperature. Nernst discovered and reported in 1899 that mixtures of zirconia with other oxides such as magnesia showed high ionic conduction at high temperatures [14]. Two years later, he patented his further observation that the material composition (15% yttria and 85% zirconia) was suitable for electric-lamp glowers [67]. Westinghouse Electric Corporation has used a similar zirconia-based electrolyte in their SOFC development since 1962 [68].

MO and M_2O_3 oxides (Y_2O_3, Yb_2O_3, ScO_3, CaO, MgO) can stabilize the high-temperature polymorphic form of zirconia to lower temperatures by forming solid solutions with ZrO_2. The divalent and trivalent metal cations substitute for Zr^{4+} in the lattice sites, reducing their valence state and also creating vacancies in the oxygen sub-lattice. These oxygen vacancies enable doped zirconia to be an oxygen-ion conductor and therefore useful as a SOFC electrolyte. Of the materials mentioned above, yttria-stabilized zirconia (YSZ) offers the best combination of ionic conductivity and stability in the SOFC environment and is currently the material of choice for the electrolyte in commercial SOFCs.

The ZrO_2-Y_2O_3 system phase diagram (Figure 1-21) indicates that 2.5-3 mol% Y_2O_3 stabilizes the tetragonal phase, and 8-9 mol% Y_2O_3 stabilizes the cubic phase at 1000°C [69], although researchers have reported slightly different Y_2O_3 dopant levels and temperatures to stabilize these phases. All compositions between 3-8 mol% Y_2O_3 are in the two-phase field at fuel cell operating temperatures, and undergo phase separation [70].

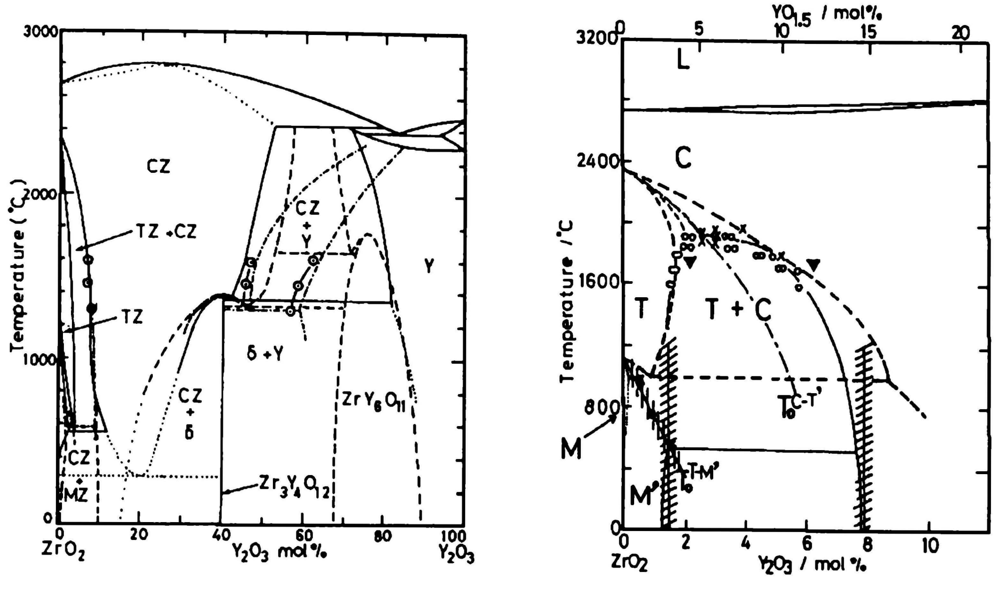

(a) (b)

Figure 1-21 (a) ZrO_2-Y_2O_3 Phase Diagrams and (b) ZrO_2 Rich Region [71].

The tetragonal phase has a small grain size (0.5 μm), high mechanical strength (~1000 MPa at room temperature), and high toughness and thermal shock resistance, but low ionic conductivity (0.055 S/cm at 1000°C) [65]. In comparison, the large grained cubic phase has lower strength but higher ionic conductivity 0.14-0.18 S/cm at 1000°C and 0.052 S/cm at 800°C [6]. Doping with 8 mol% Y_2O_3 stabilizes cubic zirconia and gives the highest ionic conductivity (~0.18 S/cm at 1000°C) while doping with 9-10 mol% Y_2O_3-ZrO_2 decreases conductivity slightly (Figure 1-22) [51]. In practice, however, yttria dopant level is maintained or slightly above the minimum required (8 mol%) for stabilization. The properties of YSZ have been extensively studied [66, 72, 73]. The operating temperatures of YSZ electrolyte based SOFCs are typically around 800-1000°C.

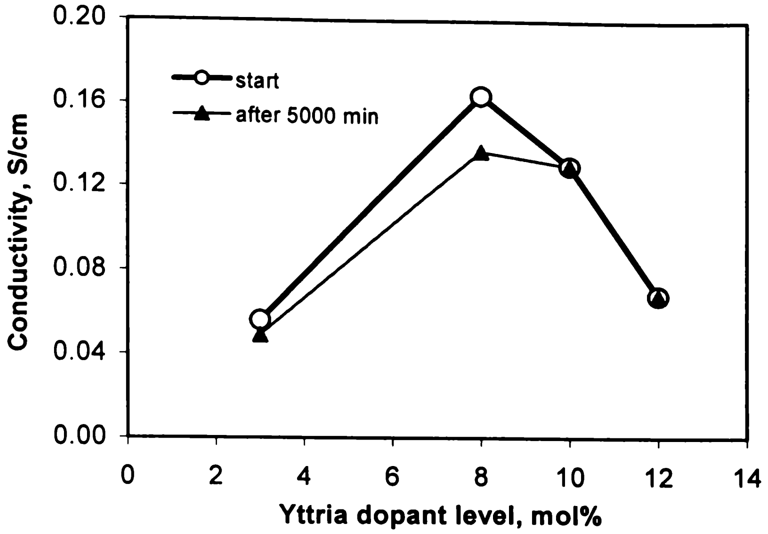

Figure 1-22 Effects of Y_2O_3 Concentration in Y_2O_3-ZrO_3 and Operating Time on Conductivity, after [65].

Adding a small amount of alumina affects the sintering behaviour, electrical properties, and mechanical properties of YSZ [74, 75]. One wt% Al_2O_3 results in dense sintered products, but additional density decreases with increasing alumina up to 20 wt%. Although maximum conductivity occurs at 1 wt%, the addition of Al_2O_3 causes an overall decrease in bulk conductivity (Figure 1-23). Common impurities in commercial YSZ powders are given in Table 1-15.

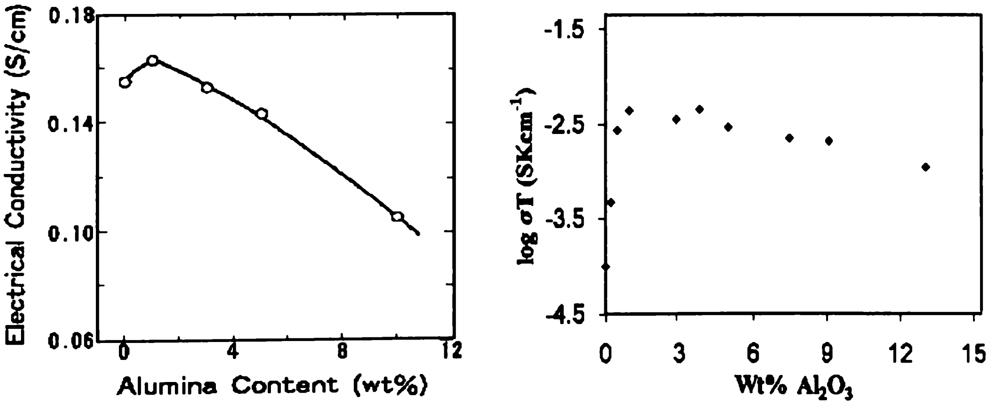

(a) (b)

Figure 1-23 Effect of Al_2O_3 Addition on Conductivity of 8YSZ (a) Bulk Conductivity at 1000°C [74]; (b) Grain Boundary Conductivity at 300°C [75].

Another group of doped zirconia electrolyte materials is scandia-doped zirconia (SDZ). SDZ has high ionic conductivity relative to other doped zirconia compounds, as shown in Figure 1-24. For example, 6-7 mol% and 8-10 mol% Sc_2O_3 doped ZrO_2 have ionic conductivities of 0.15-0.20 S/cm at 1000°C [76] and

0.11-0.12 S/cm at 800°C [51] respectively. Recent reports of cell performances with 6SDZ at 800°C are 0.6 W/cm^2 (140 μm 6SDZ support, LSM), 1.5 W/cm^2 (20 μm 6SDZ, LSM) and 2.4 W/cm^2 (20 μm 6SDZ, LSCF) [76].

Table 1-15 Typical Impurities in Commercial YSZ Powders [76-78]

Chemical specification, wt%	Commercial YSZ Powders			
	Tosoh (Japan)	MEL (UK)	AE (USA)	Nanbo (China)
ZrO_2+HfO_2+ Y_2O_3	>99.7			
Y_2O_3	13.3±0.6	13.6	13.56	13.5±0.5
Al_2O_3	≤0.1			
SiO_2	≤0.02	0.01	<0.01	≤0.01
Fe_2O_3	≤0.01	0.005	<0.001	≤0.005
TiO_2		0.01	<0.005	≤0.01
Na_2O	≤0.12		<0.005	≤0.005
MgO				≤0.003
Cl^-			<0.02	≤0.01
H_2O	≤0.4			≤0.4

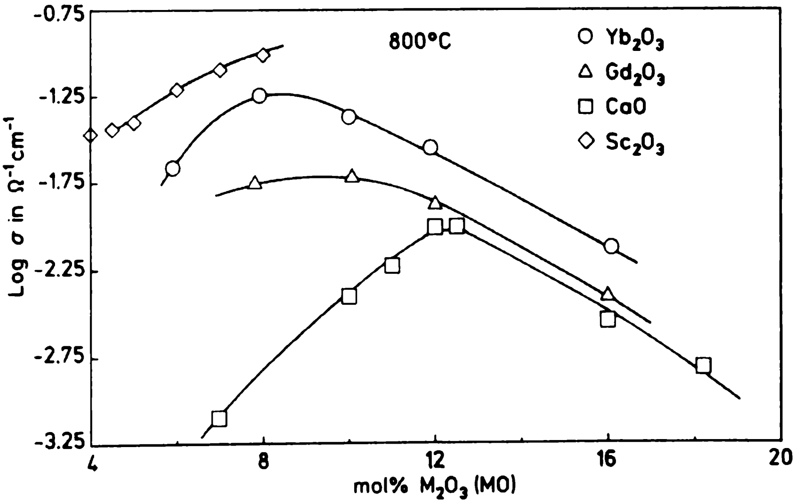

Figure 1-24 Effect of Dopants and Doping Level on Conductivity of Doped Zirconia at 800°C [73].

Although 8SDZ has about twice the conductivity of 8YSZ, this conductivity degrades rapidly at fuel cell operating temperatures (Figure 1-25) due to the metastable nature of phases formed at sintering temperatures [79, 80]. Availability and price of scandium are still uncertain [49] and scandia is very expensive.

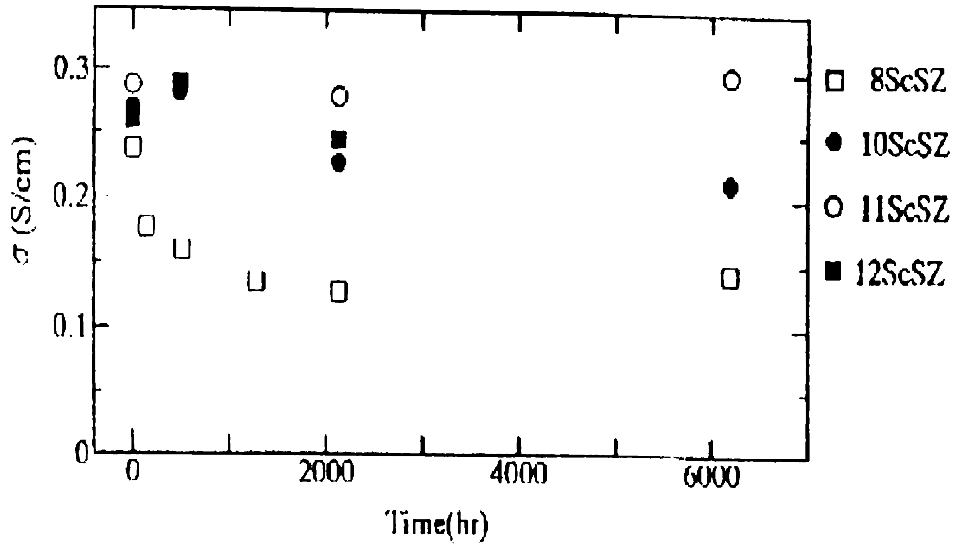

Figure 1-25 Conductivity of Scandia-Doped Zirconia (SDZ) at 1000°C [81].

1.5.2 Doped Lanthanum Gallate

Although yttria fully stabilized cubic zirconia is the most widely used electrolyte material in SOFCs, there is a need and great technological interest to identify alternative materials having higher ionic conductivity, and/or mechanical properties that will allow lower operating temperatures [65]. Ceramics currently being investigated include doped $LaGaO_3$ and doped CeO_2 [82-85].

$LaGaO_3$-based perovskite type oxides, in particular, Sr- and Mg-doped $LaGaO_3$ (LSGM), exhibit high oxide ion conductivity [85, 86]. The conductivity of $La_{0.9}Sr_{0.1}Ga_{0.8}Mg_{0.2}O_{3-x}$ is 0.12 S/cm at 800°C and 0.32 S/cm at 1000°C, which is similar to 9 mol% Sc_2O_3 doped ZrO_2 (0.31 S/cm) and higher by a factor of two compared to 8YSZ (0.16 S/cm) [87]. The major contributions to the high performance of LSGM electrolyte based fuel cells are the improvements in electrolyte conductivity and, more importantly, the exceptional structural and chemical compatibility with perovskite cathode materials, such as LSC.

Sr- and Mg-doped lanthanum gallate is a complex system, which experiences phase changes and often co-exists with secondary phases. At room temperature, this material has an orthorhombic structure, which transforms to a rhombohedral structure at 445K [88]. Recent investigations [89, 90] using high-resolution neutron diffraction have shown that the room temperature pseudo-orthorhombic changes to pseudo-rhombohedral between 250-500°C. This then transforms to the rhombohedral structure between 500-750°C.

Several phase diagrams of the La_2O_3-SrO-MgO-Ga_2O_3 system have been completed. A solubility study [91] of Mg and Sr in the perovskite LSGM phases found that the perovskite phase containing Sr and Mg had much better homogeneity range than if the perovskite phase contained only Sr or Mg. The Sr solubility in the perovskite with Sr and Mg could be as high as 20 mol% compared to if only 2 mol% Sr was present. Figure 1-26 illustrates the pure perovskite phase and impurity phases regions. LSGM must be as pure a phase as possible to optimise ionic conductivity.

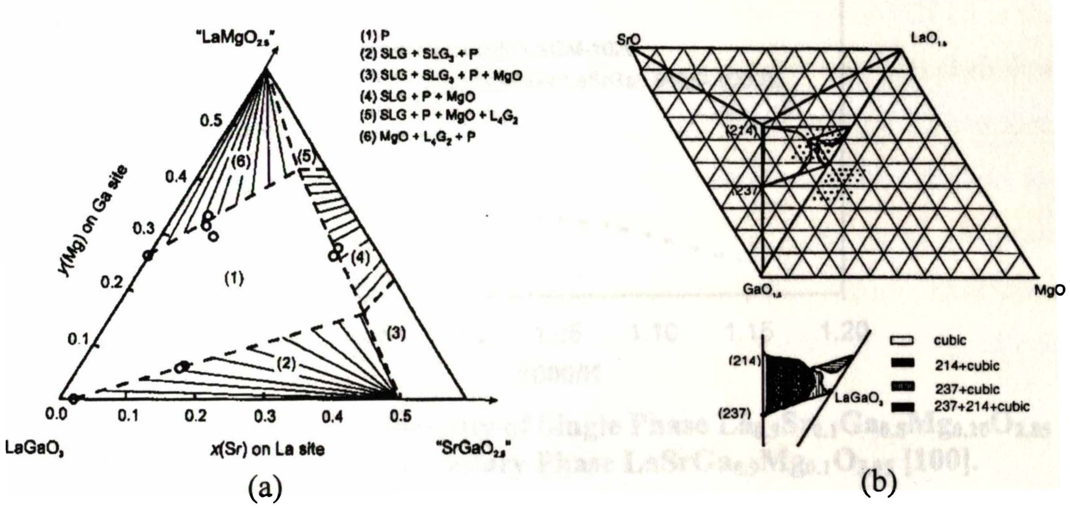

(a) (b)

Figure 1-26 Phase Diagrams of (a) $LaGaO_3$-$LaMgO_{2.5}$-$SrGaO_{2.5}$ System [91] and (b) $LaO_{1.5}$-SrO-$GaO_{1.5}$ Region (214=$LaSrGaO_4$, 237= $LaSrGa_3O_7$) [54].

LSGM materials can be synthesized using a solid state reaction [85, 92, 93], a sol-gel process [94, 95], or the Pechini [96] process. Although LSGM has attractive properties, there are technical issues that must be resolved. For example secondary phases ($LaSrO_7$, $LaSrGaO_4$, $LaSrGa_3O_7$ or $LaSrGa_{0.9}Mg_{0.1}O_{3.95}$) are often formed [97]. The instability of LSGM at 1000°C [98] and 1500°C [97] has been reported. The unit cell volume for material sintered at 1500°C increased 0.27% (from 237.74 $Å^3$ to 238.39 $Å^3$) after being heated at 1000°C for 130 hours. It is believed that the volume increase is due to the segregation of the secondary phases $LaSrO_7$ and $SrLaGaO_4$ from the parent phase. This segregation alters the LSGM crystal structure thus decreasing the concentration of oxygen-ion vacancies, and also reduces the electrolyte oxygen conductivity (Figure 1-27). However, it is possible to prevent secondary phase segregation using appropriate processing conditions. For example, material kept in H_2 at 750°C for 132 hours did not exhibit phase separation. Therefore, LSGM should not be sintered at high temperatures for extended periods during cell fabrication. Slightly decreasing the A-site composition $(La_{0.9}Sr_{0.1})_{1-x}(Ga_{0.8}Mg_{0.20})O_{3-\delta}$, (x=0.02 and 0.05) has been found to increase stability and conductivity [99].

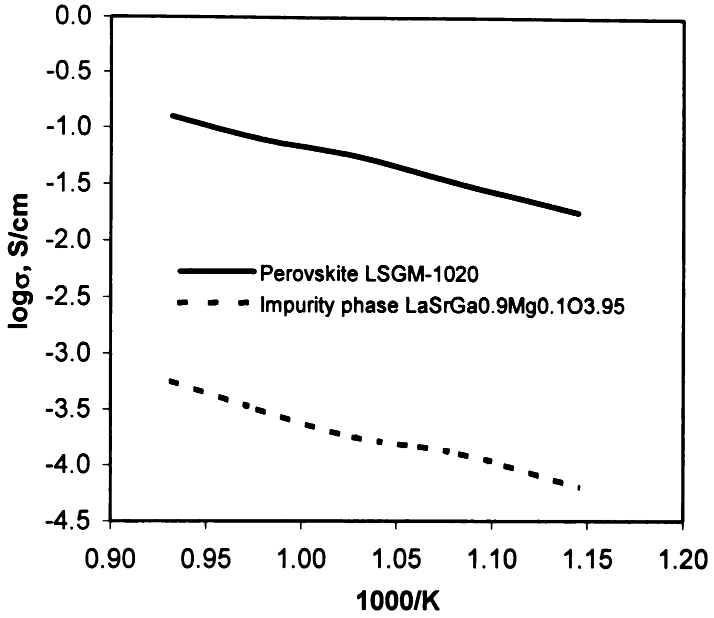

Figure 1-27 Electrical Conductivity of Single Phase $La_{0.9}Sr_{0.1}Ga_{0.8}Mg_{0.20}O_{2.85}$ (LSGM1020) and the Secondary Phase $LaSrGa_{0.9}Mg_{0.1}O_{3.95}$ [100].

Doping LSGM-2020 with Co produced $La_{0.8}Sr_{0.2}Ga_{0.8}Mg_{0.115}Co_{0.085}O_{2.8}$, with a maximum power density of 1.53 W/cm^2 at 800°C and 0.5 W/cm^2 at 600°C [101]. Another work [102] reports a similar fuel cell with a maximum power density of about 0.4 W/cm^2 at 650°C (Figure 1-28).

The mechanical and physical properties of LSGM were examined by Sammes *et al.*[103]. $La_{0.9}Sr_{0.1}Ga_{0.8}Mg_{0.2}O_{3-\delta}$ has a modulus of rupture (MOR) of 162 ± 14 MPa at room temperature and 55 ± 11 MPa at 900°C. MOR and fracture toughness of $La_{0.8}Sr_{0.2}Ga_{0.9}Mg_{0.1}O_{3-\delta}$ were 158 MPa and 1.63 MPa, respectively, which are much lower than the doped-ZrO_2 system. The TEC of 10^{-5} K^{-1} is similar to that of YSZ [104].

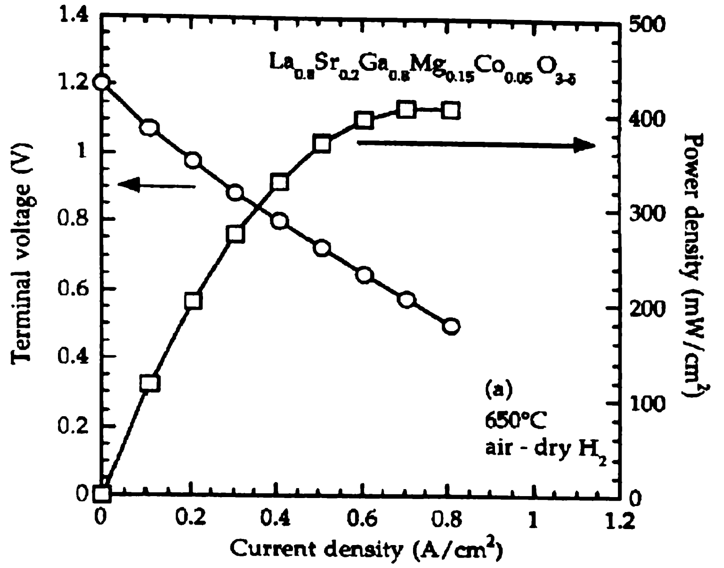

Figure 1-28 I-V/P Curves of a Fuel Cell: H_2+3 vol% H_2O, Ni/$La_{0.8}Sr_{0.2}Ga_{0.8}Mg_{0.115}Co_{0.085}O_{2.8}$/$Sm_{0.5}Sr_{0.5}CoO_3$, Dry Air [102].

The major drawback of LSGM materials as potential electrolytes in SOFCs is the expense of gallium compounds (LSGM-2020, US$1000-1500/kg), and their low mechanical strength, especially at the fuel cell operating temperatures. Therefore, it is unlikely that these materials will be used in electrolyte-supported designs for SOFCs. However, they could be used as a thin electrolyte layer on an electrode substrate [87] since thin films require much less material than support structures. Using thin film electrolytes (e.g. 10 μm) has additional benefits of increased cell performance and reduced operating temperatures (Figure 1-29).

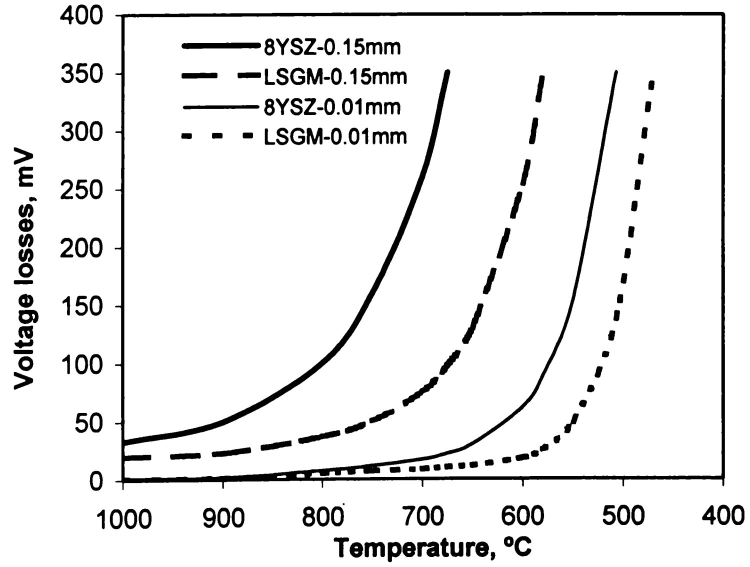

Figure 1-29 Effect of Temperature and Thickness on the Voltage Losses of YSZ and LSGM Electrolytes at 300 mA/cm² (after Tiffee [49])

Problems for applying thin LSGM films on electrode-supported system include overcoming the difficulty of densifying LSGM at lower temperatures (under 1400°C) and eliminating the chemical reactions between LSGM and the electrode materials [94, 105-107].

1.5.3 Doped Ceria

The physical, chemical and electrochemical properties of ceria-based electrolyte materials are reviewed by Mogensen *et al.* [108]. Pure ceria has a fluorite structure and is predominantly an electronic conductor. The ionic conductivity of pure ceria at 1000°C is only 0.07 S/cm less than 3% of the total conductivity of 2.5 S/cm [109]. Doping ceria with rare earth oxides such as Gd_2O_3, Y_2O_3, and Sm_2O_3 can significantly increase the oxygen ion conductivity. For example, gadolinium-doped ceria is an excellent oxygen-ion conductor with greater conductivity and lower conduction activation energy than YSZ. Samaria doped ceria has ionic conductivity close to that of LSGM in the intermediate-temperature range (600-800°C) (Figure 1-30).

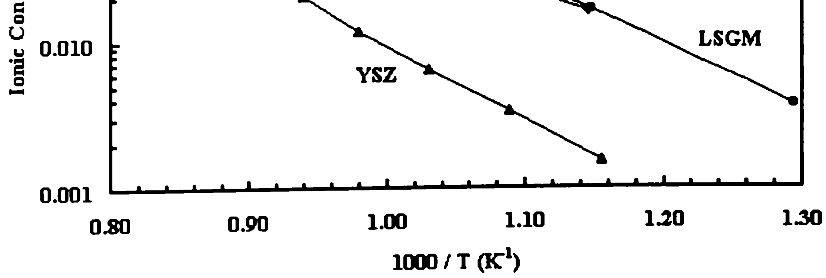

Figure 1-30 Ionic Conductivities of Intermediate-Temperature Electrolytes and Conventional YSZ Electrolyte [110].

However, in reducing environments, ceria based materials experience a partial reduction and develop electronic conductivity (becoming a mixed conductor). Ceria and zirconia in contact with each other react to form undesirable solid solutions at temperatures as low as 1200°C. The solid solutions have much lower ionic conductivity than zirconia or ceria doped electrolytes [111]. It may be necessary to protect ceria-based materials from reduction by for example an inter-material layer so that they can be used as SOFC electrolytes.

The characteristics of the most common electrolyte materials are summarized in Table 1-16. Their ionic conductivities are a strong function of temperature and the membrane thickness for equivalent resistance at different temperatures are given in Table 1-17. This relationship leads to flexibility in material selection and cell design. For example, at a given temperature, a thicker electrolyte of a better conductor could be used without increasing ohmic loses. Depending upon the temperature, SDC can be one to three times as thick as YSZ, and LSGM can be three to six times thicker than YSZ. The relationship between temperature, material and membrane thickness can also be used to estimate the temperature at which a given electrolyte thickness will have the same conductivity (Figure 1-31). For example, a design with a 15-μm electrolyte (ionic conductivity of 0.01 S/cm) requires an operating temperature of 700°C if using YSZ electrolyte; if LSGM or GDC electrolyte is used, the operating temperature could be reduced around 500°C. When considering all the requirements for an electrolyte material, zirconia based materials offer the best combination of conductivity, stability and cost, and represent the state-of-the-art electrolyte. As such, they are the most likely to be used in commercial SOFCs in a near future [49].

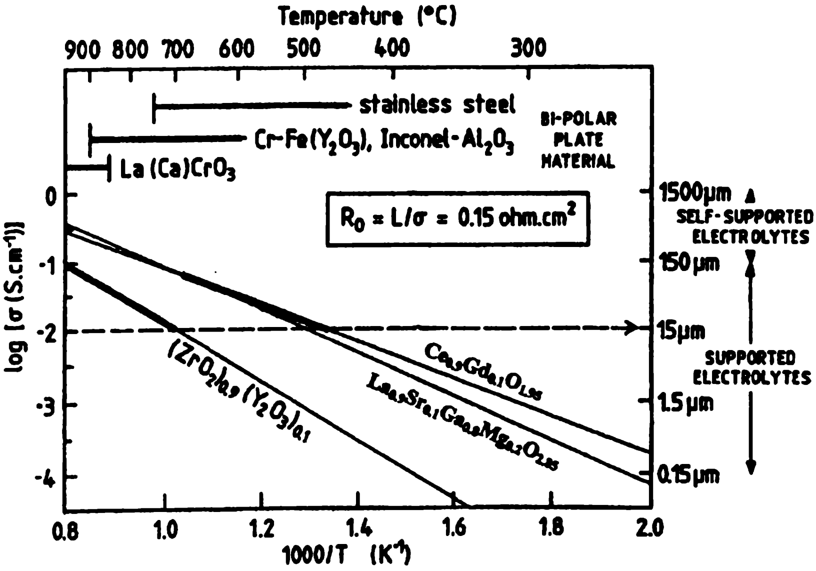

Figure 1-31 Comparison of the Specific Ionic Conductivities of the Most Commonly Interested YSZ, LSGM and GDC Electrolytes [112].

Table 1-16 Characteristics of Major Electrolyte Materials for SOFCs [51].

Electrolyte	YSZ	GDC	LSGM
Advantages	• Good oxygen ion conductivity • Excellent stability in both oxidizing and reducing environments • High quality raw materials available • Lifetime >40,000 h possible	• Good oxygen ionic conductivity • Good compatibility with cathode materials	• Excellent ionic conductivity • Good compatibility with cathode materials • $P_{O_2} = 10^{-19}$atm for ionic transference No. ≅ 1 at 800°C
Disadvantages	• Operating temperature 900-1000°C • Incompatible with LSM to form $La_2Zr_2O_7$ and/or $SrZrO_3$ during fabrication (>1200°C)	• Electronic conduction at low oxygen partial pressure • Mechanical stability	• Ga-evaporation at low Po_2 • Incompatible with NiO during cell fabrication • Mechanical stability • High cost due to limited gallium resources

Table 1-17 Comparison of the Membrane Thickness for Equivalent Resistance (Ω-cm^2) at Different Temperatures [8].

Electrolyte	800°C	700°C	600°C
YSZ	15 mm	5.5 mm	1.5 mm
SDC	35 mm	14.5 mm	6.5 mm
LSGM	56 mm	26 mm	9.5 mm
Y-doped Bi_2O_3	131 mm	75 mm	34 mm

1.6 Status of Tubular SOFC Technology and Challenges for Commercialisation

It has been stated that "fuel cell technologies offer unique opportunities for significant reductions in both energy use and emissions for transportation and stationary power applications."[5] Worldwide nearly 1000 companies, organizations, government agencies, and universities are performing R&D on fuel cell technology with about 20-25% of these working on SOFCs [113]. Some of the largest potential fuel cell markets include primary power plants, distributed stationary power (residential and commercial), transportation (auto and trucks), and portable personal. The fuel cell market is projected to be about $1 billion in

2005 and $20 billion by 2010 [114]. "Significant addition R&D would need to be conducted to achieve cost reductions and improved durability."[5] Some on-going fuel cell programs include: SECA Program (US, Solid State Energy Conversion Alliance, US$47 million for SOFC and MCFC), New Sunshine Program (Japan, US$220 million in 2002, of which US$15 million for SOFC) [5]. SECA's goals for SOFC development are given in Table 1-18.

Table 1-18 SECA's Goals for SOFC Development [17].

Time		2005	2008	2011
Power rating (net)		3-10 kW	3-10 kW	3-10 kW
Fuel cell system cost		$800/kW	$600/kW	$400/kW
Efficiency	Mobile	25-45%	35-50%	30-50%
	Stationary	35-55%	40-60%	40-60%
Power degradation, 500 h		≤ 2%	≤ 1%	≤ 0.1%
Lifetime	Mobile	5,000	5,000	5,000
	Stationary	40,000	40,000	40,000

Most of the SOFC stacks and systems are in the development or pre-commercialising stage. Stack integration, cell long-term stability and reliability, and cost reducing manufacturing techniques are still being investigated. Technical trends are towards reducing operating temperatures but increasing operating pressures [21, 40]. Operating a SOFC at elevated pressures increases cell voltage and thus power output for a given current. Operating at elevated operating pressure also allows SOFCs to be integrated with a turbine in a hybrid system, which significantly increases overall fuel cell system efficiency. Operating a SOFC at reduced temperatures provides benefits such as selection of less costly and better performing cell and structural materials, higher reliability, lower rates of cell degradation, and less thermal stress [115].

The SOFC patents granted in recent years indicate that significant progress has been made towards commercialisation. In Japan, there are more patents for tubular than for planar and monolithic SOFC designs. However, European patents tend to favour planar designs while US patents tend to be for SOFC stack configurations. An overview [116] of SOFC patents show that the trends are: easy assembly and installation, increased gas flow, increased power efficiency, longer life with less or no maintenance, and higher power output. The preferred materials are: YSZ for electrolyte, NiO-YSZ for anode, $La_{1-x}(A)_xMe_{1-x}(B)_xO_3$ for cathode, and noble metals and superalloys for current collectors.

As a leading company in tubular SOFC technology development, SWPC focuses on developing large and pressurized SOFC/GT (gas turbine) systems for power plants [6]. A single tubular SOFC can generate up to 210 W DC at atmospheric pressure and 1000°C, with 85% fuel utilization and 25% air utilization [117]. The maximum power density is 0.202 W/cm^2 [i.e. 210W/(150cm×2.2cm×3.14)] and the volumetric power density is 0.289 W/cm^3 [i.e. 210W/(2.2cm×2.2cm×150cm)]. A 300-MW Pressurized SOFC/GT power plant has been built at $1320/kW [21]. SWPC believes cell life for commercial cells will be 10-20 years [11].

All of the three basic SOFC designs (planar, tubular and monolithic) are being developed in Japan. MHI is considered the leading SOFC developer and has developed multi-kW stacks. For example, a stack made up of 414 tubular cells, each 1.5 cm in diameter and 70 cm active length, achieved a maximum output of 21 kW [40]. Maximum power density can be calculated as: 0.154 W/cm^2 [i.e. 21,000W/(414x1.5cm×3.14×70cm)]. Toto and Nippon Steel [99] have developed a 36-cell-bundle (2.2 cm diameter, 90 cm effective length) run on natural gas (70% fuel utilization) at 1 atm. The output is 3 kW, with a cell performance 0.134 W/cm^2 [i.e. 3000W/(2.2cmx3.14×90cmx36)].

Although SOFCs have the potential to be used on large scale relative to other fuel cell types, significant materials, cell and stack assembly challenges are to be resolved to reduce cost and to increase durability. The principle areas for R&D include [3]: system designs (the way that cells are constructed and stacks are integrated); materials (developing electrolyte and electrode materials compatible with reduced operating temperatures of 600-800°C; interconnect/current collector materials); and cheap manufacturing technology. The following are the specific technical challenges for SOFC commercialisation [118]:

- Electrolyte: intermediate temperature electrolytes (CeO_2-based, $LaGaO_3$-based, and Sc_2O_3-doped ZrO_2);

- Cathode: better mixed (electronic and ionic) conducting materials (cobaltites, ferrates);
- Anode: redox (reduction-oxidation) tolerant materials (ceramic or cermet);
- Interconnection: high oxidation resistant and low cost metallic alloys;
- Seals: glass, glass-ceramic, or non-glass seals, especially for planar designs;
- Manufacturing: low cost and mass production fabrication techniques; and
- BOP: integration and low cost.

For commercialisation, SOFC system costs must be well below $2000/kW, while cell costs must be less than $400/kW (Figure 1-32). SOFC costs consist of three main parts: single cells, stack, and BOP. Most of the SOFC development and cell construction have been performed by highly labour-intensive processes. With large volume requirements and new cost-effective manufacturing techniques, the cost could be significantly reduced.

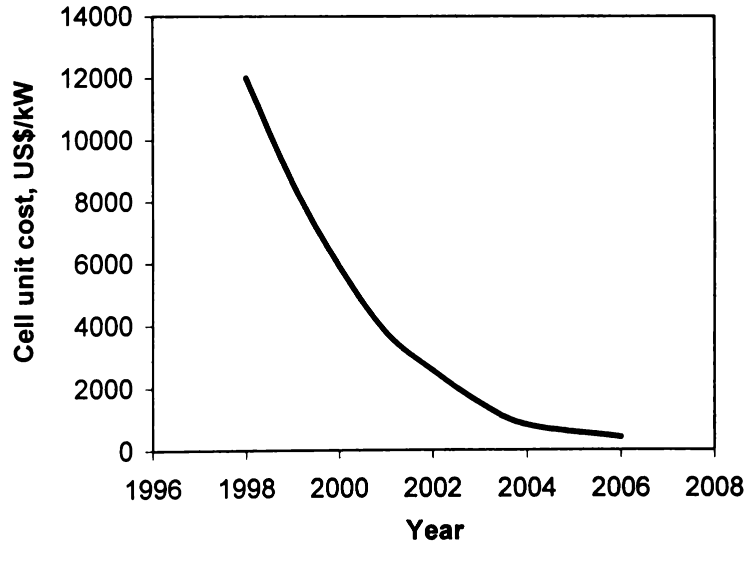

Figure 1-32 Tubular SOFC Cost Forecast [60].

1.7 References

1. Bossel, U., *The birth of fuel cell*: European Fuel Cell Forum. 2000.
2. Grove, W.R., "On voltaic series and the combination of gases by platinum," in *The London and Edinburgh Philosophical Magazine and Journal of Science*. 1839. p. 127-130.

3. Acres, G.J.K., "Recent advances in fuel cell technology and its applications." *J. Power Sources*, 2001. **100**: p. 60-66.
4. Cacciola, G., Antonucci, V. and Freni, S., "Technology up date and new strategies on fuel cells." *J. Power Sources*, 2001. **100**: p. 67-79.
5. Department of Energy, *Fuel cell report to Congress,* ESECS EE-1973, 2003.
6. Badwal, S.P.S. and Foger, K., "Solid Oxide Electrolyte Fuel Cell Review." *Ceramics International*, 1996. **22**: p. 257-265.
7. EG & G Services Parsons, *Fuel cell handbook (fifth edition)*: US Department of Energy. 2000.
8. Singh, P., Pederson, L.R., Simner, S.P., Stevenson, J.W. and Viswanathan, V.V., "Solid oxide fuel cell power generation systems." in *36th Annual intersociety Energy Conversion Engineering Conference Advance Program*. 2001, p. 953-958.
9. Siemens, http://www.pg.siemens.com/en/fuelcells/benefits/index.cfm, 2003.
10. Department of Energy, http://www.dodfuelcell.com/pafc/index.php3, 2003.
11. Williams, M.C., "Status and market applications for the solid oxide fuel cell in the U.S.-a new direction." in *Seventh International Symposium on Solid Oxide Fuel Cells (SOFC VII)*. 2001. Tsukuba, Japan: The Electrochemical Society, Inc., p. 3.
12. Tietz, F., Dias, F.J., Simwonis, D. and Stover, D., "Evaluation of commercial nickel oxide powders for components in solid oxide fuel cells." *J. Eur. Ceram. Soc*, 2000. **20**: p. 1023-1034.
13. Larminie, J. and Dicks, A., *Fuel cell systems explained*: John Wiley & Sons, Ltd. 2002.
14. Nernst, W., "On the electrolytic conduction of solid bodies at high temperatures." *Zeischrift fur Elektrochemie*, 1899. **6**: p. 41.
15. Baur, V.E. and Preis, H., "Uber Brennstoff-Ketten mit Festleitern." *Zeitschrift Elektrochemie*, 1937. **43**(9): p. 727-732.
16. Cameron, D.S., "World development of fuel cell." *Int. J. Hydrogen Energy*, 1990. **15**(9): p. 669.
17. Surdoval, W.A., Singhal, S.C. and McVay, G.L., "The SECA-a U.S. Department of Energy initiative to promote the development of mass customized SOFCs for low-cost power." in *Seventh International Symposium on Solid Oxide Fuel Cells (SOFC VII)*. 2001. Tsukuba, Japan: The Electrochemical Society, Inc., p. 53.
18. http://www.spice.or.jp/~fisher/sofc.html, 2002.
19. Atkins, P.W., *Physical chemistry*, ed. 3rd. New York: W.H. Freeman and Company. 1986.
20. Fee, D.C. and Zwick, S.A., "High-temperature solid oxide electrolytes. 1983. Brookhaven National Laboratory, p. 29.
21. Lundberg, W.L. and Veyo, S.E., "Conceptual design and performance analysis of a 300 MWe LNG-fueled pressurized SOFC/gas turbine power plant." in *Seventh International Symposium on Solid Oxide Fuel Cells (SOFC VII)*. 2001. Tsukuba, Japan: The Electrochemical Society, Inc., p. 78.
22. Yasuda, I., Baba, Y., Ogiwara, T. and Yakabe, H., "Development of anode-supported SOFC for reduced-temperature operation." in *Seventh International Symposium on Solid Oxide Fuel Cells (SOFC VII)*. 2001. Tsukuba, Japan: The Electrochemical Society, Inc., p. 131.
23. Williams, M.C., "Status and market applications for the solid oxide fuel cell in the U.S." in *Third European Solid Oxide Fuel Cell Forum*. 1998. France, p. 27.
24. Minh, N.O. and Takahashi, T., *Science and technology of ceramic fuel cell*. Amsterdam: Elsevier Science B.V. 1995.

25. Singhal, S.C., "Advances in tubular solid oxide fuel cell technology." in *The Fourth International Symposium on Solid Oxide Fuel Cells (SOFC-IV)*. 1995: The Electrochemical Society, Inc., p. 195-207.
26. Minh, N.Q., "Ceramic fuel cells." *J. Am. Ceram. Soc.*, 1993. **76**(3): p. 563-588.
27. Myleys, K.M. and McPheeters, C.C., "Monolithic solid oxide fuel cell development." *J. Power Sources*, 1990. **29**: p. 311-319.
28. Stover, D., Henne, R., Otschik, P. and Schichl, H., "Recent developments of SOFC technology in Germany." in *Seventh International Symposium on Solid Oxide Fuel Cells (SOFC VII)*. 2001. Tsukuba, Japan: The Electrochemical Society, Inc., p. 38.
29. Bele, H.J., Blum, L., Drenckhahn, W., Greiner, H., Schichi, H., "Development of planar SOFC at Siemens - status and prospects." in *Third European Solid Oxide Fuel Cell Forum*. 1998. Nantes, France, p. 3-13.
30. Schafer, W., Koch, A., Herold-Schmidt, U., Stolten, D., "Materias, interfaces and production techniques for planar SOFCs." *Solid State Ionics*, 1996. **86-88**: p. 1235-1239.
31. Billingham, J., King, A.C., Copcutt, R.C., Kendall, K., “Analysis of a model for a loaded, planar, solid oxide fuel cell.” *J. Applied Mathematics*, 2000. **60**(2): p. 574-601.
32. Murata, K., Shimotsu, M., "Fabrication and evaluation of electrode supported planar SOFC stack performance." *Electrochemistry*, 2001. **69**(8): p. 587-591.
33. Sohn, S.B., Choi, S.Y., Kim, G.H., Song, H.S., Kim, G.D., "Stable sealing glass for planar solid oxide fuel cell." *J. Non-Crystalline Solids*, 2002. **297**: p. 103-112.
34. Larsen, P.H., Bagger, C., Linderoth, S. and al., e., "Status of the Danish SOFC Program." in *Seventh International Symposium on Solid Oxide Fuel Cells (SOFC VII)*. 2001. Tsukuba, Japan: The Electrochemical Society, Inc., p. 28.
35. Badwal, S.P.S. and Foger, K., "SOFC development at Ceramic Fuel Cells Limited." *J. Aust. Ceramics Soc.*, 1998. **34**(1): p. 1-6.
36. Lequeux, G., "Status of the European SOFC Programme." in *Seventh International Symposium on Solid Oxide Fuel Cells (SOFC VII)*. 2001. Tsukuba, Japan: The Electrochemical Society, Inc., p. 14.
37. Ghosh, D., Tang, E., Perry, M. and, "Status of SOFC developments at Global Thermoelectric." in *Seventh International Symposium on Solid Oxide Fuel Cells (SOFC VII)*. 2001. Tsukuba, Japan: The Electrochemical Society, Inc., p. 100.
38. Singhal, S.C., "Siemens Westinghouse solid oxide fuel cell technology." in *The 12th International Conference on Solid State Ionics*. 1999. Greece.
39. Siemens, http://www.pg.siemens.com/en/fuelcells/sofc, 2003.
40. Iritani, J. and Kougami, K., "Pressurized 10 kW class module of SOFC." in *Seventh International Symposium on Solid Oxide Fuel Cells (SOFC VII)*. 2001. Tsukuba, Japan: The Electrochemical Society, Inc., p. 63.
41. Song, R.H., Song, K.S., Ihm, Y.E. and Yokokawa, H., "Fabrication and performance characteristics of anode-supported tubular solid oxide fuel cell." in *Seventh International Symposium on Solid Oxide Fuel Cells (SOFC VII)*. 2001. Tsukuba, Japan: The Electrochemical Society, Inc., p. 1073.
42. Kendall, K., "*Fuel cell power generating system*," USA, US patent No.: 6358640, 2002.
43. Kendall, K. and Prica, M., "Integrated SOFC tubular system for small scale cogeneration." in *First European Solid Oxide Fuel Cell Forum*. 1994. Lucerne, Switzerland, p. 163.
44. Sammes, N.M., "*Integrated solid oxide fuel cell and reformer*," USA, US patent No.: 6492050, 2002.

45. Du, Y., Sammes, N.M. and England, R., "Novel SOFC tubular design configuration." in *Eighth International Symposium on Solid Oxide Fuel Cells (SOFC VIII)*. 2003. Paris, France, p. 1077.

46. Du, Y., Sammes, N.M., Tompsett, G.A. and al., e., "Extruded tubular strontium- and magnesium-doped lanthanum gallate, gadolinium-doped ceria, and yttria-stabilized zirconia electrolytes: Mechanical and thermal properties." *J. Electrochem. Soc.*, 2003. **150**(1): p. A74.

47. NEDO, http://www.eeca.govt.nz/default2.asp?Target=Search/Search.asp, 2003.

48. Gao, W. and Sammes, N.M., *An introduction to electronic and ionic materials*. Singapore: World Scientific. 1999.

49. Tiffee, E.I., Weber, A. and Herbstritt, D., "Materials and technologies for SOFC-components." *J. Eur. Ceram. Soc.*, 2001. **21**: p. 1805-1811.

50. Kofstad, P., *High temperature corrosion*: Elsevier. 1998.

51. Badwal, S.P.S., "Stability of solid oxide fuel cell components." *Solid State Ionics*, 2001. **143**: p. 39-46.

52. Fukui, T., Ohara, S., Naito, M. and Nogi, K., "Morphology and performance of SOFC anode fabricated from NiO/YSZ composite particles." *J. Chemical Engineering of Japan*, 2001. **34**(7): p. 964-966.

53. Kim, J.W., Virkar, A.V., Fung, K.Z., Mehta, K. and Singhal, S.C., " Polarization effects in intermediate temperature, anode-supported solid oxide fuel cells." *J. Electrochem. Soc.*, 1999. **146**(1): p.69-78.

54. Huang, K., Wan, J. and Goodenough, J.B., "Increasing power density of LSGM-based solid oxide fuel cells using new anode materials." *J. Electrochem. Soc.*, 2001. **148**(7): p. A788-A794.

55. Roosmaen, J.A.M.v. and Cordfunke, E.H.P., "Chemical reactivity and interdiffusion of (La,Sr) MnO_3 and $(Zr,Y)O_2$, solid oxide fuel cell cathode and electrolyte materials." *Solid State Ionics*, 1992. **52**: p. 303-312.

56. Yokokawa, H., Horita, T., Sakai, N., Dokiya, M. and Kawada, T., "Thermodynamic representation of nonstoichiometric lanthanum manganite." *Solid State Ionics*, 1996. **86-88**: p. 1161-1165.

57. Chen, G., Liu, J., He, F., Su, W., Wang, B., "Fabrication and properties of $La_{0.7}Sr_{0.3}CoO_3$ cathode for solid electrolyte fuel cells" *China Rare Earth Elements*, 1993. **11**(2): p. 131-134.

58. Skinner, S.J. and Kilner, J., "Oxygen ion conductors," in *Materials Today*. 2003 p. 30.

59. Jiang, Y., Virkar, A.V. and Zhao, F., "The effect of testing geometry on the measurement of cell performance in anode-supported solid oxide fuel cells." *J. Electrochem. Soc.*, 2001. **148**(10): p. A1091-A1099.

60. Bessette, N.F., Borglum, B.P., Schichl, H. and Schmidt, D.S., "Siemens SOFC technology on the way to economic competitiveness," in *Power Journal - Magazine of the Siemens Power Generation Group*. 2001 p. 9.

61. Takahashi, T. and Iwahara, H., "Oxide ion conductors based on bismuthseaquioxide." *Mater. Research Bulletin.*, 1978. **13**: p. 1447.

62. Tompsett, G.A., PhD Thesis: *Characterisation and phase equilibrium of doped-Bi_2O_3 and doped-CeO_2 systems*. Department of Technology, University of Waikato. 1997.

63. Shuk, P., Wiemhofer, H.D., Guth, U. and Gopel, W., "New solid electrolytes based on bismuth oxide." *Ionics*, 1996. **2**: p. 46-52.

64. Ishihara, T., Matsuda, H. and Takita, Y., "Doped $LaGaO_3$ perovskite type oxide as a new oxide ionic conductor." *J. Am. Chem. Soc.*, 1994. **116**: p. 3801-3803.

65. Badwal, S.P.S., "Zirconia-based solid electrolytes: microstructure, stability and ionic conductivity." *Solid State Ionics*, 1992. **52**: p. 23-32.

66. Somiya, S., Yamamoto, N. and Yanagida, H., *Science and technology of zirconia III*, in *Advances in Ceramics*. 1988, American Ceramic Society: Columbus, OH.

67. Nernst, W., "*Material for electric-lamp glowers*," USA, US patent No.: U 00685730, 1901.

68. Hooger, G., ed. *Fuel cell technology handbook*. CRC Press. 2003.

69. Estell, T.H. and Flengas, N., "The electrical properties of solid oxide electrolytes." *Chemical Reviews*, 1970. **70**(3): p. 340-376.

70. Scott, H.G., "Phase relationships in the zirconia-yttria system." *J. Mater. Sci.*, 1975. **10**: p. 1527-1535.

71. Yoshimura, M., "Phase stability of zirconia." *Ceramic Bulletin*, 1988. **67**(12): p. 1950-1955.

72. Heuer, A.H. and Hobbs, L.W., *Science and technology of circonia*, in *Advances in Ceramics*. 1981, American Ceramic Society: Columbus, OH.

73. Claussen, N., Ruhle, M. and Heuer, A.H., *Science and Technology of Zirconia II*, in *Advances in Ceramics*. 1984, American Ceramic Society: Columbus, OH. p. 555.

74. Bredikhin, S., Maeda, K. and Awano, M., "NO decomposition by an electrochemical cell with mixed oxide working electrode." *Solid State Ionics*, 2001. **144**(1-2): p. 1-9.

75. Feighery, A.J. and Irvine, J.T.S., "Effect of alumina additions upon electrical properties of 8 mol% yttria-stabilised zirconia." *Solid State Ionics*, 1999. **121**: p. 209-216.

76. Sumi, H., Ukai, K., Hisada, K., Mizutani, Y. and Yamamoto, O., "High performance cell development using scandia doped zirconia electrolyte for low temperature operating." in *Eighth International Symposium on Solid Oxide Fuel Cells (SOFC VIII)*. 2003. Paris, France, p. 995.

77. Tosoh, "Product information--zirconia powder." 2003 p. 1.

78. Ciacchi, F.T., Crane, K.M. and Badwal, S.P.S., "Evaluation of commercial zirconia powders for solid oxide fuel cells." *Solid State Ionics*, 1994. **73**: p. 49-61.

79. Badwal, S.P.S., Ciacchi, F.T., Rajendran, S. and Drennan, J., "An investigation of conductivity, microstructure and stability of electrolyte compositions in the system 9 mol% (Sc_2O-Y_2O_3)-ZrO_2(Al_2O_3)." *Solid State Ionics*, 1998. **109**: p. 167-186.

80. Ciacchi, F.T., Badwal, S.P.S. and Drennan, J., "The system Y_2O_3-Sc_2O_3-ZrO_2: phase characterisation by XRD, TEM and optical microscopy." *J. Eur. Ceram. Soc.*, 1991. 7: p. 185-195.

81. Yamamoto, O., Arati, Y., Takeda, Y., Imanishi, N., Mizutani, Y., Tamura, M. and Kawai, M., "Zironia based solid oxide ion conductors in solid oxide fuel cells." in *4th Asian Conference on Solid State Ionics*. 1994. Malaysia: World Scientific Publishing Co., p. 51-58.

82. Sammes, N.M., Keppeler, F.M., Nafe, H. and Aldinger, F., "Mechanical properties of solid-state-synthesized strontium- and magnesium-doped lanthanum gallate." *J. Am. Ceram. Soc.*, 1998. **81**(12): p. 3104-3108.

83. Huang, K., Tichy, R.S. and Goodenough, J.B., "Superior perovskite oxide-ion conductor; strontium- and magnesium-doped $LaGaO_3$: I, phase relationships and electrical properties." *J. Am. Ceram. Soc.*, 1998. **81**(10): p. 2565-2575.

84. Huang, K., Tichy, R.S. and Goodenough, J.B., "Superior perovskite oxide-ion conductor; strontium- and magnesium-doped $LaGaO_3$: II, AC impedance spectroscopy." *J. Am. Ceram. Soc.*, 1998. **81**(10): p. 2576-80.

85. Ishhara, T., Matsuda, H. and Takita, Y., "Doped $LaGaO_3$ Perovskite Type Oxide as a New Oxide Ionic Conductor." *J. Am. Chem. Soc.*, 1994. **116**: p. 3801-3803.

86. Feng, M. and Goodenough, J.B., "A superior oxide-ion electrolyte." *Eur. J. Solid State Inorg. Chem.*, 1994. **t31**(8-9): p. 663-672.

87. Drennan, J., Zelizko, V., Hay, D., Ciacchi, F.T., Rajendran, S. and Badwal, S.P.S., "Characterisation, conductivity and mechanical properties of the oxygen-ion conductor $La_{0.9}Sr_{0.1}Ga_{0.8}Mg_{0.2}O_{3-x}$." *J. Mater. Chem.*, 1997. **7**(1): p. 79-83.

88. Marti, W., "Crystal structures and phase transitions of orthohombic and rhombohedral $RGaO_3$ (R=La, Pr, Nd) investigated by neutron powder diffraction." *J. Phys.: Condens. Matter*, 1994. **6**: p. 127-135.

89. Slater, P.R., Irvine, J.T.S., Ishihara, I. and Takita, Y., "The structure of the oxide ion conductor $La_{0.9}Sr_{0.1}Ga_{0.8}Mg_{0.2}O_{2.85}$ by powder neutron diffraction." *Solid State Ionics*, 1998. **107**: p. 319-323.

90. Lerch, M., Boysen, H. and Hansen, T., "High-temperature neutron scattering investigation of pure and doped lanthanum gallate." *J. Phys. and Chem. Solids*, 2001. **62**: p. 445-455.

91. Matraszek, A., Kobertz, D., Singheiser, L. and Hilpert, K., "Thermodynamic studies of perovskietes on the basis of LaGaO3 and implications for SOFC." in *Seventh International Symposium on Solid Oxide Fuel Cells (SOFC VII)*. 2001. Tsukuba, Japan: The Electrochemical Society, Inc., p. 319.

92. Feng, M., Goodenough, J.B., Huang, K. and Milliken, C., "Fuel cells with deoped lanthanum gallate electrolyte." *J. Power Sources*, 1996. **63**: p. 47-51.

93. Huang, P.N. and Petric, A., "Superior oxygen ion conductivity of lanthanum gallate doped with strontium and magnesium." *J. Electrochem. Soc.*, 1996. **143**(5): p. 1644-48.

94. Polini, R., Pamio, A. and Traversa, E., "Sol-gel syntheses and phase purity of $La_{1-x}Sr_xGa_{1-y}Mg_yO_{3-z}$ solid electrolytes." in *Eighth International Symposium on Solid Oxide Fuel Cells (SOFC VIII)*. 2003. Paris, France, p. 324.

95. Huang, K., Feng, M. and Goodenough, J.B., "Sol-gel synthesis of a new oxide-ion conductor Sr- and Mg-doped $LaGaO_3$ perovskite." *J. Am. Ceram. Soc.*, 1996. **79**(4): p. 1100-1104.

96. Pechini, M.P., "*Method of preparing lead and alkaline earth titanaties and niobates and coating method using the same to form a capacitor*," USA, US patent No.: 3330697, 1967.

97. Djurado, E. and Labeau, M., "Second phases in doped lanthanum gallate perovskites." *J. European Ceramic Soc.*, 1998. **18**: p. 1397-1404.

98. Tao, S., Poulsen, F.W., Meng, G. and Orensen, O.T.S., "High-temperature stability study of the oxygen-ion conductor $La_{0.9}Sr_{0.1}Ga_{0.8}Mg_{0.2}O_{3-x}$." *J. Mater. Chem.*, 2000. **10**: p. 1829.

99. Nakayama, T. and Suzuki, M., "Current status of SOFC R&D program at NEDO." in *Seventh International Symposium on Solid Oxide Fuel Cells (SOFC VII)*. 2001. Tsukuba, Japan: The Electrochemical Society, Inc., p. 8.

100. Yamaji, K., Xiong, Y., Horita, T., Sakai, N. and Yokokawa, H., "Characterization of $(La_{0.9}Sr_{0.1})_{1+x}(Ga_{0.8}Mg_{0.2})O_{3-z}$ electrolytes with nonstoichiometric compositions." in *Seventh International Symposium on Solid Oxide Fuel Cells (SOFC VII)*. 2001. Tsukuba, Japan: The Electrochemical Society, Inc., p. 413-421

101. Ishihara, T., Shibayama, T., Honda, M., Nishiguchi, H. and Takita, Y., "Solid oxide fuel cell using Co doped $La(Sr)Ga(Mg)O_3$ perovskite oxide with notably high power density at intermediate temperature." *Chem. Commun.*, 1999: p. 1227.

102. Ishihara, T., Shibayama, T., Honda, M., Nishiguchi, H. and Takita, Y., "Intermediate temperature solid oxide fuel cells using $LaGaO_3$ electrolyte II. improvement of oxide ion conductivity and power density by doping Fe for Ga site of $LaGaO_3$." *J. Electrochem. Soc.*, 2000. **147**: p. 1332.

103. Sammes, N.M., Keppeler, F.M., Nafe, H., Aldinger, F. and Tompsett, G.A., "The high temperature mechanical properties of $La_{0.8}Sr_{0.2}Ga_{1-x}Mg_xO_{3-z}$." *J. Aust. Ceramic Soc.*, 1998. **34**(1): p. 99-105.

104. Hayashi, H., Suzuki, M. and Inaba, H., "Thermal expansion of Sr- and Mg-doped $LaGaO_3$." *Solid State Ionics*, 2000. **128**: p. 131-139.

105. Zhang, X., Ohara, S., Okawa, H., Maric, R. and Fukui, T., "Interactions of a $La_{0.9}Sr_{0.1}Ga_{0.8}Mg_{0.2}O_{3-z}$ electrolyte with Fe_2O_3, Co_2O_3 and NiO anode materials." *Solid State Ionics*, 2001. **139**: p. 145-152.

106. Elangovan, S., "Lanthanum gallate electrolyte for intermediate temperature operation." in *Eighth International Symposium on Solid Oxide Fuel Cells (SOFC VIII)*. 2003. Paris, France, p. 299.

107. Jacobson, C.P., Visco, S.J. and Jonghe, C.D.,"Cathode supported thin film SOFCs." in *Eighth International Symposium on Solid Oxide Fuel Cells (SOFC VIII)*. 2003. Paris, France, p. 1035-1039

108. Mogensen, M., Sammes, N.M. and Tompsett, G.A., "Physical, chemical and electrochemical properties of pure and doped ceria." *Solid State Ionics*, 2000. **129**: p. 63-94.

109. Mogensen, M., Lindegaard, T., Hansen, U.R. and Mogensen, G., "Physical properties of mixed conductor solid oxide fuel cell anodes of doped CeO_2." *J. Electrochem. Soc.*, 1994. **141**: p. 2122.

110. Sammes, N., *High temperature fuel cell engineering,* Lecture of ME 320, 2003.

111. Tsoga, A., Naoumidis, A., Skarmoutsos, D. and Nikolopoulos, P., "Performance of a double-layer CGO/YSZ electrolyte for solid oxide fuel cells." *Ionics*, 1998. **4**: p. 234-240.

112. Steele, B.C.H., "Material science and engineering: The enabling technology for the commercialisation of fuel cell systems." *J. Mater. Sci.*, 2001. **36**(5): p. 1053-1068.

113. FuelCell2000, http://www.fuelcells.org/, 2003.

114. Prell, F., "Fuel cell industry perspective." 2003 p. 1.

115. Hou, P.Y., Huang, K. and Bakker, W.T., "Promises and problems with metallic interconnects for reduced temperature solid oxide fuel cells." in *Solid Oxide Fuel Cells (SOFC VI)*. 1999. Hawaii: The Electrochemical Society, Inc., p. 737-748.

116. Kozhukharov, V., Machkova, M., Ivanova, M. and Brashkova, N., "Patents state-of-the-art in SOFCs application." in *Seventh International Symposium on Solid Oxide Fuel Cells (SOFC VII)*. 2001. Tsukuba, Japan: The Electrochemical Society, Inc., p. 244.

117. Siemens, http://www.pg.siemens.com/en/fuelcells/sofc/tubular/index.cfm, 2003.

118. Singhal, S.C., "Solid oxide fuel cells for clean and efficient power generation." in *Blue Skies Energy Technologies*. 2002. Atlanta, Georgia.

Chapter Two

Fabrication Techniques for Tubular Solid Oxide Fuel Cells

This chapter reviews the various techniques for fabricating tubular solid oxide fuel cells (SOFCs) with particular emphasis on the ceramic extrusion process. Paste formulation, extrusion die design and thin film technology are also covered.

2.1 Introduction

Several ceramic and thin film techniques such as paste extrusion, slip casting, slurry coating, plasma spraying and electrochemical vapor deposition (EVD) have been adapted for tubular SOFC fabrication. When selecting or developing a fabrication technique, processing cost should be one of the major goals. Although the fuel cell stack itself is only about one third of the system costs [1], it is critical that the SOFC developmental activities recognize and address the issue of stack cost. Reducing the cost of cell components and simplifying of the process are important foci of ongoing development. There are two main processes for manufacturing tubular SOFCs (Table 2-1): tubular support fabrication technique and thin film application.

Table 2-1 Tubular SOFC Structures and Associated Fabrication Techniques

Cell Structure	Electrolyte	Anode	Cathode
Electrolyte supported	Extrusion Slip casting	Slurry coating EVD Plasma spraying	Slurry coating EVD Plasma spraying
Anode supported	Slurry coating EVD Plasma spraying	Extrusion Slip casting	Slurry coating EVD Plasma spraying
Cathode supported	Slurry coating EVD Plasma spraying	Slurry coating EVD Plasma spraying	Extrusion Slip casting

Hollow ceramic tubes can be fabricated, using slip casting, isostatic pressing, powder pressing or paste extrusion methods. In slip casting, thick slurry is fed into a porous mould and the liquid is withdrawn through the porous surface, thereby forming an item of required shape. Although powder pressing is reproducible, product density is non-uniform and productivity is low. Isostatic pressing offers high and well distributed product-forming pressure but throughput rate is low. In extrusion, shaping occurs by forcing a cohesive plastic material through the orifice of a rigid die. Paste extrusion is particularly suitable for high-speed manufacturing of articles with constant cross section and the process has the following advantages [2]:

- Very complicated cross-sections can be formed;
- Relatively small amounts of liquid are added to the solid;
- Very hard powders can be shaped;
- A uniform density distribution is obtained;
- Long thin sections can be made;
- Capital costs and operating costs are generally competitive.

In contrast to forming methods, such as powder pressing and slip casting, paste and flow extrusion is not fully understood [2]. The plastic ceramic body has a complex structure and mechanisms for plastic flow are also complex [3, 4]. Although many tests have been proposed to measure extrudate plasticity, methods for predicting the mechanical properties of ceramic extrudates under well defined stress conditions are limited [5]. Advancements in ceramic extrusion have come more from engineering observation and imagination rather than from understanding the basic science of the process [6].

2.2 Formulation and Process Additives

Because extrusion is a plastic forming method, the material to be extruded must have good flowability and the extrudate must have enough wet strength to resist deformation due to its own weight or handling stresses. If either of these conditions is not met, a good extrusion will not be obtained. Formulation is to select proper additives and to optimise processes for a certain ceramic system.

Adsorbed organic additives such as binders, plasticizers and lubricants are critical for good compaction and green strength. Compaction behavior is controlled by deformability and lubricating effects of the additives. Binder properties are significant at every step of a production system. The strength imparted by the binder helps in handling the green extrudates. Microstructure developed during sintering is linked to the green microstructure formed during compaction. Many key properties of advanced ceramic parts depend on completely removing binder during the early stages of heat treatment [7]. The formulation for a zirconia casting slurry is given in Table 2-2. This Section focuses on describing each component and its contribution to the forming process.

Table 2-2 Compositions of a Zirconia Casting Slurry [8]

Composition	Volume (%)	Weight (%)
Zirconia powder	41.52	80.58
Water	52.33	16.92
Polyacrylate deflocculant	4.42	1.79
Polyvinyl alcohol binder	1.73	0.71
	100.00	100.00

2.2.1 Ceramic Powder

Chemical and physical properties of a ceramic powder such as particle size, particle size distribution and particle shape affect extrusion flow and extrudate packing density. A criterion to identify the preferred physical properties of a powder for making electrolyte is to have high packing density with least liquid in the formulation.

For good extrusion, the largest particle must be much smaller than the smallest dimension of the extrudate. The maximum dimension of angular, needle-like, or plate-like particles should be less than a tenth of the smallest die cross-section such as the gap to form the tube-wall thickness [2]. Micron size particles are normally used in advanced ceramic extrusion. Particles in crushed or ground powders are often angular while powders prepared by precipitation contain agglomerates. Spray dried powders are nearly spherical and the preferred shape for paste extrusion.

Particle size distribution significantly affects particle packing and pore structure. Theoretical packing densities for uniform spheres range from 52% to 74% depending on the sphere arrangements (cubical, orthorhombic, tetragonal, pyramidal and tetrahedral) [9], while experimental densities for non-ordered arrangements of uniform spheres are between 60% to 64% [10]. Packing density can be increased by filling the interstitial pores with finer particles. When the ratio between nearest sizes is greater than 7, for example for a quaternary sphere system (size ratio 320/39/7/1), a maximum packing density of 95% can be achieved [11]. In practice, continuous particle size distributions are used and their form and breadth also affect packing density. Rough surfaces prevent particle motion and reduce the extrudate packing density.

2.2.2 Liquid

Sufficient liquid must be added to wet the ceramic powder and obtain an extrudable paste. Liquid spaces the particles and lubricates particle movement and motion along the flow path. After extrusion, the liquid is removed by drying, which will usually shrink the extrudate and leave pores in the product. Thus, the amount of liquid is critical (Figure 2-1). A mix with insufficient liquid requires higher shear stress for a given shear rate, which may exceed the pressure limits of the extruder [12]. If there is too much liquid, the paste has low cohesiveness and may become too soft to retain its shape after extrusion.

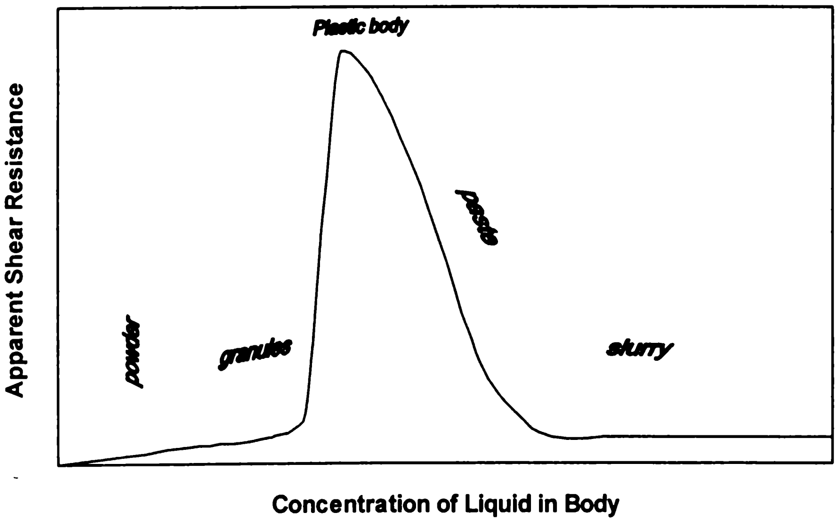

Figure 2-1 Effect of Liquid Concentration on Processing Consistency [8].

2.2.3 Binders

Binders provide green strength so the extrudate will retain its shape and can be handled. Average green strength after drying increases with binder concentration. This increase is rapid up to 4% binder. The selection of a binder system affects the internal and external rheological behavior of an extrudate. The internal flow property describes the stress-stain rate behavior of an extrudate when shear occurs between the particles. The external property describes the shear between the extrudate and the die-wall. In general, binders for ceramic extrusion should have: (a) high green strength and high green density; (b) low viscosity; (c) insensitive to humidity; (d) mixing easily; and (f) excellent burnout in air [6].

Widely used organic polymer binders include: polyvinyl alcohol (PVA), polyvinyl butyral (PVB), polyethylene glycol (PEG), methyl cellulose (Methocel®), and the specific ceramic extrusion binder Duramax® system. PVA and PVB are widely used in the fully hydrolysed form. The glass transition temperature for PVA is 75-85°C. Methocel® and hydroxyethyl cellulose are commonly used for ceramic extrusion with high green strength. However, Methocel® adheres to metal in the die, which is undesirable. Adding an external lubricant may overcome this effect. PEG and polyethylene oxide (PEO) are water-soluble binders that can also act as plasticizers and lubricants. PEG has low residual ash compared with many other binders such as PVA [12].

Duramax acrylic extrusion binders, B1051 and B1052, are aqueous-based, ready-to-use emulsions made of 0.05-0.5 micron diameter polymer particles dispersed in water (Table 2-3). Surfactants are added to control particle size, to stabilize emulsion particles during synthesis, and to prevent settling on storage. These binders impart high plasticity with sufficient adhesiveness and cohesiveness for the pastes. Binder B1051 is an insoluble polymer gel made of more than 30% solids dispersed and suspended in water. It has a glass transition temperature of 81°C, which means that it produces a harder extrusion. Increasing the B1051 content in dough increases the hardness of the extrusion. Binder B1052 is also an insoluble polymer gel of more than 55% solids suspended in water. It has a lower glass transition temperature so it produces a softer extrusion but the extrusion is tougher. A binder level of 2-15% based on powder weight is recommended.

Table 2-3 Typical Properties of Duramax Extrusion Binders [13].

Additives	Duramax B1051	Duramax B1052
Appearance	Milky light yellow liquid	Milky white liquid
Total solids	30% (49%*)	55% (62%*)
Particle size, median	0.08 μm	0.3-0.4 μm
Glass transition temperature	81°C	6°C
Density at RT (23°C)	1.0 g/ml	1.1 g/ml
Viscosity (60 rpm)	40 cP (Brookfield #1)	<150 cP (Brookfield #2)
pH	2.7 (2.48*)	5 (4.62*)
Residue after firing	0.26% (air)	1.3% (air)

* Measured in this work.

The mechanical properties of the extrudates can be tuned by varying the binder combinations (Figure 2-2). For instance, B1051 provides moderate plasticity and extrudability whilst B1052 is a softer binder and provides high plasticity. Combining binders, as in the Duramax binder system, can improve performance. Extrudates with low B1051/B1052 ratios will have low elastic modulus and high ductility. To get round and straight green tubes or avoid wet green tube collapse due to the gravity, the ratio should be high.

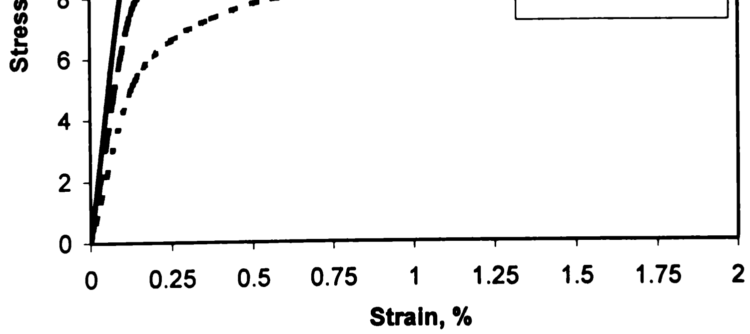

Figure 2-2 Mechanical Properties of Extruded Alumina with 4% Duramax Binders [13].

2.2.4 Lubricant

Lubricant is needed to enhance surface smoothness of the extrudates and reduce extrusion pressure. An internal lubricant reduces the pressure drop in the die-entry region, while an external lubricant decreases the pressure drop in the die-land (the section where cross-sectional area and shape are constant) [12]. The Benbow equation (Equation 2-1) can be used to evaluate the die-land pressure loss (P_2) and analyse the effects of lubrication [2].

$$P_2 = 4(\tau_0 + \beta V)(\frac{L}{D}) \qquad \textbf{Equation 2-1}$$

Where τ_0 (wall shear stress at zero velocity) and β (wall velocity factor) are parameters characterizing the paste, V is the paste velocity in the die-land, D is die-land diameter and L is die-land length.

Polyethylene glycol (PEG) is often used as a lubricant and sometimes a binder. Flexibility of the dried extrudates can be tailored by adjusting lubricant level. Mechanical properties of polymers are temperature dependent. At low temperatures, polymers are elastic. As temperature increases, they go through a glass transition, T_g, to viscoelastic behaviour, becoming viscous liquids as temperature increases further. Good compaction depends on granule deformability, which is greater when granules are pressed at temperatures above the T_g [3]. PEG's glass transition temperature (T_g) is less than 20°C, depending on the molecular weight [3]. PEG400 is mainly an external lubricant and has a slight internal lubricant function [12].

2.2.5 pH Control Agent

The electrical charge on fine ceramic particles is called zeta potential. The zeta potential is positive at low pH, negative at high pH and zero at the isoelectric point (IEP). For example, the IEP for silica (SiO_2), zirconia (ZrO_2), alumina (Al_2O_3) and magnesia (MgO) are pH 2, 4, 9 and 12 respectively [14]. The pH of pastes should be near the IEP to obtain maximum pseudo-plasticity and a pH control agent is usually needed for most ceramic powders. For example, the zeta potential of yttria-stabilized zirconia (Figure 2-3) can be adjusted with AMP-95, an organic amine with 90 wt% 2-amino-2-methyl-1-propanal, 5 wt% 2-

(methylanino)-2-methyl-1-propanol and 5 wt% water. Usually 0.5-2% AMP-95 is sufficient to coat the surface with charged particles so the ceramic particles repel each other.

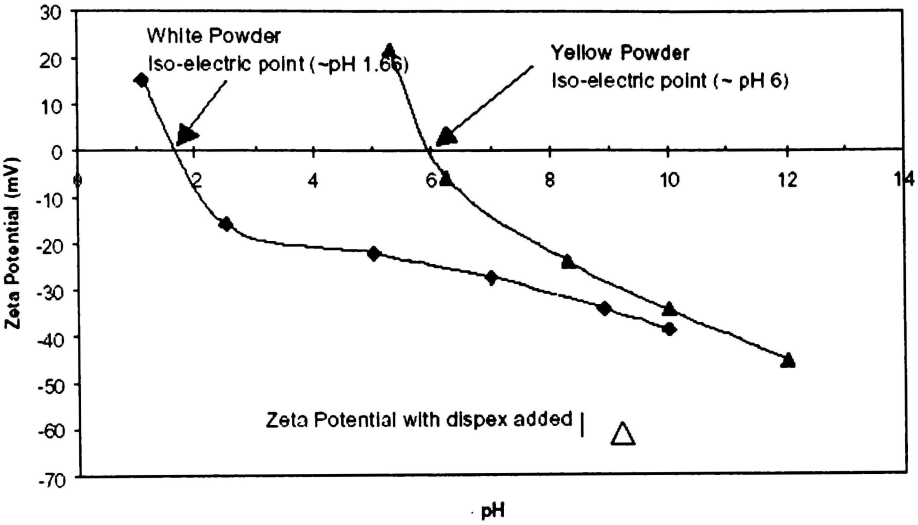

Figure 2-3 Zeta Potential of Yttria-Stabilized Zirconia [15].

2.3 Processing

Ceramic extrusion involves several steps including paste preparation, extrusion, drying and final sintering (Figure 2-4). Preparing the paste is the critical step.

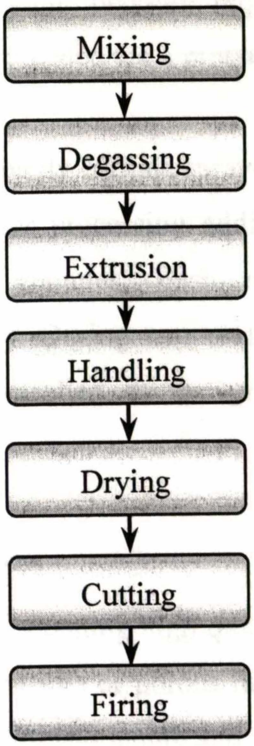

Figure 2-4 Basic Process of Paste Extrusion.

2.3.1 Mixing

The fundamental purpose of mixing is to produce a physically and chemically uniform extrusion batch. To improve uniformity and extrudability, each particle as well as die-land should be coated with a thin liquid film. The mean thickness of the liquid layer at die-land wall is estimated to be between 0.5-20 μm depending on the liquid content [16]. There are three steps in making a paste: (a) breaking and homogenizing agglomerates in the powder; (b) coating the particles with wetting agents; (c) producing a dough with further mixing and kneading [17]. High-shear may be needed to break agglomerates in the powder and obtain uniform dough. However, over mixing may cause the binder to drop out of the solution and form a gel of agglomerate. The average size of the dough (sometimes called lump) should be in 1.3-10 cm, depending on the mixer. A large lump indicates that too much liquid has been added whereas small lumps indicate that more liquid may be required. If the mixer wall is not clean at the end mixing, the formulation probably has too much liquid.

To predict accurately the manner in which dough behaves during extrusion, it is highly desirable to test their rheological behaviour under similar conditions, for example using extrusion rheometer, at which extrusion is carried out at a series of steady speeds, and the equilibrium pressure required to extrude the material through the die at that speed is recorded via a pressure transducer [18].

Another extrusion route is to directly extrude spray-dried granules [9]. Slurry with water, powder, binder and other processing additives is sprayed into a warm drying medium to produce granules. Each near-spherical granule has a homogeneous coating of binder. Drying temperature and moisture in the dried material must be properly controlled so the granules can be extruded after evacuation.

2.3.2 Die Design and Extrusion

The extrusion die is critical for obtaining high quality extrudates such as straight, long and thin walled electrolyte tubes or porous tubular electrodes. Die entrance-angle, die-land length, ratio of die-land length and die diameter, die materials, and ram force/extrusion pressure influence the extrusion process and extrudate quality.

In a simplified ram extrusion system (Figure 2-5), paste fed to cylinder (barrel) is packed and forced through a die-land to form an extrudate.

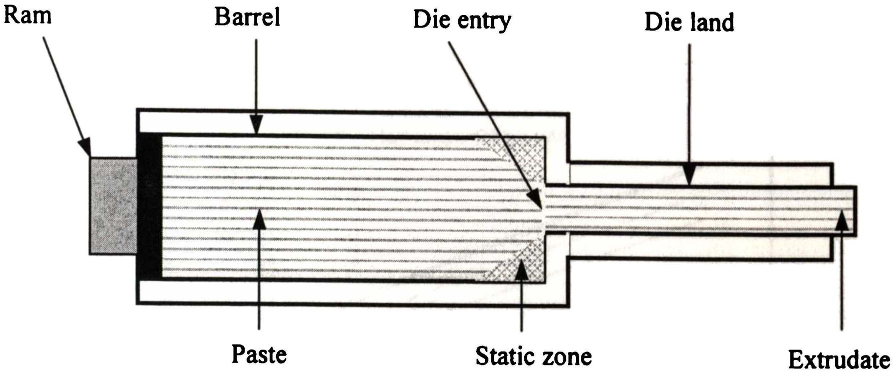

Figure 2-5 Illustration of a Basic Ram Extrusion System.

Pressure of the extrudate in a convergent conical die (D=6 mm, L=59 mm, and θ=30°) are shown in Figure 2-6 and the effect of die entrance angle on extrusion pressure is shown in Figure 2-7.

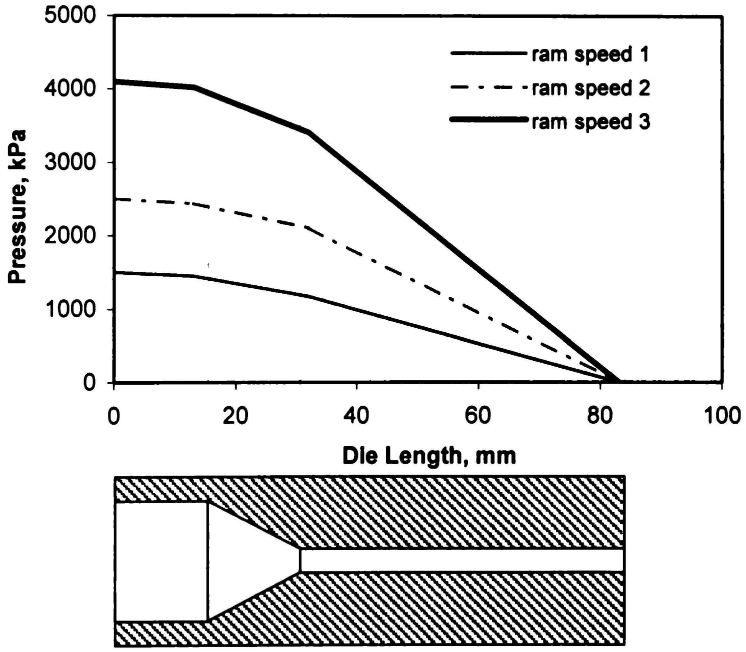

Figure 2-6 The Pressure of the Extrudate in a Convergent Conical Die [19].

The pressure generated in the paste packs the coated particles densely as well as forcing them through a die of suitable size and shape. Lower dough pressures (e.g. using a short die-land die) give less packing effect. Excessive pressures, however, may make liquid phase seep from the dough. Industrial extrusion pressures are up to about 4 MPa for porcelain bodies and up to 15 MPa for some organically plasticised materials [9].

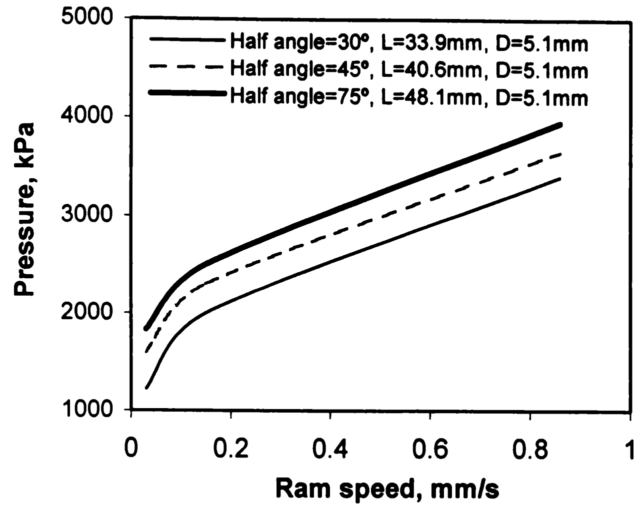

Figure 2-7 Influence of the Die Entrance Angle on the Extrusion Pressure [19].

The extrusion pressure for a given system (extruder, die design) is a function of paste rheologic properties (stiffness and uniformity). The overall pressure drop (*P*) for paste in a cylindrical die-land with a square entry (see Figure 2-6) can be evaluated from the pressure drop at the die-entry (P_1) and the die-land (P_2) using Equation 2-2, where pressure P_2 is used to shape and pack the extrudate [2]. For the alumina system, there was a single, linear relationship between the failure shear stress and the forming pressure [20]. To improve paste flow, tapered dies are preferred. Equation 2-3 can be used to calculate the pressure drop at the die-entry P_1 for a conical entry die cone half-angle, θ [2]. Reducing the die entrance angle will reduce the pressure drop at die entry. However, if the die entrance angle is too small (e.g. less than 20°), the extrudates are not packed sufficiently and do not retain their shape [9].

$$P = P_1 + P_2 = 2(\sigma_0 + \alpha V)\ln(D_0 / D) + 4(\tau_0 + \beta V)(L / D)$$ **Equation 2-2**

$$P_1 = 2(\sigma_0 + \alpha V + \tau_0 \cot\theta)\ln(D_0 / D) + \beta V \cot\theta$$ **Equation 2-3**

Where

P	Extrusion pressure drop	D	Die-land diameter
P_1	Pressure drop at die-entry	L	Die-land length
P_2	Pressure drop in the die-land	V	Paste velocity in the die-land
D_0	Barrel diameter	σ_0	Paste yield stress at zero velocity

τ_0	Wall shear stress at zero velocity	β	Wall velocity factor
α	Velocity factor	θ	Die entry half-angle

Defects are imperfections formed during processing. The two major flow defects in paste extrusions are lamination and surface tearing. Lamination defects are formed by internal stresses where there is poor cohesion between adjacent layers in the extrudate. The streams flowing around each arm of the spider (the mandrel support) are potential sources of laminations when extruding cylindrical tubes. Weak zones may develop into cracks during subsequent drying or firing. Reducing cross-section after the streams meet produces internal plastic flow, which may help reduce lamination. Surface tearing, which can occur in a wide variety of materials, produces periodic cracks on the surface. Material may curl from the extruder if the paste is not homogeneous or the mandrel pin is off center.

2.3.3 Cutting and Extrudate Handling

Cutting the extrudate into short units always causes distortion. A 90° angle between the cut face and the die-land axis can reduce distortion [2]. Cutting also involves handling the extrudate. The extrudate can be difficult to handle, especially since it is usually not strong and deforms readily. If accurate cuts are required, the wet extrudate may be cut longer and exact dimensions cut after drying.

2.3.4 Drying

Drying removes liquid before the extrudate is fired. Dried green product has enough strength to allow further accurate cutting, machining and loading. Drying rate affects how the extrudate retains its shape. The extrudate shrinks as liquid between the particles is removed and interparticle separation decreases. Differential shrinkage will give distortions or cracks.

2.3.5 Sintering

Sintering describes consolidation of material during firing while *firing* is a general describing heating a product to elevated temperatures. Sintering forms strong interparticle bonds in ceramics and usually requires high firing temperatures. In the firing process, organic binders burn out at low temperatures (Figure 2-8) and strength gradually develops at higher temperatures. The product may be very weak as the binder is removed before the solid bonds are formed.

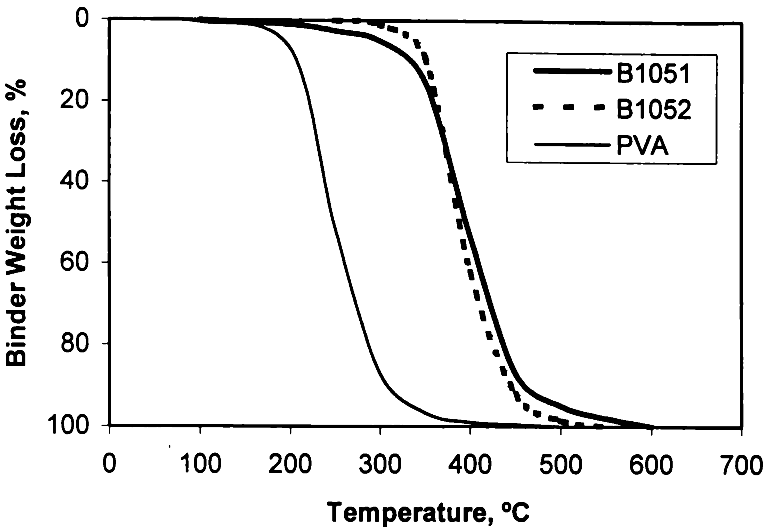

Figure 2-8 Binders Burnout Temperatures of Duramax and PVA [3, 13].

Sintering strength and ceramic microstructure are related to maximum sintering temperature, time at this temperature, and chemical composition. The sintered product can be dense (e.g. for an electrolyte), or porous (e.g. for electrodes). Electrolytes used in SOFCs are typically made with a density of greater than 95% of theoretical density to minimize the crossover current and to separate the oxidant and the fuel gases (Figure 2-9).

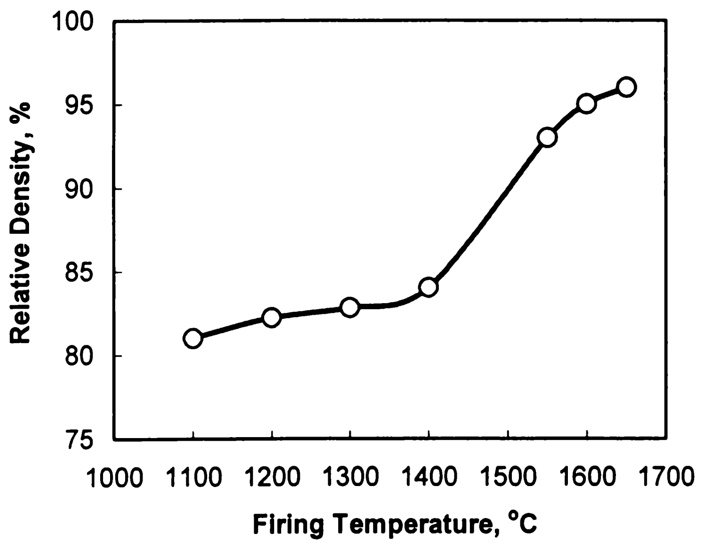

Figure 2-9 Effect of Firing Temperature on Relative Density of Slurry Cast YSZ Electrolytes [21].

Sintered density is also related to green density (Figure 2-10) and pore size in the green body. A low green density means some particles compacted less dense, which will lead to a lower sintering density and higher sintering shrinkage. Pores below a critical size are eliminated during sintering but large pores persist. Eliminating small pores reduces volume, so shrinkage occurs and is related to the matrix density.

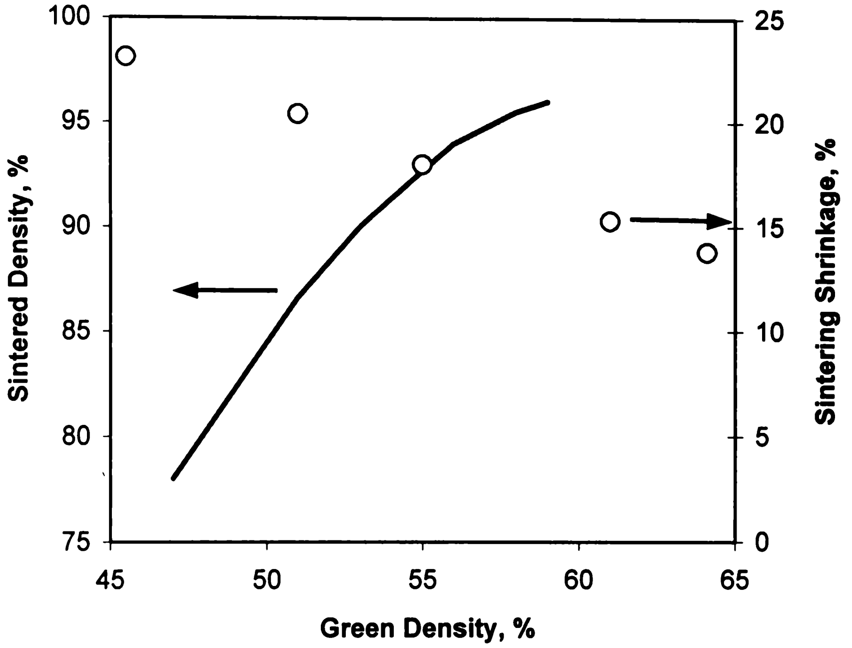

Figure 2-10 Relationship Between the Densities of Sintered and Green Body, after [7] (sintered density) and [20] (shrinkage).

2.4 Thin Film Application

Present SOFC designs use thin film concepts to enhance cell performance and reduce material costs. Those thin films can be a single thin ceramic layer or multiple layers with a certain microstructures: as dense as possible for the electrolyte or with optimum porosity for electrodes. Both must have good mechanical integrity. Several thin film techniques have been used to fabricate SOFCs including EVD, chemical vapor deposition (CVD), jet vapor deposition (JVD), spray pyrolysis, electrophoretic deposition, dip coating, spin coating, tape calendering, tape casting, vacuum slip casting, sputtering, and plasma spraying. The methods given in Table 2-4 may be used for fabricating thin films on tubular supports.

Fabrication techniques differ depending on cell type, configuration and developer. For example, Siemens Westinghouse developed EVD technique to produce thin layers for electrolyte, anode and interconnection in its early tubular SOFC development. After 1999, the company used an EVD process for electrolyte deposition only, and slurry deposition for anode and plasma spraying for interconnection [22, 23]. For planar SOFCs, cost effective wet ceramic techniques such as tape casting [24], screen printing [25] and spray painting [26] are widely used for the fabrication of thin films.

Table 2-4 Thin Film Techniques for Fabrication Tubular SOFCs.

Process	Description	Ref.
Spraying coating	Thin films are spray-coated onto outside surfaces of support tubes by a spray gun.	[27]
Spin coating	Thin films are coated onto inside surfaces of support tubes by spin coating a sol-gel precursor or slurry to spinning tube. For outside surface coating, fine brushes are used to carry slurries.	[28, 29]
Dip coating	Films are formed on outside or inside surfaces by dipping or immersing support tube in slurries or colloidal suspensions.	[30]
Vacuum infiltration	The layers, especially electrolyte layers, are produced on inside or outside surfaces of partially sintered porous electrode tubes by vacuum slurry coating.	[31]
Electrophoretic deposition	A DC electrical field is applied to deposit preferred particles from a suspension onto a substrate electrode of opposite charge.	[32-34]
Sputtering	Thin films are sputter-deposited from metal targets onto porous electrode substrate using an electric discharge in an oxygen/argon mixture.	[35]
EVD	Thin films are deposited on a substrate by spraying atomized precursor droplets across a heated environment.	[36-39]
Plasma spraying	Thin films are produced using a plasma spray gun and powder injected. The fine particles become molten and adhere to the prepared surface. Using this technique can eliminate firing process.	[40, 41]
Screen printing	A squeegee forces a thick paste through a stencil screen to form a thin film on the surface below.	[25, 42]

Many researchers have investigated plasma spraying. The Electrochemical Laboratory in Japan [40] applied YSZ to a substrate and found the sprayed material maintained its crystalline structure during the process. Multilayer coatings can be formed, so electrolyte and electrode layers can be laminated without needing additional firing [43]. The technique is currently limited to R&D scale because it is costly and difficult to mass-produce.

EVD can be carried out above 1200°C with metal halides in an H_2/CO_2 atmosphere to produce excellent but very expensive thin electrolyte layers. Alternative cheaper fabrication methods, such as CVD and JVD are receiving more attention. CVD is one of the most versatile processes for manufacturing thin films and is currently used to manufacture products ranging from semiconductors to low-emissivity coatings on glass [44]. JVD is a thin film technique where sonic gas jets serve as the deposition source. It can be used to make dense and pinhole free YSZ films that seal highly porous electrode surfaces and are gas tight [45].

All thin film processes, other than plasma spraying and EVD, need a final sintering step to create a strongly bonded structure. One approach for decreasing densification temperature of electrolyte coatings is to use submicron active powers, preferably nanosize powders. High densities may be achieved at 1300°C and below with nanosize powder compared with 1500°C or above for micron YSZ powder.

2.5 Aims and Layout of this Thesis

2.5.1 Aims

This review shows that cost and durability are the major barriers to commercialising SOFC technology. The overall objectives of this thesis are to develop a cost-effective process for fabricating micro-tubular SOFCs using new intermediate temperature electrolyte materials as well as YSZ electrolytes, and to understand the interplay of material-process-microstructure-performance of these tubular SOFCs. The research has the following specific aims:

(1) To investigate how to lower cell-operating temperatures, for example using LSGM electrolyte;

(2) To investigate how to minimize electrolytic polarization by reducing electrolyte thickness;

(3) To characterise mechanical, thermal and electrical performance of tubular SOFCs;

(4) To develop a process suitable for cost-effective mass production of support components;

(5) To identify factors that have major effects on the processing characteristics, and to measure their effects on the properties and performance; and

(6) To identify ways of increasing tubular stack volumetric power density.

2.5.2 Thesis Layout

This thesis starts with introduction and literature review on SOFC technology (Chapter 1) and tubular SOFC fabrication techniques (Chapter 2). Chapter 3 describes generally the materials used, methods, equipment and techniques to fully characterize the materials and fuel cells developed. Chapters 4–7 are devoted to the fabrication and characterization of the micro-tubular SOFCs and the resulting fuel cells. Finally Chapter 8 describes the general conclusions reached and recommendations for future work.

2.6 References

1. Elangovan, S., Hartvigsen, J., Cable, T.L. and Barringer, E.A. “Status of planar solid oxide fuel cell development”, in *2000 Fuel Cell Seminar*, Portland, Oregon, 2000.
2. Benbow, J. and Bridgwater, J., *Paste flow and extrusion*. Oxford: Clarendon Press. 1993.
3. Walker, W.J., Reed, J.S. and Verma, S.K., "Polyethylene glycol binders for advance ceramics." *Ceram. Eng. Sci. Proc.*, 1993. **14**(1112): p.5879.
4. Kharton, V.V., Naumovich, E.N. and Marques, F.M.B., "Ionic and electronic transport in perovskite-type La(Ga,M)O_{3-z} (M=Mg, Cr, Fe, Co, Ni, Nb)." *Ionics*, 1999, **5**: p. 183-193.
5. Reed, J.S., Martin, T.J. and Carlson, W.G., *Mechanics of extrusion*, in *Science of Whitewares*, V.E. Henkes, G.Y. Onoda, ed. 1996, The American Ceramic Society. p. 157-169.
6. Wright, J.F. and Reed, R.S., "Polymer-plasticized ceramic extrusion, part 1." *Am. Ceram. Soc. Bulletin*, 2001. **80**(4): p. 31-35.
7. Mosser, B.D., Reed, J.S. and Verma, S.K., "Strength and Weibull modulus of sintered compacts of spray-dried granules." *Am. Ceram. Soc. Bull.*, 1992, **71** [1] p. 105109.

8. Reed, J.S., *Principles of ceramics processing.* 2^{nd} ed. New York: John Wiley & Sons, Inc. 1995.
9. Reed, J.S., *Introduction to the principles of ceramic processing.* New York: John Wiley & Sons. 1988.
10. Scott, G.D. and Kilgour, D.M., "Packing density determination." *Br. J. Appl. Phys. Ser.*, 1969. **2**(2): p. 863.
11. McGeary, R.K., "Packing density experiments." *J. Am. Ceram. Soc.*, 1961. **44**(10): p. 513-522.
12. Zheng, J. and Reed, J.S., "Ceramic extrusion with PEG." *Am. Ceram. Soc. Bull.*, 1994. **73**(12): p. 61-66.
13. Rohm and Haas, C., *Duramax ceramic extrusion binders,* Form 18112 2/96, 1996.
14. BIC, Zeta potential and stability, http://www.bic.com/ztheory1.htm, 2003.
15. Hellgardt, K., Binner, J., Whitehead, N. Morgan, D., "Preparation of ceramic electrolyte microtubes by means of electrodeposition", Royal Society of Chemistry, 2001. p. 1-22.
16. Benbow, J.J., Oxley, E.W. and Bridgwater, J., "The extrusion mechanics of pastes: the influence of paste formulation on extrusion parameters." *Chemical Engineering Science*, 1987. **42**(9): p. 2151-2162.
17. Pileggi, R.G., Studart, A.R., Pandolfelli, V.C. and Gallo, J., "How mixing affects the rheology of refractory castables, part 1." *Am. Ceram. Soc. Bulletin*, 2001. **80**(6): p. 27.
18. Carter, R.E., "Capillary extrusion rheometry in ceramics-processing technology." *Am. Ceram. Soc. Bulletin*, 2001. **80**(6): p. 23.
19. Benbow, J.J., Jazayeri, S.H. and Bridgwater, J., "Prediction of the extrusion of ceramic pastes through conical dies." 2002. p. 373-377.
20. Terpstra, R.A., Pex, P.P.A.C. and Vries, A.H.d., ed. *Ceramic processing.* Chapman & Hall: London. 1995.
21. He, T., Pei, L., Lu, Z., Liu, J. and Su, W., "Preparation of tubular YSZ electrolyte and its application in solid oxide fuel cells." *Functional Materials*, 2001. **32**(1): p. 55-56.
22. Singh, P., Pederson, L.R., Simner, S.P., Stevenson, J.W. and Viswanathan, V.V., "Solid oxide fuel cell power generation systems." in *36th Annual intersociety Energy Conversion Engineering Conference Advance Program.* 2001, p. 953-958.
23. EG & G Services Parsons, *Fuel cell handbook (Fifth Edition)*: US Department of Energy. 2000.
24. Minh, N.Q., "Tape-calendered monolithic and flat plate solid oxide fuel cells." in *Third International Symposium on Solid Oxide Fuel Cells (SOFC III).* 1993: The Electrochem. Soc., p. 801.
25. Yamaguchi, R., "Fabrication of porous electrode supported SOFC by wet process. 1993. *Third International Symposium on Solid Oxide Fuel Cells (SOFC III)*: The Electrochem. Soc., p. 704.
26. Larsen, P.H., Bagger, C. and Linderoth, S., "Status of the Danish SOFC Program." in *Seventh International Symposium on Solid Oxide Fuel Cells (SOFC VII).* 2001. Tsukuba, Japan: The Electrochemical Society, Inc., p. 28.
27. Ruder, A., Buchkremer, H.P., Jansen, H., Mallener, W. and Stover, D., "Wet powder spraying-a process for the production of coatings." *Surface and Coatings Technology*, 1992. **53**: p. 71-74.
28. Dieten, V.E.J.v., "Advance deposition techniques for solid oxide fuel cell components." in *Second International Symposium on Solid Oxide Fuel Cells (SOFC II).* 1991: The Electrochem. Soc., p. 183.

29. Chen, C.C., Nasrallah, M.M. and Anderson, H.U., "Synthesis and characterization of YSZ thin film electrolytes." *Solid State Ionics*, 1994. **70/71**: p. 101.

30. Souza, S.d., Visco, S.J. and Jonghe, L.C.d., "Reduced-temperature solid oxide fuel cell based on YSZ thin-film electrolyte." *J. Electrochem. Soc.*, 1997. **144**(3): p. L35-37.

31. Hart, L.J.d., Hauber, T., Mayer, K. and Stimming, U., "Electrochemical performance of an anode supported planar SOFC system." in *Second European Solid Oxide Fuel Cell Forum*. 1996. Oberrohrdorf, Switzerland: European Solid Oxide Fuel Cell Forum, p. 229.

32. Ishihara, T., Shimose, K., Kudo, T., Nishiguchi, H., Akbay, T. and Takita, Y., "Preparation of yttria-stabilized zirconia thin films on strontium-doped $LaMnO_3$ cathode substrates via electrophoretic deposition for solid oxide fuel cells." *J. Am. Ceram. Soc.*, 2000. **83**(8): p. 1921-1927.

33. Yamaji, K., "Electrophoretic deposition." in *Fifth European Solid Oxide Fuel Cell Forum*. 2002: European Fuel Cell Forum, p. 140-147.

34. Savo, G., Epitania, A.D., Polini, R. and Traversa, E., "Process and characterization of YSZ thick-films deposited by electrophoretic deposition for intermediate-temperature SOFC." in *Eighth International Symposium on Solid Oxide Fuel Cells (SOFC VIII)*. 2003. Paris, France, p. 246.

35. Thiele, E.S., Wang, L.S., Mason, T.O. and Barnett, S.A., "Deposition and properties of yttria-stabilized thin films using reactive direct current magnetron sputtering." *J. Vac. Sci. Tech.*, 1991. **A9**(6): p. 3054-3060.

36. Bai, W., Choy, K.L., Rudkin, R.A. and Steele, B.C.H., "The process, structure and performance of pen cells for the intermediate temperature SOFCs." *Solid State Ionics*, 1998. **113-115**: p. 259-263.

37. Tanner, C., Jue, J.F. and Virkar, V.A., "Temperature Dependence of the Kinetics of Electrochemical Vapor Deposition of CeO_2." *J. Electrochem. Soc.*, 1993. **140**: p. 1073.

38. Pal, U.B. and Singhal, S.C., "Electrochemical vapor deposition of yttria stabilized zirconia." *J. Electrochem. Soc.*, 1990. **137**: p. 1937.

39. Basu, R.N., Randall, C.A. and Mayo, M.J., "Fabrication of dense zirconia electrolyte films for tubular solid oxide fuel cells by electrophoretic deposition." in *Fuel Cell Seminar*. 2001, p. 266.

40. Nicoll, A.R., Barbezat, G. and Salito, A., "The potential of plasma spraying for the deposition of coatings on SOFC components." in *The International Fuel Cell Conference*. 1992. Tokyo, Japan.

41. Franco, T., "Metallic components for a plasma sprayed thin film SOFC concept." in *SOFC VIII*. 2003. Paris, p. 923.

42. Xia, C., Chen, F. and Liu, M., "Reduced-temperature solid oxide fuel cells fabricated by screen printing." *J. Electrochem. Soc.*, 2001. **148**(5): p. A52-A54.

43. Lang, M., Henne, R., Schaper, S. and Schiller, G., "Development and characterisation of vacuum plasma sprayed thin film SOFCs." *J. Thermal Spray Techn.*, 2001. **10**(4): p. 618-625.

44. Wagner, H.E. and Wagner, F., "Chemical vapor deposition." in *Chemical Vapor Deposition XVI (CVD-VXI) and EUROCVD 14 -- CVE-SVI & EUROCVD*. 2003. Paris. P. 588.

45. Halpern, B.L., Golz, J.W. and Di, Y., "Jet vapor deposition of thin films for solid oxide and other fuel cell applications." in *Proceedings of the Fourth Annual Fuel Cells Contractors Review Meeting*. 1992: U.S. DOE/METC.

Chapter Three

Experimental Methods and Equipment

This chapter provides detailed information on the starting materials, doped lanthanum gallate powder synthesis, generic experimental apparatus, examination and characterization techniques and overall experimental procedures used in the research, although each chapter in the result part of this thesis will describe experimental methodologies specific to that chapter.

3.1 Materials

3.1.1 Starting Chemicals and Materials

Starting chemicals include: (1) chemicals for synthesizing LSGM, (2) commercial LSGM and yttria stabilised zirconia (YSZ) electrolyte powders, (3) groups of electrode materials for different electrolyte systems and current collectors, and (4) processing additives.

Lanthanum oxide La_2O_3 (99.9%), gallium oxide Ga_2O_3 (99.99%), and magnesium oxide MgO (99+%) (Aldrich Chemical Company, Inc., USA), and strontium carbonate $SrCO_3$ (99+%) (Ajax Chemicals, Australia) were used to synthesize doped lanthanum gallate materials. Commercial LSGM powers from Anan Kasei Co., Ltd (Japan) (co-precipitation process, 99.9% purity) and Praxair Inc. (USA) (combustion spray pyrolysis, 99.9% purity) were compared with the powder made via the solid-state method from this work (see next Section for LSGM powder synthesis).

Commercial 8 mol% yttria stabilised zirconia (8YSZ) powder (Tosoh Corporation, Japan) was used as a baseline for process evaluation. The reported characteristics of some Japanese, UK and USA YSZ powders are given in Table 3-1. Magnesium Elektron Ltd. (MEL) powder was not pure cubic phase and had a much lower bulk density and sintered density than the other two powders. American Elements (AE) powder had very high pH, which is likely to be due to the Cl^- impurity (Table 1-15). Tosoh YSZ powder had regular spherical shape granules with good flowability desired for extrusion processes (Figure 3-1) and a high sintering density (99% of theoretical density).

Table 3-1 Characteristics of YSZ Powers from Japan, UK and USA.

Characteristic	Producer		
	Tosoh, Japan	MEL, UK	AE, USA
Y_2O_3, wt% [a]	13.3	13.6	13.56
Ig. Loss [a]	≤1.5	0.16	
D_{50} μm	0.62	1.08	1-2 (double peaks)
Specific Surface Area, m^2/g [a]	16±3	8.0	17.2
Crystal Structure[b]	Cubic	Cubic and tetragonal	Cubic
pH	8-9	6.5	12
Bulk Density, g/cm^3	1.25	0.6	0.94
Sintered Density, g/cm^3 [a]	5.96	5.57	5.91

[a] *Data from [1-3], rest from this study.*
[b] *Raman measurements.*

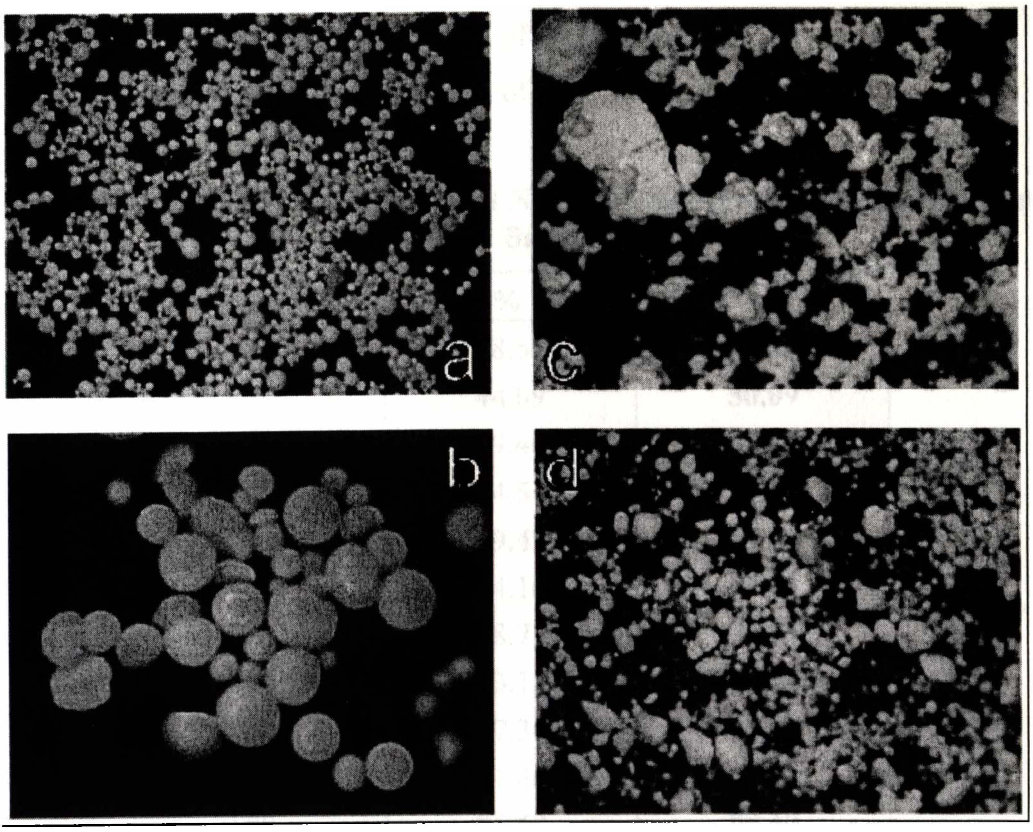

Figure 3-1 Morphology of YSZ Powders from Tosoh (a, b), MEL (c) and American Elements (d).

Strontium-doped lanthanum manganite $La_{0.8}Sr_{0.2}MnO_3$ (LSM) (99.9%) (Praxair) cathode and nickel-YSZ cermet anode (Praxair) were selected for the YSZ electrolyte fuel cells. The anode was formed by making the NiO/YSZ composite, and then reducing NiO to elemental Ni. The relationship between vol% Ni, wt% Ni and wt% NiO (Table 3-2) used to calculate the nickel/YSZ cermet composition was determined from Equation 3-1 (vol% Ni to wt% Ni) and Equation 3-2 (wt% Ni to wt% NiO). Typically, 50 wt% NiO or 50 vol% Ni was used.

$$
\begin{aligned}
Wt\%Ni &= \frac{W_{Ni}}{W_{Ni} + W_{YSZ}} \times 100\% \\
&= \frac{Vol\%Ni \times D_{Ni}}{Vol\%Ni \times D_{Ni} + (100 - Vol\%Ni) \times D_{YSZ}} \times 100\%
\end{aligned}
\qquad \textbf{Equation 3-1}
$$

$$
\begin{aligned}
Wt\%NiO &= \frac{W_{NiO}}{W_{NiO} + W_{YSZ}} \times 100\% \\
&= \frac{Wt\%Ni \times (M_{NiO} / M_{Ni})}{Wt\%Ni \times (M_{NiO} / M_{Ni}) + (100 - Wt\%Ni)} \times 100\%
\end{aligned}
\qquad \textbf{Equation 3-2}
$$

Where:	D_{Ni}	Density of Ni, 8.92 g/cm³
	D_{YSZ}	Density of YSZ, 6.09 g/cm³
	M_{Ni}	Molecular weight of Ni, 58.69 g/mol
	M_{NiO}	Molecular weight of NiO, 74.69 g/mol

Table 3-2 Converting Volume Percent Ni in Ni/YSZ Anode to Weight Percent NiO for Batching.

vol% Ni	wt% Ni	wt% NiO
30	38.56	44.41
35	**44.09**	**50.09**
40	49.40	55.41
45	54.51	60.40
50	**59.43**	**65.08**
55	64.16	69.50
60	68.72	73.66
65	73.12	77.59
70	77.36	81.31
75	81.46	84.83
80	85.42	88.17
90	92.95	94.37
100	100.00	100.00

Using nickel oxide, instead of nickel, in the starting material simplified the fabrication process because anode firing could be done in air. If using nickel as the starting anode material, firing process must be done in a protective atmosphere to avoid nickel oxidation.

Pure silver wire (99.9%, Silver State Wire, USA), and nickel wire and mesh (Alfa Aesar, USA) were used as cathode and anode current collectors respectively.

3.1.2 LSGM Powder Synthesis

The composition of LSGM powder used in this study was $La_{0.8}Sr_{0.2}Ga_{0.8}Mg_{0.2}O_{2.8}$ although other compositions with Sr and Mg doping levels from 0.1-0.25 were examined for single-phase range determination. Cell performance with $La_{1-x}Sr_xGa_{0.8}Mg_{0.2}O_3$ electrolyte (Figure 3-2) shows that x=0.1~0.2 gives the highest cell performance. In the Sr- and Mg-doped $LaGaO_3$, oxygen vacancies are introduced by substitution of Sr^{2+} for La^{3+} and Mg^{2+} for Ga^{3+} ions, according to the following equation.

$$xSrCO_3 + \frac{1-x}{2}La_2O_3 + yMgO + \frac{1-y}{2}Ga_2O_3 \Rightarrow La_{(1-x)}Sr_xGa_{(1-y)}Mg_yO_{3-\frac{x+y}{2}} + xCO_2$$

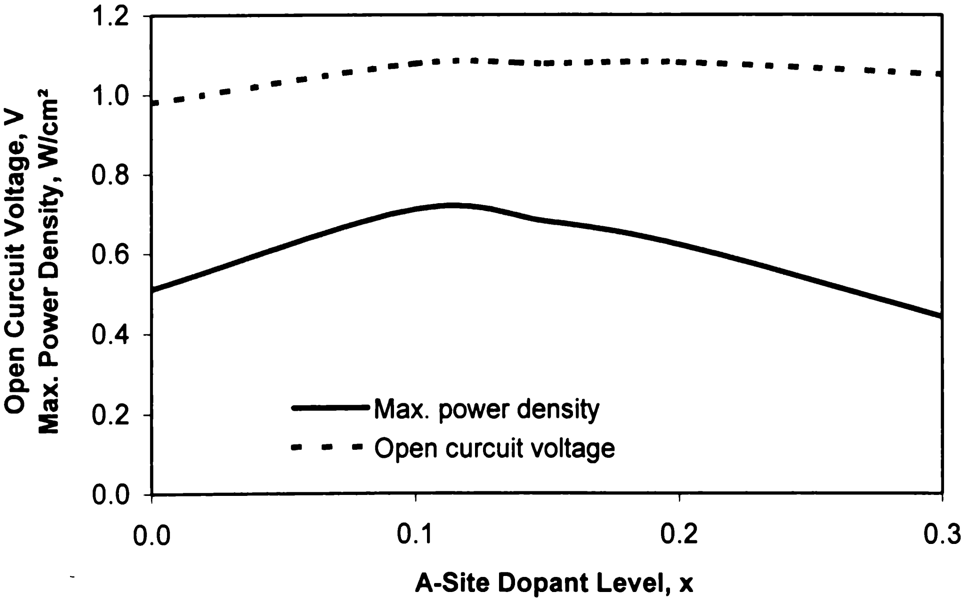

Figure 3-2 Effect of A-Site Dopant Level in $La_{1-x}Sr_xGa_{0.8}Mg_{0.2}O_3$ on Cell Performance [4].

LSGM materials can be synthesized using a solid-state reaction [5-8], sol-gel [9, 10], or the Pechini [11] process. The solid-state reaction method was used to synthesize the LSGM material. $SrCO_3$ and Ga_2O_3 were dried at 105°C overnight, and MgO and La_2O_3 were calcined at 1000°C and 1500°C respectively for 6 h before using. After considering impurities of the raw materials, stoichiometric amount of chemicals to synthesize $La_{0.8}Sr_{0.2}Ga_{0.8}Mg_{0.2}O_{2.8}$ composition are La_2O_3 (0.5445W, where W is the total amount of LSGM being synthesized) $SrCO_3$ (0.1245W), Ga_2O_3 (0.3130W), and MgO (0.0340W). These chemicals were thoroughly mixed using a mortar and pestle, then isostatically pressed (150-200 MPa), followed by sintering at 1500°C for 12 h. Repeating the pulverization-pressing-sintering process helped obtain a single-phase material.

3.1.3 Electrode Materials for LSGM Electrolytes

The following cathode compositions, selected from the literature (Table 3-3), were used for LSGM fuel cells: $La_{0.6}Sr_{0.4}CoO_3$ (LSCo), $Sm_{0.5}Sr_{0.5}CoO_3$ (SmSrCo) and $La_{0.8}Sr_{0.2}MnO_3$ (LSM) (99.9%, Praxair). Depending on the cell type, anodes were made from NiO (99%, Alfa Aesar), Co (II, III) oxide (99.7%, Alfa Aesar), NiO with $Ce_{0.8}Sm_{0.2}O_{1.9}$ (SDC) (99.9%, Praxair), or NiO with YSZ. The effect of SDC as an interlayer on cell performance was examined.

3.1.4 Processing Additives

The following binders and other processing additives were used for extrusion: polyvinyl butyral (PVB) (Aldrich Chemicals, USA), methylcellulose (Methodcel® A4M) (The Dow Chemical Company, USA), B-1501 and B-1502 (Dramax™, Rhom and Haas Formulation Chemicals, USA), polyethylene glycol 400 (PEG-400) (Union Carbide Co., CT, or The Dow Chemical Company), 2-amino-2-methyl-1-propanal (AMP-95) (Angus Chemical, IL), HYPERMER® (KD1) (ICI, USA), Octanol-1 (BDH, UK), acetone, and distilled water. Weight loss of liquid binders and other wetting agents after drying overnight at 105°C are given in Table 3-4.

Table 3-3 LSGM SOFC Performance with Various Electrode Combinations*.

Anode	Electrolyte (500 μm)	Cathode	Maximum power density (W/cm²), at 800°C	Reference
Pt	LSGM-1020	Pt	0.09	[4]
Ni	LSGM-1020	Pt	0.15	[4]
Ni	LSGM-1020	LSM	0.31	[4]
Co	LSGM-1020	LSCo	0.53	[4]
Ni-LSGM	LSGM-1020	LSM	Poor	[12]
Ni-CeO_2	LSGM-1020	LSCo	0.27	[12]
Ni-LSGM	LSGM-1020	LSCo	0.30	[12]
Ni	LSGM-1020	SmSrCo	0.58	[13]
Ni-SDC	LSGM-1020	LSCo	0.43	[14]
Ni-SDC/SDC	LSGM-1020	LSCo	0.55	[15]
Ni	LSGM-1020	LSCo	0.71	[13]
Ni-SDC	LSGMCo (400 μm)	$Ba_{0.6}La_{0.4}CoO_3$	0.72	[16]
Ni-LDC	LSGM-2017 (620 μm)	SCF	0.80	[17]
Ni-LDC/LDC	LSGM-2017 (600 μm)	SCF	0.90	[17]

* LSGM-1020: $La_{0.9}Sr_{0.1}Ga_{0.8}Mg_{0.2}O_{3-\delta}$, LSGM-2017: $La_{0.8}Sr_{0.2}Ga_{0.83}Mg_{0.17}O_{3-\delta}$, LSM: $La_{0.9}Sr_{0.1}MnO_3$, LSCo: $La_{0.6}Sr_{0.4}CoO_3$, LSGMCo: $La_{0.8}Sr_{0.2}Ga_{0.8}Mg_{0.15}Co_{0.05}O_{3-\delta}$, SDC: $Sm_{0.2}Ce_{0.8}O_{1.9}$, SmSrCo: $Sm_{0.5}Sr_{0.5}CoO_2$, SCF: $SrCo_{0.8}Fe_{0.2}O_3$, LDC: $Cer_{0.6}La_{0.4}O_{1.8}$.

Table 3-4 Weight Loss after Overnight Drying at 105°C and Contribution to Extrudate Drying Weight Loss.

Gradients	Weight loss (%)	Amount in formulation (%)	Equivalent contribution to the extrudate drying weight loss (%)
B1051	38.5	10	3.85
B1052	17.0	2.5	0.43
AMP-95	24.1	1.5	0.37
PEG-400	~0	3.0	~0

3.2 Equipment

3.2.1 Mill

Ball mills made in-house (Figure 3-3) were used to grind powders or to mix powders and additives into homogeneous slurries. High wear-resistant zirconia grinding balls (3-10 mm diameter Tosoh YTZ® ceramic balls,) and plastic milling jars were used to minimize product contamination. Milling and grinding were carried out at 250 rpm (milling jar rotation speed).

3.2.2 Mixer

A lab mixer with two contra-rotating sigma blades (3 litres total capacity, 1-1.5 litres working capacity) (Jaygo Incorporated, USA) (Figure 3-4) was employed to produce dough for extrusion. A sigma mixer generates high shear and efficiently produces a uniform ceramic extrusion paste. The surfaces of the blades and mixing chamber were coated with alumina to prevent metal contamination during the high shear mixing process. A vacuum was applied to degas the paste before it was transferred to the extruder.

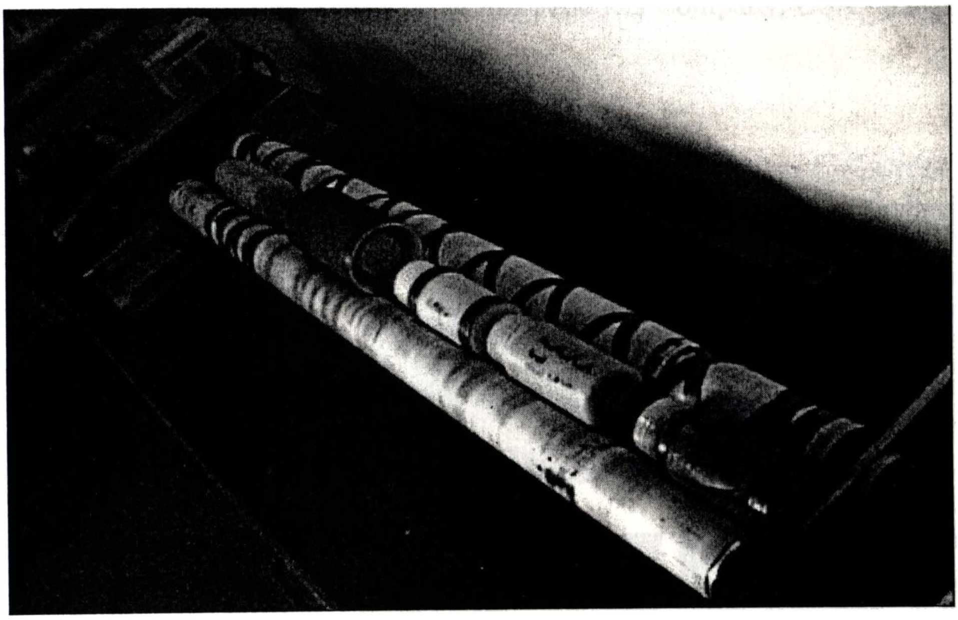

Figure 3-3 In-House Made Ball Mill.

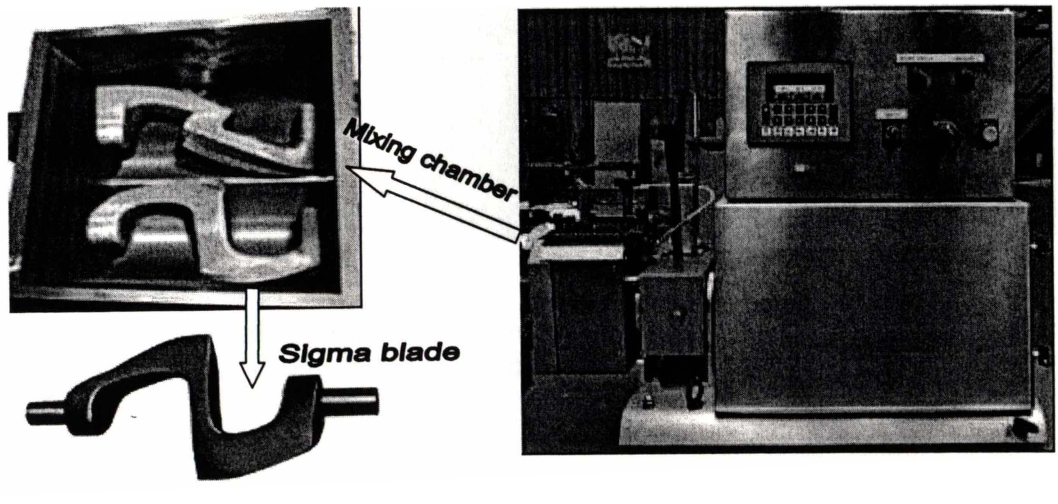

Figure 3-4 Sigma Blade Mixer (Jaygo Inc. USA).

3.2.3 Extruder and Extrusion Die

Various commercial extruders are available such as rotary extruders, screw extruders and ram extruders. The former two extruders are widely used in the ceramic industry. Screw extruders are normally used for high volume continuous production while ram extruders can be operated batch-wise, semi-continuously, or continuously. Batch operated ram type extruders are more suitable for short runs and for studying extrusion process and were therefore used in this research. A simple ram extruder (Figure 3-5a and b) coupled with a universal testing machine (Lloyd LR100K) was initially used to investigate the extrusion processes. An industrial ram extruder (Figure 3-5c) (Loomis Products Company, USA) was used for larger runs.

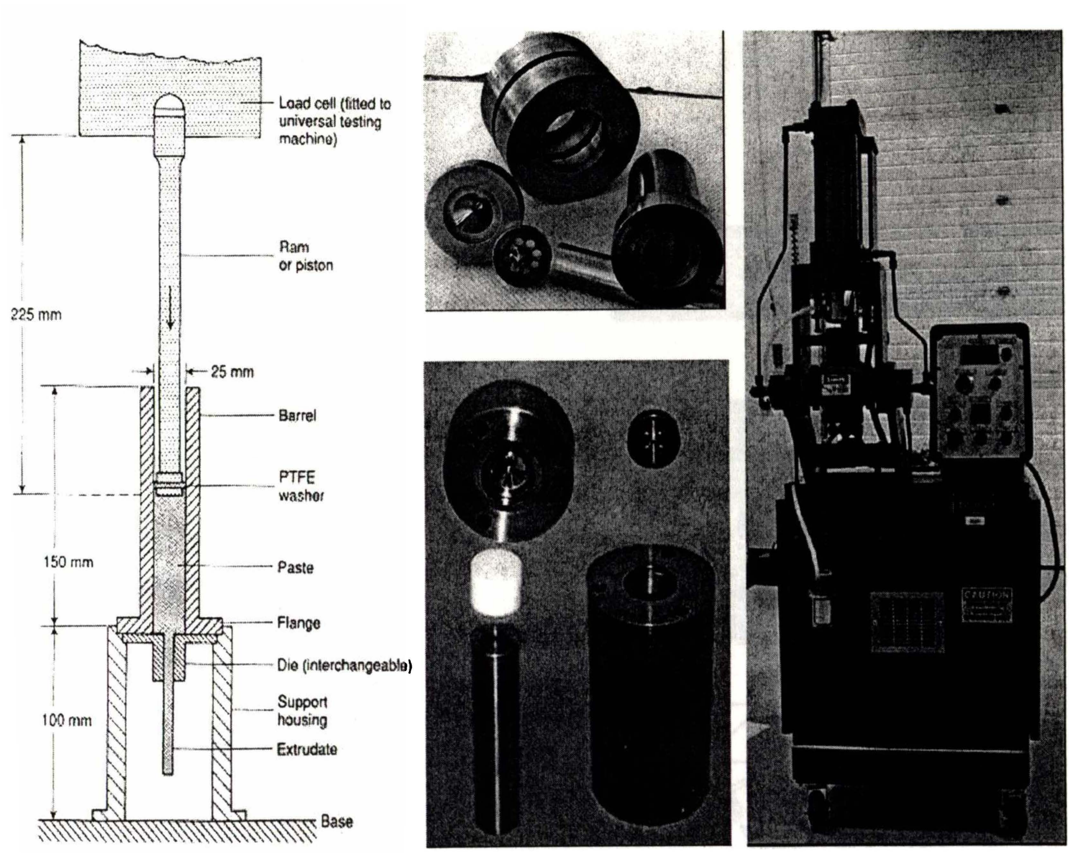

(a) **(b)** **(c)**

Figure 3-5 Extrusion Equipment Used: (a) Illustration of Ram Extrusion Die on a Universal Tester, (b) Photograph of 4-Hole and 8-Hole Extrusion Dies, (c) Ram Extruder (Loomis Products Co.).

The electrolyte and electrode tubes were formed when forcing pastes through an extrusion die. Several different size tubes were fabricated to study different support systems and the effect of wall thickness on the electrical and mechanical performances of the fuel cells. Simple four- and eight-hole extrusion dies (Figure 3-5b) were used for initial extrusion study. The extrusion die affects paste flow and quality of extrudates. Yield strength at the die-entry (shear flow in paste) is more than one order of magnitude higher than the yield strength at die-land (slippage at wall) [18]. Various die designs to reduce the pressure drop at the die-entry and to improve extrudate quality were investigated in the present study.

3.2.4 Drying Units

Great efforts were made to dry extrudates quickly and uniformly by controlling temperature and humidity of the drying air. To keep extrudates straight and round, several methods were investigated including V-shape (Figure 3-6a) and C-shape (Figure 3-6b) tube holders, and rotating the tubes while they dried (Figure 3-6c and d). Tube holder materials of paperboard, wood, glass, metal, ceramic, and plastics were evaluated.

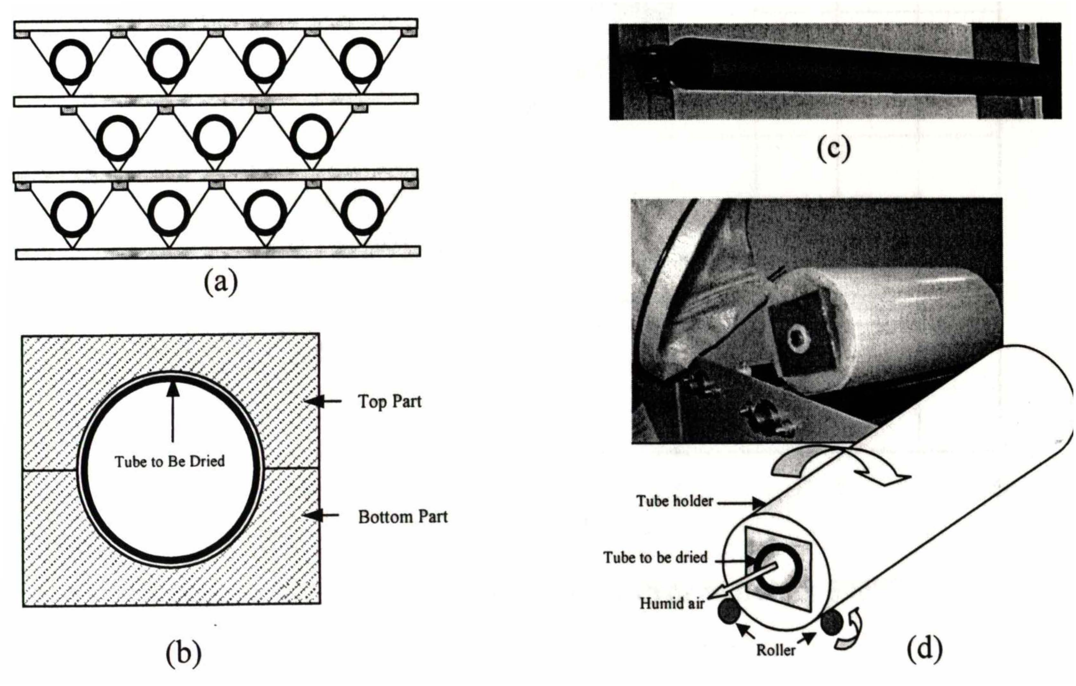

Figure 3-6 Tube Holders Developed: (a) V-Shape Tube Holder in Still Air, (b) C-shape Tube Holder with Moving Air, (c) Roller Drying in Air, (d) Rotating Tube Holders in Moving Air.

3.2.5 Furnaces and Kiln Furniture

After drying, the green tubes and coatings were fired in chamber furnaces (Ceramic Engineering, Carbolite, and Thermolyne) in air. Thermal shock resistance tests were conducted using a Tetlow furnace. The extrudates sintering regime was determined from differential thermal analysis data. A slow heating rate (1°C/min) was used during heating up 500°C to burn-out the organic additives, and then a higher rate in the range of 3-6°C/min was used during heating to the sintering temperature. A second reason for using an initial slow heating rate was because the furnace exhibited large temperature gradients at temperatures below 500°C (Figure 3-7). Sheltering the samples reduced the temperature gradient caused by radiation.

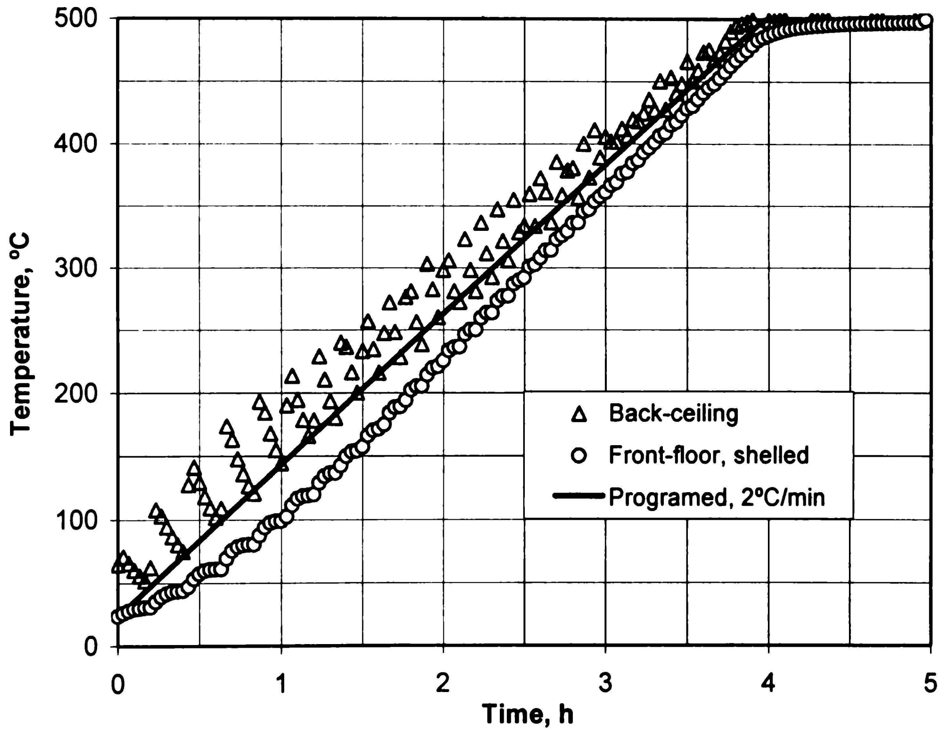

Figure 3-7 Furnace Temperature Profile Below 500°C.

Several methods were developed to hold the tubes during firing (Figure 3-8). They can be placed horizontally on a V-shaped kiln frame (Figure 3-8a) or hung vertically on a specially designed sample holder. Applying a weight can help keep the horizontal tube straight during firing, while the weight of the hanging tubes (gravity) played a similar role. Pre-sintered grain powder can be used as a firing bed (Figure 3-8b). As the tubes shrink, the sand-grain powder will fall accordingly to maintain the contact with the tube. A combination of light but straight spacers with half-oval or half-round cross-sections was effective for keeping the tubes straight (Figure 3-8c, d and e). The kiln furniture was made either from zirconia or alumina or the same material as the fired samples.

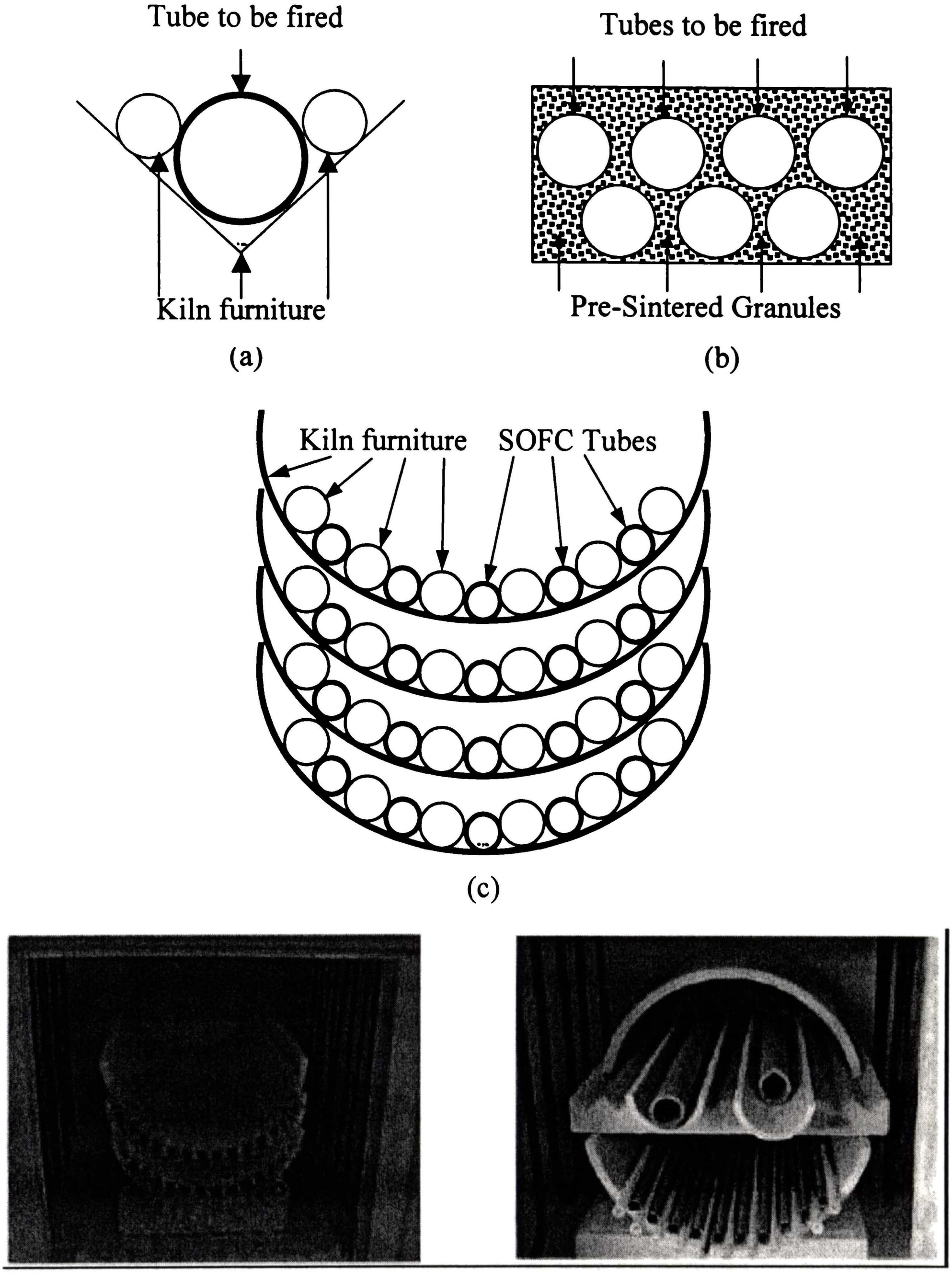

(a) (b)

(c)

(d) (e)

Figure 3-8 Tube Firing Support Methods: (a) V-Shape Kiln Frame, (b) Sintered Granular or Coarse Powder, (c, d and e) Half-Oval or Half-Round Frames with Spacers.

3.3 Analysis Techniques

3.3.1 Particle Size

Particle size analysis was performed using a laser diffraction particle sizer (Malvern Mastersizer) or laser scattering particle size distribution analyzer (Horibal LA-910). Relative refractive (RR) index and measuring liquid had to be determined before the measurement. For new materials, for example LSGM and GDC, the RR indexes were determined by the equipment lab to be 2.00 for LSGM and 2.31 for GDC. For other compositions of SOFC materials, the closest oxide RR indexes were used in the measurement. Table 3-5 gives the RR indexes used for the particle size measurements in distilled water. A small amount of powder was slowly added in the cell that contained water. The powder was dispersed in water by ultrasonic waves and particle size distribution was then determined.

Table 3-5 Relative Refractive Index Used for Particle Size Measurements.

Material	RR Index
LSGM: $La_{0.8}Sr_{0.2}Ga_{0.8}Mg_{0.2}O_{2.8}$	2.00
YSZ: $Y_{0.08}Zr_{0.92}O_2$	1.80
GDC: $Ga_{0.2}Ce_{0.2}O_{1.9}$	2.31
LSM: $La_{0.8}Sr_{0.2}MnO_3$	1.60
LSCo: $La_{0.6}Sr_{0.4}CoO_3$	1.40
SDC: $Sm_{0.2}Ce_{0.8}O_2$	1.65
SmSrCo: $Sm_{0.5}Sr_{0.5}CoO_3$	1.50
NiO	1.64
NiO+8YSZ	1.7
Co (II, III) oxide	1.3

3.3.2 Particle Surface Area

Surface area of the powder particles was determined using the BET (Brunauer-Emmett-Teller) method, and the measurement was carried out on a standard gas sorption analyzer (Nova–1000, Quantachrome Co.). Powder samples (1-5 grams to fill the cell volume) were degassed under vacuum (770 mm Hg) overnight at 150°C and then specific surface area was measured using nitrogen gas adsorption method (multi-points).

3.3.3 Mechanical Properties

To obtain the MOR at high temperatures, samples were put in a tubular furnace connected to the Instron. Samples were equilibrated at the high temperature for one hour before measurements were taken. The jigs were made from high temperature alloy (352A, Sandvik, Ltd.) and all measurements were adjusted to allow for the thermal expansion of the jigs. The lower span of the jig was 8.34 mm and the crosshead speed was 0.2 mm/min. Flexure samples were 12-mm long extruded, sintered rods (2 mm in diameter) or bars (2×2 mm). The bars were cut from sintered discs and the surfaces were ground and polished to 1 μm finish. The MOR of rectangle bars (MOR_R), cylindrical rods (MOR_C) and tubes (MOR_T) were calculated using Equations 3-3, 3-4 and 3-5 respectively. Data were expressed as the mean and standard deviation of at least five samples at each condition.

$$MOR_R = \frac{3FL}{2WH^2}$$

Equation 3-3

$$MOR_C = \frac{FL}{\pi R^3}$$

Equation 3-4

$$MOR_T = \frac{8FLD}{D^4 - (D-2t)^4}$$

Equation 3-5

Where

F	Rupture force	W	Width of bar
L	Span between the lower supports	H	Height of bar
R	Radius of rod	D	Inside diameter of tube
t	Thickness of tube		

Burst failure strength of the LSGM, YSZ and Ni-YSZ tubular support components was evaluated using a custom P-3100 test rig (Instron), as shown in Figure 3-9. Tube specimens, 115 mm long, were mounted onto the stainless steel end-cap blocks and sealed using resin or rubber O-rings. Pressurized water (up to 103 MPa) was fed into the tube at a controlled rate and the pressure was recorded when the tube burst. Tensile burst stress can be derived from tensile force (Figure 3-10) and calculated using Equation 3-6.

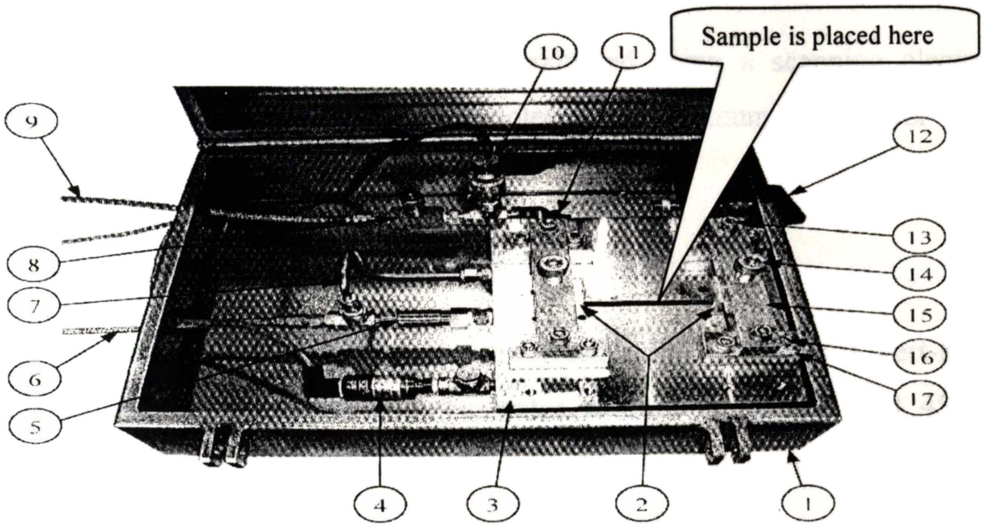

1. Enclosure
2. Endcap Block
3. Manifold
4. Pressure Transducer
5. High Pressure Check Valve
6. Fill Line
7. Intensifier Reset Line
8. Needle Valve
9. Pressure Line from Supply
10. Burst Detect Switch
11. Intensifier
12. Bleed Valve
13. 5/16 Bolt
14. 1/2-13 Bolt
15. Endcap Clamp Bar
16. Spacer Block

Figure 3-9 Tube Burst Test Device.

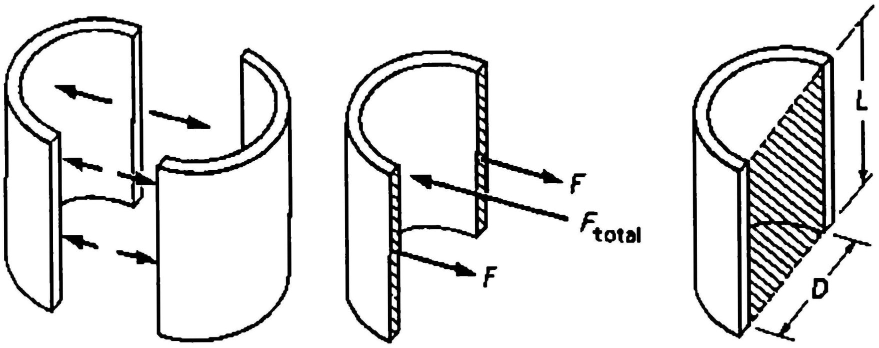

Figure 3-10 Forces on a Longitudinal Seam (Tube) [19].

$$\sigma = \frac{Pd}{2t} \qquad \textbf{Equation 3-6}$$

Where

σ	Tensile or burst stress of the tube	P	Burst pressure
d	Inside diameter of the tube	t	Wall thickness of the tube

3.3.4 Scanning Electron Microscopy

The microstructure of the products was examined using a scanning electron microscope (SEM, Hitachi S4000). Samples were platinum coated for high magnification investigation at 5 kV.

3.3.5 X-ray Diffractometer

Powder X-ray diffraction (XRD) was performed using a Philips X'pert-MPD PW3035 X-ray diffractometer with generator settings of 40 mA and 45 kV incident CuK_α X-ray radiation at 1.54056 Å. The LSGM perovskite materials were scanned at 0.02°/S over the 2θ-angle range of 20-80°.

3.3.6 Dilatometer

Linear thermal expansion measurements were performed in air using a push-rod differential dilatometer (Harrop HT) over the range 25°C to 1000°C with a heating and cooling rate of 5°C/min. The reference was a quartz rod. The average thermal expansion coefficients (α) were calculated using Equation 3-7, the initial sample length (L_0), and sample length change (ΔL) over the temperature range (ΔT) used.

$$\alpha = \frac{1}{L_0}\frac{\Delta L}{\Delta T} \qquad \textbf{Equation 3-7}$$

3.3.7 Density Measurements

Bulk density of regular shape samples or powders were calculated by measuring the volume and weight of a sample. Density of irregular shapes or porous samples density was measured in water using Archimedes' Law and set up in Figure 3-11. Samples were kept in boiling water for one hour and cooled to room temperature before being measured. A more accurate and faster technique to measure volume of different kinds of samples (with regular and irregular

Figure 3-11 Archimedes Density Measurement Set up.

shapes, dense and porous, powder and bulk pieces) is pycnometry. A helium gas absorption pycnometer (UltraPycnometer 1000, Quantachrome Instruments) was employed to carry out the density measurements. Helium can penetrate very fine pores approaching on angstrom (Å), assuring very high accuracy. Multi-run (10 runs) was set up and the average volume of the closest five runs were used for calculation. Samples were dried in an oven at 105°C for 2 hours before weighing the 4 to 15 g sample needed to fill the sample container. Apparent density was calculated using the dried weight and the sample volume reported from the pycnometer.

3.4 Single Cell Test

The single cells constructed in this study were electrically tested using dry hydrogen as a fuel and air as an oxidant. Fuel cells were placed in a test furnace to maintain the temperatures (Figure 3-12). The anode was reduced for one hour by passing hydrogen through before drawing current from the cell. Cell voltage and power versus current curves were measured at temperature of 600-850°C and continuous cell performance was evaluated at 0.6-0.7 V.

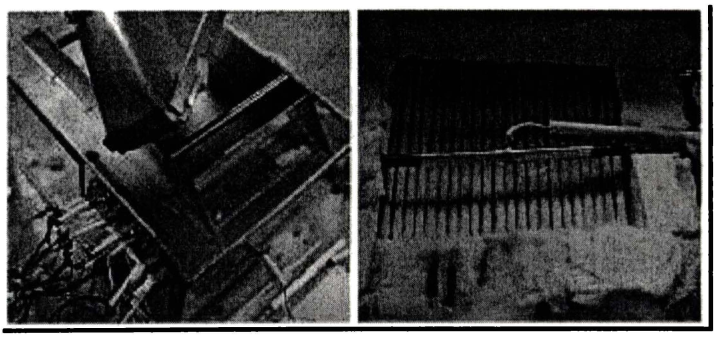

(a) (b)

Figure 3-12 Fuel Cell Test Set-up: (a) Test Furnace, (b) Cell Being Tested.

3.5 Overall Experimental Procedure

Figure 3-13 gives the overall experimental procedure used to perform this research. As-received powders and the LSGM powder synthesized in the lab were characterized for their crystal structure, particle size and surface area before extrusion. The particle size and particle size distribution of the powders were then modified through calcination and ball milling. Electrolyte and anode support tubes were extruded after optimising the formulation and mixing processes. Several coating methods such as dip coating, painting, and vacuum infiltration were investigated for applying thin films. Silver wire cathode current collector, brush and coil nickel anode current collectors were examined. Single tubular SOFCs were tested.

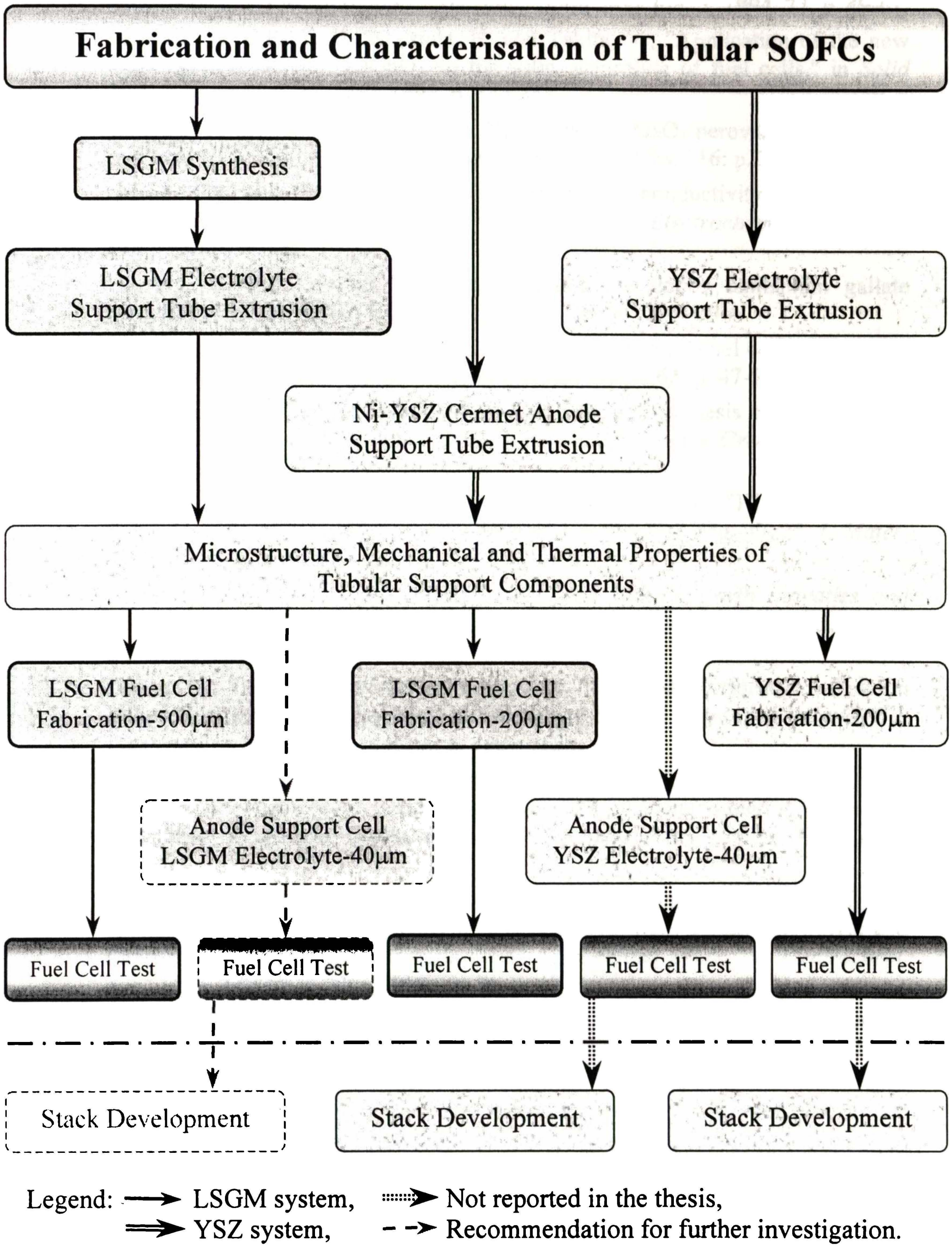

Figure 3-13 Layout of Overall Experimental Procedure.

3.6 References

1. Tosoh, "Product information--zirconia powder." 2003 p. 1.
2. Greenwood, R., Kendall, K., "Acoustophoretic studies of aqueous suspensions of alumina and 8 mol% yttria stabilised zirconia powders." *J. Eur. Ceram. Soc.*, 2000. **20**: p. 77-84.
3. Ciacchi, F.T., Crane, K.M. and Badwal, S.P.S., "Evaluation of commercial zirconia powders for solid oxide fuel cells." *Solid State Ionics*, 1994. **73**: p. 49-61.
4. Ishihara, T., Minami, H., Matsuda, H. and Takita, Y., "Application of the new oxide ionic conductor, $LaGaO_3$, to the solid electrolyte of fuel cells." in *Solid Ixide Fuel Cells (SOFC-IV)*. 1995, p. 344-352.
5. Ishihara, T., Matsuda, H. and Takita, Y., "Doped $LaGaO_3$ perovskite type oxide as a new oxide ionic conductor." *J. Am. Chem. Soc.*, 1994. **116**: p. 3801-3803.
6. Huang, P.N. and Petric, A., "Superior oxygen ion conductivity of lanthanum gallate doped with strontium and magnesium." *J. Electrochem. Soc.*, 1996. **143**(5): p. 1644-48.
7. Djurado, E. and Labeau, M., "Second phases in doped lanthanum gallate perovskites." *J. European Ceramic Soc.*, 1998. **18**: p. 1397-1404.
8. Feng, M., Goodenough, J.B., Huang, K. and Milliken, C., "Fuel cells with doped lanthanum gallate electrolyte." *J. Power Sources*, 1996. **63**: p. 47-51.
9. Huang, K., Feng, M. and Goodenough, J.B., "Sol-gel synthesis of a new oxide-ion conductor Sr- and Mg-doped $LaGaO_3$ perovskite." *J. Am. Ceram. Soc.*, 1996. **79**(4): p. 1100-1104.
10. Tao, S., Poulsen, F.W., Meng, G. and Orensen, O.T.S., "High-temperature stability study of the oxygen-ion conductor $La_{0.9}Sr_{0.1}Ga_{0.8}Mg_{0.2}O_{3-x}$." *J. Mater. Chem.*, 2000. **10**: p. 1829.
11. Pechini, M.P., "*Method of preparing lead and alkaline earth titanaties and niobates and coating method using the same to form a capacitor*," USA, US patent No.: 3330697, 1967.
12. Huang, K., Feng, M. and Goodenough, J.B., "Electrode Performance Test on Single Ceramic Fuel Cells Using as Electrolyte Sr- and Mg-doped $LaGaO_3$." *J. Electrochem. Soc.*, 1997. **144**(10): p. 3620-3624.
13. Ishihara, T., Honda, M., Shibajama, T., Furutani, H. and Takita, Y., "An intermediate temperature solid oxide fuel cell utilizing superior oxide ion conducting electrolyte, doubly doped $LaGaO_3$ perovskite." *Ionics*, 1998. **4**: p. 395-402.
14. Maric, R., Ohara, S., Fukui, T., Yoshida, H., Nishimura, M., Inagaki, T. and Miura, K., "Solid oxide fuel cells with doped lanthanum gallate electrolyte and $LaSrCoO_3$ cathode, and Ni-samaria-doped ceria cermet anode." *J. Electrochem. Soc.*, 1999. **146**(6): p. 2006-2010.
15. Lewinsohn, C.A., Colombo, P., Reimanis, I. and Unal, O., "Stresses occurring during joining of ceramics using precermic polymers." *J. Am. Ceram. Soc.*, 2001. **84**(10): p. 2240-44.
16. Kilner, J., Skinner, S.J., Ishhara, T., Otsuka, K., Irvine, J.T.S., McColm, T. and Jiang, Y., "Zero emission power generation using an all perovskite fuel cell." in *Seventh International Symposium on Solid Oxide Fuel Cells (SOFC VII)*. 2001. Tsukuba, Japan: The Electrochemical Society, Inc., p. 224.
17. Huang, K., Wan, J. and Goodenough, J.B., "Increasing power density of LSGM-based solid oxide fuel cells using new anode materials." *J. Electrochem. Soc.*, 2001. **148**(7): p. A788-A794.

18. Reed, J.S., Martin, T.J. and Carlson, W.G., *Mechanics of extrusion*, in *Science of Whitewares*, V.E. Henkes, G.Y. Onoda, Carty, W.M., Ed. 1996, The American Ceramic Society. p. 157-169.

19. Thrower, J.R., *Technical statistics and strength of materials*. 2nd ed: Delmar Publishers Inc. 1986.

Chapter Four

Optimising Extrusion of Thin YSZ Tubes For SOFC Electrolytes*

4.1 Introduction

Yttria-stabilised zirconia (YSZ) is a typical electrolyte material used in SOFCs [1-3]. Extruded thin walled tubes have been examined as possible electrolyte configurations by several researchers [4,5]. The small size tubes have a number of advantages over traditional tubular electrolytes in that they have superior mechanical properties, withstand thermal shock, and they are cheap and relatively easy to fabricate. Bending strength of the YSZ tubes with 2.4 mm diameter and a wall thickness of 0.2 mm was reported [6] as 407 MPa, while the strength of 0.56 mm rods was 734 MPa. Although traditional ceramic tubes, for example alumina tubes, are commercial products, little information appears in the literature about the thin walled zirconia electrolyte tubes for SOFCs and their manufacturing technique in detail.

Extrusion is an economic process for making objects with constant cross section such as rods and tubes. The selection and use of additives play an important role in the extrusion process. Chevalier *et al.* [7] modelled the behaviour of the paste made of a ceramic powder (TiO_2). The organic removal process was investigated by Sproson and Messing [8]. For binders to be useful in extrusion, their rheology, burnout behaviour, and green strength properties must be known. This chapter discusses developing the fabrication process, formulations and the effect of processing parameters on the tube quality in laboratory scale and manufacturing scale. Electrolyte tubes fabricated from this process were used to investigate tubular SOFC stack designs.

---

* Some data in this Chapter have been published as: Yanhai Du, N.M. Sammes and G.A. Tompsett, *J. European Ceramic Society*, **20** (2000) 959-965.

4.2 Materials and Experimental Procedure

Eight mol% YSZ and other processing additives used in the study presented in this chapter can be seen in Section 3.1.1 and 3.1.4. Various processing steps were used to extrude YSZ tubes (Figure 4-1). The commercial YSZ powder was heat treated at 900°C for 2 h to reduce the surface area and various amount of additives required for extrusion was then added. The calcined powders were then milled either manually using a mortar and pestle or in a roller mill in 250-mL Naglene containers with acetone and 10-mm diameter zirconia grinding balls. The effect of milling time on particle size was investigated. Particle size analysis was performed using a laser diffraction particle sizer (Malvern Mastersizer). The desirable powders were mixed/ground with the surfactant, plasticiser, binders, and/or solvent (if ball milling). The ball-milled slurry was tape cast onto an acetate sheet. The mixtures were then aged in sealed plastic bags overnight to produce pastes.

Workable pastes were extruded into tubes, using an in-house designed high-strength steel piston extruder (Figure 4-2). The die-head surfaces in contact with the extrudate were polished to a 1 μm finish to reduce the friction between the die wall and extrudate. A Lloyd LR100K tensile tester coupled to a personal computer was used to move a piston slowly down and force the extrudate through the die to form a tube. The effect of piston speed on extrusion quality was determined. The piston speed was typically set at 4 mm/min.

The extrudates were dried on V- or C-shaped tube holders (See section 3.2.4 for more details). After drying, the green tubes were sintered in air in a chamber furnace. Below 500°C, a slow heating rate (1°C/min) under was used to burn out the organic content. Sintering was performed at a ramp rate of 6°C/min to 1500°C followed by a dwell time of 2 h at 1500°C. The tubes were placed horizontally on V- or C-shaped kiln stands, or hung vertically on especially designed sample holders. Spacers were used to keep the tubes straight during firing. The kiln stands were made either from zirconia or alumina. Rheological properties of the dough were determined with a ram rheometer. The mechanical properties and microstructure of the sintered tubes were examined using the techniques as described in Sections 3.3.3 and 3.3.4.

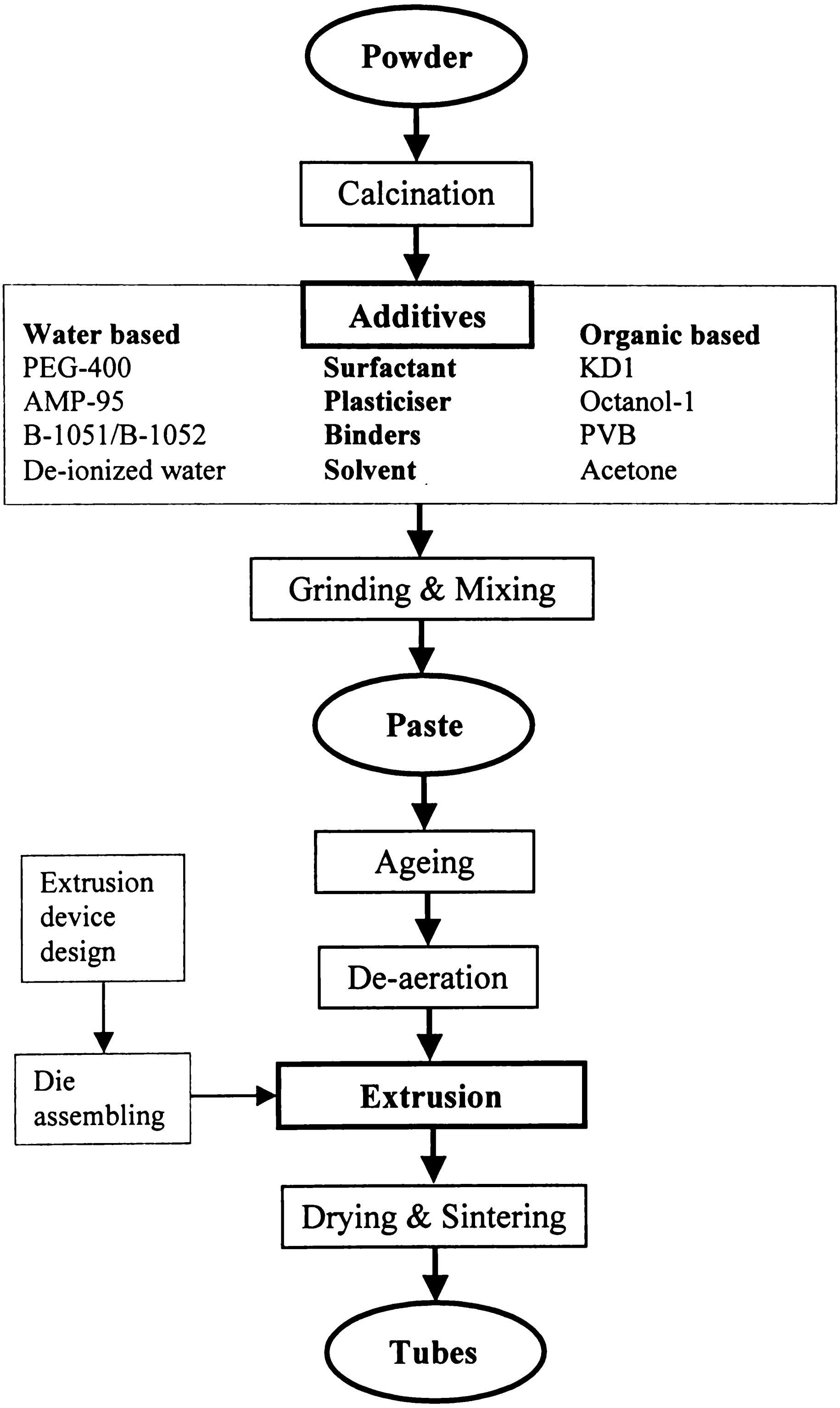

Figure 4-1 Procedure Developed for Extruding Thin YSZ Tubes.

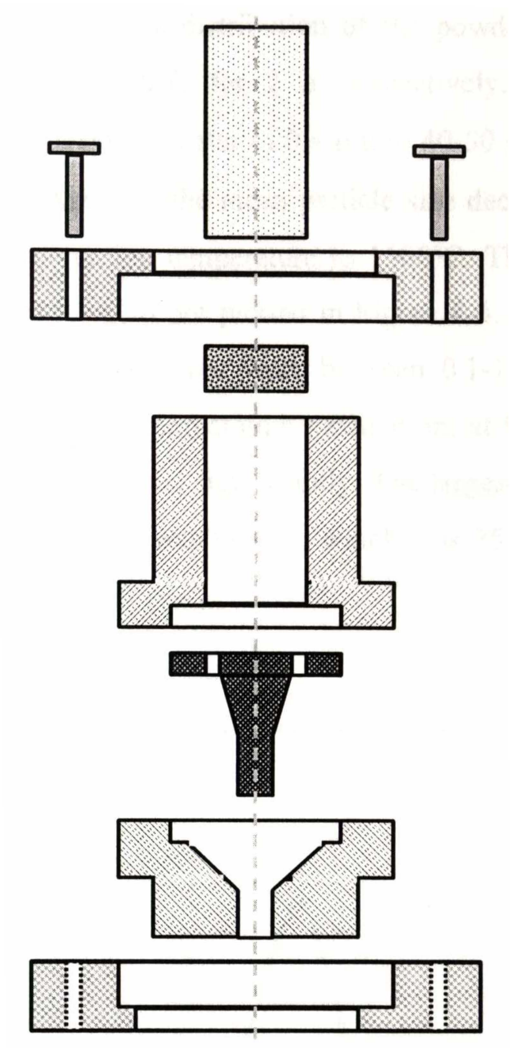

Figure 4-2 Schematic of Extrusion Device.

4.3 Results and Discussion

4.3.1 Powder Treatment and Particle Size Analyse

Particle size is one of the most important parameters for ceramic green body extrusion. Most non-clay ceramic powders are non-plastic so particle sizes greater than 5 μm may give problems in batch formulation. Extrusion problems are generally not so severe if powder particle size is below 1 μm [9]. However, smaller particle sizes have higher specific surface areas, therefore significant amounts of organic additives are needed to produce workable ceramic pastes for extrusion. Having high additive content can make it difficult to obtain high sintered densities. To understand how particle size and amount of additive affected the characteristics of the tubes, the as-received powder was first calcined and ground.

Figure 4-3 shows the particle size distribution of the powders as-received and calcined at 800, 900, and 1500°C for 2 h, respectively. The particle size distribution shifted from a mean diameter of 0.4 μm to 40-50 μm with calcination temperature up to 900°C, and then the mean particle size decreases slightly with further increase of the calcination temperature to 1500°C. The particle volumes covered by these two distributions are plotted in Figure 4-4. For the as-received powder, most (80 vol%) particle sizes were between 0.1-1.0 μm with a high specific surface area. After high temperature calcination, at 900°C for example, the particle surface area was reduced significantly. The largest particle size of the powder calcined at 1400-1500°C was 90 μm, which was 25% smaller than that formed with calcining at 900°C.

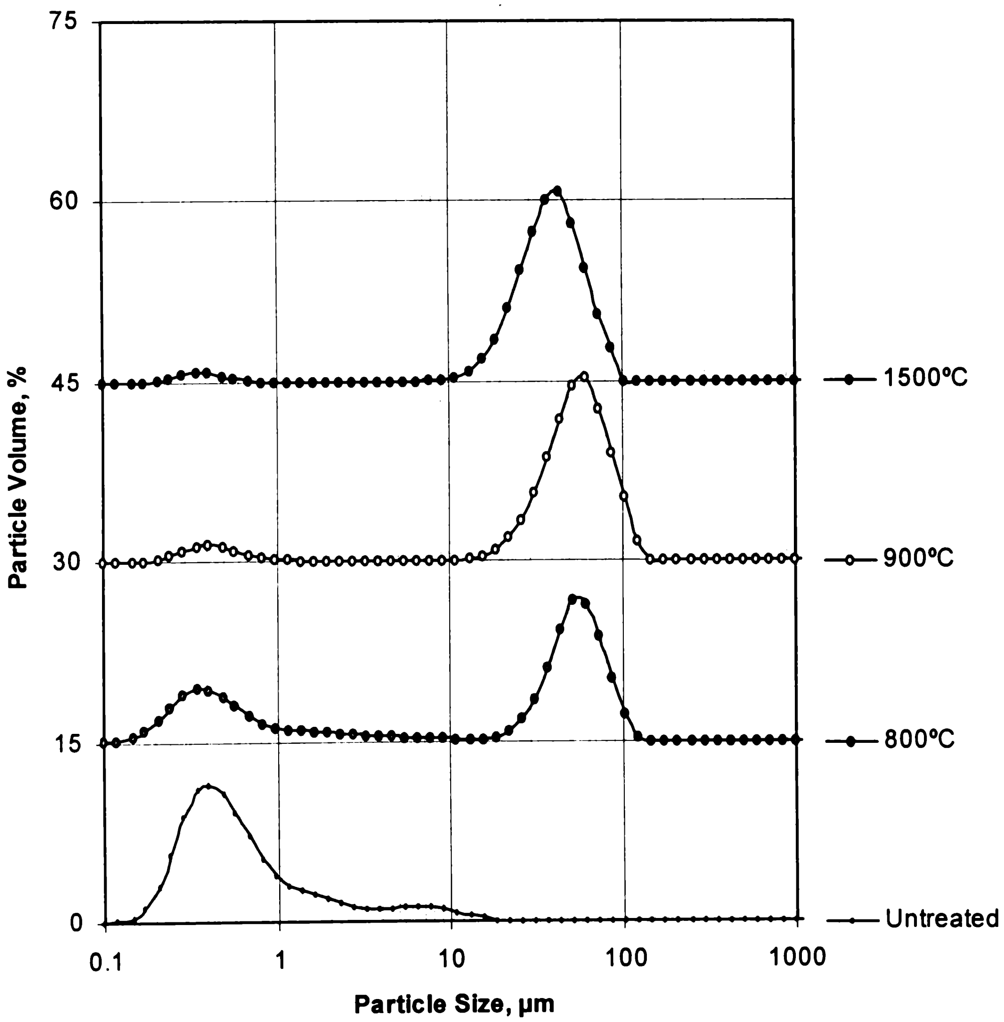

Figure 4-3 Effect of Calcining Temperature on Particle Size Distribution.

SEM micrographs of the as-received powders and calcined powders are shown in Figure 4-5. It can be seen that the agglomerates after calcination at 1400°C are much smaller, and this indicates that the powder has been partially sintered. The optimal calcining temperature was determined to be 900°C. The powder calcined at 900°C had a lower surface area and was easier to grind.

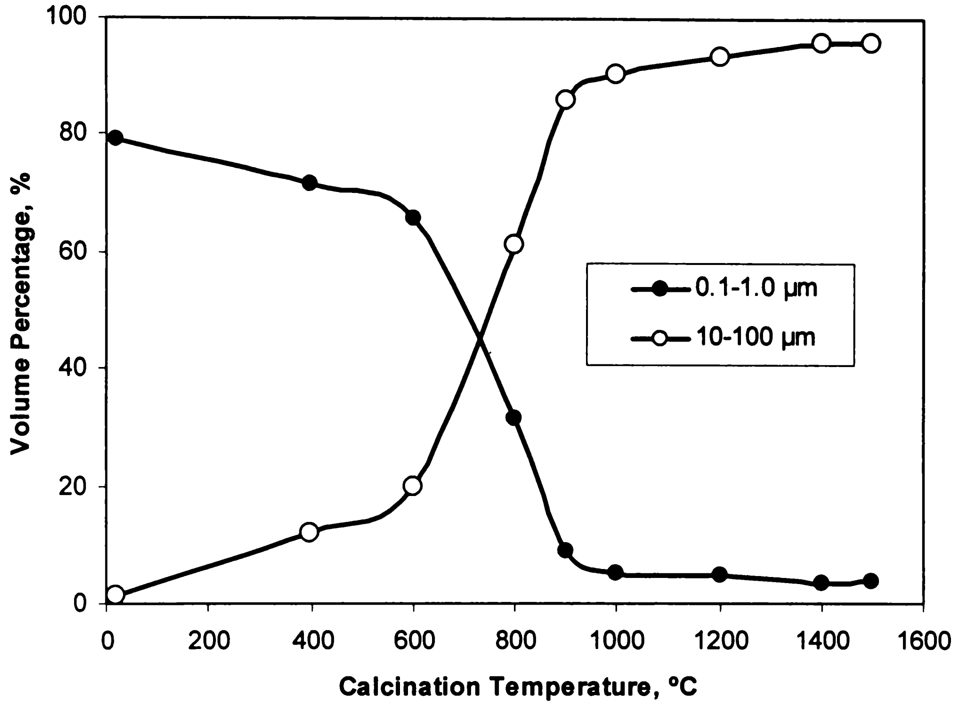

Figure 4-4 Effect of Calcination Temperature on Particle Volume of Specific Sized Particles.

The calcined powders were ground to obtain the maximum packing density. Hand grinding in a mortar and pestle for 15 minutes was needed to produce a fine powder. Longer grinding time reduced particle size but this process was considered inefficient. Figure 4-6 shows the particle size distribution after different dry ball mill duration. It can be seen that at milling times less than 10 h, increasing the dry ball milling time greatly reduced the proportion of agglomerates. However, milling for more than 10 h did not significantly affect particle size distribution. Agglomerates (with an average particle size of 10 μm) could not be completely eliminated from the powders, although the proportion of the agglomerates could be significantly reduced by using various grinding techniques (manual, dry ball mill and wet ball mill) or optimising grinding time.

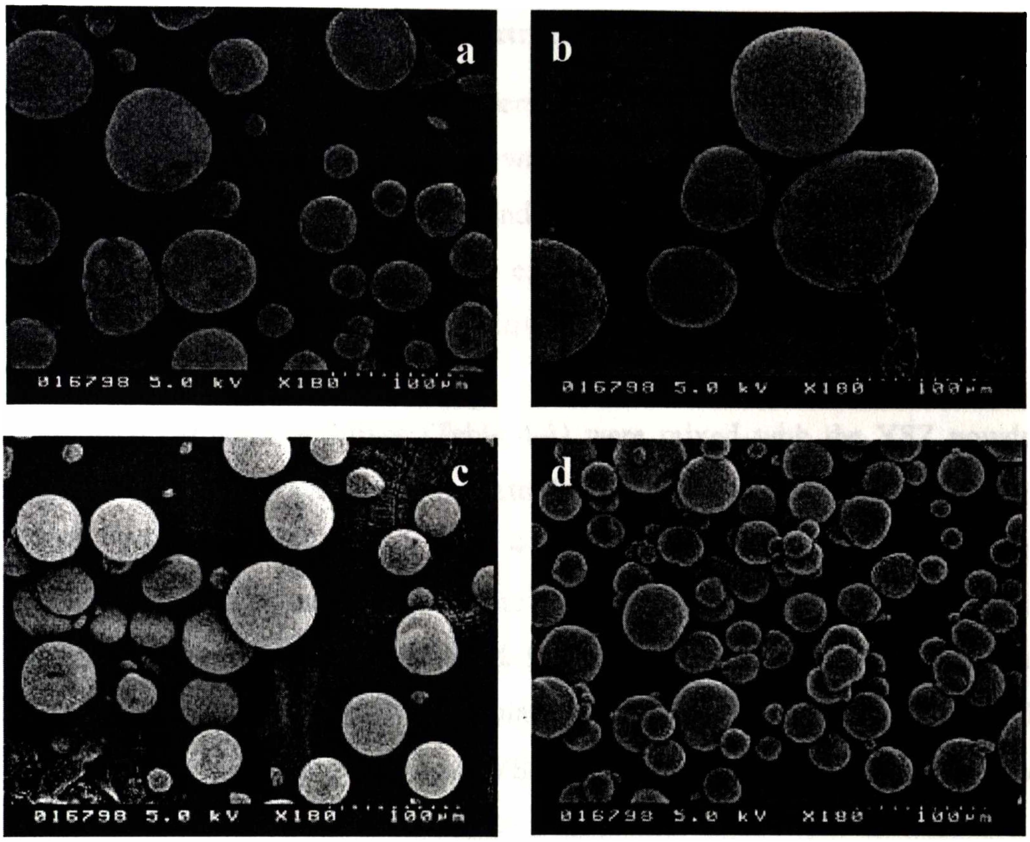

Figure 4-5 Micrographs of As-Received 8YSZ Powder (a); and Powders Calcined for 2 h at 900°C (b); 1200°C (c); and 1400°C (d).

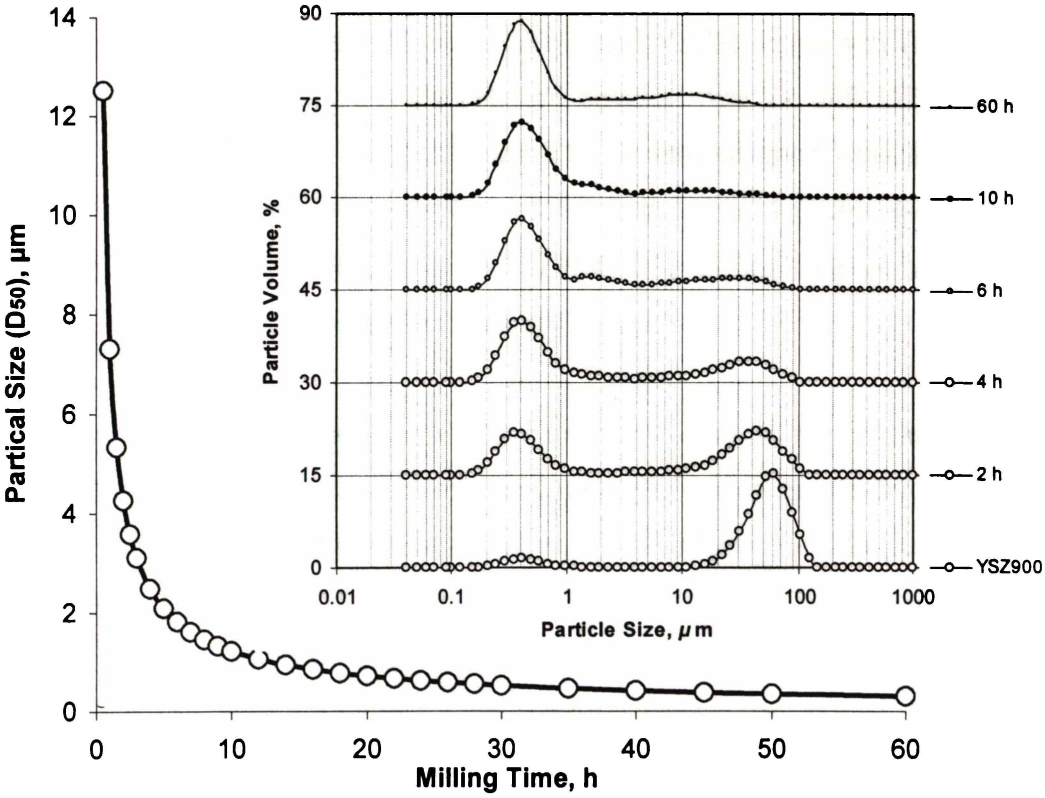

Figure 4-6 Effect of Milling Time on Particle Size Distribution.

4.3.2 Formulating and Preparing Extrudate Paste

The effect of the additives such as binders, dispersants, lubricants and pH control agents used to produce YSZ extrudates was studied. The binders play at least two roles: thickening the solvent phase and giving the green body wet and dry strength. Binders selected for the YSZ extrusion include PVB, one of the most popular binders, and specific ceramic extrusion binders B-1501 and B-1502.

Water-based extrudate additives (Table 4-1) were mixed with the YSZ powder using a mortar and pestle. Tubes extruded from 100% as-received powder (YSZ3b, YSZ5a and YSZ5b in Table 4-1) are very porous and coarse. Pastes made of 100% fine powder (YSZ9) were too plastic to be successfully extruded. Samples YSZ10 and YSZ11 with 50% 900°C calcined and 50% fine particles could be extruded into symmetric tubular shape. Dense, straight and even wall thickness tubes were obtained from YSZ12, which contained 900°C calcined powder and was ball milled in acetone for 8 h.

Obtaining extrudable organic-based pastes (Table 4-2) was depended on the particle size and distribution of the YSZ powder. Pastes made of 100% as-received powder were either too sticky (YSZ1 and YSZ3) or too stiff (SZ80s) to be extruded. Pastes made of 100% calcined powder were too soft (YSZ7b and YSZ89s). However, mixes of YSZ7a and YSZ7b showed good workability and had a particle size contribution similar to YSZ10 and YSZ11 (Table 4-1), which was made from 50% powder calcined at 900°C and 50% fine powder. The resulting tubes were smooth, dense and straight.

Obtaining extrudable pastes is the most important step in the manufacturing process. Powders and additives were mixed manually with a mortar and pestle or in a roller mill. Mixing helps increase uniformity. Poor mixing can occlude binder within the agglomerates, which can give dilatant behaviour. Non-homogeneous pockets of binder and powder may become voids in the final fired object.

Table 4-1 Formula and Appearance Extrudates with Water Based Additives.

Sample code	Powder treatment	Additives, wt% of powder					Ageing time and paste appearance	Tubes green/sintered	Comments
		PEG-400	AMP-95	B-1501	B-1502	H_2O			
YSZ3a	Untreated	0.6	3.6	8.3	9.2	27	24 h, very sticky		Too sticky to be extruded
YSZ3b	900°C @ 2 h	0.6	3.6	8.3	4.6	27	24 h, not sticky ☺	Rough surface	Porous tubes
YSZ5a	100%-900°C @ 2 h	6.6	1.8	8.3	4.6	25	3 days, workable ☺	Good shape ☺	Similar surface, porous
YSZ5b	80%-900°C @ 2 h 20%-fine powder	6.6	1.8	8.3	4.6	25	3 days, workable ☺	Good shape ☺	
YSZ9	100%-fine powder	6.6	1.8	8.3	4.6	25	2.5 h, very plastic	Worm-shape	Paste plastic
YSZ10	50%-900°C @ 2 h 50%-fine powder	6.6	1.8	8.3	4.6	25	20 h, a little sticky ☺	Straight ☺	Paste de-aired, green tubes dried 4 days ☺
YSZ11	50%-900°C @ 2 h 50%-untreated	6.6	1.8	8.3	4.6	25	20 h, easy to extrude ☺	Straight ☺	
YSZ12	900°C @ 2 h	6.6	1.8	8.3	4.6	20	24 h, easy to extrude ☺	Straight ☺	Ball mill 8 h in acetone
YSZ13	900°C @ 2 h	6.6	1.8	8.3	4.6	25	44 h, workable	Not smooth	Ball mill 12 h in ethanol
YSZ14	Untreated	6.6	1.8	8.3	4.6	133	40 h, loose	Cracked after extruding	Ball mill 10 h in Ethanol

☺ Satisfactory at that stage.

Table 4-2 Formula and Appearance Extrudates with Organic Additives.

Sample code	Powder treatment	Additives, wt% of powder				Mixing and grinding	Paste	Tubes green/sintered	Comments
		KD1	Acetone	PVB	Octanol-1				
YSZ1	Untreated	3	96	6	24	Ball mill 24 h			Too sticky to be extruded
YSZ3	Untreated	3	52	6	9	Stirring 9 h		Extruded rods	Too sticky to be extruded
YSZ7a	900°C @ 2 h	6	60	6	6	Ball mill 8 h	Rigid, plastic	Using (a+b), tubes with smooth surface ☺	The particle size distribution 50%-900°C, 2 h 50%-fine powder ☺
YSZ7b	900°C @ 2 h	6	60	6	6	Stirring 8 h	Dry, loose, soft		
YSZ80s	Untreated	5	50	6	6	Stirring 4 h	Rigid, plastic	Cracked while drying	Unworkable
YSZ80b	Untreated	4	50	6	6	Ball mill 4 h	Soft, plastic	Workable ☺	
YSZ89s	900°C @ 2 h	5	50	6	6	Stirring 4 h	Dry, soft, loose	Un-extrudable	Particles too coarse
YSZ89b	900°C @ 2 h	4	50	6	6	Ball mill 4 h	Loose, plastic	Cracked while drying	Ball mill time should > 4 h

☺ Satisfactory at that stage.

In the organic-based system, slurry consisting of the milled powder and solvent (acetone) was poured onto a plastic sheet and dried until the mixture could be easily removed from the sheet. Drying the tape-cast slurry is a critical step. If the slurry is not dried sufficiently, it is too adhesive and soft. Conversely over-dried paste is too stiff to be extruded. Drying time is affected by the thickness of the cast tape, solvent content, and ambient temperature. Ten to 30 minutes was sufficient for tape-cast slurries 1-2 mm thick.

For the water-based system, PEG-400 dispersed in distilled water (10% wt/wt PEG-400) and AMP-95 were manually mixed with YSZ powder for 15 min using a mortar and pestle before adding B-1051 and B-1052. Rigidity and flexibility of the paste were adjusted by varying the ratio of B-1051 and B-1052. A 1.8:1 ratio of B-1051: B-1052 produced rigid extrudates. Solvent (water or acetone) had to be added to adjust the paste workability. The resultant mix was placed in polyethylene bags to prevent solvent evaporation and aged overnight. It was necessary to knead the pastes properly just prior to performing the extrusion process. Rheological properties, plasticity, flexibility, rigidity, and stiffness were used to evaluate the paste extrudability.

4.3.3 Forming and Extrusion Die Design

As a plastic forming method, there exist certain mechanical requirements [9] for extrusion to occur. The first requirement is flow. During extrusion, the paste must be plastic enough to form the desired cross-section when pressure is applied. The second requirement is wet strength. After extrusion, the green body must be strong enough to resist deformation from its own weight or from handling.

Velocity of the die piston affected tube wall thickness. The faster the piston speed, the thinner the tubes formed, as shown in Figure 4-7. Extrusion speed was also determined by the way of extrudate being picked up. Extrudate speed in 10-50 mm/s was manageable. Although thin-walled electrolytes have lower cell resistances, there is a lower limit on wall thickness because it is very difficult to avoid green-tube deformation. Secondly, the sintered tubes may have insufficient strength to be a self-supported electrolyte in a fuel cell assembly.

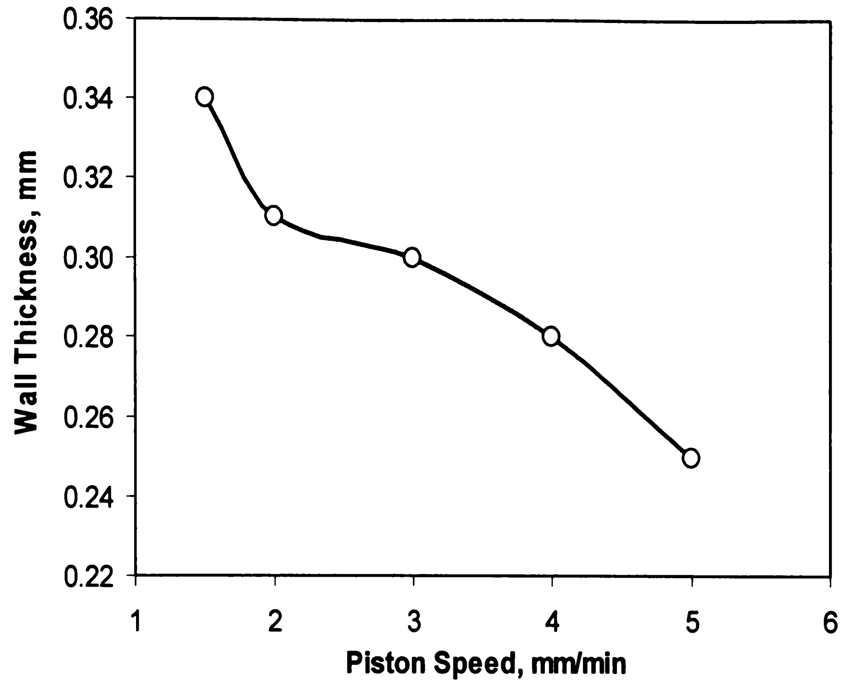

Figure 4-7 Effect of Piston Speed on Wall Thickness of Sintered Tubes.

The load to produce optimum extrusion quality depended on the extrudate stiffness and was 1-7 kN for water based pastes and 15-30 kN for organic based pastes. To prevent tubes flattening during extrusion, the tube end was kept open after cutting so the air pressure on the inside and outside of the tube was the same.

As an extrusion die significantly affects paste flow and quality of extrudates, great efforts have been made to improve extrusion die designs and reduce die-entry pressure drop. These include enlarging the paste flow pathways, tapering the flow entry and exit regions, and reducing the cross-section of the die (tapered mandrel) (Figure 4-8). These approaches effectively reduced static flow zones, enhanced the separated flow streams joining, and reduced the amount of material left in the die.

Bending or ribbing defects occurred when the paste was not homogeneous or extrusion die was not appropriate (Figure 4-9). Other common ceramic extrusion defects such as tearing and lamination did not occur in the optimum formulation developed.

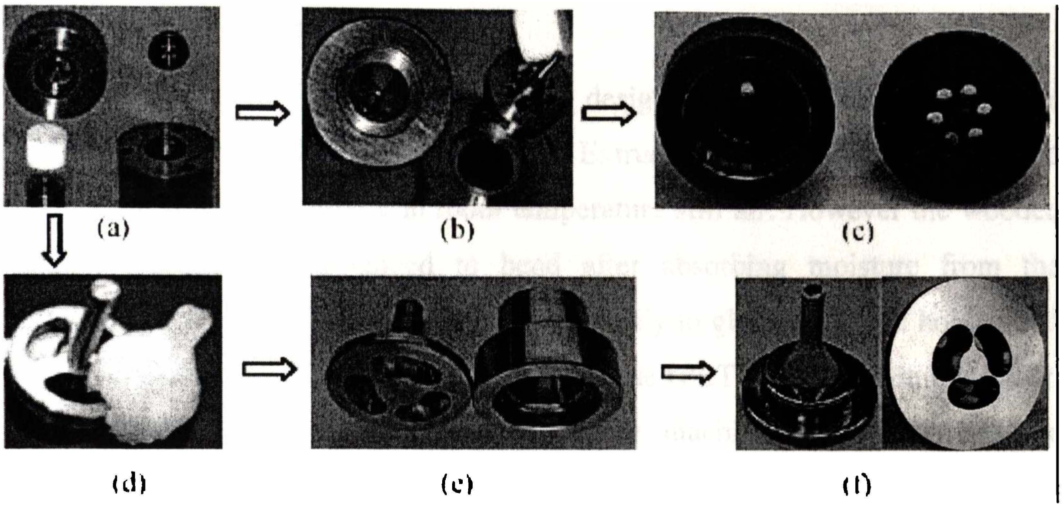

Figure 4-8 Improvements in Extrusion Die Designs: (a) a Simple 4-Hole Die, (b) Enlarged Flow Pathway (8-hole) and Tapered Mandrel, (c) Tapered Entry Region, (d) Further Enlarged Flow Entry Pathway Using a 3-Spider Design, (e) 3-Spider with Tapered Mandrel, (f) 3-Spider Design with Tapered Mandrel, Entry and Exit Regions.

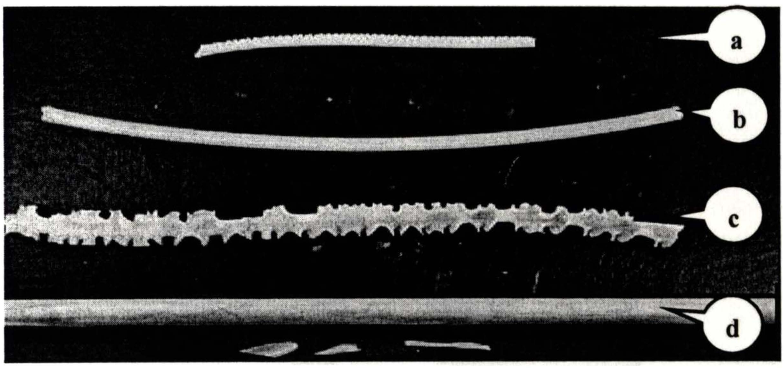

Figure 4-9 Examples of Extrusion Defects: (a) Ribbed, (b) Bends, (c) Splits, and (d) Laminated.

Various diameter tubes were also fabricated using isostatic press method (Figure 4-10). These tubes can be put one into another to build serial cells. Tubes were dense but the productivity was low.

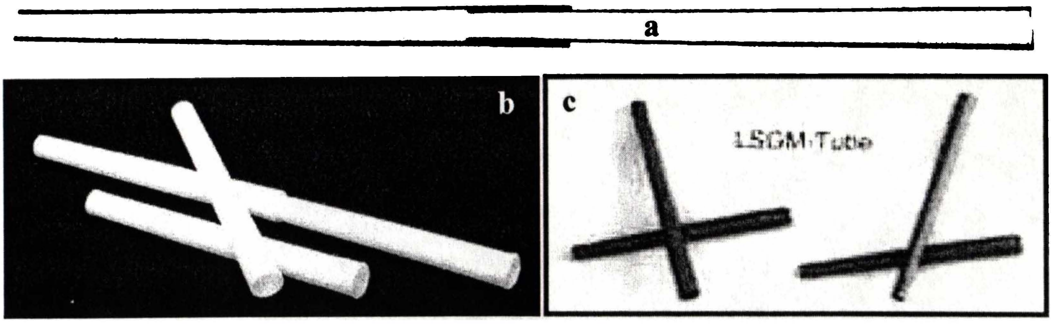

Figure 4-10 Tubes Fabricated Using Isostatic Method: (a) Schematic, (b) Photo of the YSZ Tubes and (c) Photo of the LSGM Tubes.

4.3.4 Drying and Sintering

Extruded tubes were kept in the in-house designed tube holders to retain the straightness and roundness during drying. Extrudates in wood and paperboard holders can be dried naturally in room temperature still air. However the wooden holders and paperboard tended to bend after absorbing moisture from the extrudates (10-15%). Wet extrudates adhered easily to glass and metal holders but plastic holders made of polyethylene terephthalate (PET) and teflon in particular, were suitable because these materials can be machined accurately and the extrudates did not adhere to them (Figure 4-11a). When using plastic holders, the humid air inside the extruded tubes must be removed gradually by vacuum or pressure. This means the inner tube surface dried faster than the outer. When the inner part shrank, the soft outer surface adapted to the change in shape. Tubes dried in this nature were straight and round (Figure 4-11b).

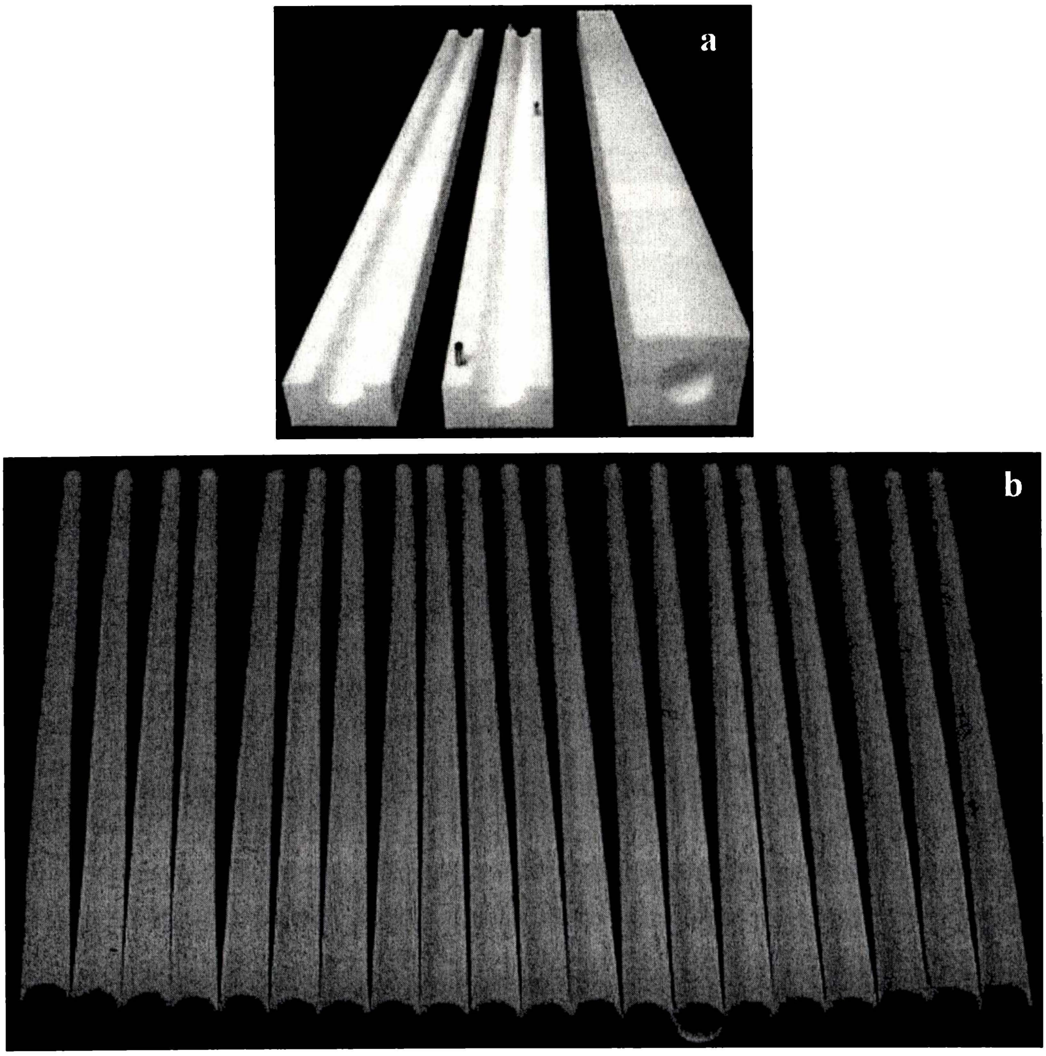

Figure 4-11 Photographs of (a) C-Shaped Plastic Tube Holders and (b) Dried Tubes.

Dried tubes were dense with close uniformly micro-pores as shown in Figure 4-12. After drying, the tubes were then sintered. The firing regime was designed based on the properties of the binders. A slow ramp 1°C/min up to 500°C was utilised to burn out the organic components and then a ramp rate 6 °C/min to 1500°C for 2 h was undertaken. No sintering micro-cracks were detected (using SEM) under this sintering regime. Linear sintering shrinkage of the tubes was calculated at 20% for the water-based system and 25% for the organic based system (Figure 4-13).

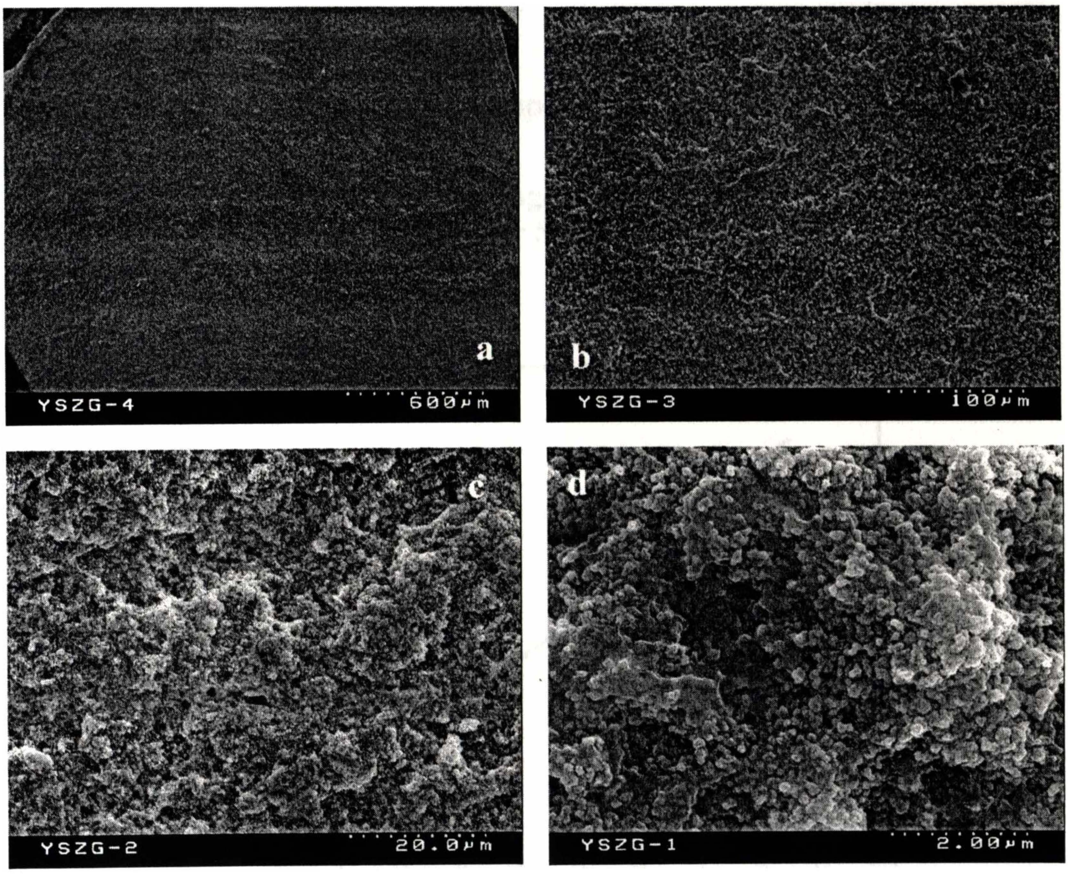

Figure 4-12 Micrographs of the Cross-Section of the Green Extrudates at Different Magnifications.

There was a linear relationship between the sintered body and the extrusion die size as shown in Figure 4-14. Equation 5-1 derived from experiment data can be used to estimate die size needed to produce given diameter tubes for YSZ material and sintering at 1500°C for 2 h; the accuracy of the equation was approximately 2%.

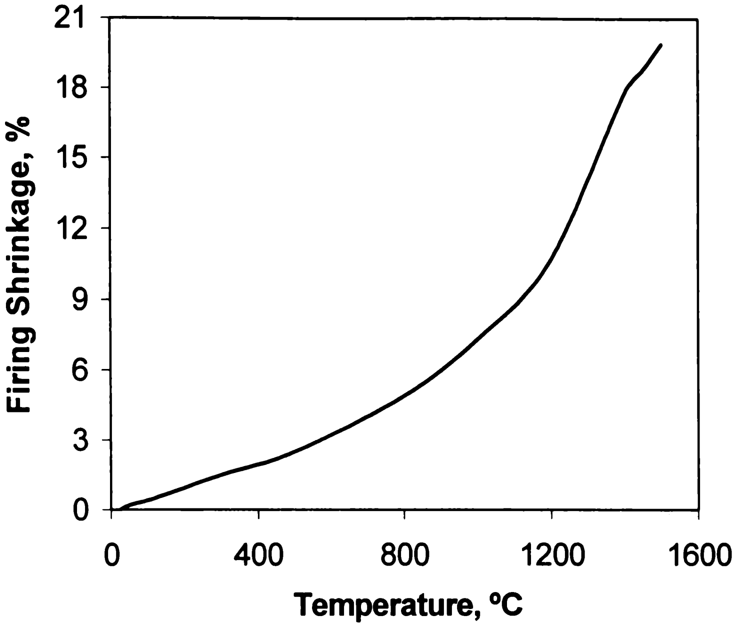

Figure 4-13 Linear Firing Shrinkage of Extrudate Tubes for Duramax Binder System.

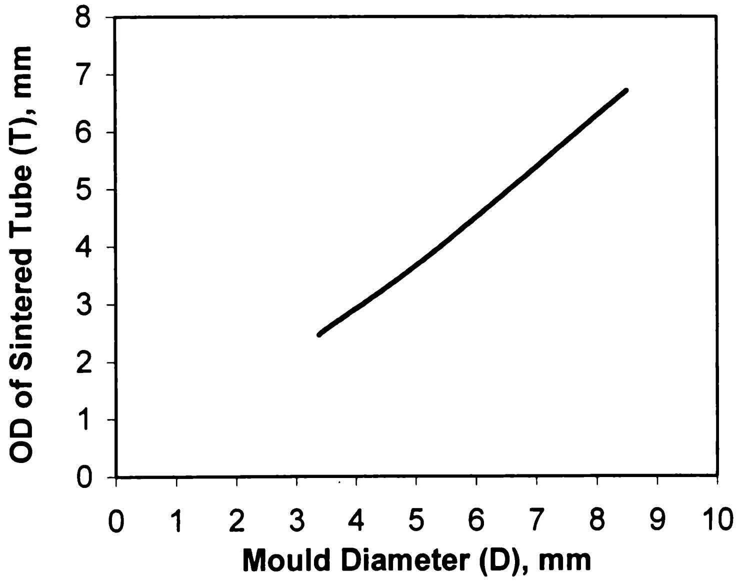

Figure 4-14 Dimensional Relationship Between Mould and Sintered Body (8YSZ, Sintered at 1500°C for 2 h).

$$T=0.828D-0.339 \qquad \textbf{Equation 5-1}$$

Where T is the OD of sintered tubes, D is the extrusion die size, both in mm.

4.3.5 Effects of Additives on Extrudability and Yield

Based on the above results, the Duramax binder system had the best processing characteristics and was used in scale up. Mixing uncalcined powder with binders and other wetting agent into uniform dough is possible with a high-shear blade mixer. This mixing regime allowed the water content of the mixtures (Table 4-3) to be reduced by more than 50% of the lab formula (Table 4-1), eliminated the need for solvent (acetone or ethanol), and allowed the B1051/B1052 binder ratio to be increased from 1.8:1 to 5:1. Having a lower liquid content increases extrudate green density. A higher B1051/B1052 binder ratio produces stiffer dough, which helps the extruded green tubes retain their round shape. The formulation test results are shown in Figure 4-15 and the effect of each additive is discussed below.

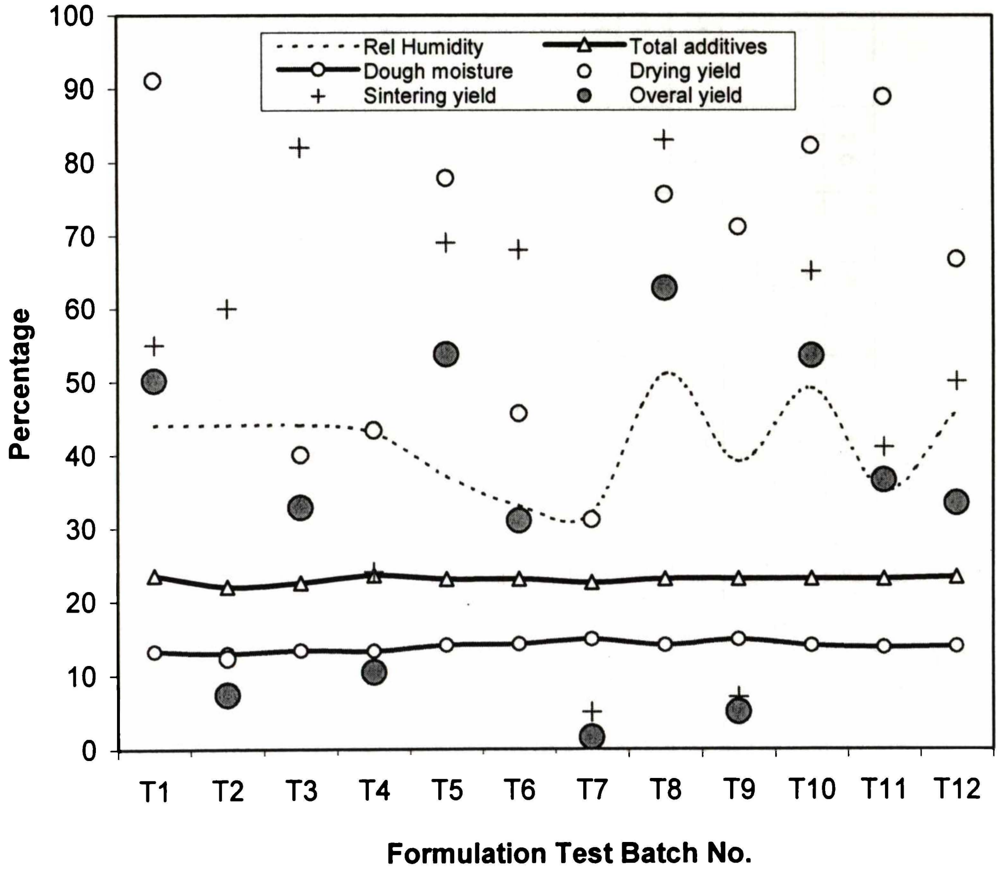

Figure 4-15 Characteristics of Extrudates Produced in Different Scale up Formulation Tests.

Table 4-1 Formulations for Scale up Using a High Shear Blade Mixer and a Ram Extruder.*

Test No.	PEG-400 %	AMP-95 %	B1051 %	B1052 %	H_2O %	Total additives* %	Binder Ratio: B1051:B1052	pH	Dough moisture %	Extrudability and/or extrusion pressure (psi)	Overall yield, % (after drying and sintering)
T1	3	1.5	10	2.5	6.5	23.5	4:1	9.4	13.2	Very good; 650 to 1500-2000	50
T2	1.5	1.5	10	2.5	6.5	22	4:1		12.9	Poor, too dry, bend; 2980	7
T3	1.5	1.5	10	2.5	7	22.5	4:1		13.3	Too hard to extrude; 3000	33
T4	3	1.5	10	2	7	23.5	5:1		13.2	580 to 1200-1500	10
T5	1.5	1.5	10	2	8	23	5:1		14.0	Good; 620 to 1500-2000	54
T6	1.5	1.5	10.28	1.72	8	23	6:1		14.2	Bend; 500 to 1200-1700	31
T7	1.5	1.5	6	2	11.5	22.5	3:1		14.8	Too soft; 340 to 1000-1200	2
T8	1	1.5	10	2	8.5	23	5:1		14.0	Very good; 700 to 1200-1600	63
T9	0.5	1.5	10	2	9	23	5:1	9.6	14.7	Good; 700 to 1200-1600	5
T10	1.5	1	10	2	9	23.5	5:1	7.9	13.9	Dough hard; 1800 to 2800	53
T11	1.5	2	10	2	7.5	23	5:1	10.1	13.7	Good; 1300 to 2000-2400	36
T12	1.5	1.5	10	2.5	7.5	23	4:1	9.4	13.8	330 to 1100-1200	33

* Weight percentage related to the dry powder.

Binder B1051/B1052 ratio was varied from 3:1 to 6:1 (T7, T1/T3, T5, and T6) while other individual and total additives were kept constant (23±0.5%). Tubes extruded from dough with lower ratios of the two binders were straight but green tubes went out of round on drying. Tubes extruded from dough with higher ratios of the binders (stiffer dough) were round but not sufficiently straight (T6). Yield was highest when the binder ratio was 4:1 to 5:1 (Figure 4-16).

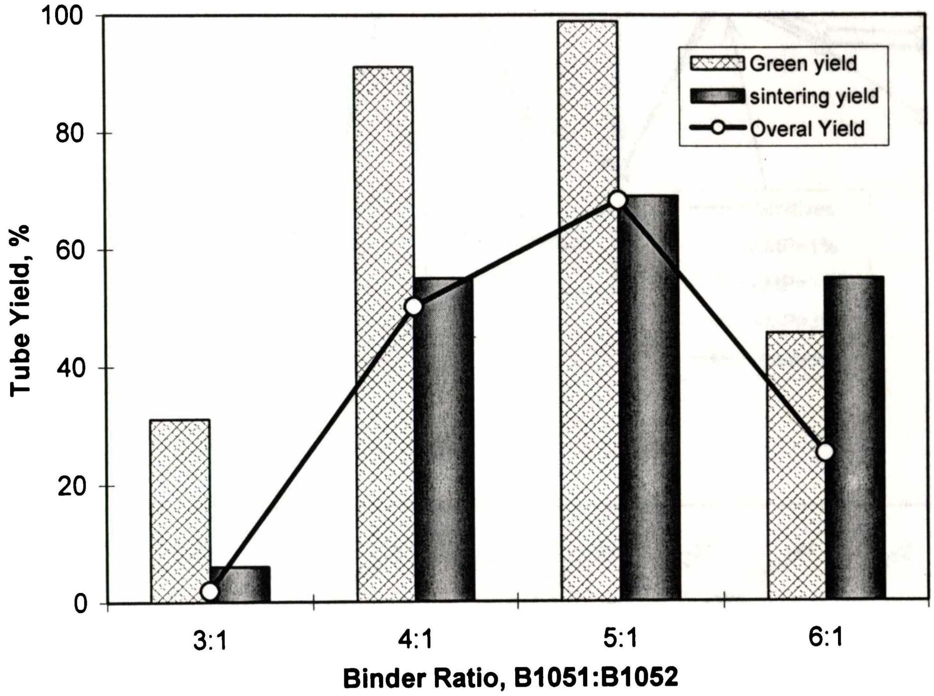

Figure 4-16 Effect of Binder Ratio on Tube Yield.

Content of pH agent significantly affected dough workability and pH. The aim was to obtain dough with a pH near the isoelectric point (IEP) by adjusting the AMP-95 content. Tosoh 8YSZ with Duramax binder and 1-1.5% AMP-95 (T10, T5, T11) had good plasticity. Dough with less than 1% AMP-95 had pH under 8 and was difficult to extrude. In contrast, dough with more than 2% APM-95 had a pH greater than 10 and the extrudate retained its shape well after extrusion (Figure 4-17; Table 4-3).

Lubricant PEG-400 content was varied between 0.5%-3% while binder, pH control agent and total additives were kept constant (T4, T5, T8, and T9), using water to balance the difference of PEG for each test. Green tube yield was increased with lubricant content and higher overall yield occurred at the lubricant level of 1-1.5% (Figure 4-18).

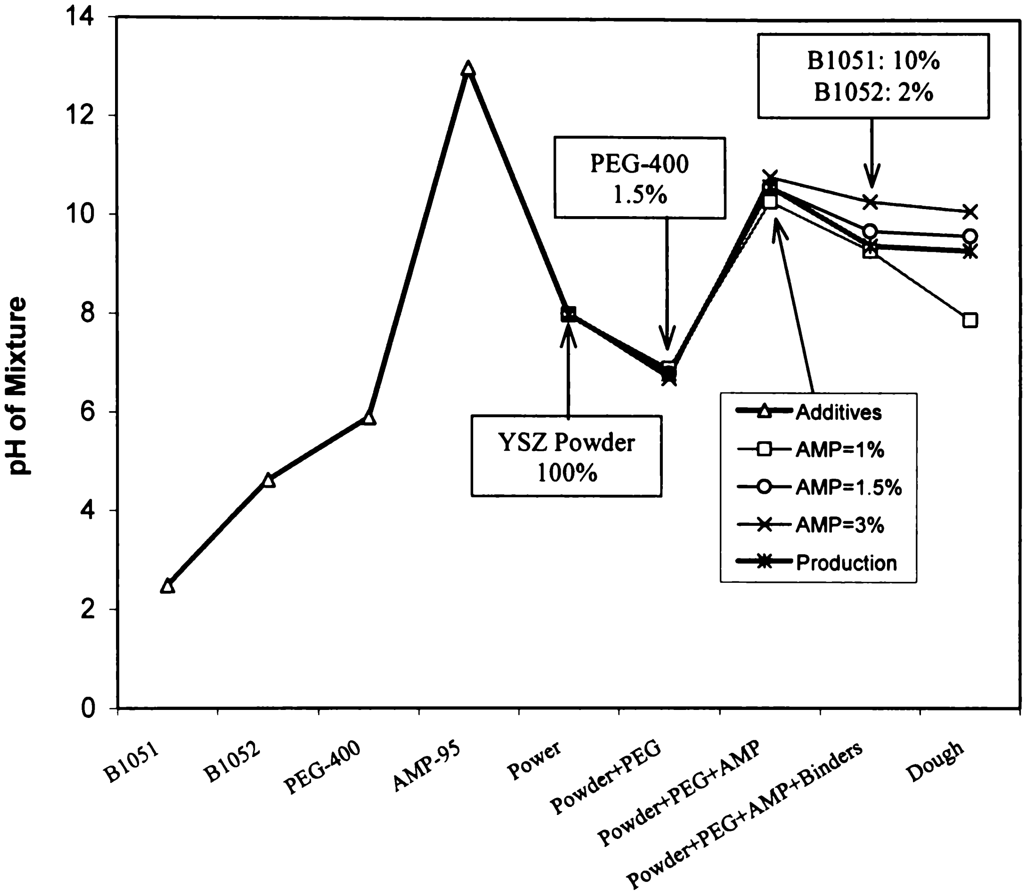

Figure 4-17 pH of Duramax Additives and Mixes at Different Stages.

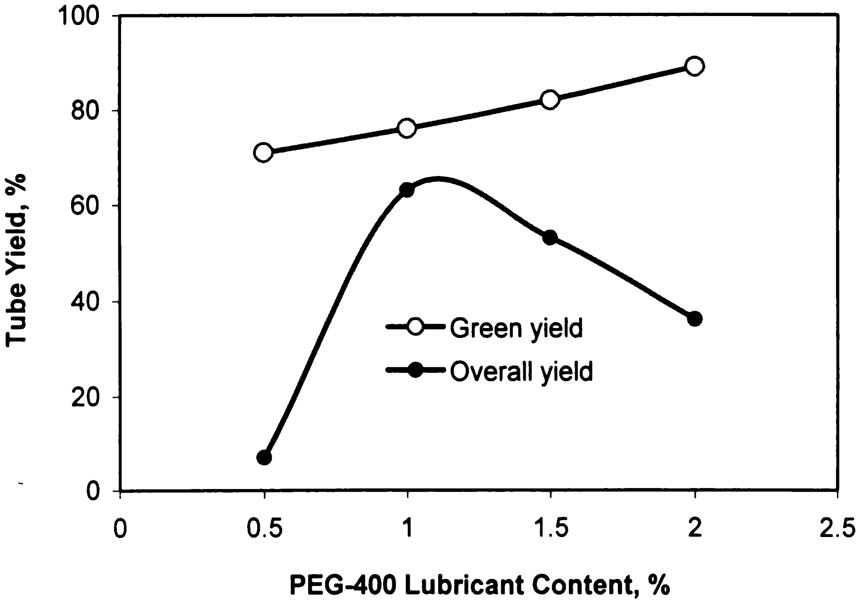

Figure 4-18 Effect of PEG-400 on Tube Yield.

Water content was changed between 7-9% (T4, T8, T10 and T12) while additives were kept relatively constant, for example, 12-12.5% binder (binder ratio 4:1 to 5:1), 1-1.5% AMP-95, and 1-1.5% PEG-400 (except T4, 3%). High water content gave low cohesive dough and therefore low green yield. Water content of 8-9% gave higher both green and sintered yield (Figure 4-19).

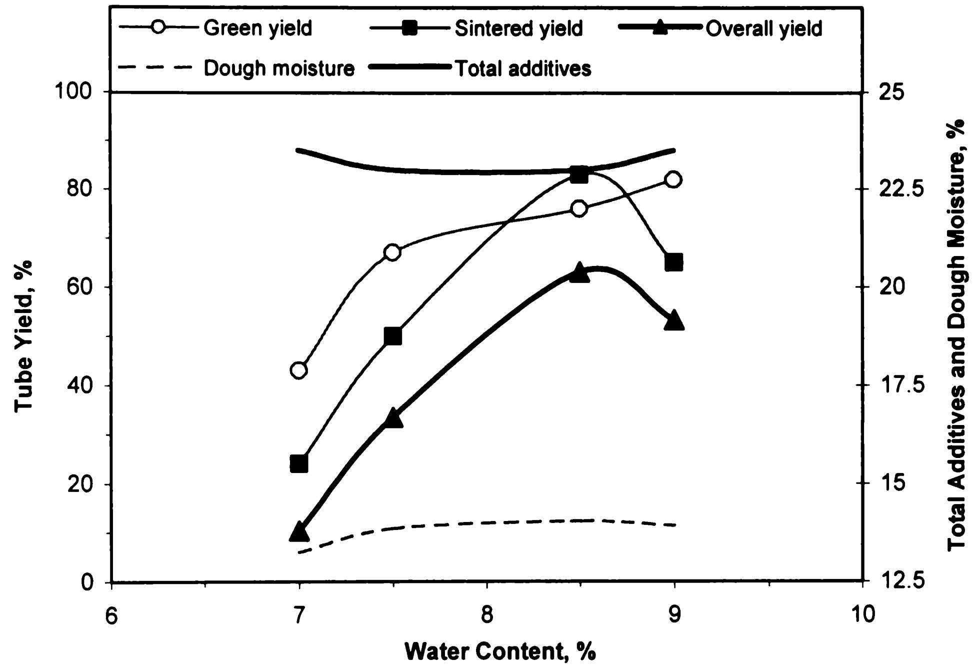

Figure 4-19 Effect of Water Content on Tube Yield.

Rheological behaviour of the dough reflects the effects of all the additives and processes discussed above. Figure 4-20 shows the equilibrium extrusion pressure as a function of apparent shear rate obtained from a ram rheometer when conducting rheological test on different formulations. The extrusion pressures of the different mixes at the maximum apparent shear rate (500 /s) can be grouped into three: under 60 MPa (T4 and T7 and T9), 70-90 MPa (T1, T8, T10 and T12) and above 100 MPa (T2, T3, T5, T6 and T11). Low binder ratio (3:1) or high moisture content (14.8%) caused the softness. Tubes extruded from the soft dough (T7, T9) could not retain their roundness during drying and sintering because of the low cohesiveness. On the other hand, high binder ratio (6:1, T6) and low moisture content (12.9%, T2) resulted in stiffer dough that needed high pressure for extrusion due to the high interparticle force and external friction in the die. For a constant mixing time, it is more difficult to make stiffer dough homogeneous. Phase separation can occur during extrusion in inhomogeneous dough (T6).

Extrudates from proper stiffness and homogeneous dough obtained from formula T8 that had a bind ratio 5:1 and moisture content of 14% had high green and sintering yields.

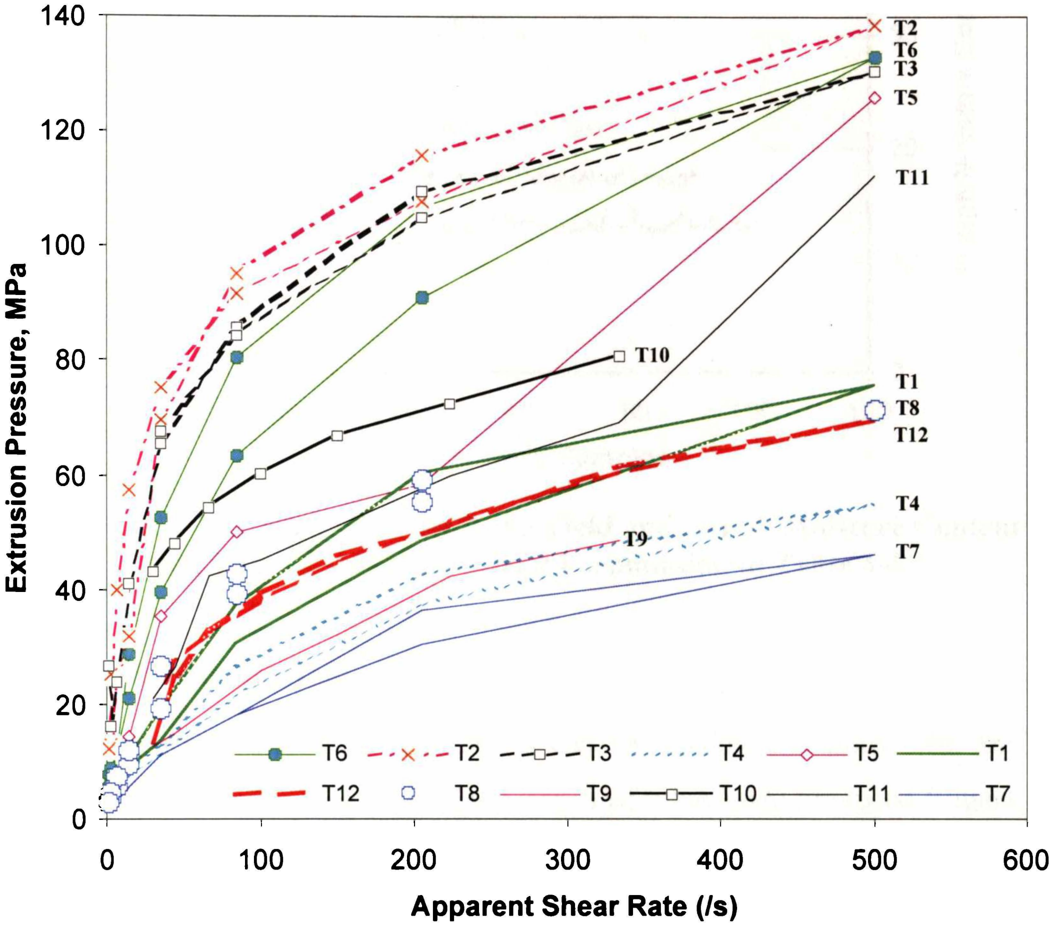

Figure 4-1 Rheological Behaviour of Different Dough Formulations.

Optimised formulation (Table 4-4) was then determined from the above analysis and Test No. T1, T5, T8 and T10. However, there was still a 60-98% variation in green tube yield (Figure 4-21), even though dough moisture was constant at 13.3±1% and the other additives were the same. Ambient relative humidity and moisture content in the starting powder may influence moisture content in the dough. However, no correlation was found between green tube yield, moisture content and relative humidity in the 13.3±1% dough moisture range.

Table 4-1 Optimal Formula for Producing YSZ Electrolyte Tubes.

Binders		pH Control Agent	Surfactant	Water
B1051	B1052	APM-95	PET-400	
10%	2%	1.5%	1.5%	8.5%

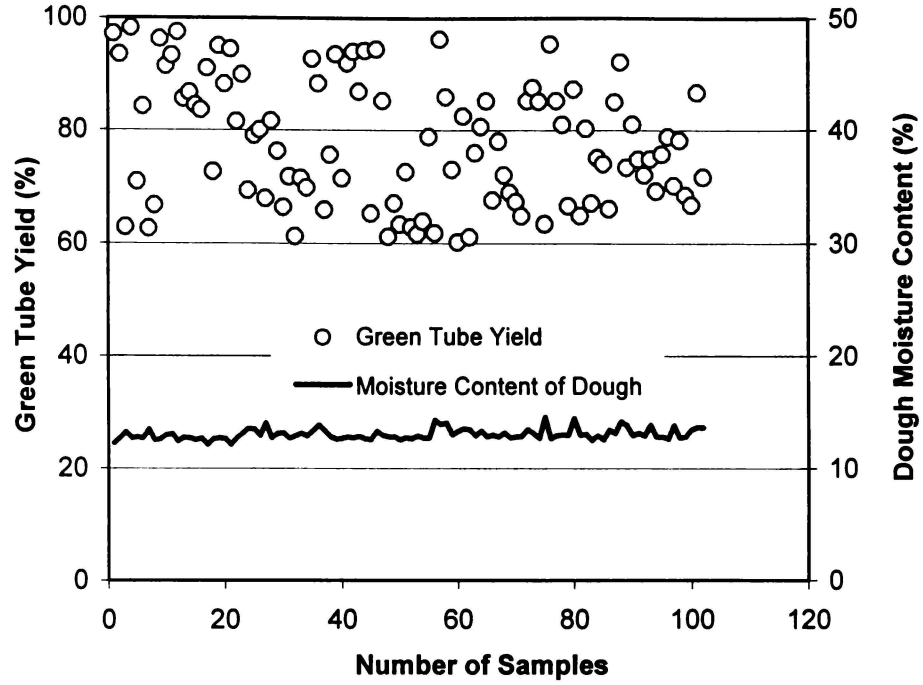

Figure 4-21 Variation of Green Tube Yield and Dough Moisture Content with Batch Using the Optimal Formulation in Table 4-4.

4.3.6 Tube Examination

Tube length, roundness and straightness can be quickly examined with an in-house designed device (Figure 4-22). A series of tubes were produced (Figure 4-23). Tubes fabricated from optimised parameters had tight tolerances:

OD and roundness: 4.0±0.1 mm;

Wall thickness: 0.20±0.02 mm;

Length: (200-300)±1 mm.

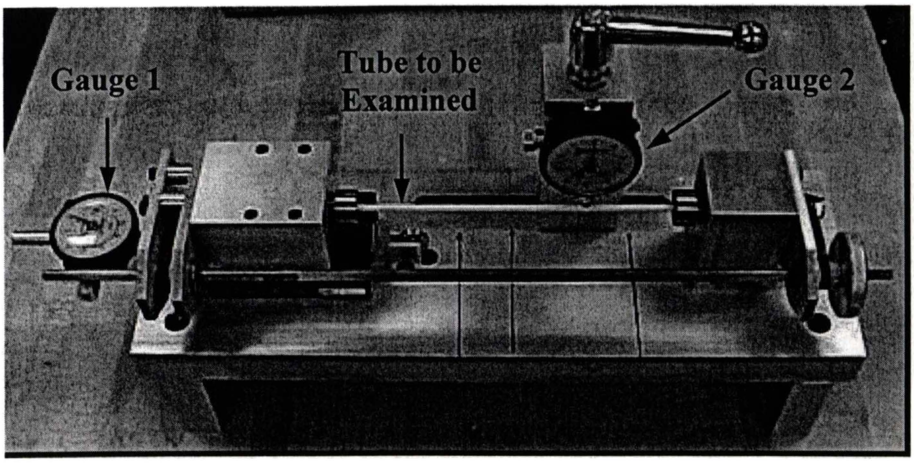

Figure 4-22 Device for Examining Sintered Tube Dimensions.

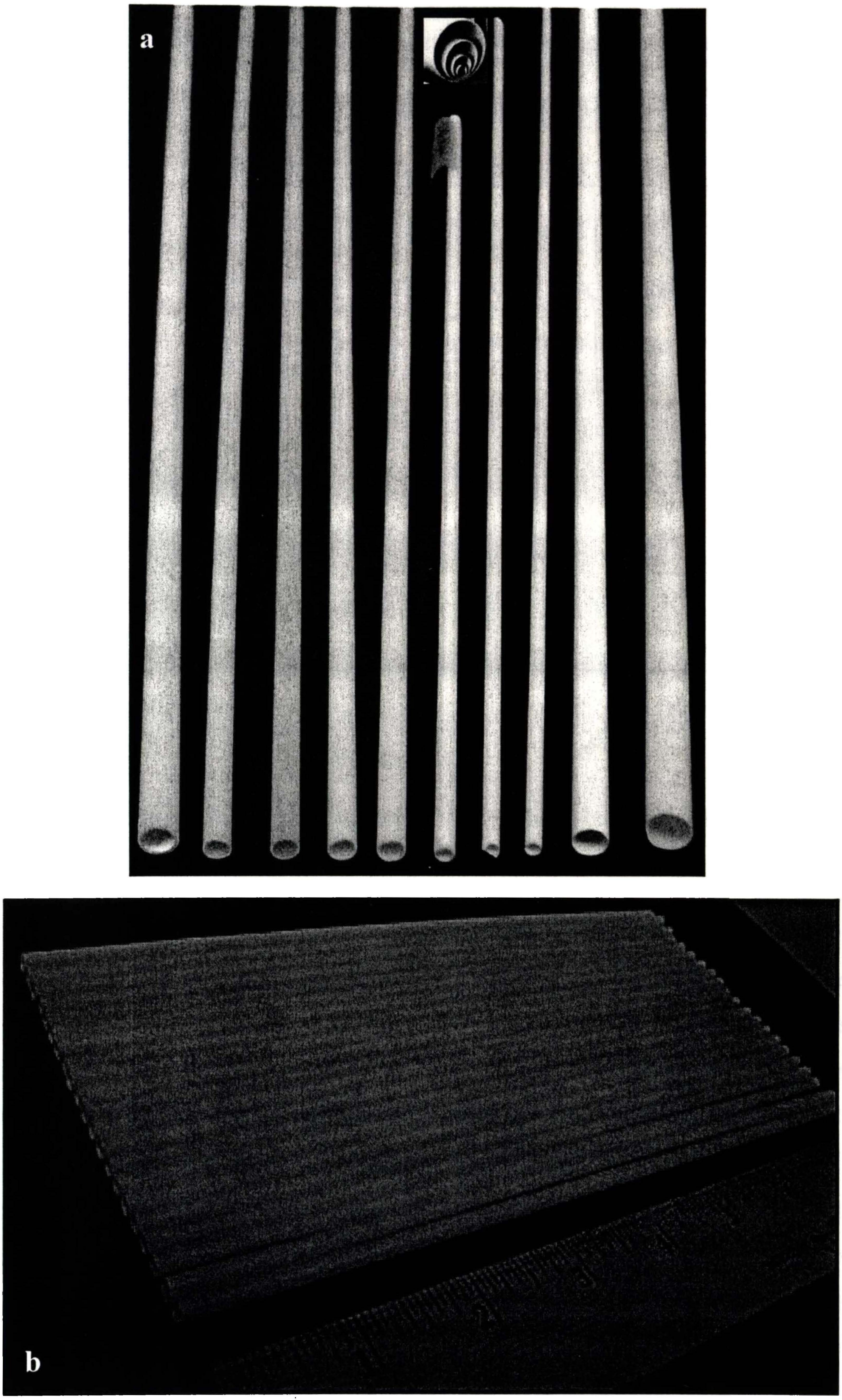

Figure 4-23 Sintered Tubes of (a) Varying Diameter and Thickness, (b) Fabricated from Optimised Process and Formulation.

Mechanical strength of the sintered tubes examined using the in-house designed burst tester, showed that the tubes were strong and had high burst strengths of 70-80 MPa (Figure 4-24).

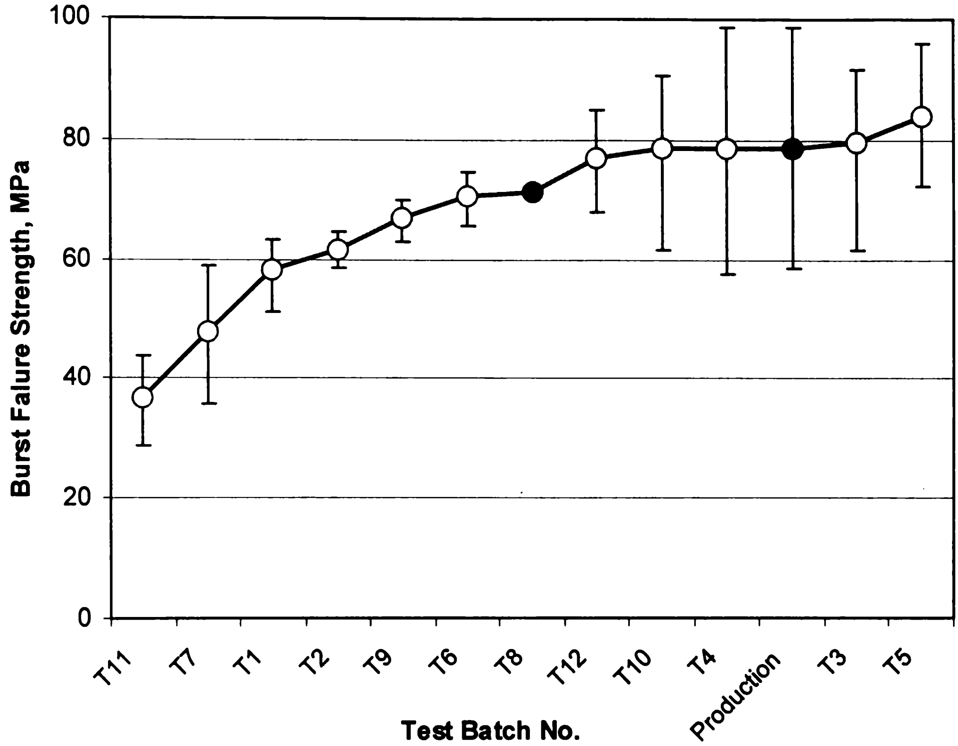

Figure 4-24 Burst Strength of Sintered YSZ Tubes Made from Various Test Batches and Production.

The microstructure and density of the sintered tubes (Figure 4-25) depended on how the green tubes were prepared. Tubes made from organic additives were dense and had a smooth surface. The tubes broke in a brittle manner as can be seen in sample YSZ7 in Figure 4-25a. Tubes made from water-based additives exhibited superior mechanical integrity, although SEM micrographs showed micro-pores approximately 1 μm diameter (sample YSZ9 in Figure 4-24b). In both cases, approximately 5-10 μm diameter holes caused by inhomogeneity were detected (samples YSZ7 and YSZ10). The presence of porosity or porous regions in sintered ceramic objects may be a major strength-controlling defect. This microstructure can be improved by using optimally prepared paste to give dense cross-section and smooth surface sintered tubes (Figure 4-24d and f).

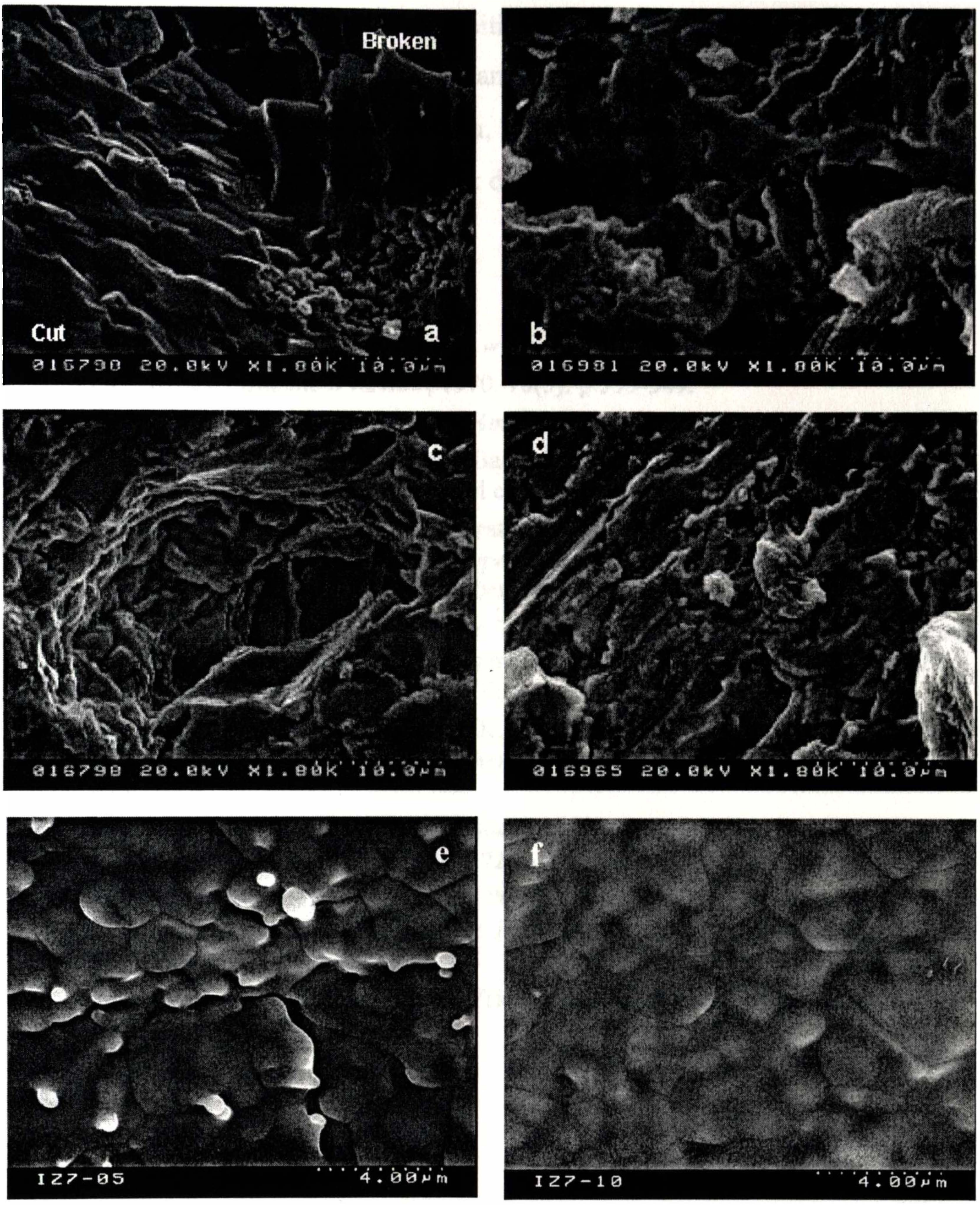

Figure 4-25 SEM Micrographs of Sintered Tubes: (a) YSZ7; (b) YSZ9; (c) YSZ10; and (d) YSZ12; (e) and (f) Tube Surface.

4.4 Summary

Procedures were developed to extrude dense, smooth, straight, round and thin walled tubular YSZ electrolytes from pastes with water-based or organic additives. The success rate for producing well-shaped tubes was greater with water-based additives. Particle size distribution played an important role in achieving extrudable pastes and thus even-shaped tubes. The microstructure of the sintered tubes exhibited a well-sintered body with micro-pores. Holes in the sintered objects, caused by inhomogeneities in the dough, could be removed by optimising extrudate formulation and manufacturing procedures. The thin walled YSZ electrolyte tubes (wall 150-350 μm, 2-6 mm OD, up to 300 mm long) have been used in micro tubular fuel cell stack development.

4.5 References

1. Etsell, T.H. and Flengas, S.N., "The electrical properties of solid oxide electrolytes," *Chemical Review*, 1970. **70**(3): p.339-349.
2. Minh, N.Q., "Ceramic fuel cell," *J. Am. Ceram. Soc.*, 1993. **76**: p.563-588.
3. Ciacchi, F.T., Crane, K.M. and Badwal, S.P.S., "Evaluation of commercial zirconia powders for solid oxide fuel cell." *Solid State Ionics*, 1994. **73**: p.49-61.
4. Kendall, K. and Prica, M., "Integrated SOFC tubular system for small scale cogeneration," in *Proc. First European Solid Oxide Fuel Cell Forum*, ed. U. Bossel, Lucerne, Switzerland, 3-7. Oct. 1994, p.163.
5. Winkler, W., Krüger, J., Sax, M. and Telle, R., "Development and manufacturing of a tubular SOFC combustion system," in *Proc. 3rd European Solid Oxide Fuel Cell Forum*, ed. P. Stevens, Nantes, France, 2-5, June, 1998, p.245-254.
6. Prica, M., Alston, T. and Kendall, K., "Mechanical and thermal properties of a 200 tube SOFC reactor." *Electrochemical Proceedings*, **V97**-18, 1997, p. 619-625.
7. Chevalier, L., Hammond, E. and Poitou, A. "Extrusion of TiO2 ceramic powder paste." *J. Mater. Proc. Tech.*, 1997. **72:** p.243-248.
8. Sproson, D.W. and Messing, G.L., "Organic removal processes in closed pore powder-binder systems." in *Ceramic Transactions*, ed. G.L. Messing, E.R. Fuller, & H. Hausner, **V1**, 1988, p. 528-548.

9 Terpstra, R.A., Pex, P.P.A.C. and Vries A.H., *Ceramic Processing*, Chapman & Hall, London. 1995, p. 174-190.

Chapter Five

Synthesising and Fabricating Strontium- and Magnesium-Doped $LaGaO_3$ Tubular Electrolytes*

5.1 Introduction

This Chapter focuses on synthesizing single-phase LSGM materials, identifying the boundary of the single-phase region, and using the LSGM to fabricate tubular electrolytes for SOFCs. The mechanical strength and the microstructure of the sintered products were also examined to better understand the extruded materials and compare them with the studies where the samples were formed by non-extrusion methods.

5.2 Materials and Experimental Procedure

Details of the raw materials used to synthesize LSGM are given in Section 3.1.1. The procedure to synthesize LSGM materials using solid-state methods was described in Section 3.1.2. The sintered discs were then ground using an alumina mortar and pestle, and then milled in a polyethylene container with acetone and 10 mm diameter zirconia grinding media to obtain fine particle size powder. This wet ball milling process was found to be more efficient than dry ball milling which caused agglomeration and produced fewer submicron particles. The as-received coprecipitated powder was calcined at 800-1400°C and then milled for up to 72 h in order to modify the surface area and particle size. The effects of the calcination temperature and milling time on the particle size and specific surface area were studied. A particle charge detector (Mütek PCD 03) was used to determine the particle surface charge.

---

* Some data in this Chapter have been published in:

(1) Yanhai. Du and N.M. Sammes, *J. European Ceramic Society*, **21** (2001) 727-735.

(2) Yanhai Du and Nigel Sammes, in *Proceedings of the 4th European Solid Oxide Fuel Cell Forum*, Lucerne, Switzerland, p783-792, 2000.

(3) Yanhai Du and Nigel Sammes, in *Proceedings of the 6th Annual New Zealand Engineering and Technology Post-Graduate Student Conference*, Auckland, December, p189-194, 1999.

The basic process used to extrude LSGM tubes was similar to that used for YSZ tubes [1]. Because the morphology and surface properties of LSGM powder were very different from YSZ powder, the procedure and processing parameters were tailored for extruding LSGM. Powder was first mixed and ground with surfactants in solvent for 4-12 h in a roller mill. Binders and plasticizers were then added and the mixture was milled for a further 1-2 h. If required, additional solvent was added to maintain the slurry running after adding the binders, and to adjust the casting layer thickness for drying. The slurries were then dried in air by pouring them onto plastic or glass sheets. The mixture was removed from the sheets after most of the solvent had evaporated from the slurries. Pastes were produced through aging the mixture.

Tubes or rods were extruded from workable pastes using an extrusion die and a universal testing machine (Figure 3-5). A load was placed on the top of the piston causing it to move down at a speed of 3 mm/min, which in turn forced the paste through the die to form a tubular geometry. The loads needed for extrusion of the tubes varied from between 5 kN to 10 kN depending on the flexibility of the dough. The effects of sintering temperature (1450°C-1520°C) and dwell time (2-72 h) on the microstructure of the sintered products were examined. Mechanical strength and microstructure of the sintered products were determined using the techniques described in Section 3.3.3 and 3.3.4.

5.3 Results and Discussion

5.3.1 Synthesising LSGM Powder

Commercial $SrCO_3$ and Ga_2O_3 powders were dried at 110°C and La_2O_3 and MgO powders were calcined at 1500°C and 1000°C respectively to decompose any hydroxides and carbonates present. The XRD patterns of the powders after drying and calcining (Figure 5-1) indicate that calcined La_2O_3 and MgO were crystallized and $SrCO_3$ and Ga_2O_3 had amorphous content.

The LSGM is a complex system. Secondary phases such as La_2O_3, MgO, $La_4Ga_2O_9$, $La_3Ga_5O_{12}$, La_2SrO_x, $Sr_3Ga_2O_8$, $MgGa_2O_4$, $LaSrGa_3O_7$ and $LaSrGaO_4$ may coexist with the perovskite phase occurring in most of the dopant compositions [2-7]. The XRD patterns (Figure 5-2) of various compositions in

Table 5-1 shows that the single perovskite LSGM with orthorhombic structure existed in a narrow region (compositions 1010, 1015, 2015 and 2020) (Figure 5-3).

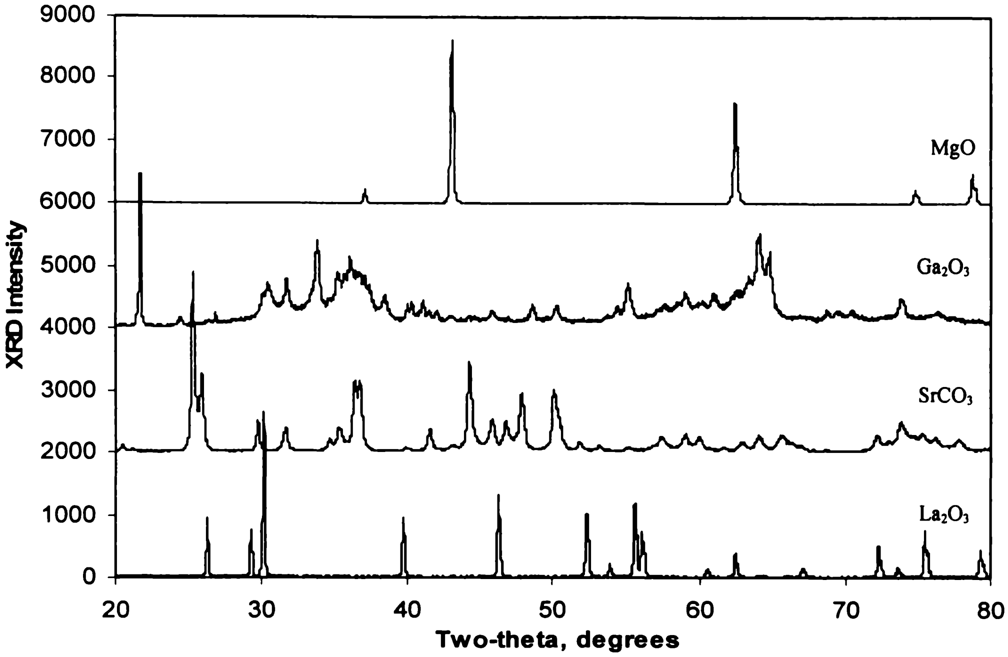

Figure 5-1 XRD Patterns of Chemicals Used to Synthesize LSGM.

Table 5-1 Compositions $La_{1-x}Sr_xGa_{1-y}Mg_yO_{3-(x+y)/2}$ Used for Investigating Phase Purity.

Sample label	A-site dopant, x mol%	B-site dopant, y mol%
1010	10	10
1015	10	15
1520	15	20
1525	15	25
2015	20	15
2020	20	20
2025	20	25
2520	25	20
2525	25	25

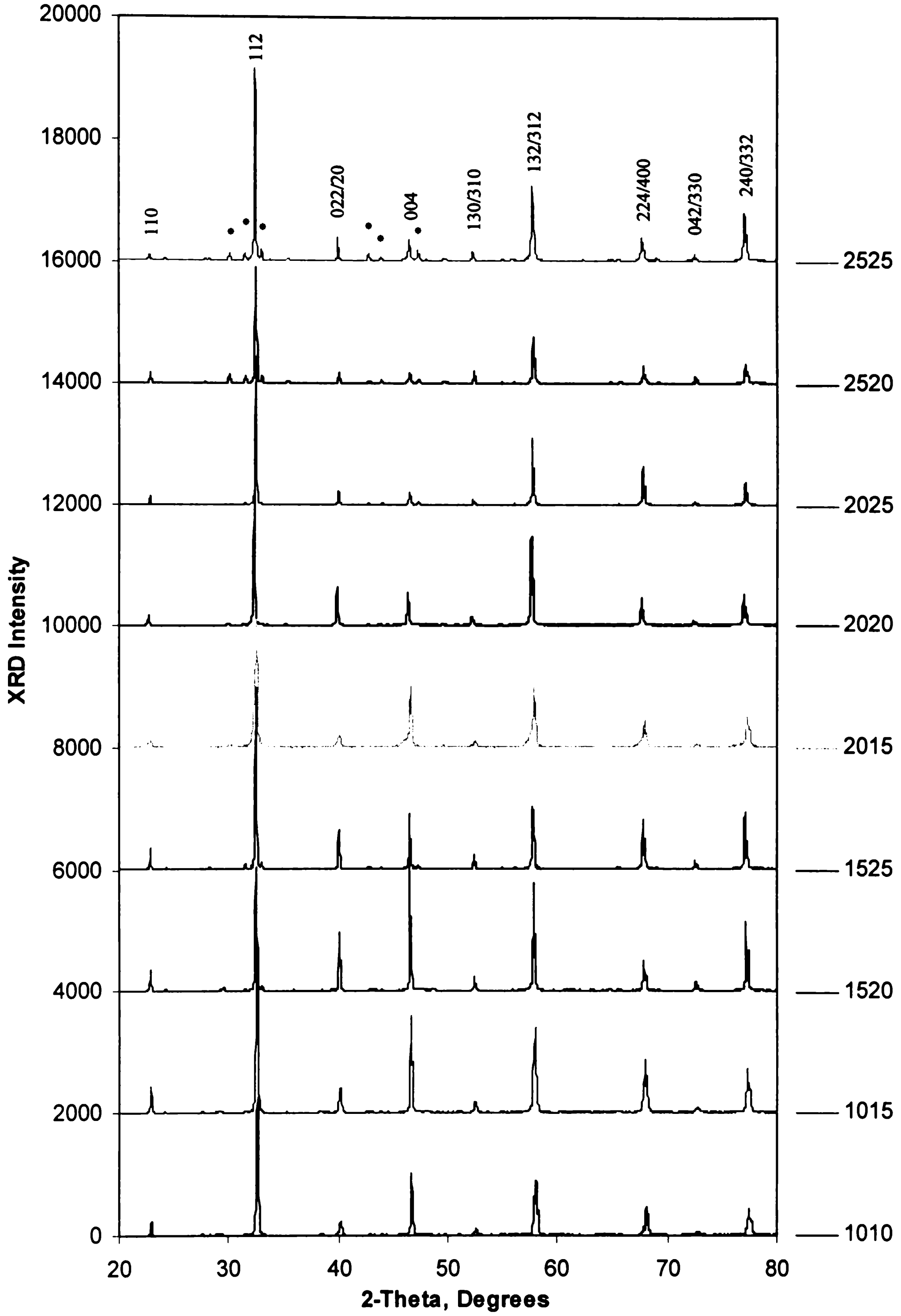

Figure 5-2 Effect of Various A-site and B-Site Dopant Concentrations on XRD Patterns of $La_{1-x}Sr_xGa_{1-y}Mg_yO_{3-(x+y)/2}$. The Perovskite Phase Peaks Are Indexed, (•) Indicates Secondary Phases.

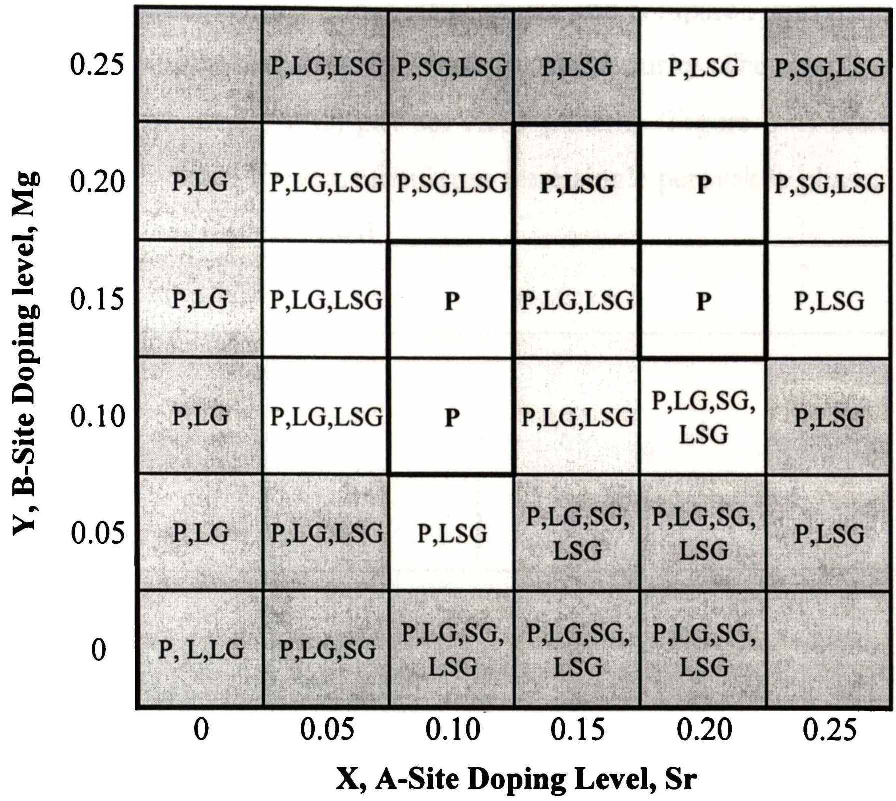

Y, B-Site Doping level, Mg

0.25		P,LG,LSG	P,SG,LSG	P,LSG	P,LSG	P,SG,LSG
0.20	P,LG	P,LG,LSG	P,SG,LSG	**P,LSG**	**P**	P,SG,LSG
0.15	P,LG	P,LG,LSG	**P**	P,LG,LSG	**P**	P,LSG
0.10	P,LG	P,LG,LSG	**P**	P,LG,LSG	P,LG,SG, LSG	P,LSG
0.05	P,LG	P,LG,LSG	P,LSG	P,LG,SG, LSG	P,LG,SG, LSG	P,LSG
0	P, L,LG	P,LG,SG	P,LG,SG, LSG	P,LG,SG, LSG	P,LG,SG, LSG	
	0	0.05	0.10	0.15	0.20	0.25

X, A-Site Doping Level, Sr

Figure 5-3 Phase Compositions of Sr- and Mg-Doped Lanthanum Gallates, $La_{1-x}Sr_xGa_{1-y}Mg_yO_{3-(x+y)/2}$.

Legend: P = Single Perovskite Phase;
L = La_2O_3;
LG = $La_4Ga_2O_9$;
SG = $Sr_3Ga_2O_8$;
LSG = $LaSrGa_3O_7$ and/or $LaSrGaO_4$.

Although composition 1520 exhibited high phase purity, which Mori *et al.* [7] claimed was a single phase, a trace impurity phase ($LaSrGaO_4$) existed in the sample examined. Composition 2520, which Huang *et al.* [2] described as a single phase, contained large amounts of secondary phases ($SrGa_2O_8$ and $LaSrGaO_4$). Huang *et al.* [2] identified the secondary phase $LaSrGa_3O_7$ in 2015 composition, and Mori *et al.* [7] reported $SrGa_2O_8$. However, the current research showed a single perovskite phase, which has good consistent agreement with the high conductivity (0.149 S/cm at 800°C [2]). Huang *et al.* [2] also reported that compositions 1510 and 1515 were in the single-phase region whilst Mori *et al.* [7] identified the secondary phases $La_4Ga_2O_9$ and $LaSrGa_3O_7$ in these compositions.

From the above examination, the composition $La_{0.8}Sr_{0.2}Ga_{0.8}Mg_{0.2}O_{2.8}$ was confirmed in the single-phase region with high conductivity of 0.14 S/cm at 800°C [2]. A large quantity of material with this composition was then obtained by coprecipitation technique from commercial source and compared with the solid-state reaction material obtained from this work for phase purity. The room temperature and high temperature (900°C) powder XRD patterns (Figure 5-4) indicated that the materials produced by both techniques were single perovskite phase, and were stable over the temperatures used.

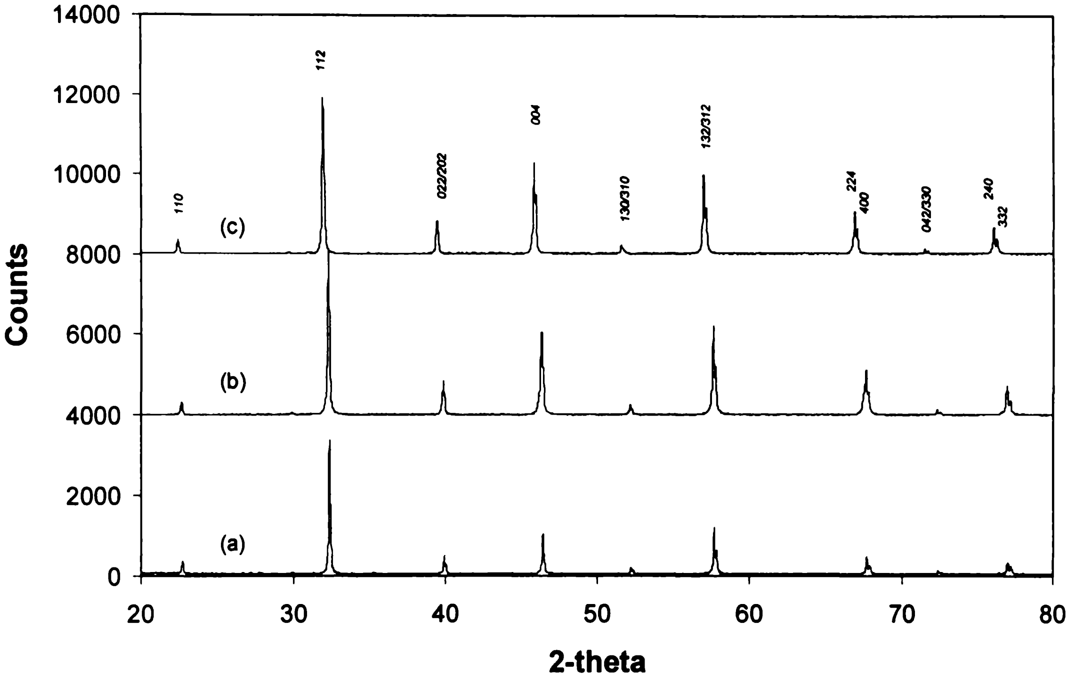

Figure 5-4 Room Temperature and High Temperature XRD Patterns of LSGM Synthesized by Solid-State Reaction and Coprecipitation Methods: (a) Co-Precipitated, Room Temperature; (b) Solid-State Reaction, Room Temperature; (c) Solid-State Reaction, 900°C. Peaks Are Labelled with Their (hkl) Indices.

5.3.2 Particle Size and Surface Area

Particle morphology and size play an important role in the ceramic extrusion process to achieve a dense material. The powder prepared by the coprecipitation technique consisted of loose and porous agglomerates with rough surfaces, which had high specific surface area and required a relatively large amount of solvent and binder for extrusion. SEM and BET data (Figure 5-5 and Figure 5-6) show that calcinating efficiently reduced particle surface area from 7.6 m^2/g to 0.3 m^2/g. Powders calcined at 1000°C and 1200°C had porous structures, but those fired at 1400°C densified. Compared with the uncalcined powder (Figure 5-5a) and the powders calcined at lower temperatures (Figure 5-5b, c), the powder fired at 1400°C (Figure 5-5d) required lower amounts of additives for extrusion to occur.

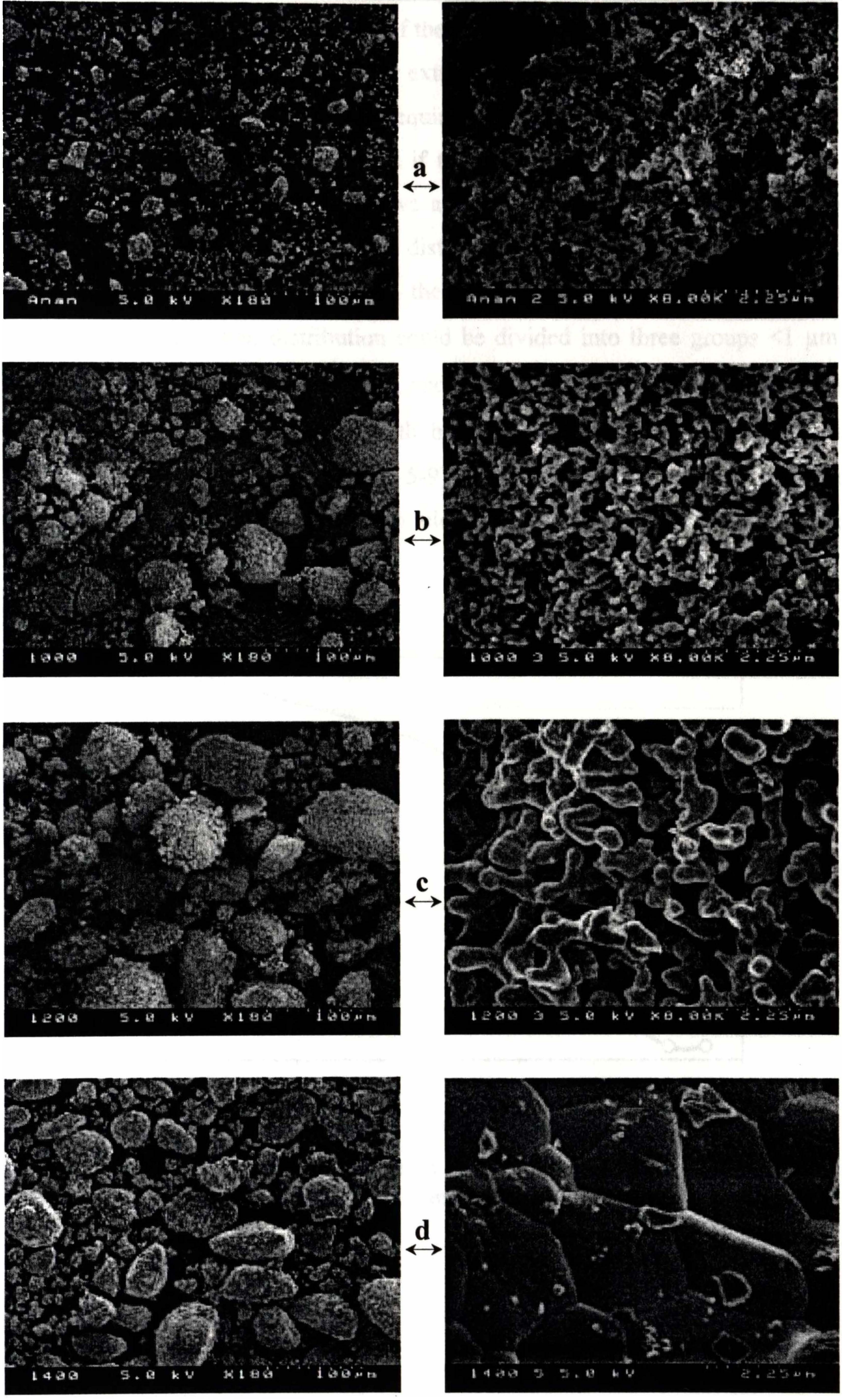

Figure 5-5 Micrographs of Coprecipitated Powder: (a) As-Received, and Calcined for 2 h at (b) 1000°C, (c) 1200°C, (d) 1400°C.

However, the maximum particle size of the calcined powders (Figure 5-7) was too large for these powders to be used for extruding the thin walled electrolyte tubes (sintered wall thickness 0.2-0.4 mm) required for this project. It is also difficult to obtain a smooth surface on the tubes if they are prepared from large particles. Moreover, in order to achieve effective and dense particle packing, the powder must have a certain particle size distribution. A favourable particle size distribution was achieved by milling the fired powders for up to 72 h. After milling, the particle size distribution could be divided into three groups <1 μm, 1~10 μm, and >10 μm (fine, medium, and coarse). The portion of large particles (>10 μm) decreased significantly with ball milling time (Figure 5-8) and the specific surface area increased (Figure 5-9). This indicated that a balance between the particle size and the surface area should be made in order to obtain a desirable extrudate.

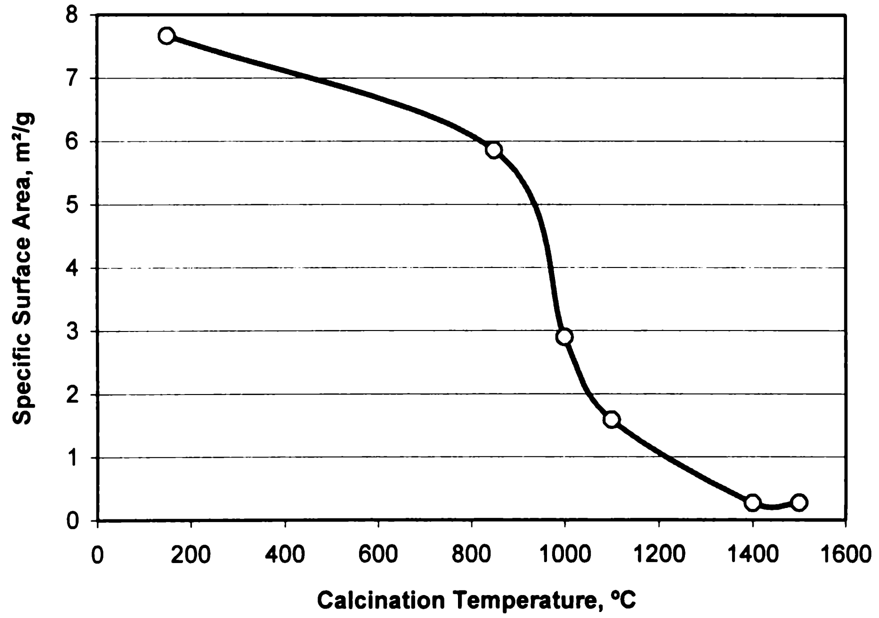

Figure 5-6 Specific Surface Area of the Powders after Calcination at Different Temperatures.

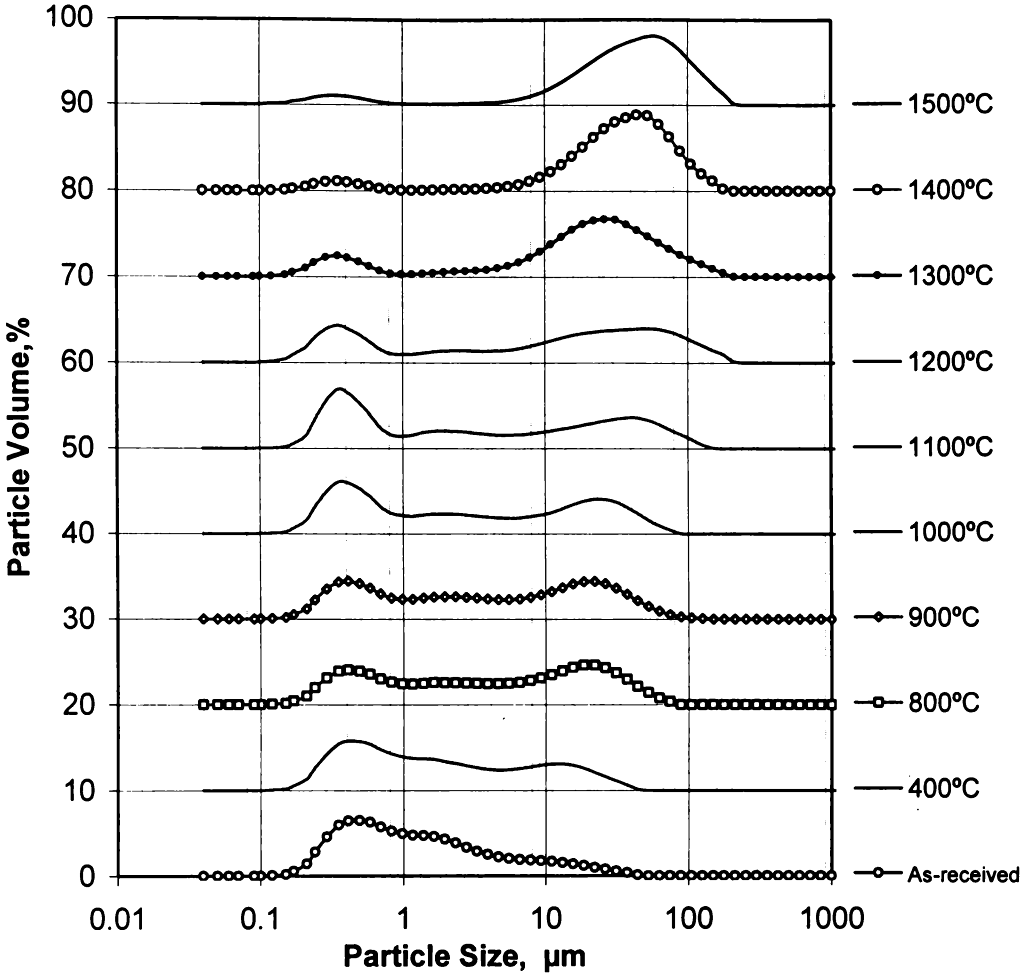

Figure 5-7 Particle Size Distribution of the Powders Calcined for 2 h at Different Temperatures.

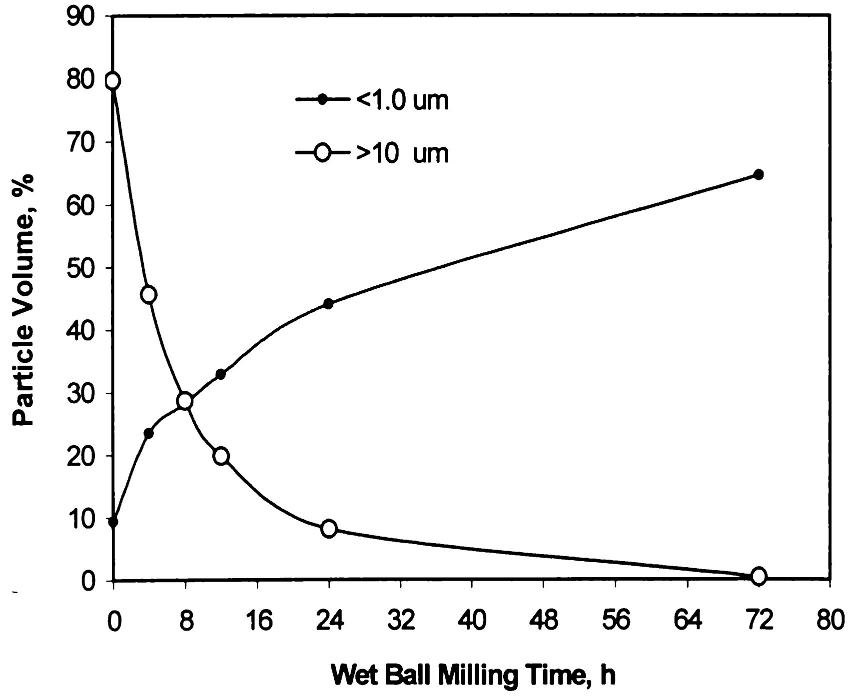

Figure 5-8 Effect of Wet Ball Milling Time on Particle Size Distribution of Calcined Powder.

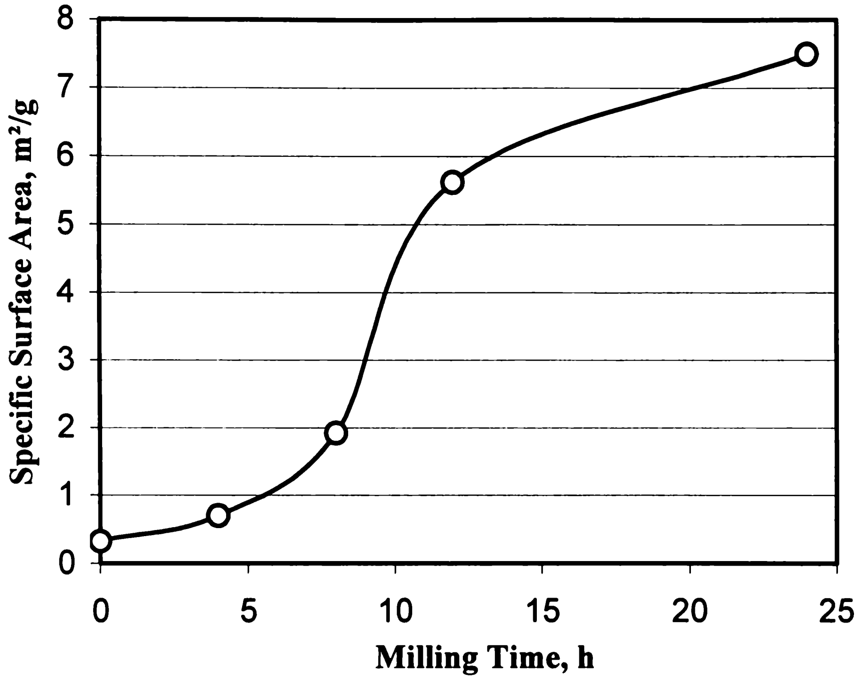

Figure 5-9 Effect of Wet Ball Milling Time on Specific Surface Area of the Calcined Powder.

5.3.3 Selecting Binders and Preparing Extrudable Pastes

Additives such as binder, lubricant, plasticizer, dispersant, and solvent are used to increase extrudability of ceramic powders. Two systems of additives, namely organic based systems and water-based systems, were studied. Organic binder PVB that dissolves in acetone but not in water due to its non-polar and non-ionic nature, surfactant PS-3 and plasticizer octanol-1 worked well with the LSGM powders. The amount of octanol-1 influenced the paste and extrudate workability. Excess plasticizer produced tacky products, which did not remain straight after extrusion. However, if there was too little plasticizer, cracks appeared during drying and sintering.

B1051 and B1052 are ceramic extrusion binders and soluble in both acetone and water. The B1051/B1052 system with plasticizer PEG-400 and surfactant/pH control agent AMP-95 was suitable for powder synthesised by solid-state technique. However, coagulation and flocculation occurred when this system was added to co-precipitated powder (Figure 5-10). It was postulated that large differences in surface charges being (1.5-2)$\times 10^{-6}$ eg/g for coprecipitation and

0.08×10^{-6} eg/g for solid-state prepared powder caused the coagulation and flocculation. The high positive surface charge on the co-precipitated powder easily attracts uncharged or negatively charged particles causing coagulation.

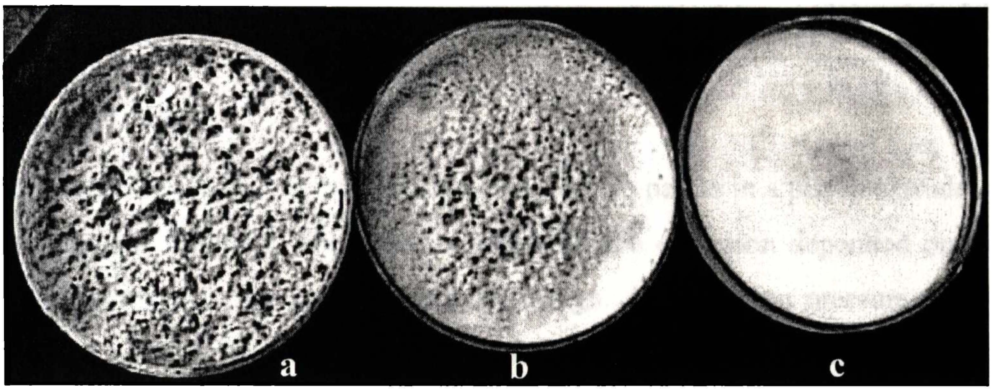

Figure 5-10 Appearances of LSGM Slurries with B1051/B1052 Binders: (a) and (b) Coagulation and Flocculation for Co-Precipitated Powder, (c) Suspension for Solid-State Powder.

The amount of solvents and plasticizers was altered to adjust slurry flowability and paste workability using characteristics and specific surface areas of the powders (Table 5-2). Solvent content varied during the processing as shown in Figure 5-11. Desirable slurries contained 100-120% solvent, while workable pastes required 3-5% solvent for extruding based on the dry powder weight.

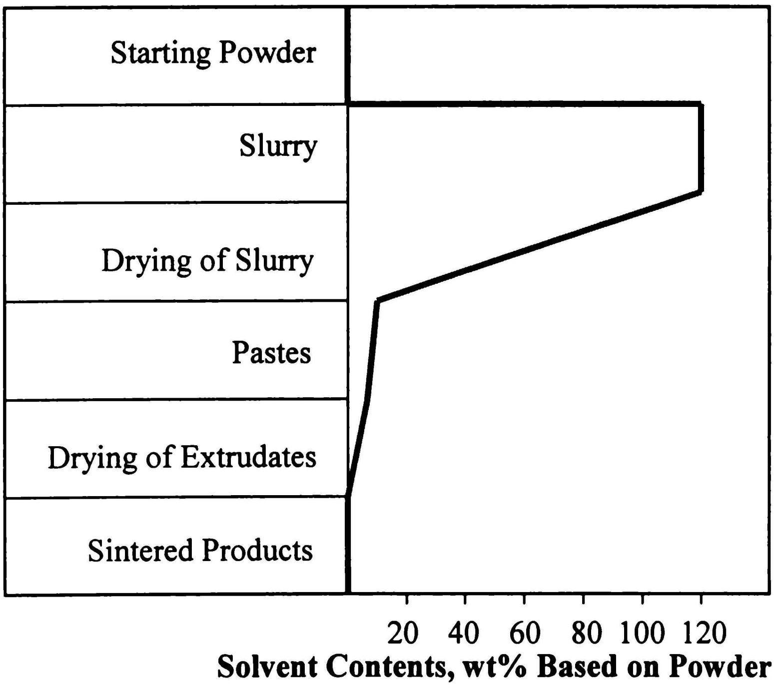

Figure 5-11 Solvent Content Variation During the Processing.

Table 5-2 Formulations (wt% based on powder) for Preparing LSGM Pastes.

System	Binders	Solvent	Surfactant	Plasticizers
Water based	B1051: 8.3 B1052: 4.6	Acetone: 110-170 Water: 0-20	AMP-95: 0-1.8	PEG-400: 6.6
Organic based	PVB: 6-8	Acetone: 100-120	KD1: 2-5	Octanol-1: 1.5-6

5.3.4 Extrusion

LSGM tubes were formed by extruding the flexible pastes in a piston extruder at a constant of 3 mm/min. The loads required for the extrusion depended on paste flexibility, extrusion speed, and extruder design. An extrusion pressure of 15-30 MPa was calculated according to the extrusion load recorded. Micrographs of the green tubes (Figure 5-12) indicated that voids could form at the extrusion stage if pastes are not deaerated and/or compaction pressure is low. Some of these pores remained in the sintered products. Glass tubes with an appropriate diameter were used to catch the green tubes during extrusion. 200-300 mm long green tubes could be fabricated (Figure 5-13).

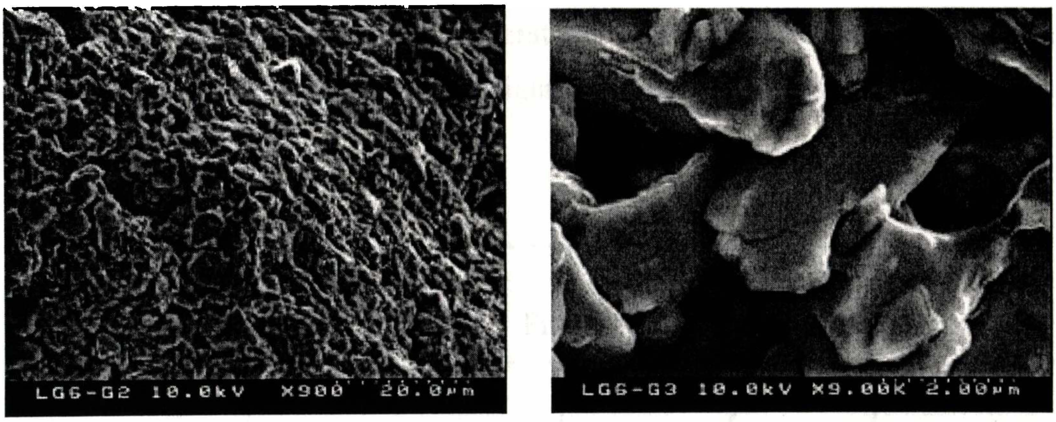

Figure 5-12 Micrographs of LSGM Extrudates: (a) Extruded Surface and (b) Internal Fracture Surface.

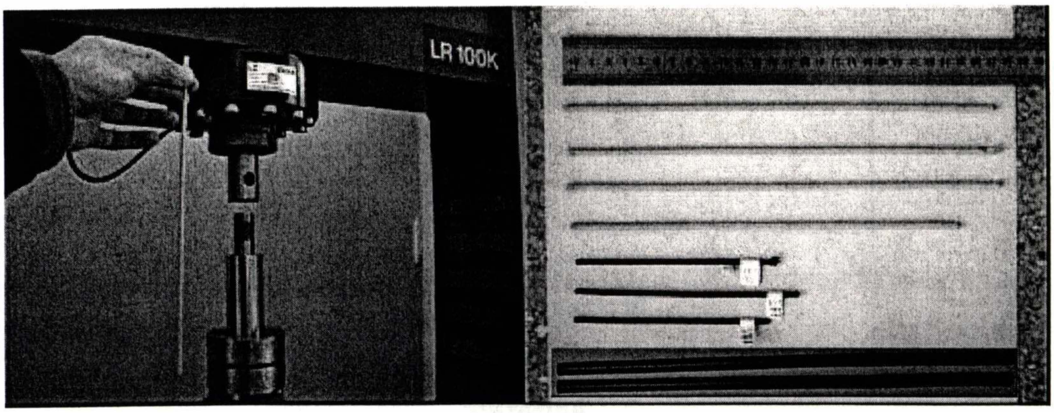

Figure 5-13 Green and Sintered (dark) LSGM Tubular Electrolytes.

5.3.5 Drying and Sintering

Drying is undertaken to remove the liquid from the green products. Controlling temperature and moisture during drying helps avoid cracks from developing by differential shrinkage during and after the solvent has evaporated from the green body. To keep the tubes straight and to control the moisture content, the green tubes were stored in plastic holders immediately after extrusion. The holder with tube in it could be slowly rolled manually or on a roller to maintain the tubular geometry. Tubes fabricated from suitable pastes were dried at room temperature overnight and then at 40-100°C for 4-12 h. The dried body had no visible cracks and could then be sintered.

Solid-state sintering was carried out in order to densify the extruded LSGM products. A slow ramp of 1°C/min from room temperature to 500°C was undertaken to burn out the additives. The rapid heating rate (6°C/min) above 500°C allowed particle binding to occur. The effects of sintering temperature and dwell time are discussed in Section 5.3.7. In general, dense sintered bodies could be obtained at higher sintering temperatures and/or longer dwell times. Data obtained during drying and sintering (Figure5-14) indicate that sintering shrinkage was approximately 20%.

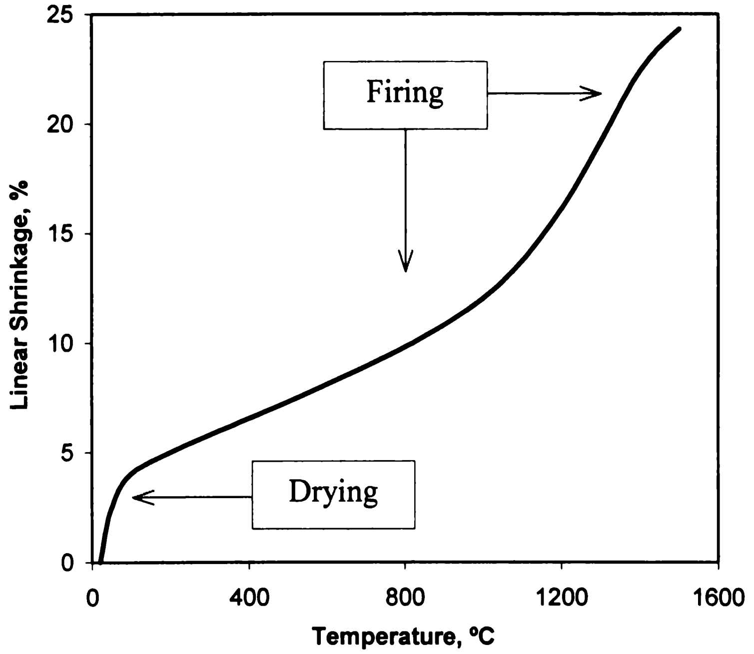

Figure 5-14 Linear Shrinkage of Extruded LSGM Tubes During Drying and Sintering.

5.3.6 Mechanical Properties of Sintered Products

Table 5-3 lists the three-point modulus of rupture (MOR) results of the LSGM materials prepared by extrusion (rods) and isostatic press (bars), together with the available reference data for comparison. The average MOR value for isostatic pressed samples were 147±20 MPa, which is slightly higher than reported in the literature [4]. The MOR value for extruded rods were 180±16 MPa at room temperature and 113±11 MPa at 800°C, indicating that mechanical strength improved when the LSGM rods were fabricated by extrusion. The wet ball milling process and binders are believed to have enhanced the binding strength of the grains after sintering.

Table 5-3 Modulus of Rupture of LSGM Materials Prepared by Extrusion and Isostatic Pressing.

Preparation Method	Test Temperature	MOR, MPa
Isostatic press	Ambient	147±20 113±8 [4]
	800°C	90 [3]
Extruded rods	Ambient	180±16
	800°C	113±11

The three-point data at room temperature were further analyzed using the Weibull distribution. The Weibull modulus, m, observed from the slope of the graph (Figure 5-15), was 16, which characterized that data spread was in a reliable range.

5.3.7 Microstructure of the Sintered Electrolyte

Micrographs of the sintered product (Figure 5-16) show that the LSGM material approached a dense sintered body when sintering temperature increased from 1400°C to 1520°C. Irregular or open pores became circular and intersected the grain boundaries. Grain growth reduced porosity that had formed during extrusion and after burning out the organic binders. Prolonging dwell time at 1500°C to over 36 h was not recommended because of the release of gallium from the system. The appearance of the sintered body had changed from a brown color (≤36 h) to black (72 h). The strength of the dark material significantly decreased because the ceramic bonds had been destroyed. This produced large pores at the grain boundaries (Figure 5-16h).

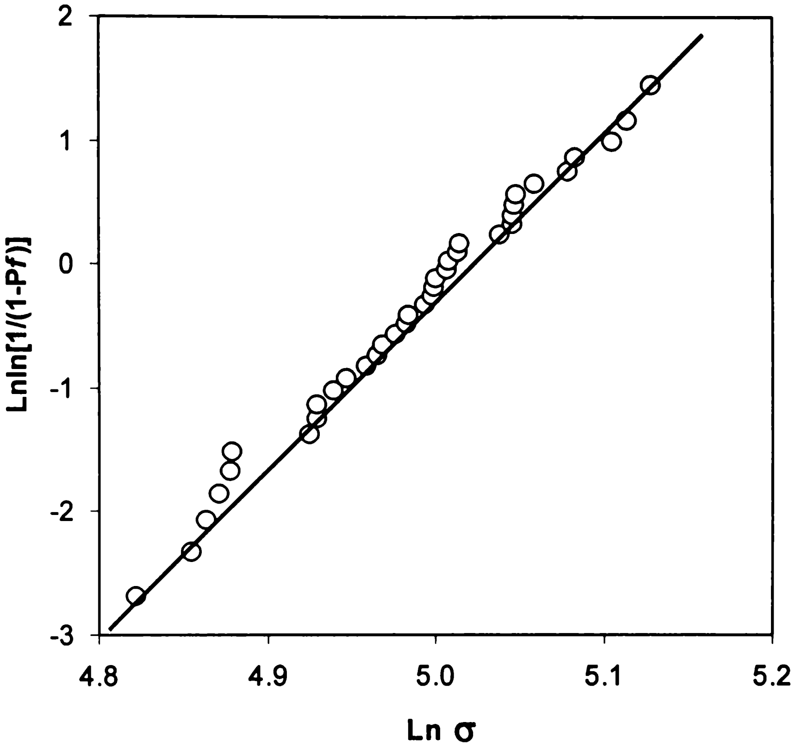

Figure 5-15 Weibull Plot of Data for Modulus of Rupture at Room Temperature for Extruded LSGM Material Sintered at 1500°C for 12 h.

The porosity in the sintered body could be grouped into two distributions by size or shape. The smaller, round micro-pores with a diameter of 1-3 μm primarily arose from the raw extruding powder. Irregular shaped voids were generally formed during the extrusion stage and after removing the solvents and organic substances from the extrudates.

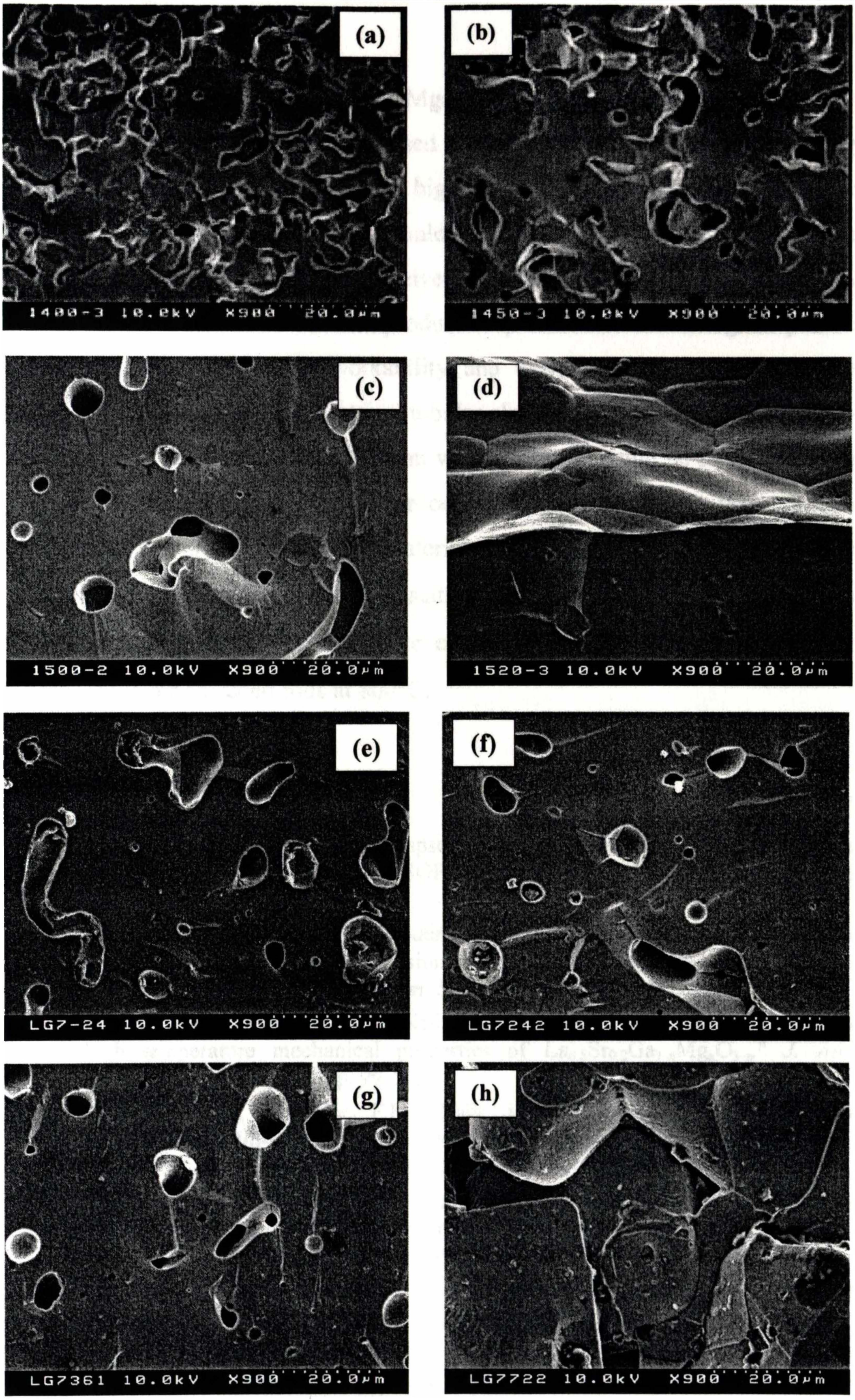

Figure 5-16 Effects of Sintering Temperature and Dwell Time on SEM Microstructures of the Extruded LSGM Tubular Electrolytes: (a) 12 h at 1400°C, (b) 12 h at 1450°C, (c) 12 h at 1500°C, (d) 12 h at 1520°C, (e) 2 h at 1500°C, (f) 24 h at 1500°C, (g) 36 h at 1500°C, (h) 72 h at 1500°C.

5.4 Summary

Single-phase perovskite $La_{0.8}Sr_{0.2}Ga_{0.8}Mg_{0.2}O_{3-\delta}$ material was synthesized using a solid-state reaction. A well-characterised powder is needed to increase reliability of the extrusion process. Powder with high density, low specific surface area and appropriate particle size distribution could be obtained by calcining at 1400°C and ball milling for 6-12 h the as-received coprecipitated LSGM powder. The microstructure of the final sintered products depended on controlling the process parameters, especially paste workability and extrudate sintering temperature. Long, straight, dense and symmetrical tubular electrolytes (200-300 mm long, 2.4-2.5 mm inside diameter and 0.3-0.4 mm wall thickness) could be fabricated using the optimised parameters and the procedure developed in this research. The modulus of rupture of the LSGM material produced by extrusion were greater than that for materials produced by isostatic pressing i.e. 147±20 MPa for isostatic pressed samples and 180±16 MPa for extruded rods at room temperature and 113±11 MPa for extruded rods at 800°C.

5.5 References

1. Du, Y., Sammes, N.M. and Tompsett, G.A., "Optimisation parameters for the extrusion of thin YSZ tubes for SOFC electrolytes." *J. Eur. Ceram. Soc.*, 2000. **20**(7): p. 959-965.
2. Huang, K., Tichy, R.S. and Goodenough, J.B., "Superior perovskite oxide-ion conductor; strontium- and magnesium-doped $LaGaO_3$: I, Phase relationships and electrical properties." *J. Am. Ceram. Soc.*, 1998. **81**(10): p. 2565-2575.
3. Sammes, N.M., Keppeler, F.M., Nafe, H., Aldinger, F. andTompsett, G.A., "The high temperature mechanical properties of $La_{0.8}Sr_{0.2}Ga_{1-x}Mg_xO_{3-z}$." *J. Aust. Ceram. Soc.*, 1998. **34**(1): p. 99-105.
4. Sammes, N.M., Keppeler, F.M., Nafe, H. and Aldinger, F., "Mechanical properties of solid-state-synthesized strontium- and magnesium-doped lanthanum gallate." *J. Am. Ceram. Soc.*, 1998. **81**(12): p. 3104-3108.
5. Baskaran, S., Lweinsohn, C.A., Chou, Y.S., Qian, M., Stevenson, J.W. and Armstrong, T.R., "Mechanical properties of alkaline earth-doped lanthanum gallate." *J. Mater. Sci.*, 1999. **34**: p. 3913-3922.
6. Djurado, E. and Labeau, M., "Second phases in doped lanthanum gallate perovskites." *J. Eur. Ceram. Soc.*, 1998. **18**: p. 1397-1404.
7. Mori, M., Sammes, N.M. and Tompsett, G.A., "Phase relationships of the doped lanthanum gallates by solid state reaction." in *5th Annual New Zealand Engineering and Technology Postgraduate Conference*. 1998. Palmerston North, New Zealand, p. 310.

Chapter Six

Mechanical and Thermal Properties of Tubular Solid Oxide Fuel Cells*

6.1 Introduction

Mechanical strength is one of the essential requirements for a support component in tubular SOFCs. It needs to be strong enough to allow handling during single cell and fuel cell stack fabrication. To successfully fabricate a multiple layer ceramic SOFC, it is desirable that the thermal expansion coefficients (TECs) of the SOFC components (anode, cathode, electrolyte, and current collector) match each other to avoid cracking during heating and cooling over the operating temperatures. Information on TECs of support components in tubular SOFCs is also essential for system design and materials selection. Thermal shock resistance is another concern for building a rapid heating ceramic system. The materials should withstand thermal cycling from room temperature to operating temperatures (600-900°C) with a rapid heating and cooling rate. Furthermore, for the tubular SOFCs, the temperature gradients along the tubes during operating conditions can be large and therefore create large stresses depending on the stack design [1, 2].

Sr- and Mg-doped $LaGaO_3$ (LSGM) and gadolinia-doped ceria (GDC) are alternatives to yttria-stabilized zirconia (8YSZ) because of their higher oxide-ion conductivity at comparative temperatures [3, 4]. In this chapter, the mechanical strength, thermal expansion and thermal shock resistance of the most important LSGM, YSZ and GDC electrolytes are characterized and compared. Mechanical

---

* Some data in this Chapter have been published as:

(1) Yanhai Du, N.M. Sammes, G.A. Tompsett, D. Zhang, J. Swan and M. Bowden, *J. Electrochemical Society*, **150** (1) A74-A78, 2003.

(2) Nigel M. Sammes and Yanhai Du, *J. Materials Science*, **38**, 1-6, 2003.

(3) Yanhai Du, N.M. Sammes, G.A. Tompsett, and M. Bowden, *7th International Symposium on Solid Oxide Fuel Cells (SOFC-VII)*, ed. S.C. Singhal and H. Tagawa, *Electrochemical Society Proceedings Volume 2001-16*, p.311-320, 2001.

strengths of anode supported tubular SOFCs at different processing stages were also evaluated. The data can help optimise electrolyte and electrode materials so they meet the electrical, mechanical and thermal requirements as support components of tubular SOFCs.

6.2 Experimental

The following specimens were made: $La_{0.8}Sr_{0.2}Ga_{0.8}Mg_{0.2}O_{2.8}$ (LSGM), $Ce_{0.8}Gd_{0.2}O_{1.9}$ (CGO), 8 mol% yttria stabilized zirconia (YSZ), NiO-YSZ (65:35 wt%) using techniques described in Chapter 4 and 5 [5, 6]. The final sintering regimes were: 1500°C for 2 h (YSZ), 1500°C for 12 h (LSGM), 1600°C for 6 h (CGO), and 700-1600°C for 2 h (NiO-YSZ anode).

The electrolyte tubes had an outside diameter of 3.0±0.2 mm and a wall thickness of 0.3±0.05 mm, and were 25±0.5 mm long (115 mm for burst test). The rods: had a diameter of 2.0±0.2 mm, and were 25±0.5 mm long. The anode tubes had an outside diameter of 5-10 mm, a wall thickness of 0.5-1 mm, and were 100-150 mm long. Figure 6-1 shows the appearance of the anode tubes fired at various temperatures. The unfired tube was grey from the white YSZ and black nickel oxide starting materials. With increasing firing temperatures, the tubes turned green and dark green because the Ni_2O_3 lost oxygen and formed green NiO.

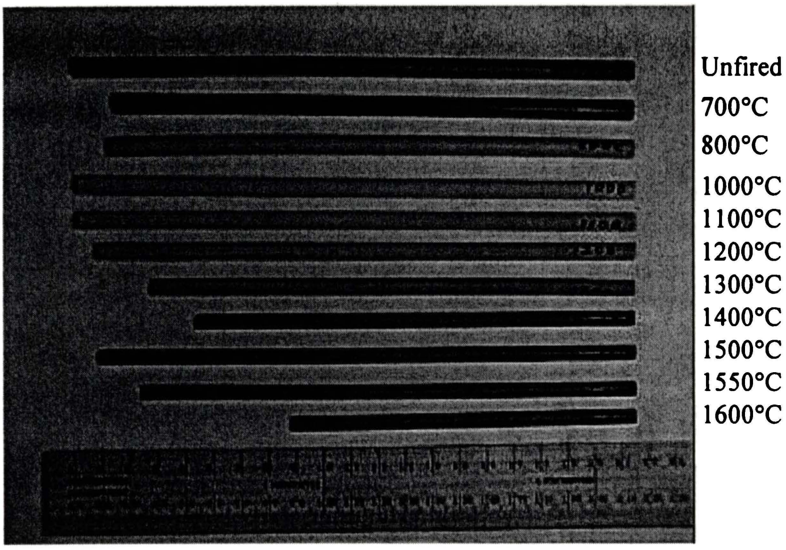

Figure 6-1 Photograph of NiO-YSZ Anode Tubes Fired at Various Temperatures.

Burst failure strengths were measured using the technique described in Section 3.3.3 and a unique device (Figure 6-2). The burst failure was calculated using Equation 3-6. Three-point bending strengths of electrolyte rods were done at room temperature, 600°C, 800°C and 1000°C in air, using a span of 8.34 mm and 0.2 mm/min crosshead speed. At least 10 samples were measured at each temperature.

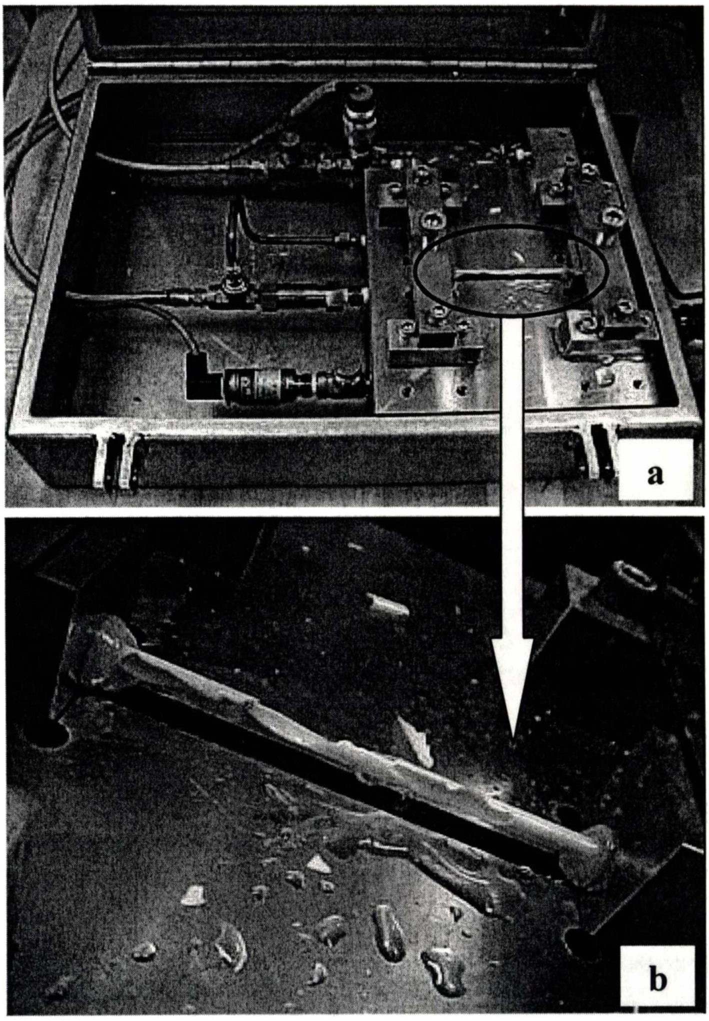

Figure 6-2 Burst Test Device (a) and YSZ Tube After Burst Test (b).

Thermal shock resistances of the electrolytes were determined by heating the samples to 800°C in a Tetlow furnace, keeping them at 800°C for 30 minutes and then quenching to room temperature (~25°C) in air or water. For air quenching, the samples were taken from the furnace and allowed to cool for 30 minutes in air to approximately 50°C. For water quenching, the samples were placed in 1 litre of water and cooled to approximately 50°C in 0.5 minutes. Quenched samples were then returned to the furnace for the next quench cycle. The temperatures of the air, water were recorded using a thermometer. Furnace temperature was read from the temperature gauge. The temperature profile of the samples and the furnace during the thermal shock resistance test is shown in Figure 6-3. The experimental set-up, and the samples before and after thermal quench test are shown in Figure 6-4. Thermal cycling between room temperature and 1300°C was conducted in a programmed furnace at 6°C/min ramp rate. Linear thermal expansion measurement was described in Section 3.3.6.

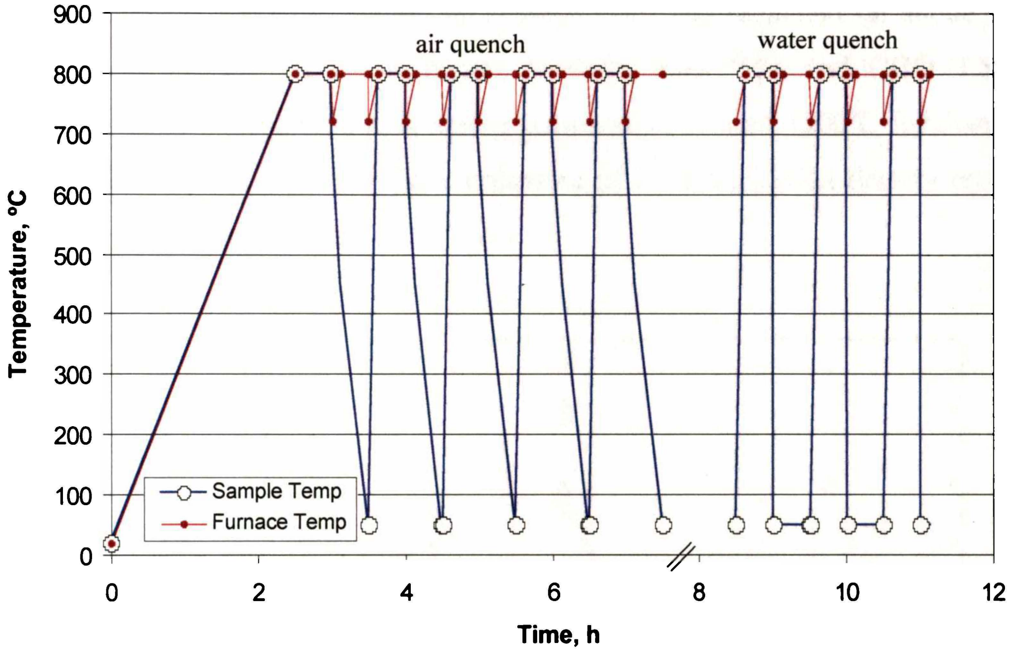

Figure 6-1 Illustration of the Temperatures the Samples and the Furnace Underwent During Thermal Shock Resistance Test.

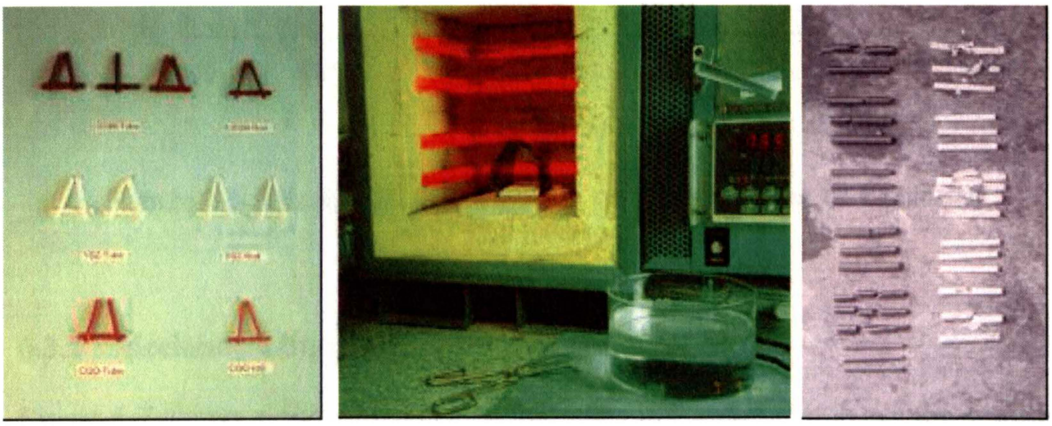

(a) (b) (c)

Figure 6-2 Photographs of Thermal Shock Test Set-up and Samples: (a) Samples before Test; (b) Thermal Shock Test Set-up; (c) Samples after Thermal Shock Test (20 Cycles Air Quench and 1 Cycle Water Quench from 800°C

6.3 Results and Discussion

6.3.1 Electrolyte Density

Electrolyte firing regimes were determined according to the effect of firing regimes on the densification (Figure 6-5) to ensure that the relative densities of the sintered body were greater than 97% of the theoretical value. Electrolytes sintered under these firing regimes have dense microstructures with micro-pores (Figure 6-6). Dense electrolytes have low oxygen ion transfer resistance, high mechanical strength and can separate oxidant (at cathode side) and reductant (at anode side) from direct contact. LSGM is harder to sinter than YSZ and CGO. LSGM densities reached maximum at sintering temperature around 1500°C for dwelling time of 6 hours. At the sintering temperature of 1500°C, LSGM density reached the highest for dwelling time of 12 hours.

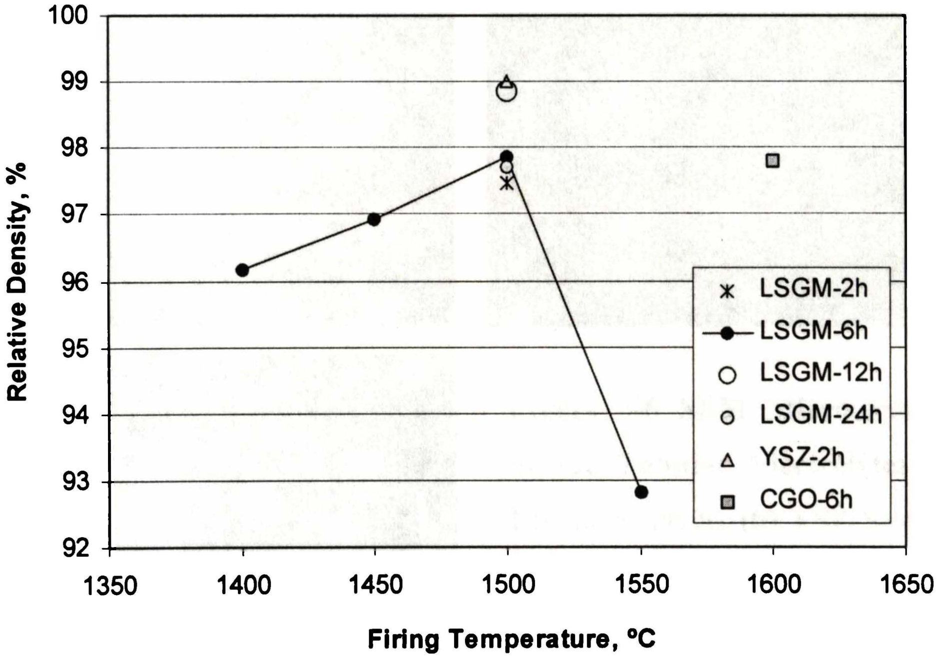

Figure 6-5 Effect of Firing Regimes on Densification of Extruded Electrolytes.

6.3.2 Mechanical Strength

Figure 6-7 shows a comparison of the modulus of rupture (MOR) of the extruded electrolyte materials (rods) tested at room temperature and at high temperature in air. In general, mechanical strength of the electrolyte materials (LSGM, CGO, YSZ) decreases as temperature increases. The LSGM electrolyte has a lower

MOR than CGO and YSZ at any given temperature. Above 800°C, the MOR of LSGM and CGO decrease rapidly, while the MOR of YSZ at 1000°C is greater than that at medium temperatures (600°C and 800°C). The latter trend for YSZ has also been reported by Minh [7] and Mori [8], however, the reason is not known.

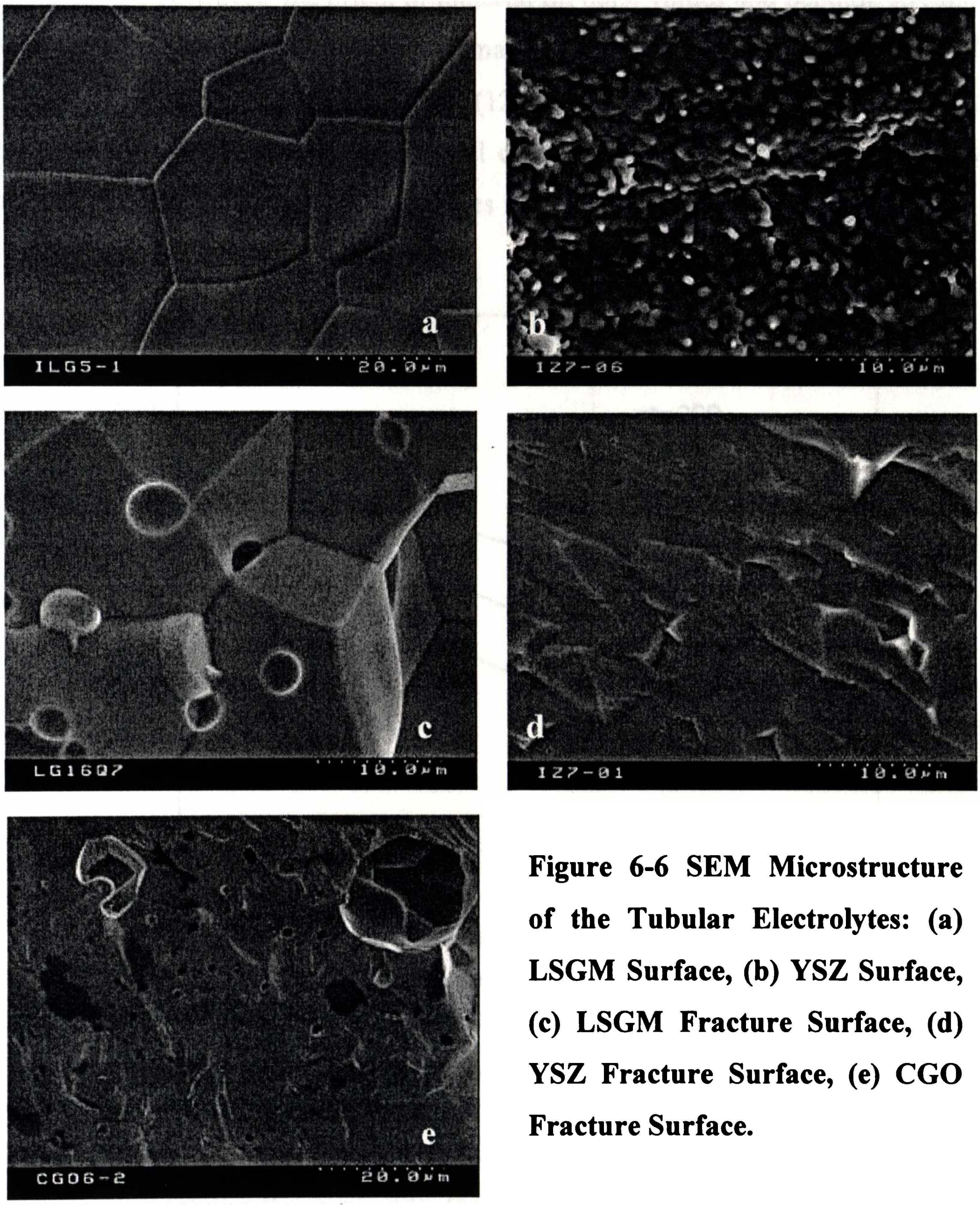

Figure 6-6 SEM Microstructure of the Tubular Electrolytes: (a) LSGM Surface, (b) YSZ Surface, (c) LSGM Fracture Surface, (d) YSZ Fracture Surface, (e) CGO Fracture Surface.

Burst test is an efficient way to detect the weakest point (i.e. includes both surface defects and body flaws) in the sample because the breaking pressure is distributed evenly over the whole tube. This is more important for thin walled ceramic tubes where it is difficult to obtain accurate results from the three-point bending test because the thin walls can crush easily. Table 6-1 gives the burst failure test results before and after thermal cycling, and MOR of the tubular electrolytes. The burst strength was much smaller than the bending strength of the extruded material. One possible factor for this differential is that three-point bending creates the maximum tensile stress on the middle of the surface of the specimen, between the bottom supports. If the defect is not located here, the strength appears to be higher. However, the effect of material on burst values and bending strength was similar, with LSGM having the smallest burst-strength (40 MPa) and YSZ having the greatest burst-strength (127 MPa). Both strengths decreased significantly (by 18-37%) after thermal cycling, indicating that thermal cycling may have caused microstructural changes in the materials, such as micro-cracks.

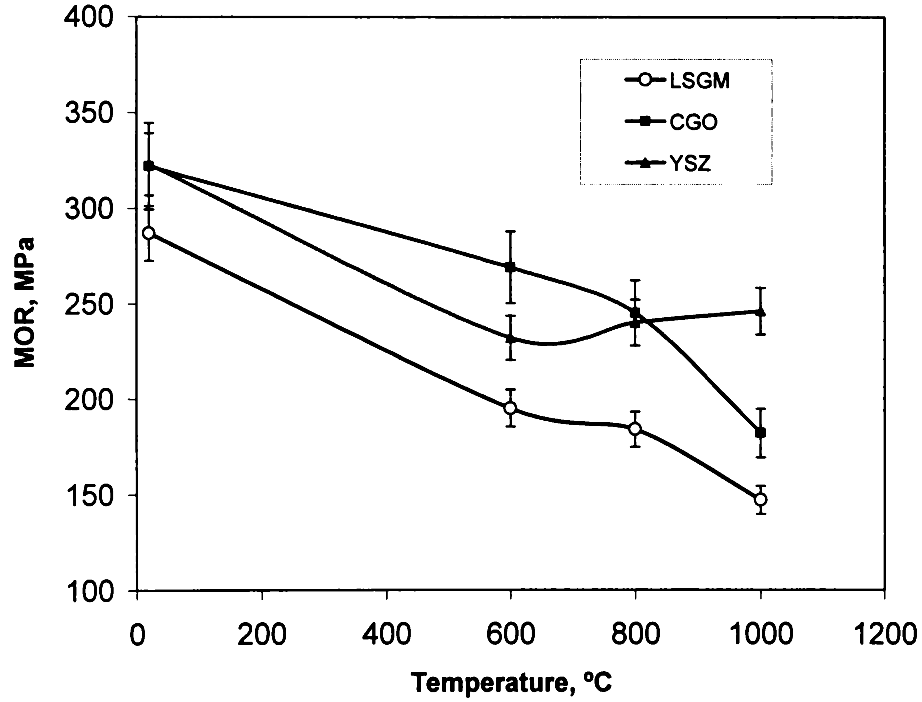

Figure 6-7 Modulus of Rupture of the Extruded LSGM, CGO, and YSZ Electrolyte Materials Tested at Room Temperature and High Temperatures.

Overall, LSGM has lower mechanical strength than either YSZ or CGO prepared in this research. In general, as the Hall-Petch relationship states that, for the same material, the smaller the grain size, the stronger the material will be (everything else being equal). In this work, the sintered materials had grain sizes of 10-20 μm (LSGM), 4-10 μm (CGO), and 1-5 μm (YSZ). However, no relationship between strength and grain size was observed between these materials, and thus the variation in strength is due to material factors and not solely to grain size differences.

Table 6-1 Burst Failure Stress and Three-Point Bending Strength of Extruded Tubular Electrolytes (Room Temperature).

	MOR (MPa)	Burst strength (MPa)	Burst strength (MPa) after thermal cycling between 1300°C and room temperature	
			22 times	30 times
LSGM	287	40	30	25
CGO	322	63		
YSZ	323	127	104	82

MOR of green and fired anode tubes (Figure 6-8) shows that the tubes were very weak at the temperature range of 200-1000°C because the green tubes lost binding strength after binder burnout and the ceramic bonding was not yet formed. The fired body shrunk 15% between 1100-1350°C indicating that material had been sintered. The shrinkage was accompanied by a significant increase in MOR. Considering the mechanical and porosity requirements, anode tube firing temperatures should be 1400-1500°C.

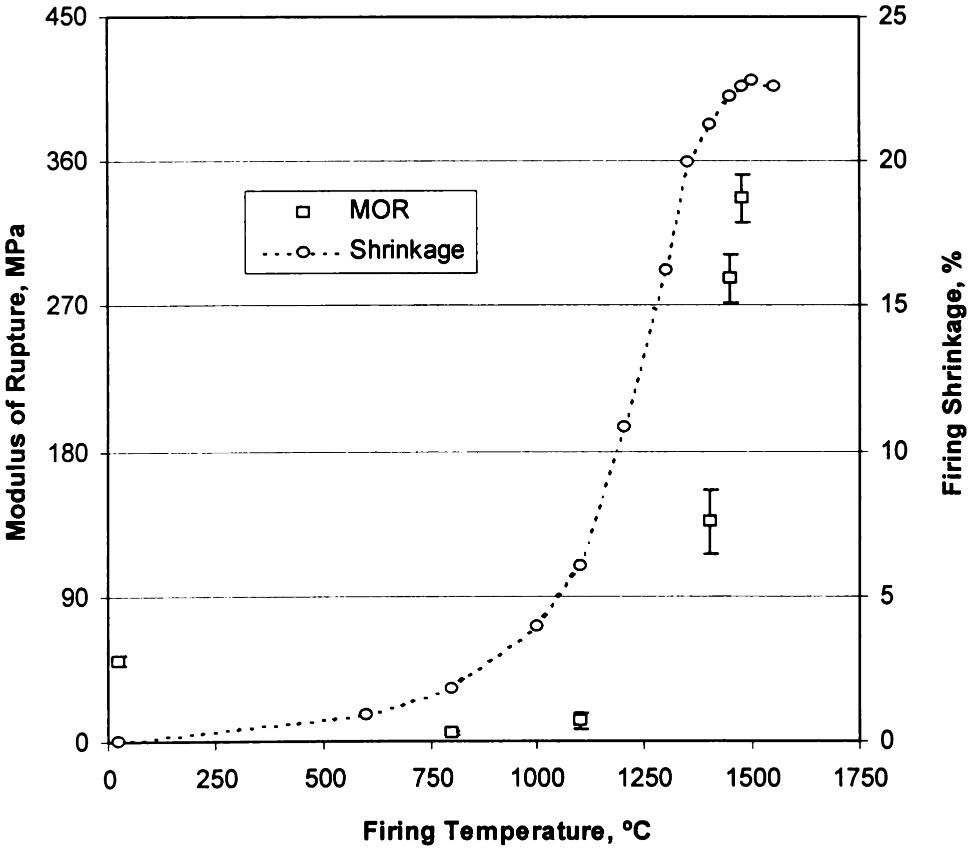

Figure 6-8 Effect of Firing Temperatures on MOR and Shrinkage of Anode Tubes.

The strength of the anode support at various process stages in fuel cell fabrication (Figure 6-9) indicated that green tubes were strong enough for handling, and sintered and reduced tubes had high strength (~300 MPa). However, the anode tubes sintered with YSZ coatings appeared to have lower strength, and this may be due to thermal stress from the YSZ thin film during sintering. From sintered state to reduction, the tubes lost approximately 14% of their mass, which occurred because NiO was reduced to Ni. However, the tube dimensions did not change. The reduced anode should be protected from re-oxidation as this will damage the anode structure and cause a big decrease in strength (Figure 6-10).

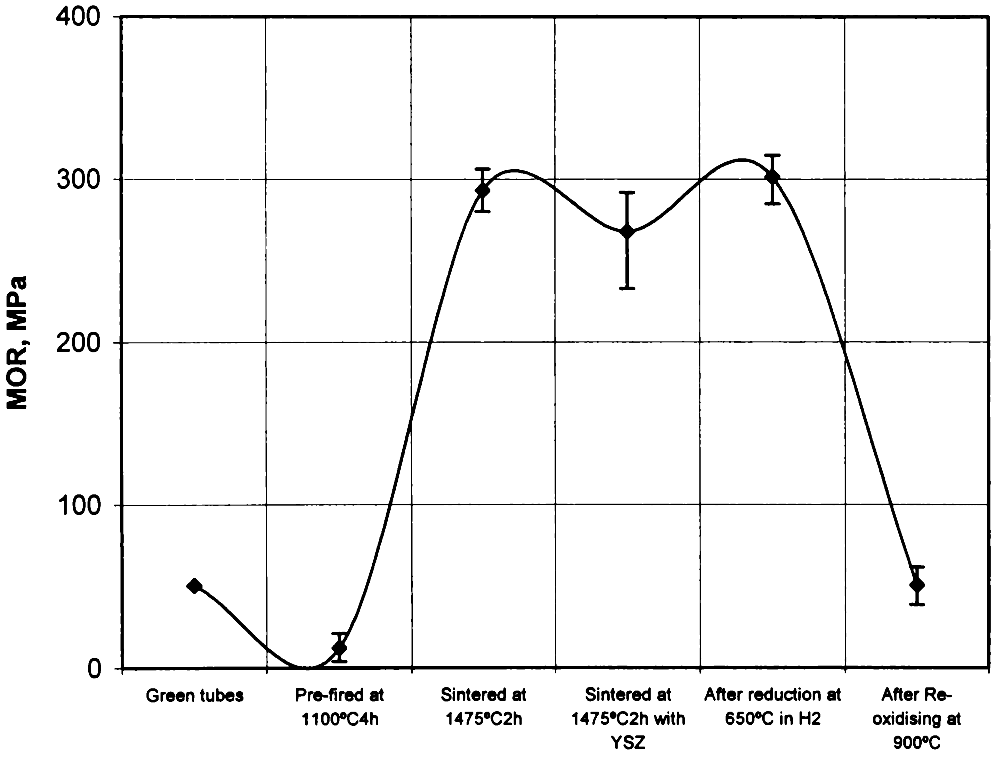

Figure 6-9 MOR of Anode Support at Different Process Stages of Fuel Cell Fabrication.

6.3.3 Thermal Expansion Coefficient

The linear thermal expansion of the electrolytes extruded from LSGM, CGO and YSZ materials increased in the order of YSZ<LSGM<CGO over the test temperature range 25-1000°C (Figure 6-11). The TECs of these materials calculated using Equation 3-7 are shown in Figure 6-12. The average TECs of LSGM are $10.45\times10^{-6}/^{\circ}C$, $11.01\times10^{-6}/^{\circ}C$ and $11.58\times10^{-6}/^{\circ}C$ at 25°C to 600°C, 800°C, and 1000°C respectively. These values are 5-10 % greater than that for

YSZ, but 5-10 % smaller than that for CGO at corresponding temperatures. The TECs of LSGM materials are in good agreement with the reported values 10.5-11.6×10^{-6}/°C (room temperature-1000°C) [8]. However, the phase transition from orthorhombic to rhombohedral for LSGM at 408°C reported by Hayashi *et al.*[9] was not detected from the TEC data. Matching the TEC values for SOFC components is critical; small differences between cell components (electrolyte, anode, cathode, and current collector) can produce large thermal stresses during single cell fabrication and fuel cell stack operation.

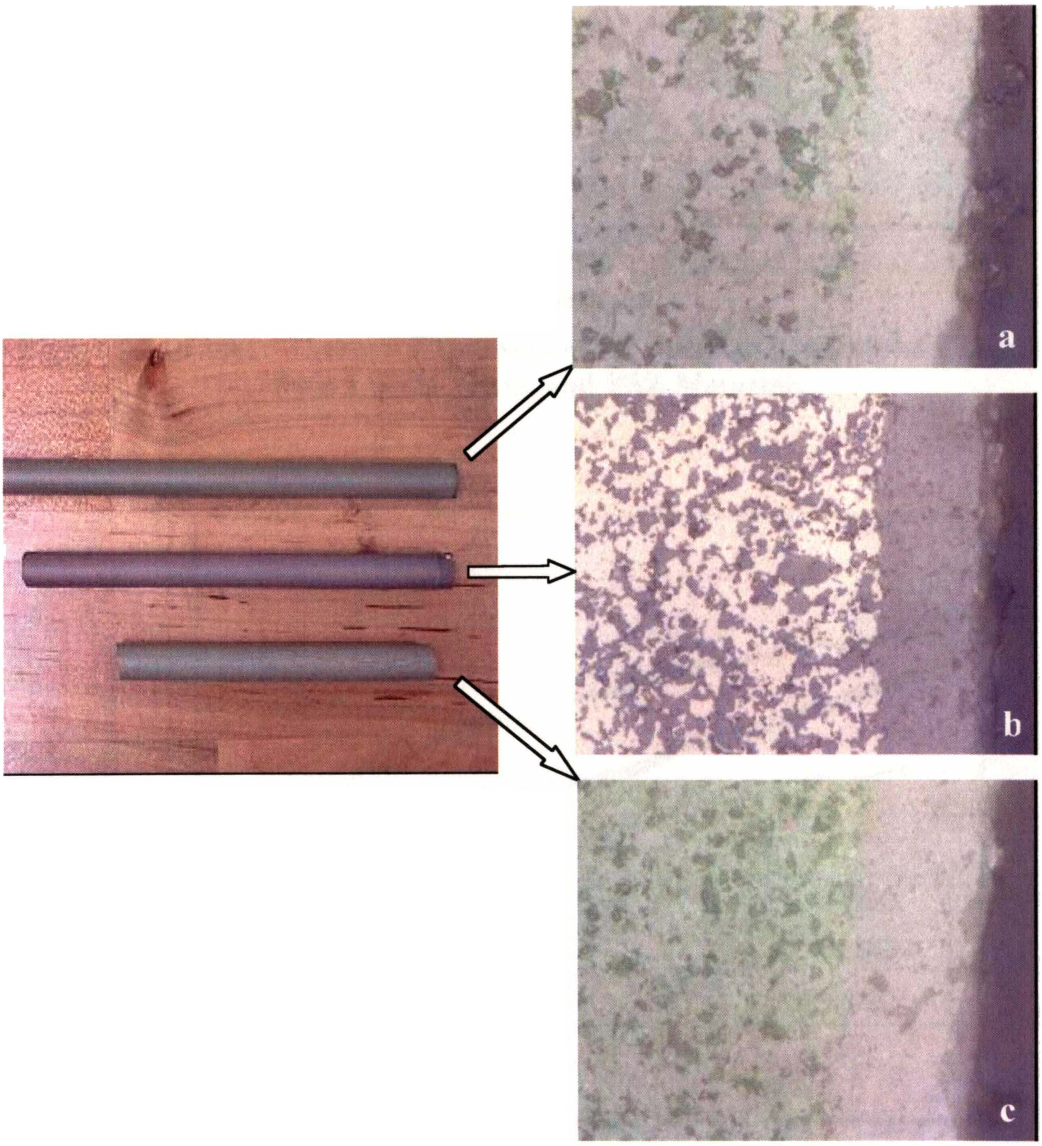

Figure 6-1 Photographs and Microstructure of Anode Support Tubes with YSZ Coating at Various Stages: (a) Sintered at 1475°C for 2 h; (b) Reduced at 650°C in H_2; (c) Re-Oxidized at 900°C.

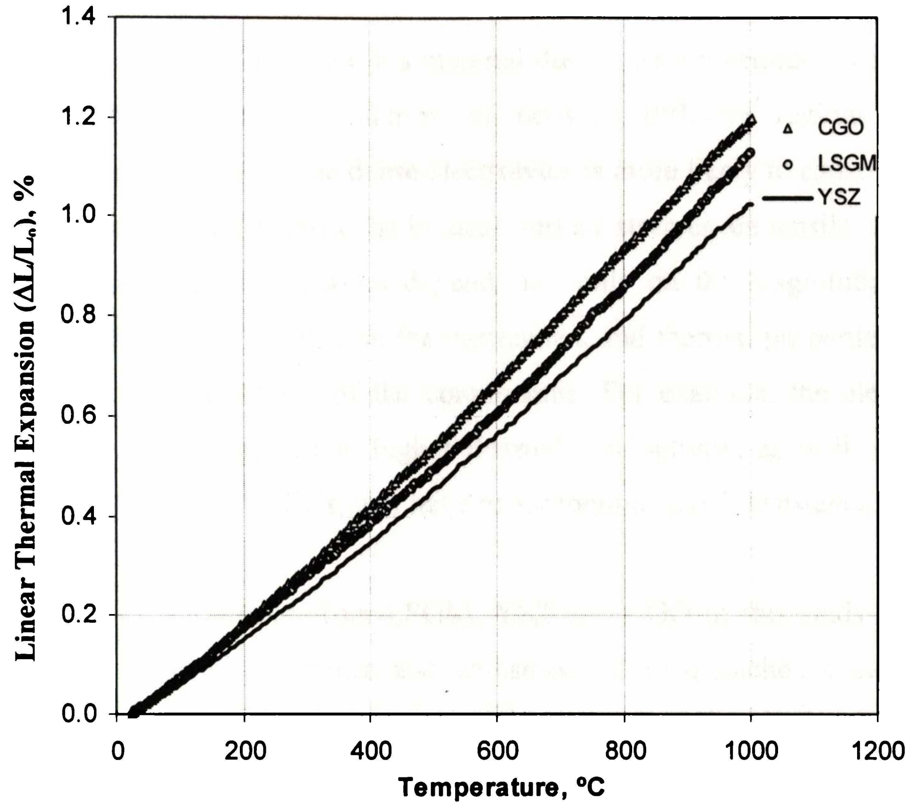

Figure 6-11 Linear Thermal Expansion of the Tubular Electrolytes Extruded from LSGM, CGO, and YSZ Materials.

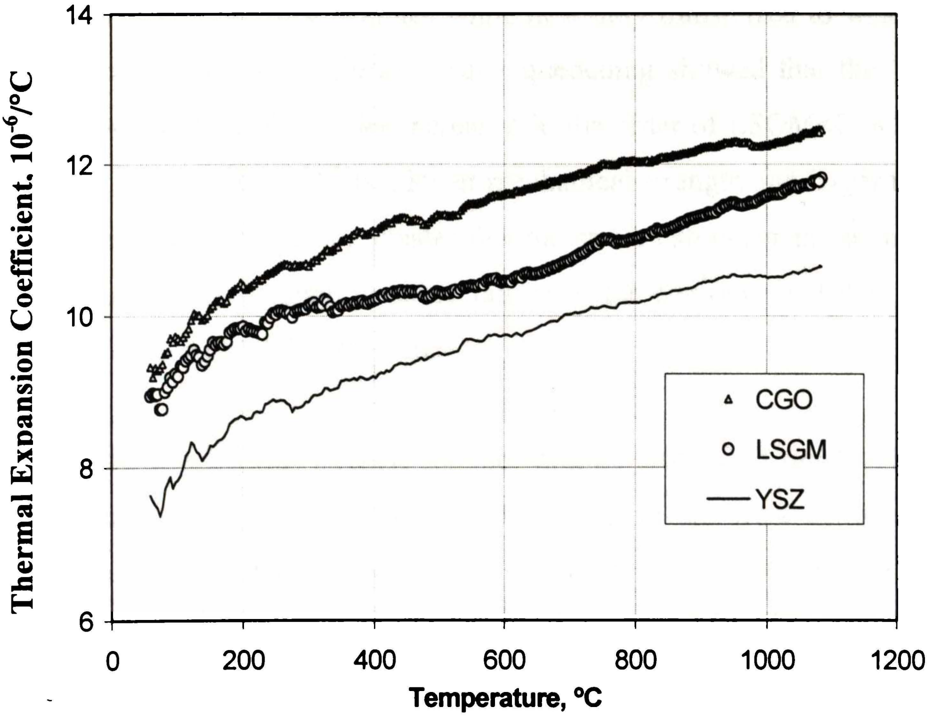

Figure 6-12 TECs of the Tubular Electrolytes Extruded from LSGM, CGO, and YSZ Materials.

6.3.4 Thermal Shock Resistance

Thermal shock is a stress induced in a material due to the temperature differences between the surface and the interior, or between different regions of the component. Rapid cooling of the dense electrolytes is more likely to cause thermal shock issues than heating because the induced surface stresses are tensile. Thermal shock resistance of the electrolytes depends not only on the magnitude of the temperature differences, but also on the mechanical and thermal properties of the materials, and the dimensions of the components. For example, the electrolyte with higher fracture strength and higher thermal conductivity, as well as lower elastic modulus and lower TECs, will have better thermal shock resistance.

The tubes and rods extruded from LSGM, YSZ and CGO in this study showed excellent thermal shock resistance and withstood 20 air-quenched cycles from 800°C without visible cracks and/or delamination (Table 6-2). The thermal shock treatment was made more severe by introducing a water quench step. After one water-quench cycle all the tube samples broke; however, the rod samples remained whole (Figure 6-4c). This was because the tube underwent two-sided quenching so heat transferred to the cooling medium (water) from both the outer and inner surfaces of the tube samples while heat only transferred to water from the outer surface of the rods. Further water quenching showed that the thermal shock resistance of the rod samples increased in the order of LSGM<CGO<YSZ. In comparison to YSZ, LSGM has a lower mechanical strength and larger thermal expansion coefficient, and thus a greater thermal stress can occur in the material. This stress can be high enough to cause failure of the component if it is greater than the tensile strength of the material.

In addition, the mechanical strength of the samples decreased drastically after thermal quenching because of micro-crack formation in the dense ceramics. The burst strength of the tubular YSZ electrolytes after 22 and 30 thermal cycles between room temperature and 1300°C at 6°C/min were 104 MPa and 82 MPa respectively (Table 6-1). Mori *et al.* [8] reported that the MOR of YSZ bars decreased from 250 MPa to 100 MPa after water quenching from 150°C. Although no phase changes were observed in YSZ, LSGM and CGO after thermal cycling, the mechanical strength decreased significantly. Because thermal cycling

Table 6-1 Effect of Thermal Shock Cycling: Air Quenching from 800°C to Room Temperature Followed by Water Quenching.

Samples		Air quench cycles	Water quench cycles									
		From 1 to 20	1	2	3	4	5	6	7	8	9	10
Tubes	LSGM-1	⇒ ⇒	Broken									
	-2	⇒ ⇒	Broken									
	-3	⇒ ⇒	Broken									
	-4	⇒ ⇒	Broken									
	-5	⇒ ⇒	Broken									
	-6	⇒ ⇒	Broken									
	-7	⇒ ⇒	Broken									
	-8	⇒ ⇒	Broken									
	CGO-1	⇒ ⇒	Broken									
	-2	⇒ ⇒	Broken									
	-3	⇒ ⇒	Broken									
	YSZ-1	⇒ ⇒	Broken									
	-2	⇒ ⇒	Broken									
	-3	⇒ ⇒	Broken									
	-4	⇒ ⇒	Broken									
	-5	⇒ ⇒	Broken									
	-6	⇒ ⇒	Broken									
Rods	LSGM-1	⇒ ⇒	⇒	⇒	⇒	⇒	⇒	Broken				
	-2	⇒ ⇒	⇒	⇒	⇒	⇒	⇒	Broken				
	-3	⇒ ⇒	⇒	⇒	⇒	⇒	⇒	⇒	⇒	⇒	⇒	Broken
	CGO-1	⇒ ⇒	⇒	⇒	⇒	⇒	⇒	⇒	Broken			
	-2	⇒ ⇒	⇒	⇒	⇒	⇒	⇒	⇒	⇒	⇒	⇒	Broken
	-3	⇒ ⇒	⇒	⇒	⇒	⇒	⇒	⇒	⇒	⇒	⇒	Broken
	YSZ-1	⇒ ⇒	⇒	⇒	⇒	⇒	Broken					
	-2	⇒ ⇒	⇒	⇒	⇒	⇒	⇒	⇒	⇒	⇒	⇒	Broken
	-3	⇒ ⇒	⇒	⇒	⇒	⇒	⇒	⇒	⇒	⇒	⇒	Broken
	-4	⇒ ⇒	⇒	⇒	⇒	⇒	⇒	⇒	⇒	⇒	⇒	Broken
	-5	⇒ ⇒	⇒	⇒	⇒	⇒	⇒	⇒	⇒	⇒	⇒	Broken
	-6	⇒ ⇒	⇒	⇒	⇒	⇒	⇒	⇒	⇒	⇒	⇒	Broken

⇒ No visible cracks or delamination.

occurs in SOFCs, it is important to select materials, designs and operating conditions that minimize effect of thermal shock.

6.4 Summary

The three point bending strength, burst strength, thermal expansion coefficient and thermal shock resistance of the electrolytes (small scale tubes and rods) extruded from LSGM, CGO and YSZ materials were investigated and compared. The modulus of rupture of LSGM was 287 MPa, 195 MPa, 184 MPa and 147 MPa at room temperature, 600°C, 800°C, and 1000°C respectively. The values were lower than that for CGO and YSZ at the same temperature. Room temperature burst strengths of the three tubular electrolytes were 127 MPa for YSZ, 40 MPa for LSGM, and 63 MPa for CGO. Thermal expansion coefficients of the three electrolyte components increased in the order of YSZ<LSGM<CGO. The average thermal expansion coefficients between room temperature and 800°C were 10.18×10^{-6}/°C, 11.01×10^{-6}/°C and 12.04×10^{-6}/°C for YSZ, LSGM and CGO respectively. All three electrolyte tubes and rods showed excellent thermal shock resistance and could withstand 20 air-quenching cycles from 800°C to room temperature without visible cracks and delamination occurring. Further water quenching showed that the thermal shock resistance of the rods was in the order of LSGM<CGO<YSZ. The mechanical strengths of anode supported tubular SOFCs at different processing stages were evaluated. Anode support cells with YSZ thin film had a room temperature MOR of ~300 MPa after sintering and/or after reduction. Re-oxidisation of the reduced anode should be avoided to protect the anode structure.

6.5 References

1. Kendall, K. and Palin, M., "A small solid oxide fuel cell demonstrator for microelectronic applications." *J. Power Sources*, 1998. **71**: p. 268-270.
2. Prica, M., Alston, T. and Kendall, K., "Mechanical and thermal properties of a 200 tube SOFC reactor." in *5th International Symposium on Solid Oxide Fuel Cells (SOFC V)*. 1997. Aache, Germany: Electrochem. Soc., p. 619-625.
3. Inaba, H. and Tagawa, H., "Review: ceria-based solid electrolytes." *Solid State Ionics*, 1996. **83**: p. 1-16.
4. Ishihara, T., Matsuda, H. and Takita, Y., "Doped $LaGaO_3$ perovskite type oxide as a new oxide ionic conductor." *J. Am. Chem. Soc.*, 1994. **116**: p. 3801-3803.

5. Du, Y. and Sammes, N.M., "Fabrication of tubular electrolytes for solid oxide fuel cells using strontium- and magnesium-doped LaGaO3 materials." *J. Eur. Ceram. Soc.*, 2001. **21**(6): p. 727-735.

6. Du, Y., Sammes, N.M. and Tompsett, G.A., "Optimisation parameters for the extrusion of thin YSZ tubes for SOFC electrolytes." *J. Eur. Ceram. Soc.*, 2000. **20**(7): p. 959-965.

7. Minh, N.O. and Takahashi, T., *Science and technology of ceramic fuel cells.* Amsterdam: Elsevier Science B.V. 1995.

8. Mori, M., Abe, T., Itoh, H., Takeda, Y. and Kawahara, T., "Cubic-stabilized zirconia and alumina composites as electrolytes in planar type solid oxide fuel cells." *Solid State Ionics*, 1994. **74**: p. 157-164.

9. Hayashi, H., Suzuki, M. and Inaba, H., "Thermal expansion of Sr- and Mg-doped $LaGaO_3$." *Solid State Ionics*, 2000. **128**: p. 131-139.

Chapter Seven

Electrical Performance of Micro-Tubular SOFCs and a Novel Stack Design Concept*

7.1 Introduction

Small-scale tubular SOFCs, as described by Kendall and co-workers [1, 2] and Sammes and co-workers [3, 4] have many advantages over other designs including excellent thermal shock resistance, rapid start-up ability, and high mechanical integrity. The traditional electrolytes used in these and other SOFC systems have been doped-ZrO_2 (YSZ) because it has good ionic conductivity at 900 to 1000°C, is stable in both oxidizing and reducing environments encountered in SOFCs, and has good mechanical integrity [5, 6]. The wish for lower temperature SOFC systems, which increase efficiencies and reduce materials cost, has meant that alternative electrolytes with superior oxygen ion conductivities are being sought.

In searching for new electrolyte materials, perovskite based systems, doped lanthanum gallate (LSGM) in particular, have been considered. Much research has been undertaken to evaluate this material. The cell performance using LSGM electrolytes and various electrode combinations reported in the literature are summarized in Table 3-3. All these results are from small but thick (0.4-0.6 mm) pellets carefully prepared in laboratory scale. The current work with tubular electrolyte design was carried out on a semi-production scale.

---

* Some data in this Chapter have been published as:

(1) Yanhai Du and N.M. Sammes, *Ionics*, **9**, 7-14, 2003.

(2) Yanhai Du, X. Huang, N.M. Sammes, K. Reifsnider and A.L. Smirnova, *5th Gordon Conference on Fuel Cells*, Rhode Island, USA, July 27- August 1, 2003.

(3) Yanhai Du and N.M. Sammes, *International Workshop on Solid Electrochemical Devices for Energy Conversion & the 11th National Conference on Solid State Ionics*, Hefei, China, October 14-19, 2002.

(4) Yanhai Du and N.M. Sammes, *9th EuroConference on Science and Technology of Ionics*, Greece, September 15-21, 2002.

One shortcoming of tubular designs over planar designs is their lower volumetric power packing density [7], therefore a tubular stack needs to be larger than a planar stack. A multiple tubular fuel cell (MTFC) configuration that increases stack volumetric power density is proposed.

This Chapter presents electrical performance test data for lanthanum gallate based SOFCs, including: cathode and anode optimisation; I-V/P curves; the effect of electrolyte thickness on cell performance; and long-term (up to 500 hours) degradation studies. The data are compared with that from YSZ micro-tubular SOFCs. A novel design concept to advance tubular stack volumetric power density is discussed.

7.2 Experimental

Single micro-tubular cells were constructed using extruded tubular electrolytes described in Chapter 4 and 5. Cells consisted of an anode, (interlayer), tubular electrolyte support, cathode and current collectors. Raw materials are described in Chapter 3.1 and electrode compositions and cell configurations for LSGM and YSZ are listed in Table 7-1. Several cells were prepared for each configuration.

Table 7-1 Cell Configurations.

Cell#	Cathode	Electrolyte	Interlayer	Anode
1	LSCo-$La_{0.6}Sr_{0.4}CoO_3$	LSGM	-	Ni
2	LSCo-$La_{0.6}Sr_{0.4}CoO_3$	LSGM	SDC-$Ce_{0.8}Sm_{0.2}O_{1.9}$	Ni
3	LSCo-$La_{0.6}Sr_{0.4}CoO_3$	LSGM	SDC-$Ce_{0.8}Sm_{0.2}O_{1.9}$	SDC+Ni
4	SmSrCo-$Sm_{0.5}Sr_{0.5}CoO_3$	LSGM	SDC-$Ce_{0.8}Sm_{0.2}O_{1.9}$	Ni
5	LSCo-$La_{0.6}Sr_{0.4}CoO_3$	LSGM	-	Co
6	LSM-$La_{0.8}Sr_{0.2}MnO_3$	LSGM	SDC-$Ce_{0.8}Sm_{0.2}O_{1.9}$	Ni+8YSZ
YSZ	LSM-$La_{0.8}Sr_{0.2}MnO_3$	8YSZ		Ni-8YSZ

Anodes were formed from NiO, Co (II, III) oxide, NiO-YSZ or NiO-$Ce_{0.8}Sm_{0.2}O_{1.9}$ (SDC) cermet (50:50 wt%). The NiO or Co oxide was reduced to elemental Ni or Co in anode reducing atmosphere. An interlayer of SDC was applied to eliminate the reaction, that occurs between Ni and Ga and forms interface metallic $LaNiO_3$ [8]. The high performance cathode materials LSCo and SmSrCo were used and compared with conventional $La_{0.8}Sr_{0.2}MnO_3$ (LSM).

Anodes, cathodes and interlayer were first made into slurries in order to apply onto the electrolyte support tubes. The ceramic powders were ball milled in ethanol with polyvinyl pyrrolidone (PVP)/methyl ethyl ketone (MEKET) binders until the mean particle size was less than 1 µm. The anode slurry was dip coated to the inside of the electrolyte tubes by sucking slurry into the tubes using a syringe-pipe configuration. The coat was fired at 1200°C for 2 hours except for Co_3O_4, which was fired at 900°C for 0.5 hours. The fired anode coat was 15-30 µm thick. Any interlayer needed was applied in the same way but fired at 1350°C for 0.5 hours. The fired interlayer was 10-15 µm thick. Cathode slurry was brush painted onto the electrolyte tubes after completing the anode/interlayer and then fired at 1100°C for 2 hours, except for $Sm_{0.5}Sr_{0.5}CoO_3$ (SmSrCo), which was fired at 900°C for 0.5 hours. The fired cathode layer was 20-30 µm thick.

The cathode current collector (silver wire) was tightly wound onto the outside of the tubes that had anode and cathode. The anode current collector (nickel mesh) was prepared and then inserted into the tubes to complete the single cells. The effective dimensions of the cells were approximately:

- LSGM cells: (a) OD 6 mm, wall thickness 0.55 mm, active length 25-50 mm; (b) OD 3.9-4 mm, wall thickness 0.22 mm, active length 30-60 mm.
- YSZ cells: OD 3.9-4 mm, wall thickness 0.22 mm, active length 30-60 mm.

The active area for each cell was calculated using the exact cell dimensions.

Electrical performances of the fuel cells were tested using a furnace test station (Figure 7-1). Dry or humidified hydrogen was fed inside the tubular cell at 50 mL/min for 0.55 mm-cells and 30 mL/min for 0.22 mm-cells. Air was used as the oxidant gas. The I-V data were collected using a potentiostat/galvanostat in the temperature range 600°C to 800°C/850°C with an interval of 50°C. Up to four cells can be tested simultaneously. Current density and power density were then calculated using raw I-V data and the fuel cell active area. Cells were tested for up to 500 hours to evaluate the electrical performance stability/degradation. Repeatability was tested by measuring several cells with the same configuration.

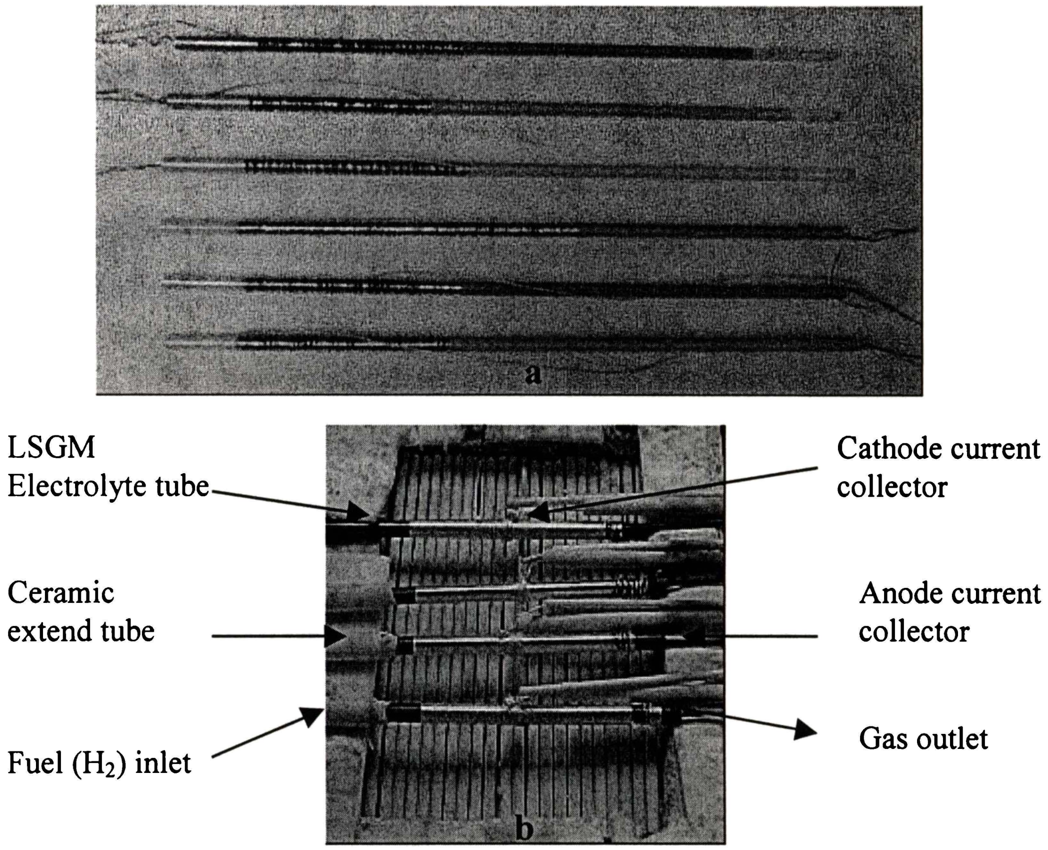

Figure 7-1 Micro-Tubular Fuel Cell and Cell Test Set-up: (a) YSZ Cells with Current Collectors, (b) LSGM Cells in Test.

7.3 Results and Discussion

7.3.1 Overall Performance of LSGM Cells

Typical voltage/power density-current density curves of the LSGM fuel cells (for example cell 2-LSCo/LSGM/SDC/Ni), with an open circuit voltage (OCV) near 1.2 V indicated there was a good gastight electrolyte seal (Figure 7-2). Cell performance increased over the first 50 h. Repeatable power output of 2.5-3 W per cell with 0.55 mm thick electrolyte was obtained. The maximum power densities of 350 mW/cm^2 for 0.55-mm thick electrolyte cells and 482 mW/cm^2 for 0.22-mm thick electrolyte cells were achieved. Overall cell performances are shown in Figure 7-3 and the effects of cathode, anode, interlayer and the electrolyte thickness on cell performances are discussed below.

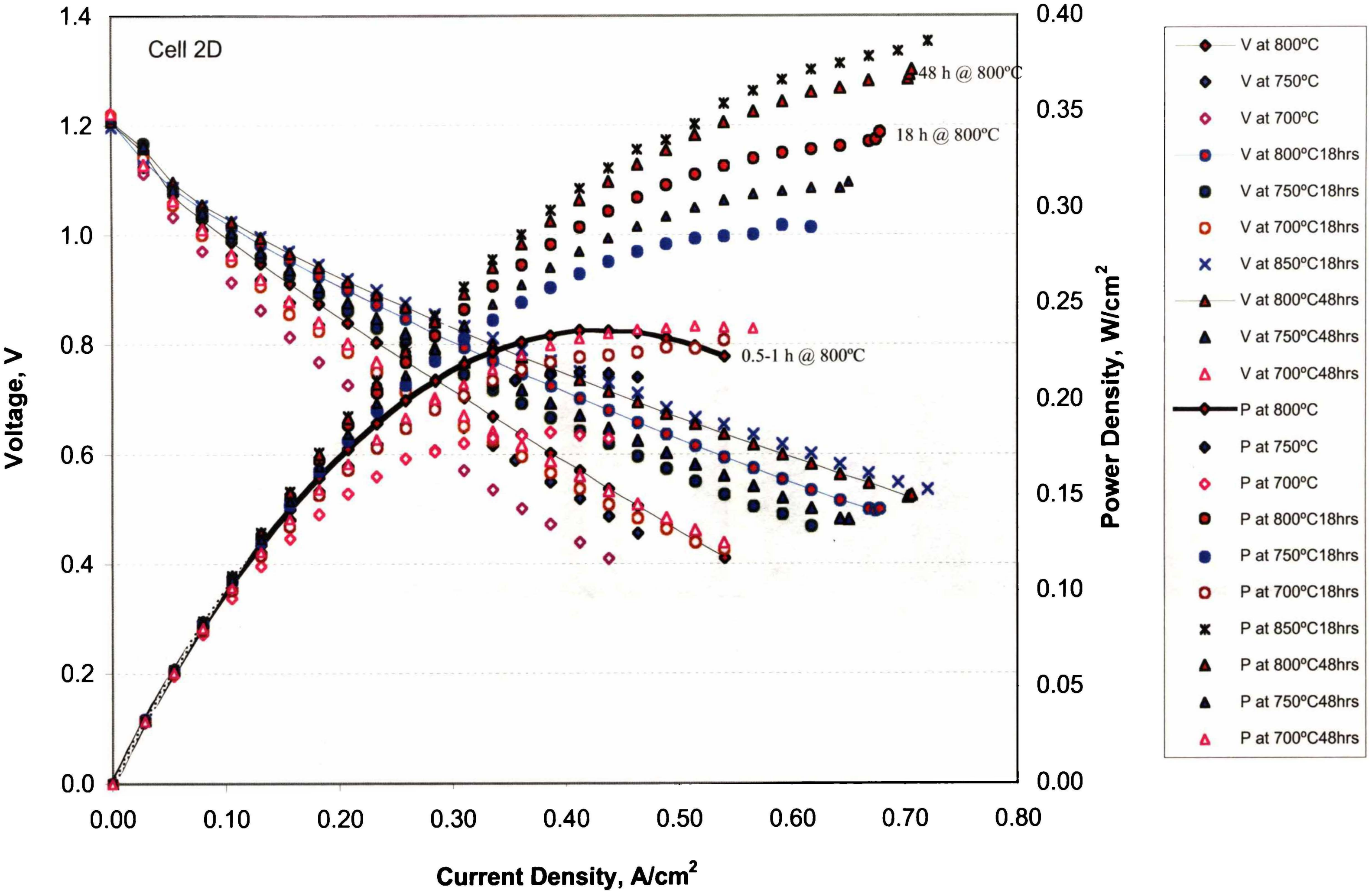

Figure 7-1 Cell Voltage and Power Density as a Function of Current Density at Various Temperatures and Operation Time. The Cell Consists of Air, LSC/LSGM(0.55 mm)/SDC/Ni, H_2.

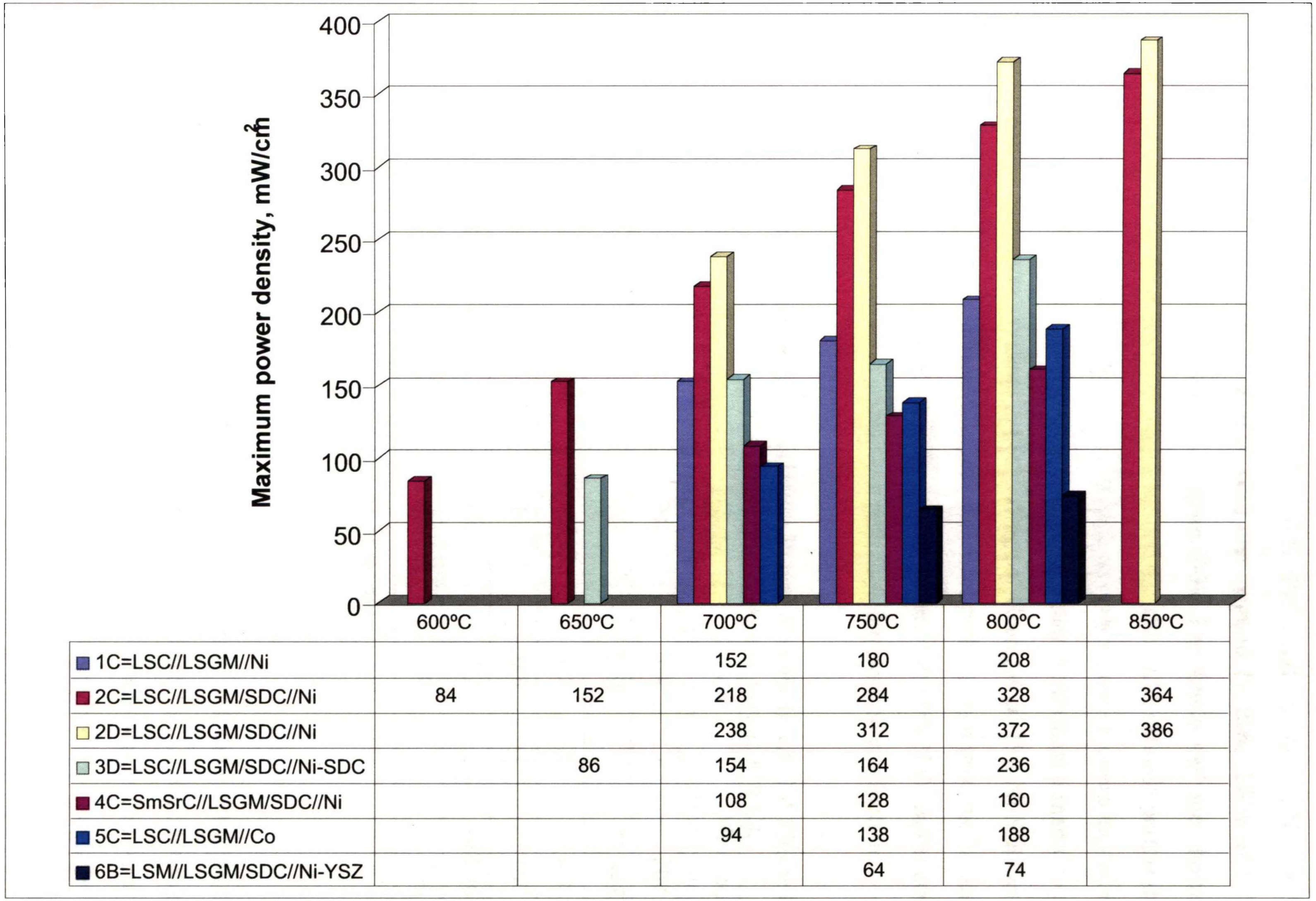

	600ºC	650ºC	700ºC	750ºC	800ºC	850ºC
■ 1C=LSC//LSGM//Ni			152	180	208	
■ 2C=LSC//LSGM/SDC//Ni	84	152	218	284	328	364
□ 2D=LSC//LSGM/SDC//Ni			238	312	372	386
□ 3D=LSC//LSGM/SDC//Ni-SDC		86	154	164	236	
■ 4C=SmSrC//LSGM/SDC//Ni			108	128	160	
■ 5C=LSC//LSGM//Co			94	138	188	
■ 6B=LSM//LSGM/SDC//Ni-YSZ				64	74	

Figure 7-2 Effect of Electrode Configurations on Maximum Power Density of LSGM Cells with 0.55-mm LSGM Electrolytes.

7.3.2 Optimising Cathode and Anode Materials

To better understand which electrode materials are more suitable for the LSGM electrolyte SOFCs, cathodes LSCo and SmSrCo and anodes Co, Ni, and SDC-Ni, were evaluated and compared with the commonly used LSM and Ni-8YSZ electrode materials (Table 7-2, Figure 7-3). The LSCo cathode showed better performance than SmSrCo (cell 2 *vs.* cell 4). The LSM cathode performed poorly compared with LSCo because of its high oxygen reduction overpotential at 800°C. Using Ni for anode gave similar or slightly better performance than Co (cell 1 *vs.* cell 5). However, contrary to the findings of Huang *et al.* [9], Ni-SDC anode (cell 3) did not give the expected higher electrical performance than the Ni anode (cell 2). This is most likely because the nickel content (50 wt% NiO) in the cermet was not high enough to form continuous pathways for electron conduction.

Table 7-2 Power and Maximum Power Density in LSGM Single Cell (0.55 mm LSGM electrolyte, H_2 and air, at 800°C).

Cell#	Cathode	Interlayer	Anode	Power at 0.7 V W	Max. power density mW/cm^2
1	LSCo	-	Ni	1.4	208
2	LSCo	SDC	Ni	2.58	372/482*
3	LSCo	SDC	Ni+SDC	1.5	236
4	SmSrCo	SDC	Ni	0.9	160
5	LSCo	-	Co	1.3	188/460*
6	LSM	SDC	Ni+8YSZ	0.6	74

* Small tube cells with 4-mm OD, 0.22-mm wall thickness

7.3.3 Interlayer

An SDC interlayer was applied between the anode and the electrolyte to inhibit the reaction of La from the electrolyte and Ni from the anode, forming $LaNiO_3$ [10]. Performance (as maximum power density) of the single cell with the SDC interlayer (cell 2) was 43-57% greater than cell without the interlayer (cell 1), indicating that the SDC interlayer effectively inhibited lanthanum nickel oxides formation.

7.3.4 Cell Performance Stability

The typical power outputs for cell type 2 are shown in Figure 7-4. These two cells (2D and 2C) were run separately at a loading of 0.7 V for about two days at 800°C and 850°C respectively. It is clear that the performance of these two cells showed similar increasing trends: power increased by 17-18% during the first day and 5-6% over the second day. The stable power outputs were 2.5 W at 800°C (cell 2D) and 2.8 W at 850°C (cell 2C) during the two-day test. An examination of the effects of operating time and temperature on performance of cell 2D (Figure 7-5) shows peak power/maximum power density tended to be stable after the first day, especially at lower temperatures.

An increase in initial performance was also observed in other cells. After cell 4C had run for 17 hours at 750°C, power increased by 15%. Cells 5B and 6A were tested for 90 hours. Between 24 and 84 hours cells were stable and power increased approximately 10% for cell 5B and 25% for cell 6A. The anomaly was the 8% power decrease in cell 3D after it had run for 12 hours at 800°C.

To evaluate the performance of LSGM cells over a long time, a three-week (about 500 h) test was conducted on cell 2E (LSC/LSGM/SDC/Ni) with air and humidified (3% H_2O) H_2 at 0.7 V and 800°C (Figure 7-6). This cell, which had been made 18 months before the test, was shorter (25 mm) than the usual cells. However, as observed for cells 2C and 2D (Figure 7-4), the performance of cell 2E increased by 25% in the first 90 h. The initial performance increase was believed to be due to conditioning the cell components (cathode, anode and interlayer), which allowed sites for oxygen ions transfer to equilibrate and re-align. After 90 hours, cell performance gradually declined. The cell degraded more quickly after thermal cycling. Degradation rate during the 500-h test was about 12%. This degradation is thought to be due to Ga depletion [11-13], possible reactions between LSGM electrolyte and Ni anode, secondary phases ($LaSrO_7$, $SrLaGaO_4$) segregation from the parent phase [14] and cell component annealing. The long time test will need to be repeated to further evaluate the stability of cell performance.

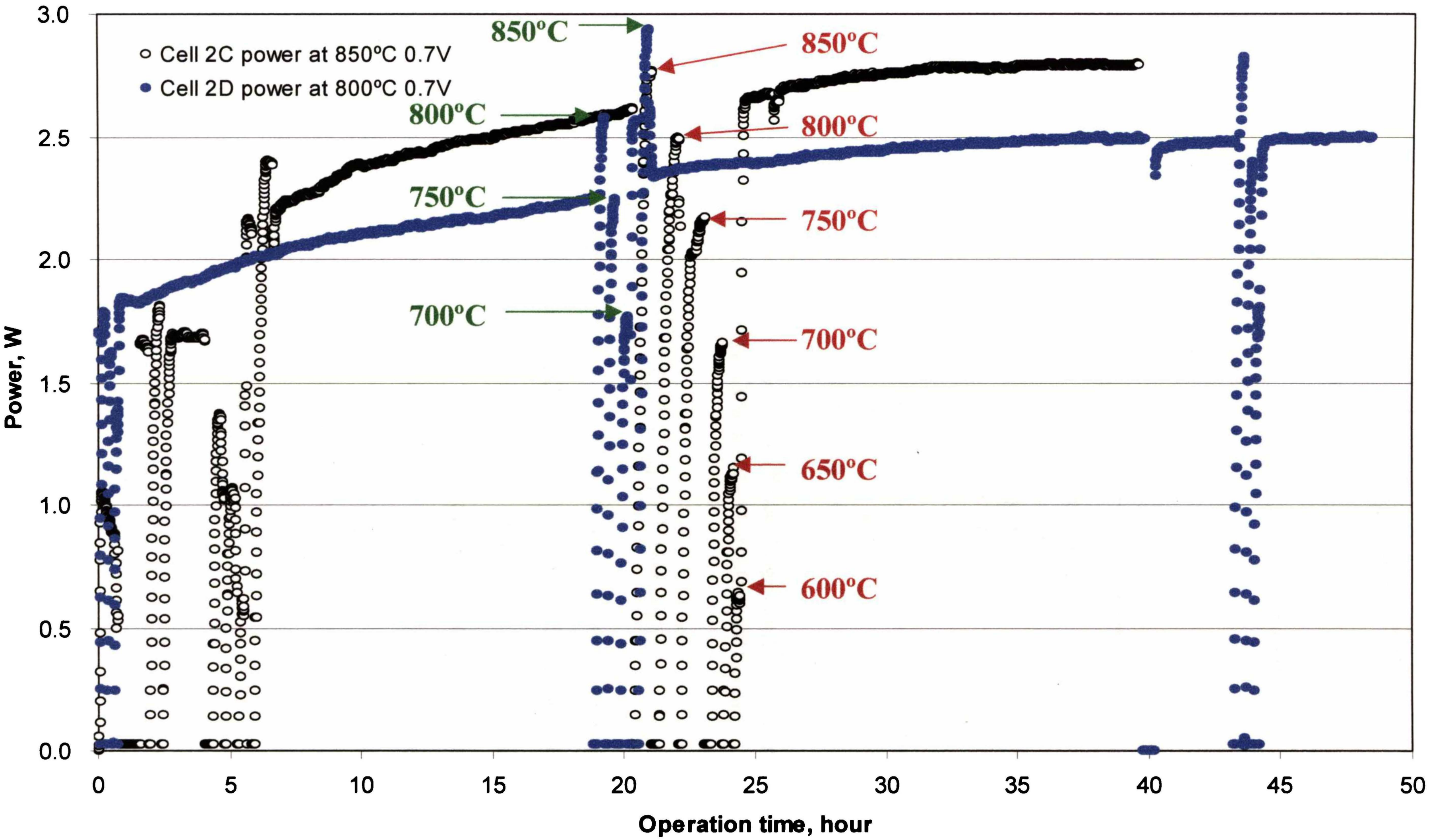

Figure 7-1 Effect of Operation Time on Cell Power, Cells Operated at 0.7 V and 800°C (cell 2D) or 850°C (cell 2C). Cells Consisted of Air, LSC/LSGM/SDC/Ni, H_2. The LSGM Electrolyte Was 0.55-mm Thick.

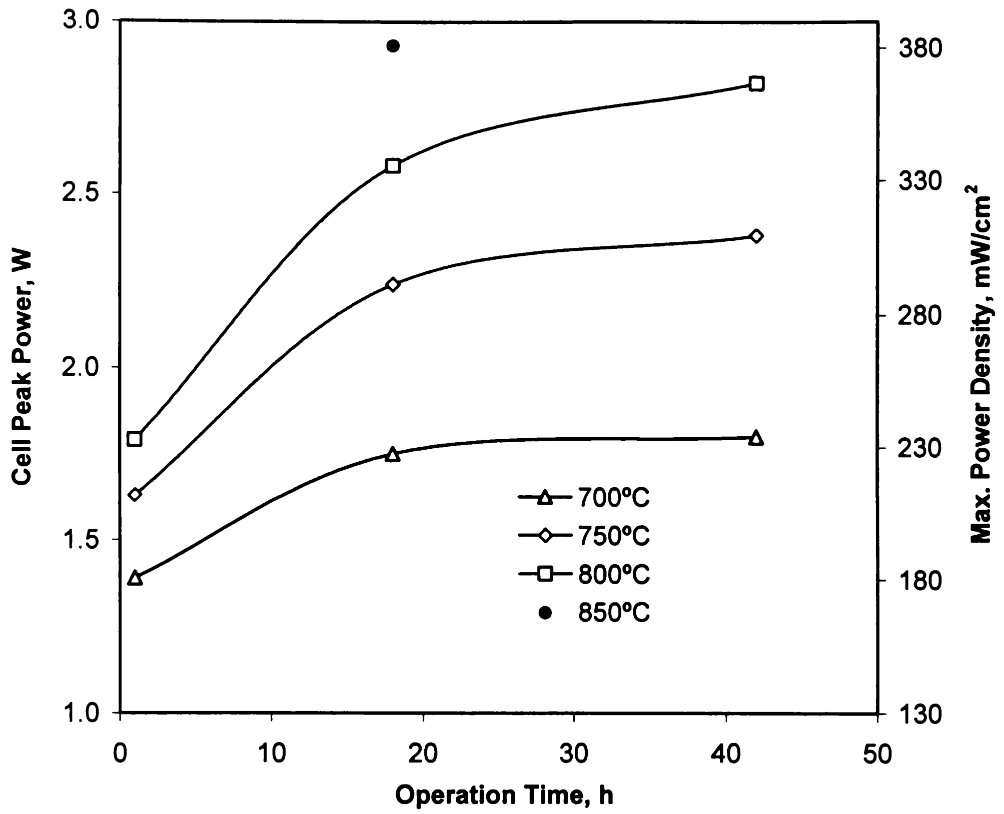

Figure 7-5 Effect of Temperature on Peak Power and Maximum Power Density During Continuous Operation (2D cell).

7.3.5 Effect of Electrolyte Thickness on Cell Performance

To evaluate the effect of electrolyte thickness on cell power density, cells with 550 μm and 220 μm thick LSGM electrolytes were fabricated and tested in parallel. Reducing cell wall thickness from 550 μm to 220 μm increased cell performance by 30-43% (Figure 7-7). For example, maximum power density at 800°C increased from 340 to 482 mW/cm^2. In the tubular electrolyte supported design, however, the mechanical strength required will limit wall thinness of the support component. One approach being investigated is to apply LSGM as a thin film on the anode or cathode support design to further reduce electrolyte resistance and increase cell performance.

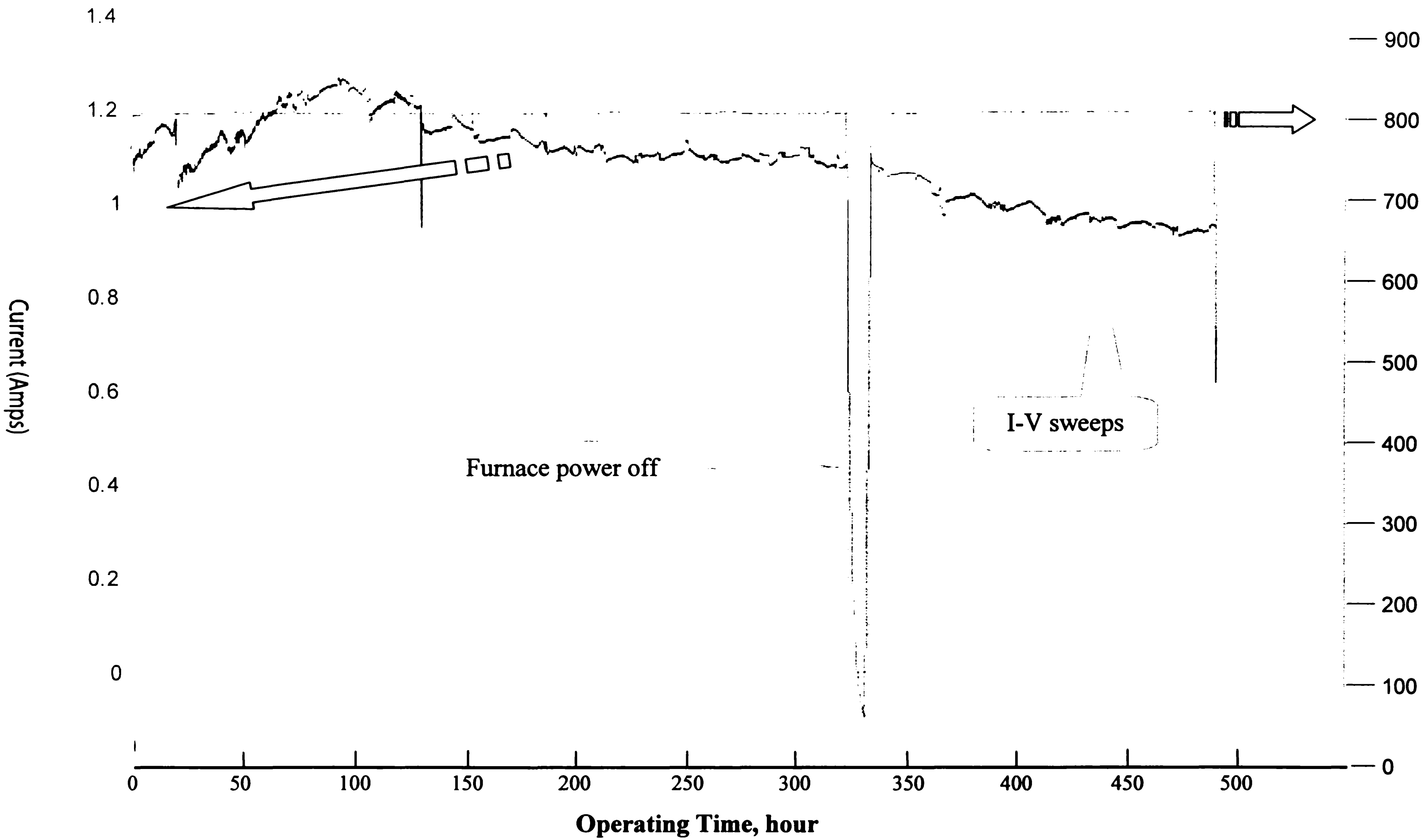

Figure 7-1 Long Time Performance of a LSGM Supported Tubular SOFC at 0.7 V and 800°C. The Cell Consisted of Air, LSC/LSGM/SDC/Ni, 3% H_2O+H_2. The LSGM Was 0.55-mm Thick.

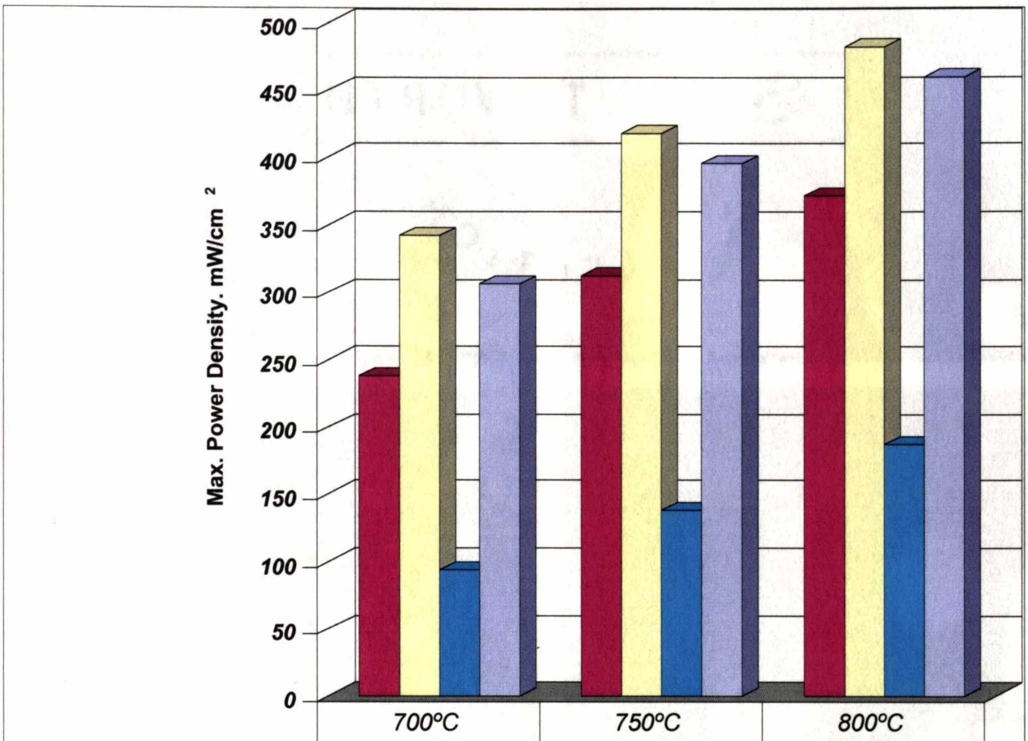

	700°C	750°C	800°C
🟥 0.55mm, 2D=LSC//LSGM/SDC//Ni	238	312	372
☐ 0.22mm, 2A=LSC//LSGM/SDC//Ni	342	418	482
🟦 0.55mm, 5C=LSC//LSGM//Co	94	138	188
🟪 0.22mm, 5E=LSC//LSGM//Co	306	396	460

Figure 7-4 Effect of Electrolyte Thickness (0.55 mm and 0.22 mm) on Maximum Power Density.

7.3.6 Microstructure of the Fuel Cells

Microstructural analysis of the cells after testing (Figure 7-8 for cell 2 and cell 3) shows the thickness of the LSC cathode (20 μm), LSGM electrolyte (550 μm), SDC interlayer (10-15 μm) and Ni anode (15-30 μm). The electrolyte was dense and gastight. Anode and cathode current collectors were in good contact with the cells. However, some of the interlayer on the anode side had cracked before the anode layer was applied and the anode coating had filled these gaps (Figure 7-8 b). The anode cermets (50/50 wt% of NiO-SDC) did not form a good enough nickel network to provide sufficient electronic conduction (Figure 7-8 c and d). Increasing nickel content in the anode cermets to 50 vol.% may improve electrical conduction.

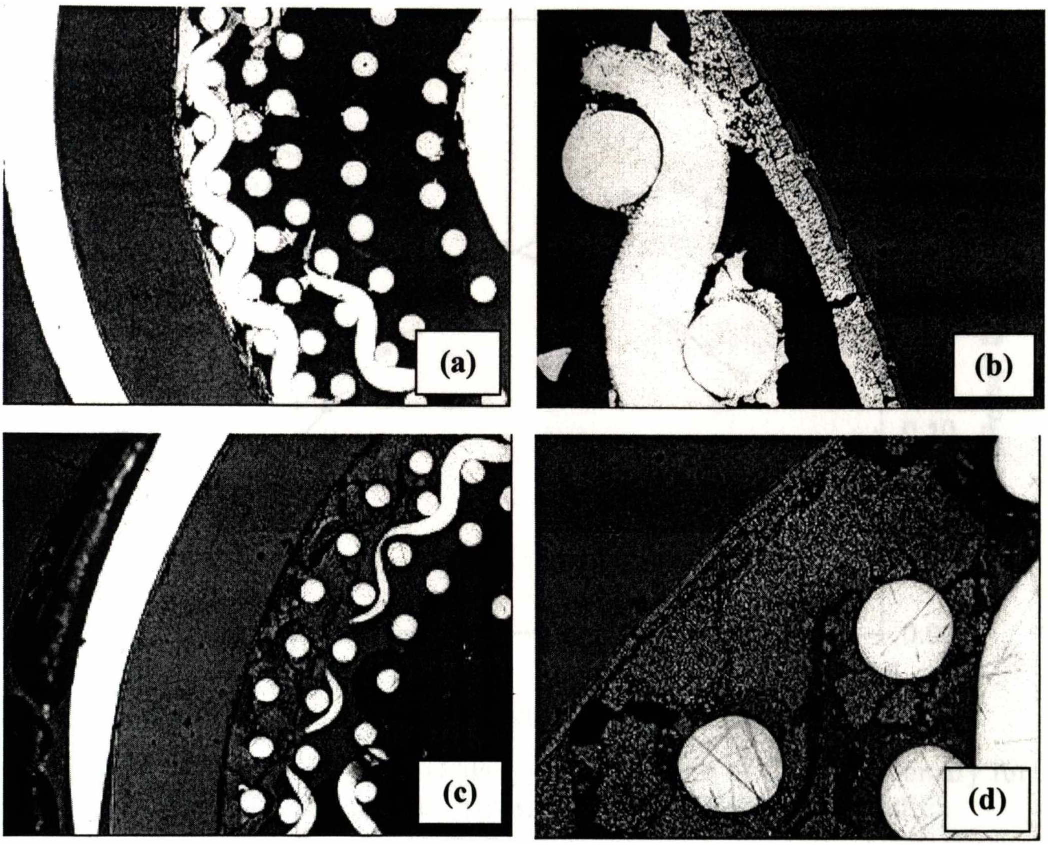

Figure 7-8 Typical Microstructure of Cell 2 and Cell 3 after Testing: (a) Cell 2, Anode and Cathode Current Collectors, (b) Cell 2, Ni Anode, SDC Interlayer, LSGM Electrolyte, (c) cell 3, Anode and Cathode Current Collectors, (d) Cell 3, SDC Interlayer and Ni-SDC Anode.

7.3.7 Characteristics of YSZ Cells

Typical I-V/P curves show that YSZ electrolyte supported micro-tubular SOFCs with LSM cathodes and Ni-YSZ anodes had an OCV of 1.1 V and a maximum power density of 0.22 W/cm² after the cell had run for 15 hours at 850°C (Figure 7-9). Maximum power density at 850°C (for example, 0.22 W/cm²) of the YSZ cells was less than 50% that of LSGM cells at 800°C (460-482 W/cm²) for the same electrolyte thickness and similar to or less than that of LSGM cells at 650-700°C. These data show that using LSGM as fuel cell electrolyte could reduce the operating temperature by ~200°C, from fuel cell using YSZ as electrolyte.

Temperatures significantly affected YSZ cell performance, as can be seen in Figure 7-10. Reducing operating temperature from 800°C to 700°C decreased the power by 35-40% for YSZ cells but only 25-35% for LSGM cells.

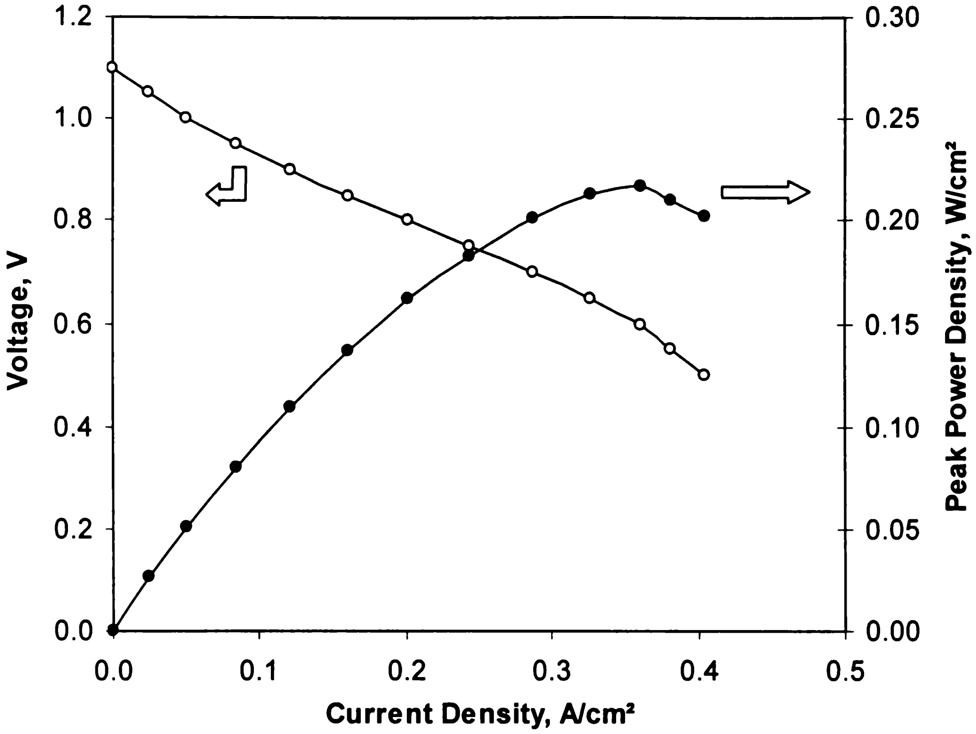

Figure 7-9 Voltage and Power Density as a Function of Current Density for an YSZ Cell Consisting of Air, LSM/YSZ/Ni-YSZ, H_2 at 850°C.

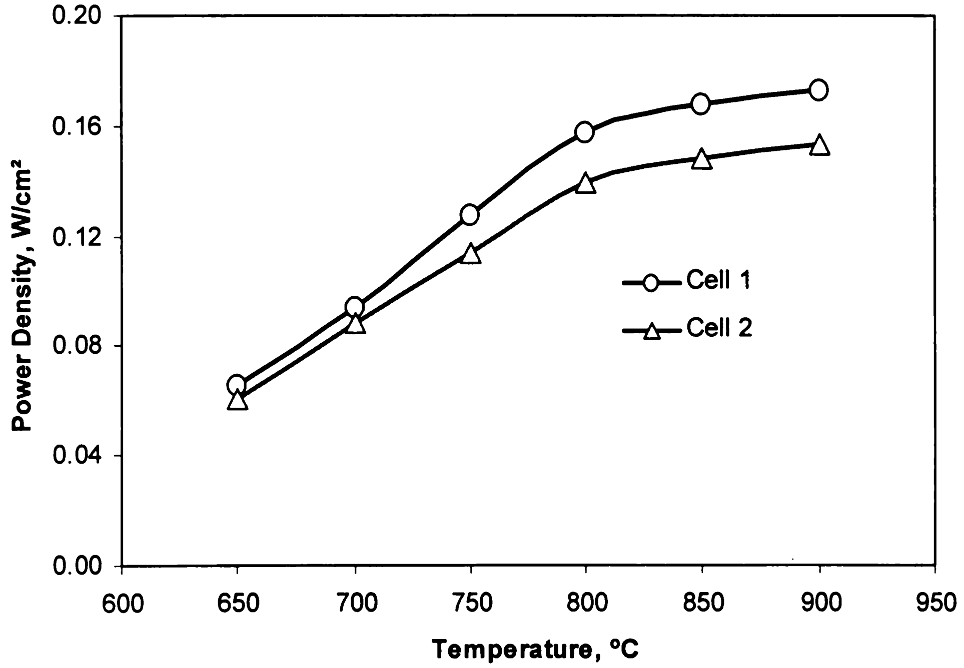

Figure 7-10 Effect of Operating Temperatures on YSZ Cell Performance, Cell Consisting of: Air, LSM/YSZ/Ni-YSZ, H_2.

Two YSZ cells were run for three days to evaluate their performance stability. I-V sweeps were performed at various temperatures after the cells had been running for 14 hours (Figure 7-11).

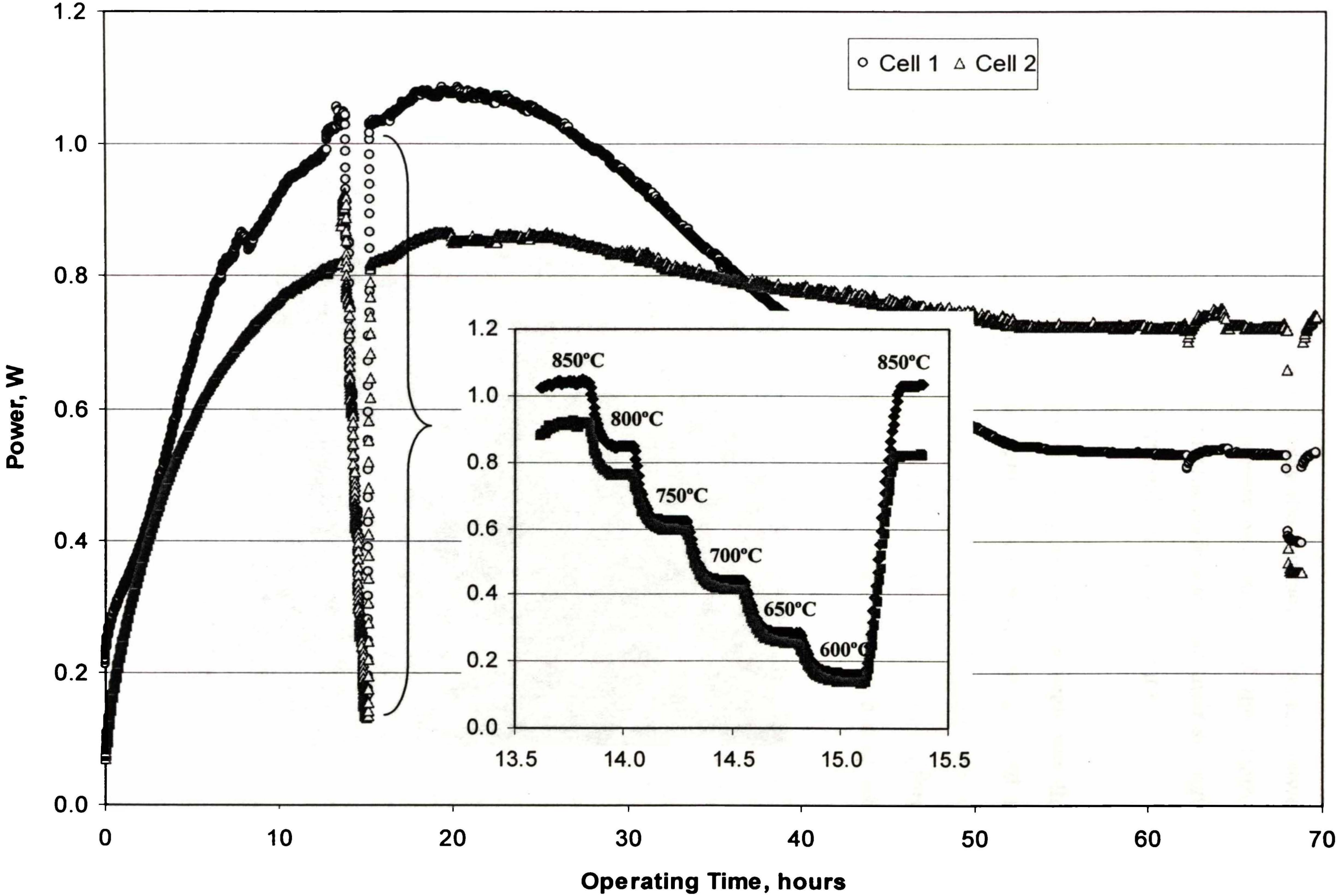

Figure 7-1 YSZ Cell Performances at 850°C and Sweeps at Various Temperatures. The Cells Consisted of Air, LSG/YSZ/Ni-YSZ, H_2 with 0.22-mm Thick Electrolyte.

The cell power was initially low and then steadily increased. This phenomenon was observed in all cells tested, although each cell may take a different time to reach maximum power. The passive species MnO_x and SrO enriched on the LSM cathode surface are believed to contribute to the initially very high cathode polarization losses [15]. Besides electrode degradation, the major contribution to degradation in cell performance was the contact resistance between the current collector (especially the anode current collector) and the electrodes. This was because the nickel mesh anode current collectors lost their springiness after high temperature annealing, which decreased contact efficiency.

Cross-sections of the tested YSZ cell (Figure 7-12) reveals that the YSZ support electrolyte was dense and gas tight. However it had cracked at some stage, perhaps in analysis. Cathode and anode current collectors remained in contact with the electrodes but the anode current collector was not uniformly distributed along the anode, which could cause poor contact (higher contact resistance).

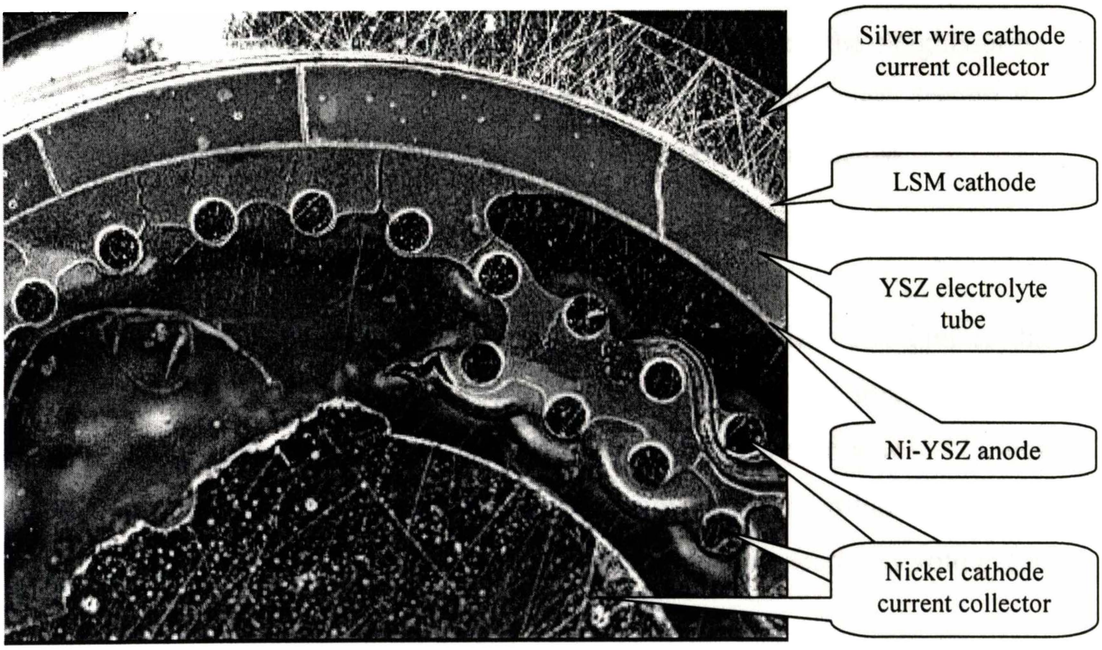

Figure 7-12 Cross-Section of an YSZ Cell after Test.

7.4 A Novel Tubular Stack Design Concept

7.4.1 Design Parameters

The volumetric power packing density (VPPD) of a tubular fuel cell, P_v, is a function of fuel cell performance and cell design, and can be expressed in the following equation developed in this research:

$$P_v = \frac{4P_a n(d_1 + \frac{n-1}{2}\Delta d)}{\left[d_1 + (n-1)\Delta d\right]^2} \qquad \textbf{Equation 7-1}$$

Where P_v = volumetric power packing density, W/cm³ or kW/L

P_a = cell area power density, W/cm^2

d_l = smallest tube ID, cm

Δd = ID difference between the two neighbouring tubes, cm

n = number of tubes in a module

Equation 7-1 shows that the four parameters affecting volumetric power packing density: (a) tube size d_l; (b) difference in tube size between the neighbouring tubes Δd; (c) number of tubes in a module n; and (d) cell area power density P_a. The effect of each of these parameters on the VPPD is explained below.

- **Tube Size**

The surface area in single tubular cells is related to tube size. The greater the active surface area, the more power could be generated. However, increasing tube size dramatically decreases volumetric packing power density (Figure 1-11). For example, increasing tube size from 5 mm to 10 mm decreases volumetric power density by 50% and increasing the size from 5 mm to 15 mm decreases volumetric power packing density by 67%.

- **Number of Tubes in a Module**

Increasing the number of tubes in a module increases power packing density of the module (Figure 7-13). For example, for a module with d_l=10 mm, Δd=2 mm, and P_a=0.5 W/cm², the power packing density P_v is calculated as 2 kW/L for a single tube (*n*=1), 3.67 kW/L for *n*=3 (a 84% increase in P_v), and 4.32 kW/L if *n*=5 (a 116% increase in P_v).

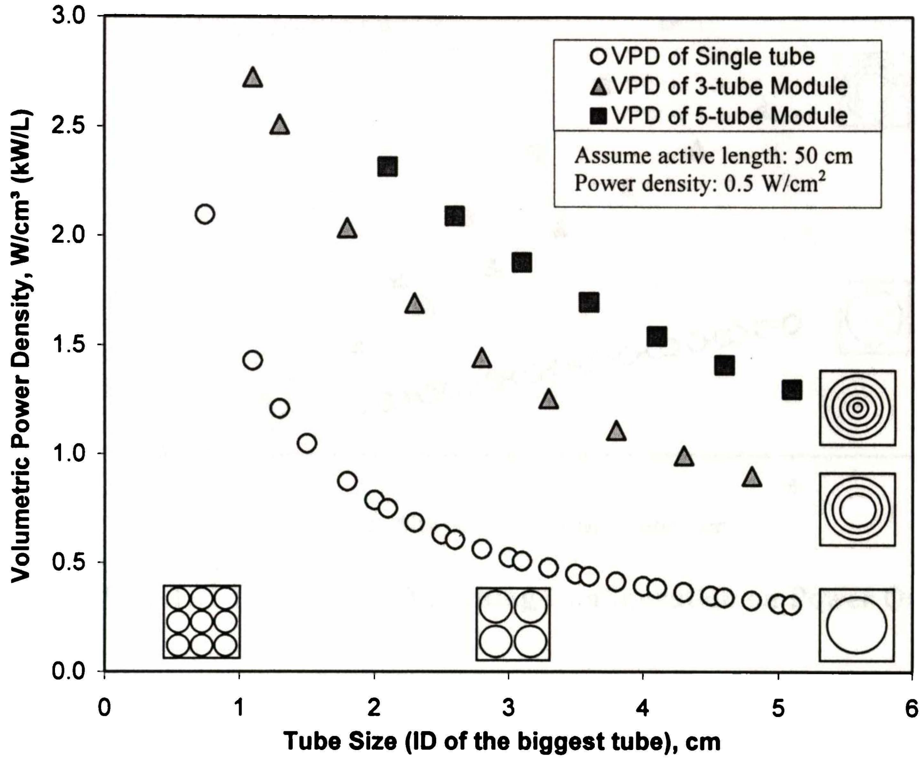

Figure 7-13 Volumetric Power Packing Density as a Function of Tube Size for Different Design Configurations.

- **Neighbouring Tube Size Difference**

With a constant configuration (e.g. same d_l and *n*), decreasing the gap between the tubes increases power packing density. For example, reducing Δd from 4 mm to 2 mm will increase power by 30-40%.

- **Cell Performance**

Single cell performance (relative area power density P_a) is essential, as this directly influences the volumetric power packing density of a module or stack. In the calculation, specific area power density P_a was assumed as 0.5 W/cm². This multiple tubular fuel cell (MTFC) design can double or triple the power generated from each module without increasing the stack size (Figure 7-14).

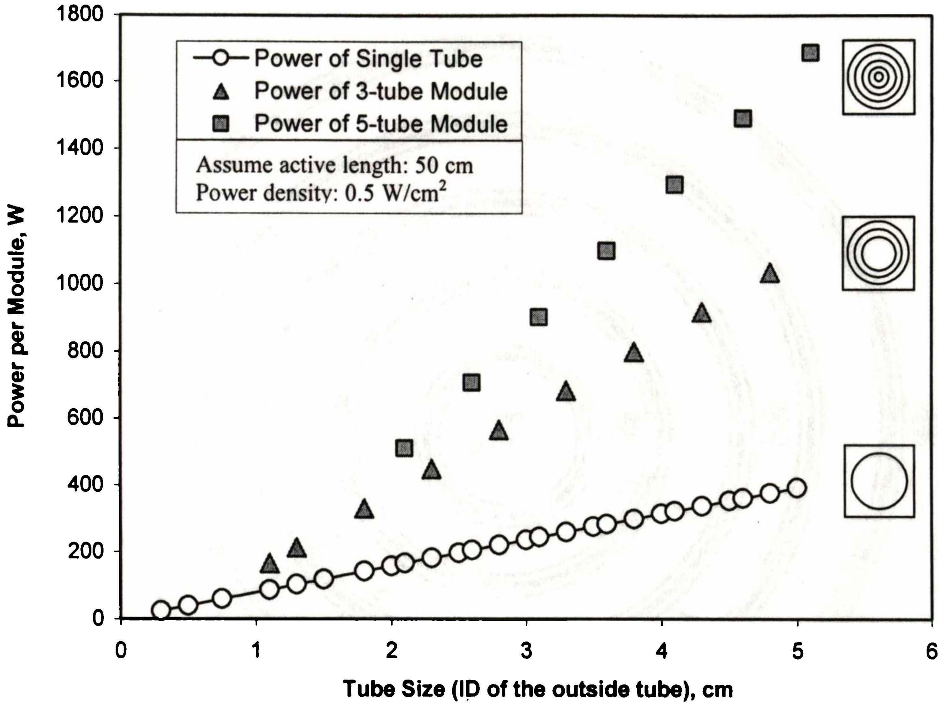

Figure 7-14 Effect of Tube Size and Packing Configuration on Power Output.

7.4.2 Benefits of Using a MTFC Design

The basic model of a MTFC design is a group of different sized tubular cells inside each other (Figure 7-15). Neighbouring tube surfaces share the same gas passage. The basic module can be assembled into a stack with high volumetric packing density. Overall, the MTFC design allows increased volumetric packing power density. The critical tube size is about 7-10 mm. There are high engineering and manufacturing costs with tubes smaller than 5 mm but having tubes greater than 15 mm gives low power packing density and larger stack size.

The MTFC design has the potential to increase fuel efficiency because two reaction surfaces contact the gas. The modular design can also increase stack reliability because each module is controlled and monitored separately. If an individual module fails, it can be switched off and replaced. However, this concept needs to be proved and the techniques to collect the current from individual cells need to be developed.

This design concept can be applied to any tubular fuel cells, such as electrolyte-, anode- or cathode-supported. The idea to increase packing densities can also be extended to other type fuel cell applications.

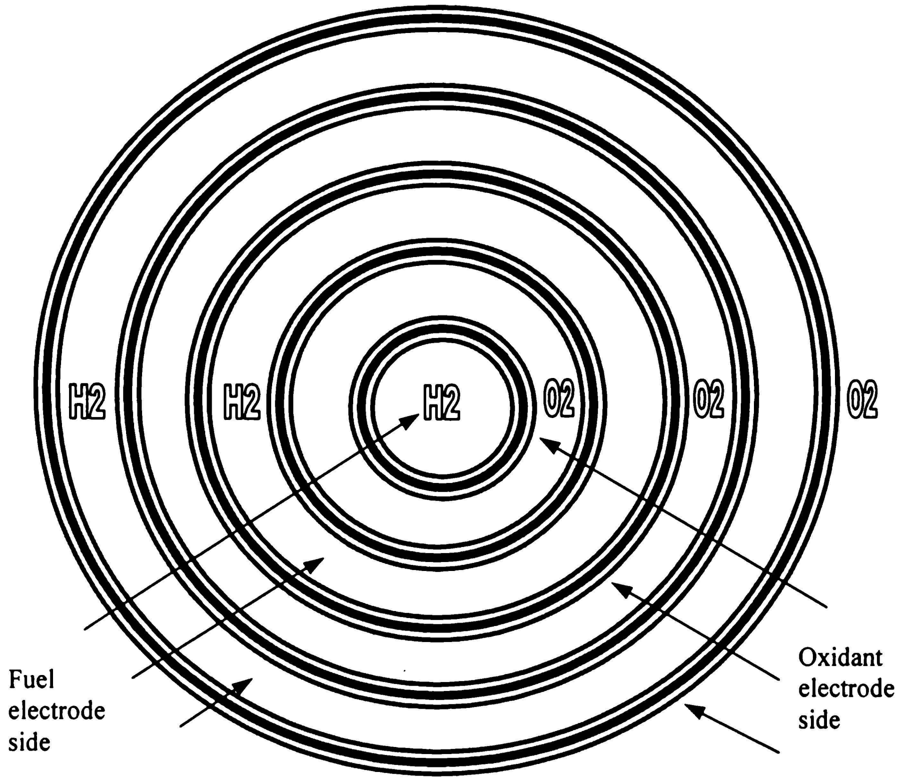

Figure 7-15 Schematic of Novel SOFC Tubular Design Configurations

7.5 Summary

Tubular SOFCs with doped lanthanum gallate electrolyte and a range of anode and cathode morphologies were fabricated, electrically tested and compared with YSZ electrolyte supported cells. LSCo was a suitable cathode material for intermediate temperature LSGM electrolyte SOFCs. Although extended lifetime tests must be done to identify the long-term stability issues, having a SDC interlayer on the anode side of the cell increased maximum power density by 43-57%, which indicated that the SDC interlayer protected against reactions between the LSGM electrolyte and the nickel based anode. Repeatable power outputs per cell of 2.5 W at 800°C and 2.8 W at 850°C were obtained. Cell performance decreased by 12% after the cell had been running for nearly 500 hours. Reducing electrolyte thickness from 550 μm to 220 μm increased maximum power density by 30-43%. The maximum power density of 482 mW/cm^2 at 800°C for a 220-μm thick electrolyte was achieved, which was two times higher than YSZ cells at 850°C (0.22 W/cm^2). From the power density data we conclude that to obtain the same power output, fuel cells using LSGM electrolyte could be operated at temperatures 200°C lower than fuel cells using YSZ as electrolyte.

The small-scale tubular cells fabricated can be electrically connected to develop a stack. A multiple tubular design could increase stack volumetric power density by 84% (three-cell module) or 116% (five-cell module), comparing to a single-tube cell. This design also has the potential to increase fuel utilization rate.

7.5 References

1. Kendall, K. and Prica, M., "Integrated SOFC tubular system for small scale cogeneration." in *First European Solid Oxide Fuel Cell Forum*. 1994. Lucerne, Switzerland, p. 163.
2. Kilbride, I.P., "Preparation and properties of small diameter tubular solid oxide fuel cells for rapid start-up." *J. Power Sources*, 1996. **61**: p. 167-171.
3. Hatchwell, C., Sammes, N.M. and Brown, I.W.M., "Fabrication and Properties of thin-walled SOFC electrolyte tubes." *Solid State Ionics*, 1999. **126**: p. 201.
4. Hatchwell, C.E., Sammes, N.M. and Kendall, K., "Cathode current-collectors for a novel tubular SOFC design." *J. Power Sources*, 1998. **70**: p. 85-90.
5. Minh, N.O. and Takahashi, T., *Science and Technology of Ceramic Fuel Cell*. Amsterdam: Elsevier Science B.V. 1995.
6. Du, Y. and Sammes, N.M., "Fabrication of tubular electrolytes for solid oxide fuel cells using strontium- and magnesium-doped $LaGaO_3$ materials." *Journal of the European Ceramic Society*, 2001. **21**(6): p. 727-735.
7. Singhal, S.C., "Solid oxide fuel cells for clean and efficient power generation." in *Blue Skies Energy Technologies*. 2002. Atlanta, Georgia, p.
8. Huang, K., Wan, J. and Goodenough, J.B., "Increasing power density of LSGM-based solid oxide fuel cells using new anode materials." *J. Electrochem. Soc.*, 2001. **148**(7): p. A788-A794.
9. Huang, K., Lee, H.Y. and Goodenough, J.B., "Sr- and Ni-doped $LaCoO_3$ and $LaFeO_3$ perovskites -- new cathode materials for solid-oxide fuel cells." *J. Electrochem. Soc.*, 1998. **145**(9): p. 3220-27.
10. Hofer, H.E. and Jock, W.F., "Crystal chemistry and thermal behavior in the $La(Cr,Ni)O_3$ perovskite system." *J. Electrochem. Soc.*, 1993. **140**: p. 2889.
11. Yamaji, K., Horita, T., Ishikawa, M., Sakai, N. and Yokoawa, H., "Compatibility of $La_{0.9}Sr_{0.1}Ga_{0.8}Mg_{0.2}O_{2.85}$ as the electrolyte for SOFCs." *Solid State Ionics*, 1998. **108**: p. 415-421.
12. Yamaji, K., Negishi, H., Horita, T., Sakai, H. and Yokoawa, H., "Vaporization process of Ga from doped $LaGaO_3$ electrolytes in reducing atmospheres." *Solid State Ionics*, 2000. **135**: p. 389-396.
13. Yamaji, K., Horita, T., Ishikawa, M., Sakai, H. and Yokoawa, H., "Chemical stability of the $La_{0.9}Sr_{0.1}Ga_{0.8}Mg_{0.2}O_{2.85}$ as the electrolyte in a reducing atmosphere." *Solid State Ionics*, 1999. **121**: p. 217-224.
14. Djurado, E. and Labeau, M., "Second phases in doped lanthanum gallate perovskites." *J. European Ceramic Soc.*, 1998. **18**: p. 1397-1404.
15. Jiang, S.P. and Love, J.G., "Origin of the initial polarization behavior of Sr-doped $LaMnO_3$ for O_2 reduction in solid oxide fuel cells." *Solid State Ionics*, 2001. **138**: p. 183-190.

Chapter Eight

Conclusions and Recommendations

8.1 Conclusions

SOFCs are a promising technology for generating high quality electricity. Cost and durability are the major barriers to commercialising this technology. The thesis in this work was to develop a cost-effective process to fabricate micro-tubular SOFCs that can be operated at intermediate temperatures (600-800°C). Two approaches have been investigated: lowering the cell operation temperatures by using a new electrolyte material LSGM; and using paste extrusion to fabricate tubular supports. The effects of materials and processing parameters on microstructure and performance of these tubular SOFCs were examined. The tubular LSGM fuel cell performance was compared to data for button cells from the literature because there are no published reports on lanthanum gallate based tubular fuel cells. A novel design concept to increase stack volumetric packing density is described. Corresponding to the aims set up in Chapter two, the major conclusions reached from this research are summarized below.

8.1.1 Using LSGM Electrolyte to Reduce SOFC Operating Temperature

Reducing operating temperatures is one significant way to reduce the cost of SOFC stacks and BOP. It prolongs life of fuel cell components, gives wider BOP material choices, and has lower heat loss and quicker start-up times. Developing a high oxygen ion conductor is key to reducing the operating temperature.

The superior oxygen ion conductor, Sr- and Mg-doped $LaGaO_3$, was synthesized using a solid-state reaction at 1500°C for 12 h. The density of the sintered body was greater than 98% of the theoretical value. The single-phase perovskite LSGM region was identified to be $La_{0.9}Sr_{0.1}Ga_{0.9}Mg_{0.1}O_{3-\delta}$ (LSGM-1010), $La_{0.9}Sr_{0.1}Ga_{0.85}Mg_{0.15}O_{3-\delta}$ (LSGM-1015), $La_{0.8}Sr_{0.2}Ga_{0.85}Mg_{0.15}O_{3-\delta}$ (LSGM-2015) and $La_{0.8}Sr_{0.2}Ga_{0.8}Mg_{0.2}O_{3-\delta}$ (LSGM-2020).

Tubular SOFCs with LSGM-2020 electrolytes and six different anode and cathode arrangements were fabricated. Their electrical performance was compared with YSZ electrolyte supported cells. $La_{0.6}Sr_{0.4}CoO_3$ (LSCo) was found to be suitable as the cathode material for intermediate temperature LSGM electrolyte SOFCs. Having a $Ce_{0.8}Sm_{0.2}O_{1.9}$ (SDC) interlayer on the anode side of the cell increased the maximum power density by 43-57% because the SDC interlayer reduced reactions between the LSGM electrolyte and the nickel-based anode. Repeatable power outputs per cell of 2.5 W at 800°C and 2.8 W at 850°C were obtained. Cell performance decreased 12% during a 500-hour test.

The maximum power density for LSGM cells with a 220-μm thick electrolyte was 460-482 mW/cm^2 at 800°C and 306-342 mW/cm^2 at 700°C, compared with 200-220 mW/cm^2 from YSZ cells with the same electrolyte thickness operating at 850°C. Thus, a LSGM electrolyte SOFC can produce the same power output as a YSZ-based system but at approximately 200°C lower operating temperatures.

8.1.2 Reducing Electrolyte Thickness to Minimize Electronic Polarization

Ohmic polarization dominates SOFC voltage losses. Resistivities of electrolytes are much greater than those of cathodes and anodes. Reducing electrolyte thickness was critical for reducing ohmic losses and enhancing cell performance. For example, reducing LSGM thickness from 550 μm to 220 μm, increased the maximum power densities by 30-43% for LSCo/LSGM/SDC/Ni cells and by 145-225% for LSCo/LSGM/Co cells. The maximum power densities at 800°C were 372 mW/cm^2 for a 550-μm LSGM cell and 482 mW/cm^2 for a 220-μm LSGM cell. There is potential to further reduce LSGM electrolyte thickness to between 10 to 30 μm on an electrode-supported system, thereby further increasing cell power output.

8.1.3 Mechanical and Thermal Properties of Tubular SOFCs

High mechanical strength and thermal shock resistance, and matched thermal expansion coefficient are essential requirements for the support components in tubular SOFCs. This technical information is required for stack designs and electrode materials selection and development. The MOR of extruded LSGM, YSZ and CGO electrolyte materials (rods) were found to be 287, 322, and 323 MPa respectively at room temperature. These strengths decreased with increasing temperatures (e.g. 184, 245 and 240 MPa respectively at 800°C). The MOR of the extruded materials was greater than that for materials produced by isostatic pressing and values reported in the literature. The MOR of Ni/YSZ anode was ~300 MPa at room temperature after firing (at 1475°C) and/or after reduction. Coating anode tubes with YSZ electrolyte decreased the mechanical strength of fired anode tubes because of the thermal stressed induced in the multilayer ceramics. Re-oxidising the reduced anode tube significantly reduced strength.

A new technique, termed the burst method, was developed to more accurately indicate the strength of micro-tubular electrolytes. Burst strengths of the LSGM, CGO and YSZ tubular electrolytes at room temperature were 40 MPa, 63 MPa, and 127 MPa respectively. After 22 thermal cycles from 1300°C to room temperature, the burst strengths decreased to 30 MPa (LSGM) and 104 MPa (YSZ). This is the first work that has reported the burst strength data of micro-tubular electrolytes. Although burst strength of the materials investigated was much smaller than bending strength, it followed the same trend, with LSGM having a lower mechanical strength than YSZ and CGO.

The average thermal expansion coefficient of YSZ, LSGM and CGO between room temperature and 800°C were 10.18×10^{-6}/°C, 11.01×10^{-6}/°C and 12.04×10^{-6}/°C respectively and agreed well with published data. This data can be used for designing or selecting thermally matching electrode materials.

Electrolyte tubes and rods made from YSZ, LSGM and CGO had excellent thermal shock resistance and could withstand 20 air-quenching cycles (800°C to room temperature) without visible cracks and delamination. Thermal shock resistance of the rods after water quenching was in the order LSGM<CGO<YSZ.

8.1.4 Cost-Effective Process for Fabricating Tubular Support Components

Paste extrusion was a suitable process for high-speed manufacturing SOFC tubular support components. Procedures were developed to extrude dense, smooth, straight, round and thin-walled tubular LSGM and YSZ electrolytes from pastes with Duramax (aqueous) and PVB (organic) additives. Well-shaped electrolyte tubes were more easily produced using water-based additives. A binder ratio of 5 parts B1051 to 1 part B1052 produced the best extrudate and gave the highest yield. Moisture content in the dough was sensitive to the quality of extrudates and adding 8-9% water gave higher both green and sintered yields. Optimal formula for extrusion of YSZ tubes was 12% binders (B1051/B1052=5:1), 1.5% pH control agent (AMP-95), 1.5% surfactant (PET-400) and 8.5% water (as a percentage of the powder). Procedures for extruding anode-supported components using methylcellulose binder were also developed.

A tapered three-spider extrusion die improved extrudate quality and using C-shaped tube holders made from PET or teflon successfully helped the extruded tubes retain their conformation during drying. Rheological behaviour of the dough affected extrudability and extrudate yield. Green tube yields of 60-98% were achieved. Various size electrolyte tubes were fabricated. The 4-mm OD YSZ tubes were mass manufactured using an industrial mixer and extruder. The tubes for fuel cell stack development had tight tolerances: OD and roundness: 4.0±0.1 mm; wall thickness: 0.2±0.02 mm; length: (200-300)±1 mm.

8.1.5 Novel Design to Increase Power Packing Density

A novel tubular stack design concept, termed a multiple tubular fuel cell (MTFC), was developed to increase stack volumetric power packing density. The MTFC has a variable number of different diameter tubular cells assembled concentrically. Compared to a single-tube cell design, the MTFC design could increase stack volumetric power density by 84% for a three-cell module or 116% for a five-cell module. The following relationships were developed to predict the effects of design parameters on volumetric power packing density:

$$P_v = \frac{4P_a n(d_1 + \frac{n-1}{2}\Delta d)}{\left[d_1 + (n-1)\Delta d\right]^2}$$

Where P_v = volumetric power packing density, W/cm³ or kW/L

P_a = cell area power density, W/cm^2

d_l = smallest tube ID, cm

Δd = ID difference between the two neighbouring tubes, cm

n = number of tubes in a module.

This design has the potential to increase fuel efficiency because neighbouring tube surfaces share the same gas passage; so two reaction surfaces contact the gas. The modular design can also increase stack reliability because each module can be controlled and monitored separately. If an individual module fails, it can be switched off and replaced. However, this concept needs to be proven further and techniques to collect the current from individual cells need to be developed.

8.2 Recommendations for Future Work

Although LSGM is an excellent oxygen ion conductor at intermediate temperatures (600-800°C), LSGM electrolyte and Ni-based anode SOFCs have technical and economical obstacles that need to be solved before commercial production. For example, the LSGM material needs to be sintered at temperatures above 1450°C in order to obtain a dense electrolyte. The LSGM reacts with traditional Ni-based anodes during cell fabrication (the firing step), producing $LaNiO_3$ (an insulating phase) and increasing anode polarization losses. If LSGM is used as a support component and sintered before applying the anode, the LSGM-Ni reaction would not occur. However, LSGM is very expensive (Ga_2O_3 is more than \$2000/kg, Alfa Aesar), so using it as a support component increases SOFC costs. To overcome these two barriers, it is recommended that the feasibilities of following three alternative avenues be investigated.

1. Developing nanosize LSGM powder and applying as thin electrolyte layer on traditional nickel-zirconia based anode support. Hopefully techniques to densify the nanosized LSGM layer below 1200°C can be developed.
2. Using a nickel-zirconia anode but applying thin LSGM layer by plasma spraying. This approach eliminates the need for high temperature firing. But has the challenges of LSGM layer densification and achieving suitable bonding strength between the LSGM layer and the support.
3. Developing a nickel-free anode, for example using $La_{0.75}Sr_{0.25}Cr_{0.5}Mn_{0.5}O_3$.
4. The MTFC design concept for increasing stack volumetric power density and fuel utilization needs to be proved, with effort going into manifold design and current collection.

Appendix: List of Publications

A number of articles have been derived directly from this research and have been published in professional journals or presented at fuel cell conferences. Two patent applications have also been filed.

Journal Articles

1. Yanhai Du, N.M. Sammes, and G.A. Tompsett, "Optimisation Parameters for the Extrusion of Thin YSZ Tubes for Use as an Electrolyte for the SOFC," *Journal of the European Ceramic Society*, **20** (7), 959-965, 2000.
2. Yanhai Du, N.M. Sammes, "Fabrication of Tubular Electrolytes for Solid Oxide Fuel Cells Using Strontium- and Magnesium-Doped $LaGaO_3$ Materials," *Journal of the European Ceramic Society*, **21** (6), 727-735, 2001.
3. Yanhai Du, N.M. Sammes, "Electrical Performance of $LaGaO_3$-Based Tubular SOFCs", *Journal of University of Science and Technology of China*, **32**, 38-48, 2002.
4. Yanhai Du, N.M. Sammes, G.A. Tompsett, D. Zhang, J. Swan and M. Bowden, "Extruded Tubular Strontium- and Magnesium-Doped Lanthanum Gallate, Gadolinium-Doped Ceria, and Yttria-Stabilized Zirconia Electrolytes: Mechanical and Thermal Properties " *Journal of Electrochemical Society*, **150** (1) A74-78, 2003.
5. Yanhai Du, N.M. Sammes, "Fabrication and Performance of $LaGaO_3$-Based Tubular SOFCs", *Ionics*, **9**, 7-14, 2003.
6. N.M. Sammes and Yanhai Du, "The Mechanical Properties of Tubular Solid Oxide Fuel Cells", *Journal of Materials Science*, **38**, 1-6, 2003.

Conference Proceedings, Presentations and Posters

1. Yanhai Du, X. Huang, N.M. Sammes, K. Reifsnider, A.L. Smirnova, "Fabrication and Performance Evaluation of Micro-Tubular SOFCs Using Doped-Lanthanum Gallate Electrolytes", *5th Gordon Conference on Fuel Cells*, Rhode Island, USA, June 27- August 1, 2003.
2. Yanhai Du and Nigel M. Sammes, "Fabrication and Performance of a small SOFC Stack Using Doped Lanthanum Gallate Electrolyte", in *Proceedings of Eighth International Symposium on Solid Oxide Fuel Cells (SOFC VIII)*, Paris, April 28-May 2, 2003. Electrochemical Society Proceedings Volume 2003-07, p1119-1125.
3. Yanhai Du, Nigel M. Sammes, Ray England, "Novel SOFC Tubular Design Configurations", in *Proceedings of Eighth International Symposium on Solid Oxide Fuel Cells (SOFC VIII)*, Paris, April 28-May 2, 2003. Electrochemical Society Proceedings Volume 2003-07, p1077-1081.
4. V. Mandakolathur, Yanhai Du, and Nigel Sammes, "Direct Methane Oxidation in Micro-Tubular SOFCs Using Doped $LaGaO_3$ Electrolyte", in *Proceedings of Eighth International Symposium on Solid Oxide Fuel Cells*

(SOFC VIII), Paris, April 28-May 2, 2003. Electrochemical Society Proceedings Volume 2003-07, p1170-1175.

5. Yanhai Du, N.M. Sammes, "Electrical Performance of $LaGaO_3$-Based Tubular SOFCs", *plenary talk* at the International Workshop on Solid Electrochemical Devices for Energy Conversion & the 11th National Conference on Solid State Ionics, Hefei, China, October 14-19, 2002.
6. Yanhai Du, N.M. Sammes, "Fabrication and Performance of $LaGaO_3$-Based Tubular SOFC's," presented at the 9th EuroConference on Science and Technology of Ionics, Greece, 2002.
7. Yanhai Du, N.M. Sammes, G.A. Tompsett, and M. Bowden, "Comparison of Mechanical and Thermal Properties of the Tubular LSGM, CGO, and YSZ Electrolytes," in *Proceedings of the 7th International Symposium on Solid Oxide Fuel Cells (SOFC-VII)*, ed S.C. Singhal, H. Tagawa, *Electrochemical Proceedings Volume 2001-16*, pp.311-320, The Electrochemical Society, Inc. Pennington, NJ, 2001.
8. Yanhai Du and Nigel Sammes, "Microstructural and Mechanical Properties of Extruded Doped-Lanthanum Gallate Electrolytes", in *Proceedings of the 4th European Solid Oxide Fuel Cell Forum*, Lucerne, Switzerland, pp.783-792, 2000.
9. Yanhai Du and Nigel Sammes, "Microstructure and Mechanical Properties of Extruded LSGM Electrolyte", in *Proceedings of the 6th Annual New Zealand Engineering and Technology Post-Graduate Student Conference*, Auckland, December, pp.189-194, 1999.
10. Yanhai Du and Nigel Sammes, "$LaGaO_3$-based Electrolyte Tubular SOFC Fabrication," in *Proceedings of the 5th Annual New Zealand Engineering and Technology Postgraduate Conference*, ed B. Teekman, P. Milliken, and N. Body, Messey, New Zealand, November, 1998.

Patent Applications

1. Yanhai Du and Nigel Sammes, "Methods of Manufacture of Electrolyte Tubes for Solid Oxide Devices and the Devices Obtained Therefrom," *United State Patent Application Serial No.: 60/458,280*, filed in March 2003.
2. Yanhai Du, Nigel Sammes and Ray England, "Solid State Electrochemical Devices," *United State Patent Application*, filed in April 2003.